PE&RS

May 2022 Volume 88, Number 5

PHOTOGRAMMETRIC ENGINEERING & REMOTE SENSING *The official journal for imaging and geospatial information science and technology*

To have your press release published in *PE&RS*, contact Rae Kelley, rkelley@asprs.org.

ANNOUNCEMENTS

URISA's GIS Hall of Fame Honors persons and organizations that have made significant and original contributions to the development and application of GIS concepts, tools, and/or resources, or the GIS profession.

Their contributions have had a significant and enduring impact on the GIS field or profession, and their work has benefited society as a whole.

Persons inducted into the GIS Hall of Fame have, in their work and professional conduct, exemplified vision, leadership, perseverance, community-mindedness, professional involvement, and ethical behavior.

URISA's Hall of Fame laureates include:

- 2005 Inductees: Edgar Horwood, Ian McHarg, Roger Tomlinson, Jack Dangermond, Nancy Tosta, and the Harvard Lab
- 2006 Inductee: Gary Hunter
- 2007 Inductees: Don Cooke and Michael Goodchild
- 2009 Inductees: Will Craig and Carl Reed
- 2010 Inductee: C. Dana Tomlin
- 2011 Inductees: William Huxhold and Barry Wellar
- 2012 Inductees: National Aeronautics and Space Administration, Natural Resources Canada, Statistics Canada, United States Census Bureau, and United States Geological Survey
- 2014 Inductee: Charles Croner
- 2016 Inductees: Alex Miller, Mark Monmonier, and Waldo Tobler
- 2018 Inductees: Peter Burrough and the National Oceanic and Atmospheric Administration
- 2021 Inductee: URISA's GISCorps

Anyone may nominate a person or organization for induction to URISA's GIS Hall of Fame. Nominations are due on or before May 31, 2022.

Visit https://www.urisa.org/awards/urisa-gis-hall-of-fame-eligibility-criteria-and-nominations/ to learn about URISA GIS Hall of Fame eligibility criteria, nominations, and review process.

Phase One has named Globe Flight GmbH as its reseller of unmanned aerial vehicle (UAV) solutions in Germany and Austria. Based in Barbing, Germany, Globe Flight plans to make the Phase One P3 DJI M300 payload a centerpiece in its comprehensive drone offerings for inspection, surveying, and other geospatial applications.

The Phase One P3 payload addresses the previously unmet commercial need for high-resolution drone imaging while covering large surface areas quickly and safely. The P3 enables Globe Flight to offer its customers a complete fully integrated drone solution for the first.

"Our P3 DJI M300 payload is a perfect complement to Globe Flight's existing products because it opens the door to millimeter-level imaging that was not available with other UAV camera systems," said Carsten Wieser, Area Sales Manager for Central and Northern Europe at Phase One. "The P3 will appeal to Globe Flight's current customers and attract additional users in inspection sectors requiring extremely detailed drone images to inspect their infrastructure."

Globe Flight is an ideal business partner for Phase One in the region, and the two companies will collaborate in Germany and Austria to further cultivate the market for UAV applications.

The German firm is an acknowledged UAV expert, offering a wealth of comprehensive solutions that include DJI sales and maintenance, product testing, regulatory advice, and pilot training. Globe Flight has traditionally equipped customers with DJI drones for use in inspection, surveying, agriculture, and others. The firm expects the P3 will expand these applications into the following specific areas:

- Inspection: Powerlines and power masts, wind turbine, bridges, railroad tracks, roads, building facades and roofs, oil and gas facilities (including flare towers), cellphone tower, solar panels, dams, digital twins.
- Surveying: High-accuracy and wide-area mapping.
- Agriculture: Phenotyping, precision agriculture.

The P3 DJI M300 is a plug-and-play system ready to fly on a DJI Matrice 300 drone with a user-selected option of either the Phase One iXM 100MP or 50MP camera mounted on a new gimbal with integrated laser rangefinder. Phase One offers other drone payloads including versions for MAVlink supported drones and the DJI M600 Pro. All are designed primarily for fast, efficient, and safe inspection of critical infrastructure, yet versatile enough to handle any end user application.

The high-resolution medium-format metric Phase One iXM cameras have four RSM lens options and boast a dynamic range that guarantees sharp image collection in high-contrast or low-light environments. The variety of lens options ensures large surface areas can be captured with millimeter-level detail – even at safe distances from the asset. The new gimbal with the integrated laser rangefinder ensures precise and fast focusing on every shot, eliminating blurry and out-of-focus images, so that large features can be covered in fewer images and shorter missions.

Learn more at https://geospatial.phaseone.com

LatConnect 60 (LC60), an Earth observation and data fusion company based in Perth, Australia, has signed an agreement to work with Gilmour Space Technologies in Queensland to build and launch the first microsatellite in a planned high-resolution hyperspectral imaging constellation. The smart satellites will be placed in 30-degree inclined orbits for frequent revisit data capture over the Earth's equatorial and mid-latitude regions.

"HyperSight 60 will deliver geospatial insights for mid-latitude areas at a level of detail and frequency not possible with other commercial remote sensing systems," said Venkat Pillay, LC60 CEO and Founder. "The addition of Gilmour Space to the LC60 team contributes significantly to the future success of our ambitious plans."

Under the agreement, Gilmour Space will develop the first 100-kilogram HyperSight 60 satellite on its G-class satellite bus (G-Sat), which will be launched on Gilmour's Eris rocket from the Bowen Orbital Spaceport in Queensland, ideally located to place satellites into equatorial and mid inclined orbits. The microsatellite and subsequent constellation will be owned and operated by LC60.

"This agreement would be our second G-class satellite mission on Eris, and we're excited to be working with the pioneering team at LC60 to bring this significant capability to market," said Gilmour Space CEO, Adam Gilmour.

The first HyperSight 60 microsatellite is planned for launch in Q4 2024. Once the entire eight-satellite constellation is operational, an hourly revisit rate will be possible at mid-latitude locations between 30 degrees north and south in Australia, Asia, South America, and Africa. This revisit, combined with the spectral bands collected in high- and medium-spatial resolution, will deliver timely information-rich insights for Agriculture, Forestry, Environmental, Mineral/Oil & Gas, Climate Change, Maritime, and Defence applications.

Established in 2019, LC60 currently owns exclusive rights to 80-centimeter imagery captured over Australia, with global access from a high-resolution multispectral satellite. The Perth-based company has leveraged this imagery along with other geospatial data sets to develop advanced artificial intelligence and machine learning-based data fusion and analysis algorithms for a variety of applications. Most notably, LC60 is now delivering insights to assist Southeast Asian palm and rubber plantations in improving productivity while enhancing environmental sustainability.

LC60 is also focused on designing 'smart' satellites equipped with onboard AI-based computing technology. For the HyperSight 60 constellation, this will enable 'tip-and-cue' capabilities among satellites within the constellation and allow pre-processing of data, including radiometric and geometric correction, to occur in orbit before the data is downlinked to the ground.

"For HyperSight 60 and other planned LC60 constellations, our unique approach to onboard AI sensors, combined with advanced data fusion on the ground, will fill gaps in the insights that can be gleaned from current remote sensing systems," said Pillay.

For more information, contact info@latconnect60.com.

CALENDAR

- 27 May, **ASPRS GeoByte—Deep Fake Geography? A Humanistic GIS Reflection upon Geospatial Artificial Intelligence.** For more information, visit https://www.asprs.org/geobytes.html.
- 23 September, **ASPRS GeoByte— Allen Coral Atlas: A New Technology for Coral Reef Conservation.** For more information, visit https://www.asprs.org/geobytes.html.
- 3-6 October, **GIS-PRO 2022**, Boise, Idaho. For more information, visit https://www.urisa.org/gis-pro.
- 23-27 October, **Pecora 22**, Denver, Colorado. For more information, visit https://pecora22.org/.

PE&RS
PHOTOGRAMMETRIC ENGINEERING & REMOTE SENSING
The official journal for imaging and geospatial information science and technology
May 2022 Volume 88 Number 5

COLUMNS

ANNOUNCEMENTS

DEPARTMENTS

Accurate ground measurements of fractional vegetation cover (FVC) are key for characterizing ecosystem functions and evaluating remote sensing products. The increasing performance of cameras equipped in smartphones opens new opportunities for extensive FVC measurement through citizen science initiatives. However, the wide field of view (FOV) of smartphone cameras constitutes a key source of uncertainty in the estimation of vegetation parameters, which has been largely ignored. We designed a practical method to characterize the FOV of smartphones and improve the FVC estimation.

Existing indoor 3D mapping solutions suffer from high cost and poor portability. In this article, a low-cost and portable indoor 3D mapping approach using biaxial line laser scanners and a one-dimension laser range finder integrated with microelectromechanical systems is proposed.

Vegetation indices (VIs), such as the green chlorophyll index and normalized difference vegetation index, are calculated from visible and near-infrared band images for plant diagnosis in crop breeding and field management. The DJI P4 Multispectral drone combined with the Agisoft Metashape Structure from Motion/Multi View Stereo software is some of the most cost-effective equipment for creating high-resolution orthomosaic VI images. However, the manufacturer's procedure results in remarkable location estimation inaccuracy (average error: 3.27–3.45 cm) and alignment errors between spectral bands (average error: 2.80–2.84 cm). We developed alternative processing procedures to overcome these issues.

A real-time imaging recognition and positioning method based on visible light communication flat light source is proposed.

In flood hazard estimation via the analytic hierarchy process (AHP), using the pixel as the basic unit might lead to accuracy relying on the optimal weighting criteria. To this end, considering the sub-watershed as the basic unit is new. In this article, taking the Chaohu Basin in Anhui Province, China, as a study case, the accuracy of the sensitivity of the pixel-based and sub-watershed-based AHP models influenced by weighting criteria was compared.

See the Cover Description on Page 284

COVER DESCRIPTION

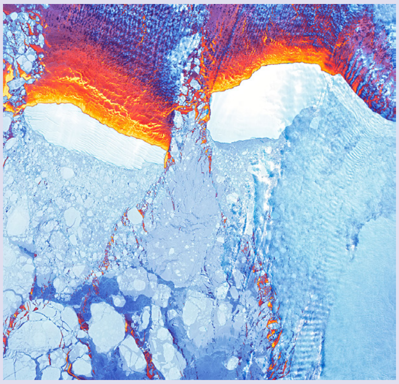

In summer 2019, a rift that began to accelerate across the Brunt Ice Shelf threatened to release an iceberg about twice the size of New York City. But as another Antarctic summer comes to an end, the ice shelf stubbornly continues to hold together. It has even escaped—so far—collisions with numerous icebergs that drifted nearby and threatened to pummel the shelf like an icy wrecking ball.

Throughout the austral summer of 2021-22, bergs in the eastern Weddell Sea drifted south with the Antarctic Coastal Current. Iceberg A-23A—currently the world's largest iceberg—floated freely after wiggling loose from the seafloor where it had been "grounded" (stuck) for decades. And in January 2022, Iceberg D-28 rounded the Stancomb-Wills Glacier Tongue, floating roughly 4,300 kilometers (2,600 miles) from where it broke free of the Amery Ice Shelf in 2019.

The drift of the icebergs has slowed as daylight hours have waned and temperatures have dropped, allowing sea ice to start growing in earnest on the Weddell Sea. The bergs will eventually become fully encased in seasonal sea ice for the austral winter. But for now, their enormous size makes them effective bulldozers, still capable of plowing through the sea ice and leaving paths of open water behind them. Notice also the striking cloud bands near the sides of icebergs D-30A and D-28. These are likely the result of vortices in the air produced by the edges of the thick, table-like bergs.

More bands of clouds are visible north of the bergs. Clouds like these, known as cloud streets or convective roll clouds, often line up when strong, cold winds blow over comparatively warm ocean water. In this instance, the air blowing off Antarctica was "quite cold," according to Bart Geerts, an atmospheric scientist at University of Wyoming. Geerts inferred from the ERA5, a reanalysis product from the European Centre for Medium-Range Weather Forecasts (ECMWF), that the winds that day were blowing from the southwest and would have been about -20°C (-4°F).

The relative warmth of seawater behind the icebergs and within leads in the sea ice is apparent in this month's cover image, acquired on March 9 by the Landsat 8 satellite. The image is false-color, created by blending data from the satellite's Operational Land Imager (for detail and texture) and its Thermal Infrared Sensor (TIRS). The warmest areas (yellow, orange, and red) depict open water and thin, newly formed sea ice. The coldest areas (blue and white) are older, thicker ice, including the icebergs and broken ice rubble in their paths.

https://landsat.visibleearth.nasa.gov/view.php?id=149592

NASA Earth Observatory images by Joshua Stevens, using Landsat data from the U.S. Geological Survey, and MODIS data from NASA EOSDIS LANCE and GIBS/Worldview. Story by Kathryn Hansen with image interpretation by Christopher Shuman, NASA/UMBC, and Bart Geerts, University of Wyoming.

Landsat imagery courtesy of NASA Goddard Space Flight Center and U.S. Geological Survey

asprs THE IMAGING & GEOSPATIAL INFORMATION SOCIETY

PHOTOGRAMMETRIC ENGINEERING & REMOTE SENSING

JOURNAL STAFF

Publisher ASPRS
Editor-In-Chief Alper Yilmaz
Director of Publications Rae Kelley
Electronic Publications Manager/Graphic Artist Matthew Austin

Photogrammetric Engineering & Remote Sensing is the official journal of the American Society for Photogrammetry and Remote Sensing. It is devoted to the exchange of ideas and information about the applications of photogrammetry, remote sensing, and geographic information systems. The technical activities of the Society are conducted through the following Technical Divisions: Geographic Information Systems, Photogrammetric Applications, Lidar, Primary Data Acquisition, Professional Practice, Remote Sensing Applications, and Unmanned Autonomous Systems Division. Additional information on the functioning of the Technical Divisions and the Society can be found in the Yearbook issue of *PE&RS.*

Correspondence relating to all business and editorial matters pertaining to this and other Society publications should be directed to the American Society for Photogrammetry and Remote Sensing, 8550 United Plaza Boulevard, Suite 1001, Baton Rouge, LA 70809, including inquiries, memberships, subscriptions, changes in address, manuscripts for publication, advertising, back issues, and publications. The telephone number of the Society Headquarters is 301-493-0290; the fax number is 225-408-4422; web address is www.asprs.org.

PE&RS. *PE&RS* (ISSN0099-1112) is published monthly by the American Society for Photogrammetry and Remote Sensing, 425 Barlow Place, Suite 210, Bethesda, Maryland 20814-2144. Periodicals postage paid at Bethesda, Maryland and at additional mailing offices.

SUBSCRIPTION. For the 2022 subscription year, ASPRS is offering two options to our *PE&RS* subscribers — an e-Subscription and the print edition. e-Subscribers can add printed copies to their subscriptions for a small additional charge. Print and Electronic subscriptions are on a calendar-year basis that runs from January through December. We recommend that customers who choose print and e-Subscription with print renew on a calendar-year basis.

The rate for a Print subscription for the USA is $1105.00 USD, for Canadian* is $1164.00 USD, and for Non-USA is $1235.00 USD.

The rate for e-Subscription (digital) Site License for the USA and Non-USA is $1040.00 USD and for Canadian* is $1089.00 USD.

The rate for e-Subscription (digital) plus Print for the USA is $1405.00 USD, for Canadian* is $1464.00 USD, and for Non-USA is $1435.00 USD.

*Note: e-Subscription, Print subscription, and e-Subscription plus Print for Canada includes 5% of the total amount for Canada's Goods and Services Tax (GST #135123065). **PLEASE NOTE: All Subscription Agencies receive a 20.00 USD discount.**

POSTMASTER. Send address changes to *PE&RS*, ASPRS Headquarters, 8550 United Plaza Boulevard, Suite 1001, Baton Rouge, LA 70809. CDN CPM #(40020812).

MEMBERSHIP. Membership is open to any person actively engaged in the practice of photogrammetry, photointerpretation, remote sensing and geographic information systems; or who by means of education or profession is interested in the application or development of these arts and sciences. Membership is for one year, with renewal based on the anniversary date of the month joined. Membership Dues include a 12-month electronic subscription to *PE&RS*. To receive a print copy of *PE&RS* there is an additional postage fee of $60.00 USD for U.S. shipping; $65.00 USD for Canadian shipping; or $75.00 USD for international shipping per year. Annual Individual Member dues for members residing in the U.S. and Other Foreign Members are $150.00 USD and $158.00 USD for Canadians. Annual Student Member dues for members residing in the U.S. are $50.00 USD; $53.00 USD for Canadian; and $60.00 USD for Other Foreign Members. A tax of 5% for Canada's Goods and Service Tax (GST #135123065) is applied to all members residing in Canada.

GIS Tips & Tricks

Al Karlin, Ph.D. CMS-L, GISP

Using GIS to Hunt for Easter Eggs – Part 2[1]

While writing GIS software is a big business and no laughing (or trivial) matter, ever since the early days of computer software programs, the authors have displayed their sense of humor, and creativity, by placing little “hidden features or Easter eggs” in their coding. Sometimes these hidden features would display the coders names when a special key sequence or click-pattern was detected. Other times, hidden features, likened to Easter eggs, would be revealed with key combinations. In this month’s column, I highlight two GIS Tips & Tricks that are hard-to-find and/or hard-to-remember.

Hard-to-Find Tip #1—You want to change the way your mouse wheel works

In ArcGIS-Desktop the default mouse wheel direction is to Zoom-OUT when rolling the mouse wheel forward, but in ArcGIS-Pro, the default is just the opposite; rotating the mouse wheel forward Zooms IN. Global Mapper’s default works like ArcGIS Pro. This can get very confusing and frustrating when switching between GIS programs, but there are options, albeit hidden, i.e., hard-to-find, in different menus.

For ArcGIS Desktop (10.X)

Use the Customize | ArcMap Options… from the Main Toolbar (Figure 1) and select the General Tab from the ArcMap Options dialog (Figure 2). Toward the bottom of the dialog are the options for the Mouse Wheel and Continuous Zoom/Pan graphic. Use the radio buttons to customize to your preferences.

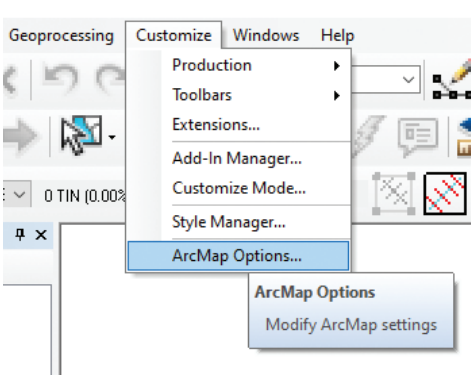

Figure 1. The Customize | ArcMap Options window in ArcGIS Desktop.

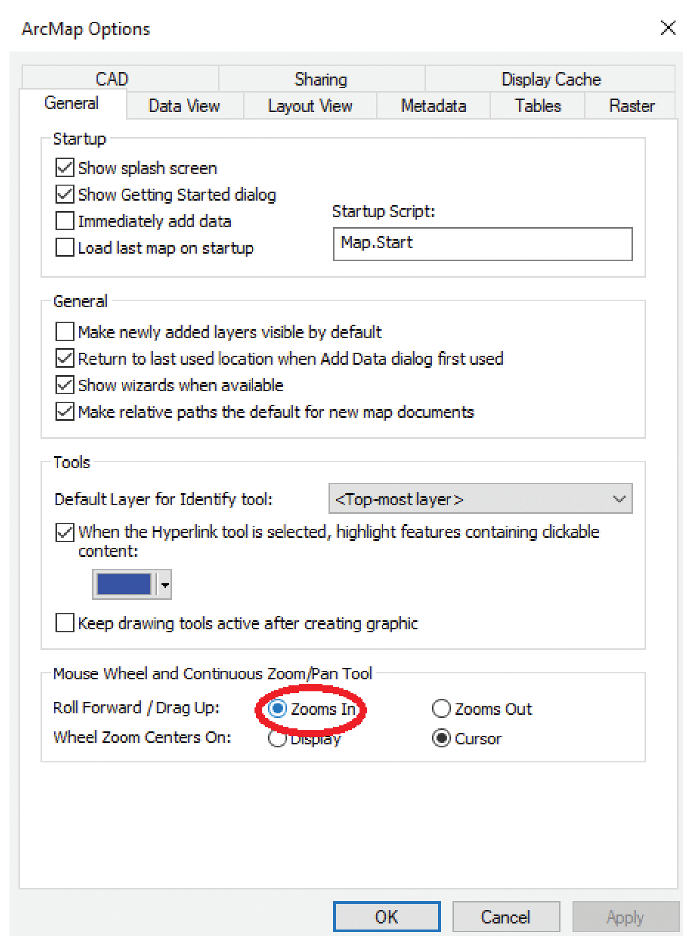

Figure 2. Change the behavior of the mouse wheel using the radio buttons

Extra Hint for ArcGIS Desktop

On this same dialog box, if you are planning on sharing your map document with others in your organization, it might be a good idea to check the:

“Make relative paths the default for new map documents” in the General portion of the dialog box.

[1]*Using GIS to Hunt for Easter Eggs – Part 1* was published in the April 2021 issue of *PE&RS*.

Photogrammetric Engineering & Remote Sensing
Vol. 88, No. 5, May 2022, pp. 285-286.
0099-1112/22/285-286

doi: 10.14358/PERS.88.5.285

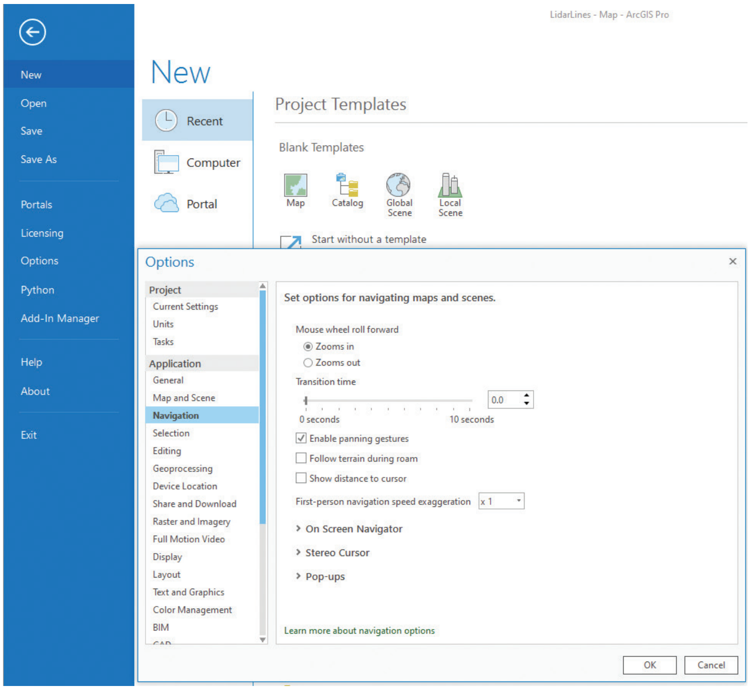

Figure 3. Use the Options | Navigation menu in ArcGIS Pro to modify the mouse wheel behavior.

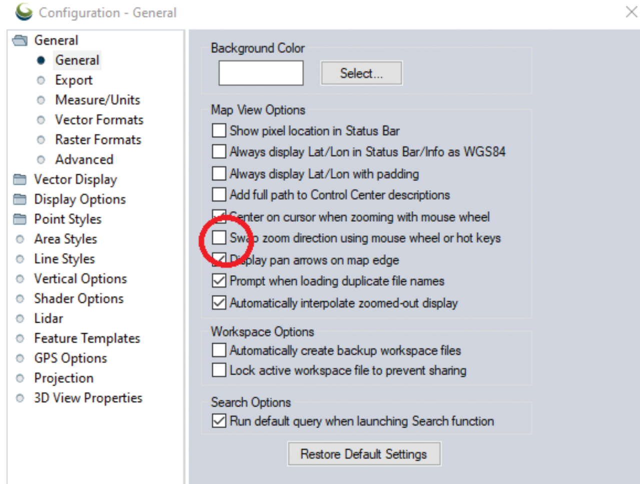

Figure 5. The "Swap zoom direction using mouse wheel or hot keys" checkbox in Global Mapper.

For ArcGIS Pro (2.x)

Use the Project | Options and go to the Navigation Tab (Figure 3). On the top dialog, use the radio button to select your preference for the mouse wheel behavior.

In Global Mapper

The default is to Zoom-IN when rotating the mouse wheel forward. To change the behavior, use the Tools | Configuration Menu (Figure 4) and select the General tab. Midway on the General Tab is a checkbox to alter the mouse wheel direction (Figure 5).

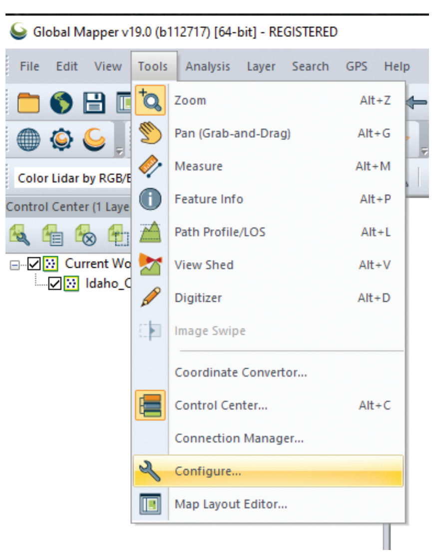

Figure 4. The Global Mapper Tools | Configuration options from the main menu bar.

Bonus Mouse Wheel Tip

While editing vector files, holding the <CTRL> key while "wheeling" may provide finer control over the zoom increment (thanks to Todd Waldorf of Dewberry for this one.)

Hard-to-Remember Tip #2—Accidentally closing the Table of Contents window in ArcGIS Desktop

This is one of those newbee things that I allow my students to ask me 5 times before I start deducting points from their grade. And every semester, I have at least 20% of the class repeatedly ask… What happened to my Table of Contents? While the solution is actually not technically hidden, it is easy to forget.

In ArcGIS-Desktop

To recover a closed Table of Contents, use the Windows | Table of Contents from the main menu (Figure 6).

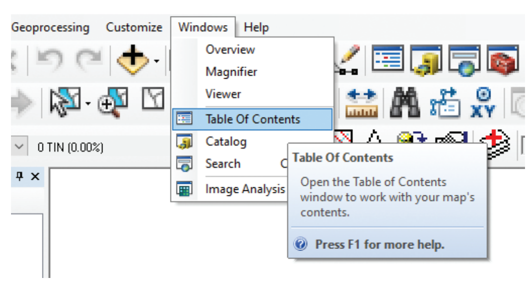

Figure 6. Opening the Table of Contents Window from the Main Menu bar.

You can also open the Arc Catalog window and a Search window from this dropdown.

And that is all there is to a few simple, sometimes hard to find, GIS tricks.

Easter eggs and other hard-to-find tricks can be found in all software packages. Please feel free to share yours with us. Send your questions, comments, and tips to GISTT@ASPRS.org.

Al Karlin, Ph.D., CMS-L, GISP is with Dewberry's Geospatial and Technology Services group in Tampa, FL. As a senior geospatial scientist, Al works with all aspects of Lidar, remote sensing, photogrammetry, and GIS-related projects.

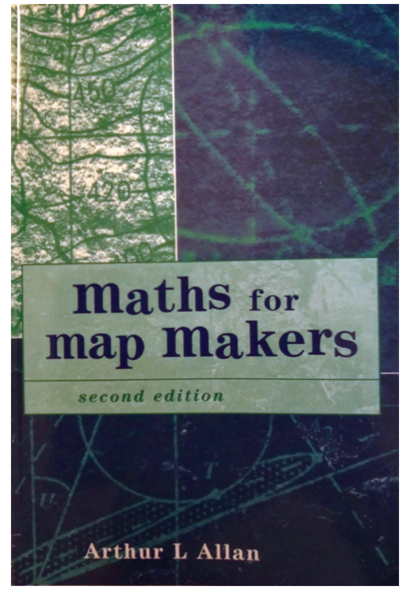

Math for Map Makers

by Arthur L. Allan. Second Edition, 2011 reprint, Whittles Publishing, Scotland, UK. Orginally published 1997.

Reviewed by Melissa J. Rura-Porterfield, Ph.D. Memphis, Tennessee.

As some folks who know me know, I tend to gravitate to indices, I might even start reading a book in the appendices and seem to as I age to find that harder and harder to abstain from. I suppose years of work on updating a glossary that has yet to see the light of day may have played a part in driving me to that but in truth often savvy authors hide their best gems in the safety of an appendix.

My first impression of "*Maths for Mapmakers*" came many years ago, being published first in 1997 while I was still a student. This impression might have been a groan or a comment something like, "***Maths***, what is that!?" but being so long ago I don't rightly recall. Needless to say since that time, reissued, twice this text has brought ***Maths*** to a large swath of mapmakers for nearly a generation.

The book consists of 394 pages, divided into 13 chapters and a reference section including 4 appendices, a summary of formulae and an index. The author encourages all readers to pause for the "How to Read this Book" section and this reviewer concurs wholeheartedly. Here the author sections his book, placing chapters 1-5, which include (1) Numbers and Calculation, (2) Plane Geometry, (3) Trigonometry, (4) Plane Coordinates, (5) Problems in Three Dimensions, into a group that should be read and the problems worked in order as if one was building or reinforcing the foundation of mathematical understanding in mapping. Whereas the later chapters 6-13, which include (6) Areas and Volumes, (7) Matrices, (8) Vectors, (9) Calculus, (10) Conic Sections, (11) Spatial Trigonometry, (12) Solutions of Equations, (13) Least Squares Estimation, can be worked more like case studies on these foundations and not necessarily in the order they are found in the book. Essentially splitting the book into lower-level and upper-level courses in mapping mathematics.

Each chapter has a list of both formulae and "key words" or vocabulary words that should have been defined within its pages. I remember as a student the frustration and relief when I finally understood the chapter 6 key word "Hero's Formula" was in the chapter 6 formula list as "$\Delta = \frac{1}{2}\, bc \sin A$" and that was the same as the area of a triangle I already knew from Chapter 3, $\Delta = \sqrt{[s(s-a)\,(s-b)\,(s-c)]}$, where $2s = a + b + c$ [see, Equation (3.31) and Equation (6.2)]. Of course, had I not started my homework before reading the chapter, I probably would have had less frustration. Nevertheless, I did get an opportunity to fumble around in chapter 3 to refresh my acquaintance with triangles and their areas which did me no harm in the end.

Another anecdote of floundering around in Chapter 3 comes from Section (3.6) *Coordinate Axes and Bearings*. The complete anecdote is too lengthy for this book review, but suffice to say in using Peter Dale's book[1] "*Introduction to Mathematical Techniques Used in GIS*," I came across his clarification of the difference between how a mathematician and a surveyor measure an angle [see, page 67, Figure (5.9) in Dale's book] and although, this may sound like the beginning of a bad science joke; if you want to know the difference between how a mathematician, a surveyor, a cartographer, and a geographer measure an angle that is on page 63 in Figure (4.1) of Allan's book. Dale's explanation of just the mathematician and the surveyor is better equated to Section (3.6) in Allan's book, but don't start there, go to Figure (4.1) first and use it like the Rosetta Stone for angle measurements.

Although each chapter is the source of many useful exercises used to learn mathematics in mapping, one of the chief complaints of this text is there is no answer key printed in the book for these exercises. And subsequent printings have pages with ink shortage running down the left side margin. Generally, it is the margin calculator symbol to indicate

[1]Dale, Peter "*Introduction to mathematical techniques used in GIS*," CRC Press/Taylor & Francis, [2014].

Photogrammetric Engineering & Remote Sensing
Vol. 88, No. 5, May 2022, pp. 287-288.
0099-1112/22/287-288

doi: 10.14358/PERS.88.5.287

an exercise problem that is obscured but in some places also words in a paragraph are also obscured. Moreover, the formulae and "key word" lists are in every chapter but as this reviewer looked for a list of figures for reference to her great disappointment there is none. The strength and usefulness of the many figures warranted a list that could be referenced. This reviewer understands the unnecessary extra work of naming each figure but indexing a Figure's or Table's chapter and section could have been very helpful.

List of Figures/Tables	Name	Chapter	Section
Figure (2.5 – 2.7)	Reference Grid	2	4
Figure (2.8)	Parallelogram, rectangle, square, and rhombus	2	5
Figure (2.9 - 2.10)	Pythagoras's theorem for a right angled triangles	2	6

My take-home jewel from this text is in Appendix 3, page 368, another Rosette Stone, this time for Least Squares Estimation. How many times have I heard someone say, "He uses the Ohio State least squares notation, I don't get it." Or "He must have learned that notation from Purdue, I am lost?!" Here, we are all reminded that we may speak using many different notations, to solve many similar problems using similar assumptions to find and adjust for error. We must learn to communicate. Don't give up, look-up! The answer is to be found!

Appendix A3: Notation for Least Squares

Author	Observation Matrix	Weight Matrix	Normal Equations Matrix	Dispersion Matrix
Allan[7]	$Ax + L = v$ $Ax + Cv + L = 0$	W	$Nx = b$	D
Cooper[1, 6]	$Ax = B + V$ $Ax + Bv = b$	W	$A^tWx = A^tb$ Note the lower case t	Q
American Manuel of Photogrammetry[2]	$B\Delta - \ell = v$ $B\Delta - \ell = Av$	P	$B^TP\Delta = B^TP\ell$	Q
Mikhail[3]	$A(\ell + v) = d$ $Av + B\Delta = f$ $C\Delta = g$	W	N	Q
Wolf[4]	$AX = L + V$	W	$Nx = A^TL$	Q
Koch[5]	$Xß = y + e$	P	$X^TXß = X^Ty$	D

[1]M.A.R. Cooper, 1987, *Control Surveys in Civil Engineering*, Collins (ISBN 0-00-383183-3,381Pages)

[2]American Society of Photogrammetry, 1966, *Manual of Photogrammetry*, Library of Congress Catalog No 65-20813 Vol 1

[3]E. M. Mikhail, 1976, *Observations and Least Squares*, Dun-Donnelley, (ISBN 0-7002-2481-5, 497 Pages)

[4]P.R. Wolf and C.D. Ghilani, 1997, *Adjustment Computations*, Wiley (ISBN 0-471-16833-5, 564 pages)

[5]K.R. Koch, 1997, *Parameter Estimation and Hypothesis Testing in Linear Models*, Springer (ISBN 3-540-65257-4 325 pages)

[6]M.A.R. Cooper and P.A. Cross, 1988, Statistical Concepts and the Application in Photogrammetry and Surveying, *Photogrammetric Record*, Vol XIII, No 73, 645-678

[7]A.L. Allan and N. Atkinson, "Back to Basics' Series Nos 14 to 24 – Least Squares Statistics and all that, Survey Review, Vols 35 and 36 Nos 272 to 282

This reviewer does recommend this text to a large swath "*of geomatics including surveying, cartography and photogrammetry, geography and civil engineering and for the use in industry or academia*" as the book's back cover suggests, but I suppose many of us have known that for years.

Grids & Datums

BY Clifford J. Mugnier, CP, CMS, FASPRS

THE KINGDOM OF SWEDEN

The Grids & Datums column has completed an exploration of every country on the Earth. For those who did not get to enjoy this world tour the first time, *PE&RS* is reprinting prior articles from the column. This month's article on the Kingdom of Sweden was originally printed in 2004 but contains updates to their coordinate system since then.

Inhabited during the Stone Age, several independent tribes lived in Sweden by the 9th century A.D. During that time, those adventurous tribes were among the Scandinavians known as the Vikings. Loosely united and converted to Christianity a couple centuries later, the Swedes conquered the Finns; they joined Norway and Denmark, and finally broke away in 1537 under Gustav I Vasa. Sweden became a constitutional monarchy in 1809.

Sweden is mostly flat with gently rolling lowlands; there are mountains in the west along the Norwegian border, and the kingdom is slightly larger than California. The lowest point is the reclaimed bay of Lake Hammarsjon, near Kristianstad (–2.41 m); the highest point is Kebnekaise (2,111 m).

According to the Lantmäteriet, "The '*geometriska jordeböcker*' are the oldest large-scale maps in Sweden. One of the main tasks of the Land Survey following its establishment in 1628 was to carry out the mapping of villages and individual farms and their lands. It was primarily Crown farms that were the focus of interest. Cultivated fields and meadowland were mapped and information concerning yields and other information related to income and economic matters was collected. It is not clear whether the original purpose of the mapping was, in fact, to form the basis for taxation, but it can definitely be seen as the predecessor to the Swedish land use maps (*Ekonomiska kartan*). The maps are unevenly distributed across Sweden. They are collected in large volumes sorted according to parish and district. The '*geometriska jordeböcker*' should not be confused with the Crown's standard '*jordeböcker*' which cover landed properties and contain fiscal information about them. The Crown's '*jordeböcker*' can be looked upon as being the first Swedish real property register and the '*geometriska jordeböcker*' as the first cadastral index maps. There are around sixty

volumes for the period between 1630 and 1650. Most of the maps are at a scale of 1:5000. We have only included in this series the volumes that have been scanned and are in digital format. To find older '*geometriska jordeböcker*' which are not yet scanned, you should go to the series Cadastral Maps. In The Land Survey map archives there are more than a hundred volumes of maps titled '*geometriska jordeböcker*' dating from the latter half of the 1600s and the early part of the 1700s. The maps are at varying scales, although most of them are large-scale maps. They mainly comprise farm maps that were produced for taxation purposes, maps to be used as the basis for the recruitment of and provision of material support of soldiers, and maps needed for the organization of the return of land by the Church to the Crown."

During the early 18th century, the French scientist, Maupertuis joined with the Swedish astronomer, Celsius on the French expedition to Lapland for the determination of the length of a degree of the meridian arc. This was considered

Photogrammetric Engineering & Remote Sensing
Vol. 88, No. 5, May 2022, pp. 289-291.
0099-1112/22/289-291

doi: 10.14358/PERS.88.5.289

an expedition for insurance in case the sister trip to South America (Ecuador, *PE&RS* May 1999), was not conclusive in proving the shape of the Earth. The area chosen for the chain of north-south triangles is now the southern land border between Sweden and Finland. Starting at the Lutheran church steeple in the city of Torneå (Torne) on the Gulf of Bothnia, the chain extended northwards along the Torne River to the (now) Finnish town of Pello. Maupertuis published his book on the Lapland expedition in 1737.

Soon after the commencement of the constitutional monarchy, the military survey of the kingdom was begun in 1811. Sweden gave up Swedish Pomerania in return for Norway, which entered into a personal union with Sweden (1814-1905). A civilian mapping authority for the compilation of an economic map was formed in 1859. The military and civilian mapping agencies were consolidated in 1894 and was known as the *Rikets Allmänna Kartverk* (RAK). After a series of consolidations and mergers, the current national mapping organization of the National Land Survey (*Statens Lantmäteriet*) was formed in 1985.

According to a personal communication from Dr. Lars Sjöberg of 7 November 1980, "The first systematic triangulation of Sweden started in 1805. All calculations were made on the ellipsoid, for Northern Sweden on Svanberg's ellipsoid and for Southern Sweden on Clarke 1880. For official maps (in general scale 1:100,000) Spens' projection, was used for Southern Sweden (up to Lat 61° 30´) and a conform conic projection for Northern Sweden. In 1903 a new triangulation started in Southern Sweden. The calculations were made in plane coordinates (x, y) (Gauss-Hannover's projection and Bessel's ellipsoid). The scale in the net was determined from a Danish baseline, which was measured in 1838. A new measurement of the baseline was made in 1911 and that measurement differed significantly from the earlier one. In 1938, when 5 Swedish baselines and 6 azimuths had been measured, the scale and orientation of the nets (obtained from the above measurements) were compared. The measurements of the Swedish baselines agreed better with the 1911 measurements than with the observations of 1838. It was then decided to enlarge the net with a factor 1.00002 and turn it clockwise 0.00005 radians around a point in Southern Sweden. Up till then all calculations had been made in 6 different zones with the longitude of origin referring to '*Stockholms gamla observatorium*' (The Old observatory of Stockholm), which is 18º 03´ 29.8˝ E of Greenwich. The longitude of origin for each zone was 6º 45´ W, 4º 30´ W, 2º 15´ W, 0º, 2º 15´ E, and 4º 30´ E of Stockholm's *gamla observatorium*. This system is still in use for large scale maps. [*Ed's. note: this letter from Dr. Sjöberg was dated 1980.*] In 1938, *Rikets Allmänna Kartverk* decided to reduce the number of projection zones to 3, namely 2º 15´ W, 0º, and 4º 30´ E for official maps with FE 1,500,000 m, 2,500,000 m and 3,500,000 m, respectively. In 1945, RAK decided to use only one projection zone for official maps namely 2º 15´ W with FE 1,500,000 m. Common for all zones are that latitude of origin is 0º and FN is 0. The scale factor along the central meridian m_o is 1.0000. For some official maps there is also a grid net in the UTM projection. This net is based upon the European Datum 1950 with $m_o = 0.9996$ and FE 500,000 m."

I later wrote back to Dr. Sjöberg in July of the following year and inquired about the Spens projection. In Dr. Sjöberg's reply of 7 August 1981, "The Spens projection differs somewhat from the Lambert conic projection. Spens' projection satisfied the following conditions:

1. The scale factor (m_o) along the parallels φ_1 = 65º 50´ 20.4˝ and φ_2 = 55º 21´ 19.4˝ are equal.
2. The minimum scale factor between φ_1 and φ_2 equals m_o^{-1}. The first condition yields log n = 9.9407276–10 and φ_o = 60º 44´ 29.6˝

(These are Spens' results from 1817 used in the tables of Spens projection. The correct values are log n = 9.94072828–10 and φ_o = 60º 44´ 30.2˝.) From the second condition one obtains $m_o = 0.997903542$. The x-axis of the Spens projection is the meridian 5º W of the Old Observatory of Stockholm, directed southward. The origin is located at the parallel circle 72º. The Spens projection was described by P.G. Rosen (1876) in *Den vid Svenska Topografiska Kartverket använder projektionsmetoden*, 32 pp. As far as I know there is no word '*Gradblätterkarten*.' '*Karten*' means maps and '*Gradblätter*' 'degree maps.' However I think you refer to the polyconic projection used for the old '*Generalstabskarten*' in the north of Sweden. This means that the conic projection is used repeatedly at each ½º parallel. Each map is made as a 'Gradblatt' limited by parallel circles of every ½º and meridian of equidistance 1½º. Clarke's ellipsoidal parameters were used. The arctriangulation in Lappland (Tornedalen) carried out in 1730-1736 under the supervision of the Paris Academy was repeated in 1801-1803. From these latter measurements Svanberg computed the Earth dimensions (published 1805)."

According to a paper published (in German) by Professor im Generalstabe Karl D. P. Rosén, Stockholm 1933, the Svandberg ellipsoid parameters used were a = 6,376,797 m and $^1/_f$ = 304.2506. Similarly, the published parameters for the Clarke 1880 ellipsoid as used for the Northland projection were a = 6,378,249.2 m and $^1/_f$ = 293.465. The specific formulae used in Sweden were discussed in 1951 by G.A. Rune in *Tabeller Till Gauss Hannoverska Projektion, Tables for Gauss's Hanoverian Projection* where he states (in English) in the Preface, "For facilitating the computation of the modern triangulation of Sweden, begun in 1903, the General Staff professor of that time Dr. Karl D. P. Rosén introduced the Gauss's Hanoverian projection, often called the Gauss-Krüger or, briefly, the Gauss's projection, a projection well fitting Sweden with it marked extension in the meridian." Note that the defining parameters of the Bessel 1841 ellipsoid are: a = 6,377,397.155 m and $^1/_f$ = 299.1528128. All of the Swedish classical datums have the same origin at the

Old Stockholm Gamla Observatory where: $\Phi = 59^\circ\ 20'\ 32.7''$ N and $\Lambda = 18^\circ\ 03'\ 29.8''$ E. The triangulation of Sweden from 1903-1938 consisted of 170 triangles and was observed with Wanschaff and Hildebrand instruments achieved an average Ferrero's formula accuracy of 0.41˝. The later Swedish triangulation of 1939-1953 consisted of 222 triangles and was observed with Wild T-3 theodolites and achieved an average Ferrero's formula accuracy of 0.40˝. That classical triangulation is defined as the RT 38 (*rikstrianguleringen* 1903-1950) datum. It has been replaced with RT 90 also called *Rikets Koordinatsystem* 1990, which is a local geodetic datum based on the Swedish third national triangulation (1967-1982), and is also referenced to the Bessel 1841 ellipsoid. The corresponding plane coordinate system is denoted **NT 90 2.5 gon V 0:–15** and is obtained by a Gauss-Krüger Transverse Mercator projection of the RT 90 latitudes and longitudes. The Central Meridian is $\lambda_o = 15^\circ\ 48'\ 29.8''$ E, the scale factor at origin $m_o = 1.0$, and FE = 1,500 km. The Central Meridian was originally interpreted as "2.5 Gon West of the Old Observatory of Stockholm," but is now defined as relative to Greenwich (1 Gon = 0.9 degrees).

According to the *Lantmäteriet*, "The original map sheet system in Sweden is based on a grid in RT 90 2.5 gon V 0:–15 with the SW corner at (North. = 6100 000 m, East. = 1200 000 m), and NE corner at (North. = 7700 000 m, East. = 1900 000 m). This area is divided into 50 km squares, which are enumerated with 0 – 32 in South-North direction, and lettered with A - N in West-East direction. Each 50 km square can be subdivided into four 25 km topographic map sheet squares, or subdivided into 100 5×5 km cadastral map sheets, which are enumerated from South to North by 0 - 9. and lettered from West to East by a - j. This original basic map sheet system has been modified in several ways for the modern series of maps, but the basic grid square notation is still frequently used, for instance in the numbering of geodetic control points. For larger scale mapping (>1:10000) there are six different zones of Transverse Mercator projections used in Sweden, in order to reduce the map projection errors. The other 5 zones apart from '2.5 gon V' differ only in the longitude of the central meridians, which are spaced by 2° 15'. The boundaries of the projection zones are adjusted to follow administrative borders if possible. The coordinate system 'RT 90 5 gon V 61:-1' has the map projection parameters: Central meridian: 13° 33´ 29˝.8 East Greenwich, False Easting: 100 000 m, False Northing: –6,100,000 m. Example of a point's coordinates in different coordinate systems: x (Northing) = 6,200,000.000; y (Easting) = 1,300,000.000 in 'RT 90 2.5 gon V 0:–15' x (Northing) = 6,195,783.588; y (Easting) = 1,440,736.999 in 'R T 90 5 gon V 0:–15' x (Northing) = 95,783.588; y (Easting) = 40,736.999 in 'RT 90 5 gon V 61:–1'."

"SWEREF 99 is a Swedish realization of ETRS 89. The processing of the GPS data was performed according to the EUREF guidelines and was based on observations made on permanent reference stations in Sweden (SWEPOS), Denmark, Finland (FinnRef), and Norway (SATREF) during the GPS-weeks 1014-1019 (June-July 1999).

SWEREF 99 coincides with WGS 84[G730] and WGS 84[G873] within some decimeters. Coordinates can be transformed from the Swedish coordinate datum RT 90, to SWEREF 99 through a 7-parameter transformation given below (estimated accuracy of 7 cm, 1 sigma, 2D). The ellipsoid used with SWEREF 99 is GRS 80: a = 6378137 $^1/_f$ = 298.257222101. SWEREF 99 replaces SWEREF 93 (the former realization of ETRS 89). If one prefers to define a transformation in the direction RT 90 to SWEREF 99, use the following parameters: ΔX= +414.1 m, R_x = +0.855 arc seconds, ΔY = +41.3 m R_y = – 2.141 arc seconds, ΔZ = +603.1 m R_z = +7.022 arc seconds, and δ = 0.0 ppm (scale = 1.0)."

For example latitude, longitude and height above the Bessel 1841 ellipsoid in RT 90: $\varphi = 58^\circ\ 00'\ 01.213296''$ $\lambda = 17^\circ\ 00'\ 11.683659''$ h = –5.397 m, latitude, longitude and height above the GRS 80 ellipsoid in SWEREF 99: $\varphi = 58^\circ\ 00'\ 00.0''$, $\lambda = 17^\circ\ 00'\ 00.0''$ h = 30.000 m. Much to my surprise, when I carefully examined the published parameters, I realized that the rotation convention is the same as that used by the United States and by Australia. Thanks to Professor Lars Sjöberg now of the Geodesy Group at the Royal Institute of Technology in Stockholm for his patient help many years ago.

The Kingdom of Sweden Update

Sweden operates the Nordic Geodetic Commission (NKG) Analysis Center and currently operates 90 GNSS station sites in cooperation with the EUREF permanent network. As of 2018, there were over 3900 current subscriptions to the SWEPOS (Swedish National network of permanent GNSS stations operated by Lantmäteriet). Of interest is that SWEPOS offers not only dual-frequency correction services, but a single frequency DGNSS service has been offered since 2016, something not offered by the U.S. National Geodetic Survey. The new national height system RH2000 was implemented in 2005 and consists of about 50,000 passive benchmarks. So far 247 municipalities have implemented the replacement of RH2000 for their legacy height systems. Sweden had upgraded its FG-5 Absolute Gravity Meter to an FG-5X (Like LSU currently uses), and has observed at 14 sites as well as at 96 sites with A-10 Absolute Gravity Meters and at 200 sites with Relative Gravity Meters. Furthermore, the superconducting gravity meter at Onsala Space Observatory installed in 2009 has been regularly calibrated by Lantmäteriet's FG-5/FG-5X in June 2018 which was the seventh performed calibration.

The contents of this column reflect the views of the author, who is responsible for the facts and accuracy of the data presented herein. The contents do not necessarily reflect the official views or policies of the American Society for Photogrammetry and Remote Sensing and/or the Louisiana State University Center for GeoInformatics (C^4G).

This column was previously published in *PE&RS*.

STAND OUT FROM THE REST

EARN ASPRS CERTIFICATION

ASPRS congratulates these recently Certified and Re-certified individuals:

CERTIFIED MAPPING SCIENTISTS GIS/LIS

Xiangheng Yang, Certification #GS309
Effective January 24, 2022, expires January 24, 2027

CERTIFIED MAPPING SCIENTIST LIDAR

Jan Lee Van Sickle, Certification #L069
Effective December 9, 2021, expires December 9, 2026

CERTIFIED PHOTOGRAMMETRIST

Benjamin Downey, Certification #CP1666
Effective January 28, 2022, expires January 28, 2027

James B Gillis, Certification #CP1660
Effective August 25, 2021, expires August 25, 2026

Christopher Reagan, Certification #CP1663
Effective January 14, 2022, expires January 14, 2027

CERTIFIED LIDAR TECHNOLOGIST

Daniel Grosche, Certification #LT071
Effective February 4, 2022, expires February 4, 2025

Jacob Gresham, Certification #LT070
Effective October 4, 2021, expires October 4, 2024

CERTIFIED GIS/LIS TECHNOLOGIST

Devin Gerzich, Certification #GST310
Effective February 3, 2022, expires February 3, 2025

Tracy Ray, Certification #GST311
Effective February 8, 2022, expires February 8, 2025

RECERTIFIED PHOTOGRAMMETRIST

Paul Badr, Certification #R1011CP
Effective May 20, 2022, expires May 20, 2027

Qassim Abdullah, Certification #R900CP
Effective February 12, 2022, expires February 12, 2027

Jeffrey L. Padgett, Certification #R760CP
Effective February 20, 2021, expires February 20, 2026

Robert H. Tuck, Certification #R907CP
Effective February 12, 2022, expires February 12, 2027

Gerard J. Gouldson, Certification #R1058CP
Effective December 6, 2021, expires December 6, 2026

John F. Schuenemann, Certification #R1614CP
Effective January 30, 2022, expires January 30, 2027

Douglas Johnson, Certification #R1512CP
Effective November 7, 2021, expires November 7, 2026

Barbora Ubar, Certification #R1611CP
Effective January 12, 2022, expires January 12, 2027

Joshua Persson, Certification #R1316CP
Effective December 26, 2021, expires December 26, 2026

Cody Condron, Certification #R1616CP
Effective April 11, 2022, expires April 11, 2027

Sagar Shriram Deshpande, Certification #R1527CP
Effective March 14, 2022, expires March 14, 2027

Thomas Jeff Young, Certification #R1010CP
Effective March 21, 2022, expires March 21, 2027

RECERTIFIED MAPPING SCIENTISTS GIS/LIS

Peter Cormish, Certification #R250GS
Effective February 7, 2022, expires February 7, 2027

Connie Li Krampf, Certification #R247GS
Effective December 27. 2021, expires December 27, 2026

Jason Zilka, Certification #R286GS
Effective July 15, 2021, expires July 16, 2026

RECERTIFIED MAPPING SCIENTIST – REMOTE SENSING

Christopher Lippitt, Certification #R188RS
Effective November 5, 2020, expires November 5, 2025

Radha Krishna Kandukuri, Certification #R197RS
Effective October 18, 2021, expires October 18, 2026

RECERTIFIED MAPPING SCIENTISTS LIDAR

Srinivasan S. Dharmapuri, Certification #R012L
Effective April 30, 2022, expires April 30, 2027

ASPRS Certification validates your professional practice and experience. It differentiates you from others in the profession. For more information on the ASPRS Certification program: contact **certification@asprs.org**, visit **https://www.asprs.org/general/asprs-certification-program.html.**

COUNCIL OF ENGINEERING AND SCIENTIFIC SPECIALTY BOARDS CESB 1990

asprs THE IMAGING & GEOSPATIAL INFORMATION SOCIETY

INTRODUCING THE MURRAY STATE ASPRS STUDENT CHAPTER!

Student chapters represent an important part of our ASPRS community. The Student Advisor Council uses this column to shine the light on these hard-working students to honor their work and to introduce them to our larger geospatial community! This month we are highlighting the Murray State student chapter, based in Murray State University, Kentucky. This chapter is in the ASPRS Mid-South region.

The Murray State chapter consists of members majoring in various backgrounds, but who all are working diligently to inspire students of how awe-inspiring and powerful the subject photogrammetry and remote sensing can be. As of right now, since the chapter is relatively new, there are roughly seven members including Pamela Rodriguez (President), Logan McGowan (Vice President), Haley Stiles (Secretary), Atherton Milford (Treasurer), Melanie Johnson (Public Relations), Marshall Thompson, and Steven Collett. Together, this chapter is collectively working towards planning educational events around campus about the everyday usage of remote sensors, promoting ASPRS through upcoming workshops that can be available to others to learn GIS software, and encouraging others to become ASPRS members to learn about career opportunities and connect with mentors in the workforce.

Although COVID has made it difficult for this chapter to plan events, the Murray State Chapter is optimistic about planning new events and activities in the future and is committed to sharing any opportunities to students in the meantime. To learn more, email Pamela Rodriguez prodriguez2@murraystate.edu.

If you are interested in participating in SAC activities:

- Join us every other Thursday from 10-11 am PST!
- Join us via this zoom link: https://tinyurl.com/SACASPRSMeeting

Murray State University Student Chapter Members

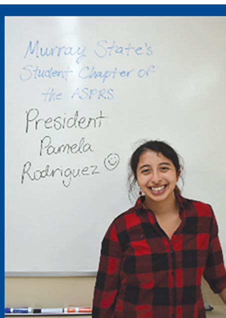

Pamela Rodriguez
President

Logan McGowan
Vice President

Atherton Milford
Treasurer

Melanie Johnson
Public Relations

Haley Stiles
Secretary

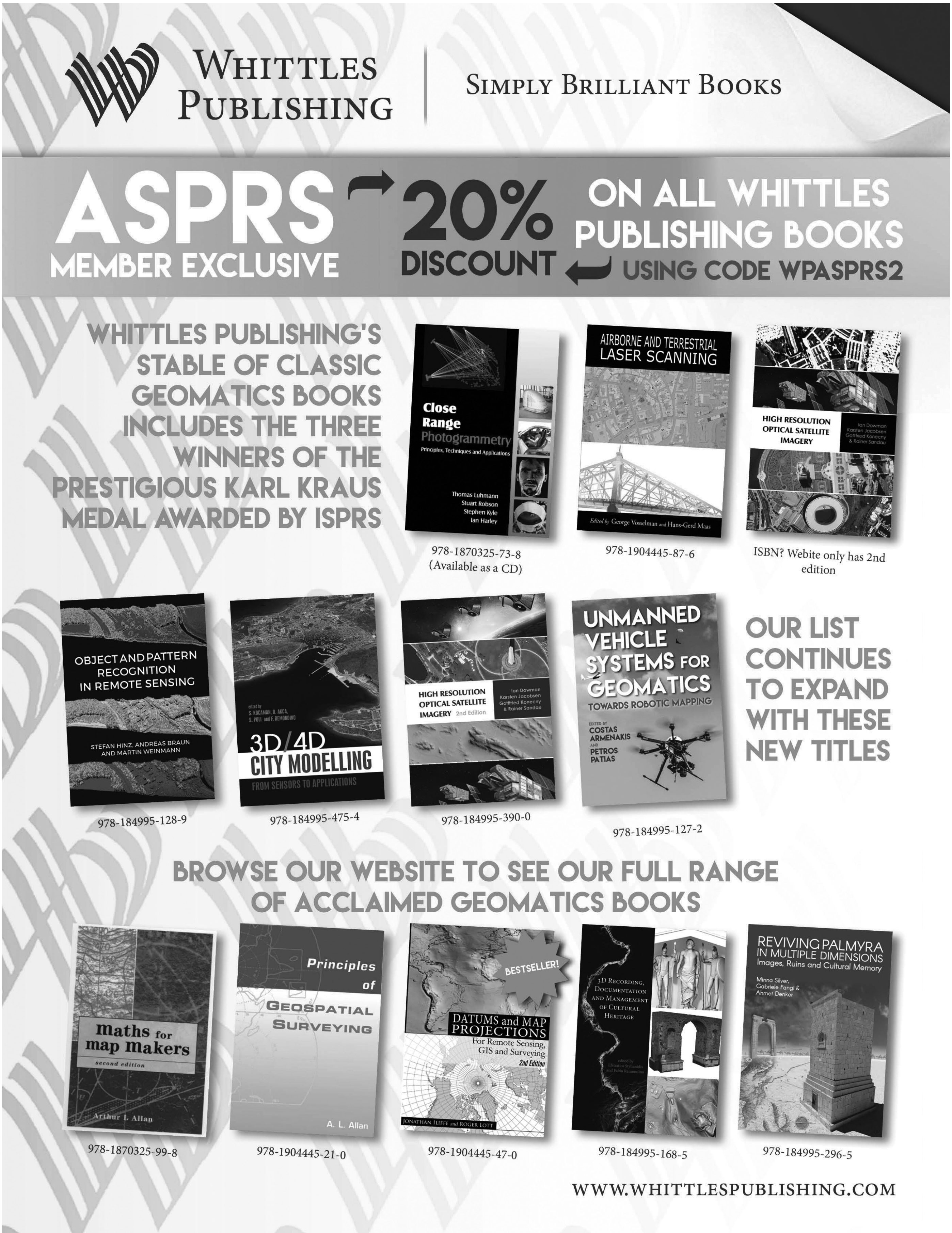

WHITTLES PUBLISHING
SIMPLY BRILLIANT BOOKS
ASPRS MEMBER EXCLUSIVE
20% DISCOUNT
ON ALL WHITTLES PUBLISHING BOOKS
USING CODE WPASPRS2
WHITTLES PUBLISHING'S STABLE OF CLASSIC GEOMATICS BOOKS INCLUDES THE THREE WINNERS OF THE PRESTIGIOUS KARL KRAUS MEDAL AWARDED BY ISPRS
Close Range Photogrammetry
Principles, Techniques and Applications
Thomas Luhmann
Stuart Robson
Stephen Kyle
Ian Harley
978-1870325-73-8
(Available as a CD)
AIRBORNE AND TERRESTRIAL LASER SCANNING
Edited by George Vosselman and Hans-Gerd Maas
978-1904445-87-6
HIGH RESOLUTION OPTICAL SATELLITE IMAGERY
Ian Dowman
Karsten Jacobsen
Gottfried Konecny
& Rainer Sandau
ISBN? Webite only has 2nd edition
OBJECT AND PATTERN RECOGNITION IN REMOTE SENSING
STEFAN HINZ, ANDREAS BRAUN AND MARTIN WEINMANN
978-184995-128-9
3D/4D CITY MODELLING
FROM SENSORS TO APPLICATIONS
978-184995-475-4
HIGH RESOLUTION OPTICAL SATELLITE IMAGERY 2nd Edition
Ian Dowman
Karsten Jacobsen
Gottfried Konecny
& Rainer Sandau
978-184995-390-0
UNMANNED VEHICLE SYSTEMS FOR GEOMATICS
TOWARDS ROBOTIC MAPPING
EDITED BY COSTAS ARMENAKIS AND PETROS PATIAS
978-184995-127-2
OUR LIST CONTINUES TO EXPAND WITH THESE NEW TITLES
BROWSE OUR WEBSITE TO SEE OUR FULL RANGE OF ACCLAIMED GEOMATICS BOOKS
maths for map makers
second edition
Arthur L Allan
978-1870325-99-8
Principles of Geospatial Surveying
A. L. Allan
978-1904445-21-0
BESTSELLER!
DATUMS and MAP PROJECTIONS
For Remote Sensing, GIS and Surveying
2nd Edition
JONATHAN ILIFFE and ROGER LOTT
978-1904445-47-0
3D Recording, Documentation and Management of Cultural Heritage
978-184995-168-5
REVIVING PALMYRA IN MULTIPLE DIMENSIONS
Images, Ruins and Cultural Memory
Minna Silver,
Gabriele Fangi &
Ahmet Denker
978-184995-296-5
WWW.WHITTLESPUBLISHING.COM

In Memoriam

J. Ronald Eyton

1942-2022

It is with a heavy heart that we announce the passing of our faculty colleague, Ron Eyton, on March 14, 2022. His death, in a hospital in Vancouver, BC, following a sudden illness was unexpected.

Ron was raised in Atikokan near present Thunder Bay, Ontario. Ron's father was a chemist at a local iron mine and helped Ron develop his life-long love of experimentation, photography, and cartography. Summer jobs in and around the mines convinced Ron to pursue a career in academic cartography. In a span of ten years, Ron completed degrees from Rochester Institute of Technology (AAS photographic science), the University of North Dakota (PhB, MS physical geography and geology), and the University of Illinois (PhD physical geography and photogrammetry). Ron's dissertation fitting first-degree trend surfaces to the flood plain and two terrace surfaces along a section of the Ohio River to determine if the terraces were of fluvial or lacustrine origin was published in the Geological Society of America Bulletin.

In the ten years following his doctorate, Ron held a variety of academic appointments at the Assistant (University of Illinois, University of South Carolina) and Associate (Penn State University, University of Alberta) Professor level. He was promoted to Professor of Earth and Atmospheric Sciences at Alberta however an institutional reorganization brought Ron to Texas State University in the Fall of 1995.

Ron was an important member of the Geography team which resulted in the Department of Geography being awarded the first doctoral program at Texas State University. Two sabbatical opportunities in his career resulted in visiting positions at the University of New South Wales and the University of Pittsburgh Semester at Sea program.

At the time of his retirement in 2006, Ron had supervised 10 doctoral and almost 30 master's students along with serving as a member of numerous doctoral and master's research advisory committees. Ron was best known to his students for his classes in cartography visualization and remote sensing. Ron wrote most of the analysis software used in these classes and freely shared his code with students. His photography hobby was made use of in the classroom as his students were encouraged to fly with him and use his digital multiband camera systems to acquire and process their own data. His most popular class was "Digital Remote Sensing and Terrain Modeling" which he offered at both the undergraduate and graduate level.

Ron was committed to sharing the work of he and his students, publishing over 50 papers, and making over 30 professional presentations, many with his students as co-authors. Ron was in demand to share his expertise at invited lectures as well, making 46 presentation on digital terrain modeling and raster data processing to government and private sector groups in the US, Canada, and Australia. He also served as an instructor in short courses at annual meetings of the American Association of Geographers and the National Council on Geographic Education. His expertise and commitment to sharing was recognized with teaching and service awards at the local level as well as from the Canadian Institute of Geomatics and the American Society for Photogrammetry and Remote Sensing (ASPRS).

Retirement did not slow Ron. Accompanied by his spouse Lynne they traveled throughout the US and Canada, wherever Amtrack or VIA Rail would take them. After brief stops in southwest MN and eastern WA , they finally settled in Pemberton in the Sea to Sky country of Western British Columbia. We will all miss their annual Christmas calendar illustrated with images of their many travels. All of us send our best wishes to Lynne and their children Ben and Tammy. Our memory of Ron will always include a short sleeve white shirt, khaki shorts, and if outside, a white Tilly hat.

Persons wishing to remember Ron are asked to contribute to the ASPRS International Educational Literature Award (IELA). More information on the IELA and the ASPRS Foundation may be found at https://www.asprs.org/education/asprs-awards-and-scholarships and https://www.asprsfoundation.org/.

~ Richard W. Dixon and David R. Butler
Department of Geography and Environmental Studies
Texas State University

Call for *PE&RS* Special Issue Submissions

Modelling, Representation, and Visualization of the Remote Sensing Data for Forestry Management

Remote sensing data includes aerial photography, videography data, multispectral scanner (MSS), Radar, and laser to map and understand various forest cover types and features. An accurate digital model of a selected forest type is developed using forest inventory data in educational and experimental forestry and extensive databases. It includes the formalization and compilation of methods for integrating forest inventory databases and remote sensing data with three-dimensional models for a dynamic display of forest changes.

Big data technology employs vast amounts of forestry data for forestry applications that require real-time inquiry and calculation. The techniques and strategies of forestry data analysis are integrated into the big data forestry framework, enabling interfaces that other Programmes may call. Virtual Reality addresses constraints in forest management such as temporal dependence, irreversibility of decisions, spatial-quantitative change of characteristics, and numerous objectives. Virtual representations integrate various computer graphics systems with display and interface devices to create a spatial presence in an interactive 3 D environment. Visualization of plant species' growth patterns, changes in species and their composition, and other morphological properties of forests are enhanced using machine learning and regression analysis methods as part of a digital model. In modelling, deep learning (DL) replicates expert observations on hundreds or thousands of hectares of trees.

Remote sensing is being used to map the distribution of forest resources, global changes in flora with the seasonal variations, and the 3D structure of forests. Graphic Information System (GIS) based visualizations depict dynamics through animations and 3D geo model visualizations and allow advanced spatial analytics and modelling in geographical phenomena for forest management. Digital forest modelling includes integrating forest inventory data, forest inventory database formation, graphics objects of forest inventory allocations with a digital forest model, and technology for visualizing forest inventory data. It helps forecast changes and visualizes situational phenomena occurring in forests using data and models involving spatial-temporal linkages.

Standard aerial shots capture images that view unseen components to the naked eye, such as the Earth's surface's physical structure and chemical composition. The challenges in remote sensing models include insufficient Remote Sensing (RS), spatial, spectral, and temporal resolution to detect degradation accurately. High costs of RS, the gap between operational and scientific uses, and lack of information sharing are some of the challenges of RS for forest management. The list of topics of interest include but are not limited to the following:

- Advancement of forest surveillance through Geographical Information Systems
- State of the art and perspectives of modelling and visualization framework for Forest type mapping and assessment of distribution
- Futuristic Satellite data analysis for stock maps and forest inventory analysis
- Big data-enabled GIS framework for forest management information
- AI-based Space Remote Sensing For Forest Ecosystem Assessment
- Enhanced visualization through deep learning for forest management solutions
- Novel approaches of multi-temporal satellite data using digital image analysis for forest management
- Advance representation of discrete objects and continuous fields in virtual environments through VR framework
- Database framework for regional and plot-based forest allotment data for model representation and visualization
- Development of scalable models for area-based metrics from Light Detection and Ranging (lidar) devices and photographic structure-for-motion (SFM)

Deadline for Manuscript Submission—June 7, 2022

Submit your Manuscript to http://asprs-pers.edmgr.com

Guest Editors

Dr. Gai-Ge Wang, gai-gewang@outlook.com and wgg@ouc.edu.cn, *Department of Computer Science and Technology, Ocean University of China*, China

Dr. Xiao-Zhi Gao, xiao.z.gao@gmail.com and xiao-zhi.gao@uef.fi, *Machine Vision and Pattern Recognition Laboratory, School of Engineering Science, Lappeenranta University of Technology*, Finland.

Dr. Yan Pei, peiyan@u-aizu.ac.jp, *Computer Science Division, The University of Aizu*, Japan.

NEW ASPRS MEMBERS

ASPRS would like to welcome the following new members!

Sara Akbarnejad Nesheli
Syeda Saleha Fatim Ali
Amanda Anderson
Tania Septi Anggraini
Braxton Lee Anzalone
Bahaa Awad
Andrew Logan Beckwith
Jhony Armando Benavides-Bolanos
Megan Blaskovich
Will Bordash
Pouyan Boreshnavard
Hannah Bowman
Carly Lynn Bradshaw
Robert Cahalan
Shelby Elaine Campbell
Zachary Canter
Ahmed Elamin
Abigail Faxon
Haidar Fazeli
Connor B. Firat
Reed P. Gallagher
Tewodros Gebre
Anish Giri
Jeff R. Green
Joshua Elliott Halsey
Yuci Han
Jeff Hand, PhD
Akula Harika
Brittany Herzberg
Xinhao Hu
Karin Ingwersen
Yufang Jin
Nicholas Johnson
Sean Michael Jones
James Arthur Kenney
Nicholas Kunz
Matthew Laird
Chen Liang
Yuan Qing Lie
Chintan Bimal Maniyar
Nancy Marek, PhD
Anjana K. Menon
Kavach Mishra
Matthew Mollica
Caleb Ohionije Ogbeta
John Agbo Ogbodo
Nicholas Gregory Orban
Maria Park
Jonathan Roeder
Sreenidhi S
Rajneesh Sharma
Kim Solomon
William Raymond Stuart
Aylin Tuzcu Kokal
Shilpi Verma
Robert Pat Wallace, PE
Caiwang Zheng

FOR MORE INFORMATION ON ASPRS MEMBERSHIP, VISIT
HTTP://WWW.ASPRS.ORG/JOIN-NOW

Who at ASPRS Do I Contact for help with…

Membership/*PE&RS* Subscription
office@asprs.org

Advertising/Exhibit Sales
Bill Spilman — bill@innovativemediasolutions.com

***PE&RS* Editor-in-Chief**
Alper Yilmaz — PERSeditor@asprs.org

Calendar — calendar@asprs.org

ASPRS Bookstore — office@asprs.org

ASPRS Foundation — foundation@asprs.org

425 Barlow Place, Suite 210, Bethesda, MD 20814
301-493-0290, 225-408-4422 (fax), www.asprs.org

GEOBYTES

https://www.asprs.org/geobytes.html

Deep Fake geography? A humanistic GIS Reflection upon Geospatial Artificial Intelligence

Presenter: Dr. Bo Zhao
When: May 27, 2022, 12:00 PM – 1:00 PM EDT

The ongoing development of Geospatial Artificial Intelligence (GeoAI) has raised deep concerns about the emergence of deep fake geography and its potentials in transforming the human perception of the geographic world (Zhao et al 2021). This seminar presents a humanistic GIS reflection upon GeoAI (Zhao 2022) and its social implications using an empirical study that dissected the algorithmic mechanism of falsifying satellite images with non-existent landscape features. To demonstrate our pioneering attempt at deep fake detection, a robust approach is then proposed and evaluated. Our proactive study warns of the emergence and proliferation of deep fakes in geography just as "lies" in maps. We suggest timely detections of deep fakes in geospatial data and proper coping strategies when necessary. More importantly, it is encouraged to cultivate critical geospatial data literacy and thus to understand the multi-faceted impacts of deep fake geography on individuals and human society.

Bo Zhao is an Associate Professor in the Department of Geography at the University of Washington, Seattle. His recent research interests include GIScience, geographical misinformation, and social implications of emerging GIS technologies, especially in the context of the United States or China.

GeoBytes are online seminars presented by ASPRS and sponsored by the ASPRS GIS Division, in cooperation with CaGIS.

Attention those seeking ASPRS Certification: ASPRS Online Seminars are a great way to gain Professional Development Hours!

Registration Emails for upcoming seminars are sent to all members with the registration link. Just click on the clink in the email to get to the online registration for each seminar. After the live seminars have aired, a videotape of the seminar will be posted.

Allen Coral Atlas: A New Technology for Coral Reef Conservation

Presenter: Brianna Bambic
When: September 23, 2022, 12:00 PM – 1:00 PM EDT

Coral reef managers and decision makers at multiple scales need information, in near real time, to react to the increasing threats facing reefs. However, more than three quarters of the world's coral reefs have never been mapped and lack monitoring. To address this knowledge gap and to support, inform, and inspire critical actions to manage and protect coral reefs, the Allen Coral Atlas combines high resolution satellite imagery, machine learning, and field data to produce globally consistent benthic and geomorphic maps and monitoring systems of the world's coral reefs. The initiative's goal is to help stakeholders ranging from local communities to regional and national governments reach their conservation targets and improve their coastal resilience. The multi-disciplinary partnership is led by Arizona State University, in collaboration with Planet, University of Queensland, and the Coral Reef Alliance.

Baseline maps have multiple uses, including: sustainable coastal development, site selection of marine protected areas, planning of restoration activities, and reef fisheries management. In this presentation, we will demonstrate how the Allen Coral Atlas supports data-driven management, conservation, and restoration of coral reefs at local, national, regional, and global scales. We have developed online courses to facilitate increased use and impact of the Atlas, and are collaborating with networks of individuals and institutions who can be alerted when changes are detected (e.g., large-scale bleaching or sedimentation events).

Brianna Bambic leads the Allen Coral Atlas Field Engagement team at the National Geographic Society and Arizona State University. With a coral reef biology and resource management background, she was an Independent Researcher for 7 years that culminated in a virtual reality experience of Half Moon Caye National Monument, Belize with a National Geographic Explorer Grant, helping communicate science to the public. Brianna received her MS in natural resource management from the University of Akureyri, Iceland in 2019. Her expertise includes coastal and marine management, global science communication, and developing capacity around remote sensing and mapping. With countless hours underwater and >700 logged dives, she loves spending time exploring the ocean.

WHO'S WHO IN ASPRS

Founded in 1934, the American Society for Photogrammetry and Remote Sensing (ASPRS) is a scientific association serving thousands of professional members around the world. Our mission is to advance knowledge and improve understanding of mapping sciences to promote the responsible applications of photogrammetry, remote sensing, geographic information systems (GIS) and supporting technologies.

BOARD OF DIRECTORS

BOARD OFFICERS

President
Christopher Parrish, Ph.D
Oregon State University

President-Elect
Lorraine B. Amenda, PLS, CP
Towill, Inc.

Vice President
Bandana Kar
Oak Ridge National Lab

Past President
Jason M. Stoker, Ph.D,
U.S. Geological Survey

Treasurer
Stewart Walker, Ph.D.
photogrammetry4u

Secretary
Harold Rempel
ESP Associates, Inc.

COUNCIL OFFICERS

ASPRS has six councils. To learn more, visit https://www.asprs.org/Councils.html.

Sustaining Members Council
Chair: Ryan Bowe
Deputy Chair: Melissa Martin

Technical Division Directors Council
Chair: Bill Swope
Deputy Chair: Hope Morgan

Standing Committee Chairs Council
Chair: David Stolarz
Deputy Chair: TBA

Early-Career Professionals Council
Chair: Madeline Stewart
Deputy Chair: Kyle Knapp

Region Officers Council
Chair: Demetrio Zourarakis
Deputy Chair: Jason Krueger

Student Advisory Council
Chair: Lauren McKinney-Wise
Deputy Chair: Oscar Duran

TECHNICAL DIVISION OFFICERS

ASPRS has seven professional divisions. To learn more, visit https://www.asprs.org/Divisions.html.

Geographic Information Systems Division
Director: Denise Theunissen
Assistant Director: Jin Lee

Lidar Division
Director: Ajit Sampath
Assistant Director: Mat Bethel

Photogrammetric Applications Division
Director: Ben Wilkinson
Assistant Director: Hank Theiss

Primary Data Acquisition Division
Director: Greg Stensaas
Assistant Director: Srini Dharmapuri

Professional Practice Division
Director: Bill Swope
Assistant Director: Hope Morgan

Remote Sensing Applications Division
Director: Amr Abd-Ehrahman
Assistant Director: Tao Liu

Unmanned Autonomous Systems (UAS)
Director: Jacob Lopez
Assistant Director: Bahram Salehi

REGION PRESIDENTS

ASPRS has 13 regions to serve the United States. To learn more, visit https://www.asprs.org/regions.html.

Alaska Region

Cascadia Region
Robert Hariston-Porter

Eastern Great Lakes Region
Michael Joos, CP, GISP

Florida Region
Xan Fredericks

Heartland Region
Whit Lynn

Intermountain Region
Robert T. Pack

Mid-South Region
David Hughes

Northeast Region

North Atlantic Region

Pacific Southwest Region
John Erickson, PLS, CP

Potomac Region
Dave Lasko

Rocky Mountain Region

Western Great Lakes Region
Adam Smith

SUSTAININGMEMBERS

ACI USA Inc.
Weston, Florida
https://acicorporation.com/
Member Since: 2/2018

Aerial Services, Inc.
Cedar Falls, Iowa
www.AerialServicesInc.com
Member Since: 5/2001

Airworks Solutions Inc.
Boston, Massachusetts
Member Since: 3/2022

Applanix
Richmond Hill, Ontario, Canada
http://www.applanix.com
Member Since: 7/1997

Ayres Associates
Madison, Wisconsin
www.AyresAssociates.com
Member Since: 1/1953

CT Consultants
Mentor, Ohio
Member Since: 3/2022

Dewberry
Fairfax, Virginia
www.dewberry.com
Member Since: 1/1985

Esri
Redlands, California
www.esri.com
Member Since: 1/1987

GeoCue Group
Madison, Alabama
http://www.geocue.com
Member Since: 10/2003

Geographic Imperatives LLC
Centennial, Colorado
Member Since: 12/2020

GeoWing Mapping, Inc.
Richmond, California
www.geowingmapping.com
Member Since: 12/2016

Halff Associates, Inc.
Richardson, Texas
www.halff.com
Member Since: 8/2021

Keystone Aerial Surveys, Inc.
Philadelphia, Pennsylvania
www.kasurveys.com
Member Since: 1/1985

Kucera International
Willoughby, Ohio
www.kucerainternational.com
Member Since: 1/1992

L3Harris Technologies
Broomfield, Colorado
www.l3harris.com
Member Since: 6/2008

Merrick & Company
Greenwood Village, Colorado
www.merrick.com/gis
Member Since: 4/1995

NV5 Geospatial
Sheboygan Falls, Wisconsin
www.quantumspatial.com
Member Since: 1/1974

Pickett and Associates, Inc.
Bartow, Florida
www.pickettusa.com
Member Since: 4/2007

Riegl USA, Inc.
Orlando, Florida
www.rieglusa.com
Member Since: 11/2004

Robinson Aerial Surveys, Inc.(RAS)
Hackettstown, New Jersey
www.robinsonaerial.com
Member Since: 1/1954

Sanborn Map Company
Colorado Springs, Colorado
www.sanborn.com
Member Since: 10/1984

Scorpius Imagery Inc.
Newark, Delaware
aerial@scorpiusimagery.com
Member Since: 6/2021

Surdex Corporation
Chesterfield, Missouri
www.surdex.com
Member Since: 12/2011

Surveying And Mapping, LLC (SAM)
Austin, Texas
www.sam.biz
Member Since: 12/2005

T3 Global Strategies, Inc.
Bridgeville, Pennsylvania
https://t3gs.com/
Member Since: 6/2020

Terra Remote Sensing (USA) Inc.
Bellevue, Washington
www.terraremote.com
Member Since: 11/2016

Towill, Inc.
San Francisco, California
www.towill.com
Member Since: 1/1952

Woolpert LLP
Dayton, Ohio
www.woolpert.com
Member Since: 1/1985

SUSTAININGMEMBERBENEFITS

Membership

✓ Provides a means for dissemination of new information

✓ Encourages an exchange of ideas and communication

✓ Offers prime exposure for companies

Benefits of an ASPRS Membership

- Complimentary and discounted Employee Membership*
- E-mail blast to full ASPRS membership*
- Professional Certification Application fee discount for any employee
- Member price for ASPRS publications
- Discount on group registration to ASPRS virtual conferences
- Sustaining Member company listing in ASPRS directory/website
- Hot link to company website from Sustaining Member company listing page on ASPRS website
- Press Release Priority Listing in *PE&RS* Industry News
- Priority publishing of Highlight Articles in *PE&RS* plus, 20% discount off cover fee
- Discount on *PE&RS* advertising
- Exhibit discounts at ASPRS sponsored conferences (exception ASPRS/ILMF)
- Free training webinar registrations per year*
- Discount on additional training webinar registrations for employees
- Discount for each new SMC member brought on board (Discount for first year only)

*quantity depends on membership level

Smartphone Digital Photography for Fractional Vegetation Cover Estimation

Gaofei Yin, Yonghua Qu, Aleixandre Verger, Jing Li, Kun Jia, Qiaoyun Xie, and Guoxiang Liu

Abstract

Accurate ground measurements of fractional vegetation cover (FVC) are key for characterizing ecosystem functions and evaluating remote sensing products. The increasing performance of cameras equipped in smartphones opens new opportunities for extensive FVC measurement through citizen science initiatives. However, the wide field of view (FOV) of smartphone cameras constitutes a key source of uncertainty in the estimation of vegetation parameters, which has been largely ignored. We designed a practical method to characterize the FOV of smartphones and improve the FVC estimation. The method was assessed in a mountainous forest based on the comparison with in situ fisheye photographs. After the FOV correction, the agreement of smartphone and fisheye FVC estimates highly improved: root-mean-square error (RMSE) of 0.103 compared to 0.242 of the original smartphone FVC estimates without considering the FOV effect, mean difference of 0.074 versus 0.213, and coefficient of determination R^2 *of 0.719 versus 0.353. Smartphone cameras outperform traditional fisheye cameras: the overexposure and low vertical resolution of fisheye photographs introduced uncertainties in FVC estimation while the insensitivity to exposure and high spatial resolution of smartphone cameras make photograph acquisition and analysis more automatic and accurate. The smartphone FVC estimates highly agree with the GF-1 satellite product: RMSE = 0.066, bias = 0.007, and* R^2 *= 0.745. This study opens new perspectives for the validation of satellite products.*

Gaofei Yin and Guoxiang Liu are with the Faculty of Geosciences and Environmental Engineering, Southwest Jiaotong University, Chengdu 610031, China (yingf@swjtu.edu.cn).

Gaofei Yin and Aleixandre Verger are with CREAF, 08193 Bellaterra (Cerdanyola del Vallès), Catalonia, Spain.

Gaofei Yin and Aleixandre Verger are with CSIC, Global Ecology Unit, CREAF-CSIC-UAB, 08193 Bellaterra (Cerdanyola del Vallès), Catalonia, Spain.

Yonghua Qu and Kun Jia are with the State Key Laboratory of Remote Sensing Science, Beijing Key Laboratory for Remote Sensing of Environment and Digital Cities, Institute of Remote Sensing Science and Engineering, Faculty of Geography Science, Beijing Normal University, Beijing 100875, China.

Aleixandre Verger is with Desertification Research Centre CIDE-CSIC, 46113 Montcada, València, Spain.

Jing Li is with the State Key Laboratory of Remote Sensing Science, Jointly Sponsored by Aerospace Information Research Institute, Chinese Academy of Sciences and Beijing Normal University, Beijing 100101, China.

Jing Li is with the University of Chinese Academy of Sciences, Beijing 100049, China.

Qiaoyun Xie is with the University of Technology Sydney, Faculty of Science, Sydney NSW 2007, Australia.

Contributed by Desheng Liu, June 30, 2021 (sent for review October 12, 2021; reviewed by Yanjun Su, Barry N Haack, Tianqi Zhang).

Introduction

Fractional vegetation cover (FVC), defined as the fraction of ground surface covered by green vegetation in the nadir direction, plays a key role in the partition between soil and vegetation contributions in the energy and water cycles between surface and atmosphere (Baret *et al.* 2013; Mu *et al.* 2018). FVC is a key controlling factor in many terrestrial processes, including photosynthesis, respiration, and evapotranspiration, and it has been extensively used to monitor vegetation dynamics and ecosystem change (Arneth 2015; Bonan and Doney 2018).

Currently, FVC can be long term monitored at the local-to-global scale through remote sensing technology (Jiapaer *et al.* 2011; Mu *et al.* 2018; Okin *et al.* 2013). Several FVC satellite products are already available including Copernicus Global Land Service (Baret *et al.* 2013; Verger *et al.* 2014), European Organization for the Exploitation of Meteorological Satellites (EUMETSAT) Satellite Application Facility on Land Surface Analysis (LSA SAF) (García-Haro *et al.* 2018), Global Land Surface Satellite (GLASS) (Jia *et al.* 2019), and GaoFen-1 (*GF-1*) (Jia *et al.* 2016) products. In situ FVC measurements are indispensable for the calibration and validation of these FVC estimation algorithms and products (Laliberte *et al.* 2007; Mu *et al.* 2015; White *et al.* 2000). Optical instruments based on gap fraction measurements are commonly used for *in situ* estimation of FVC which corresponds to the complementary of the gap fraction in the nadir direction. The Li-Cor plant canopy analyser (PCA) and digital hemispherical photography (DHP) are widely used (Demarez *et al.* 2008; Garrigues *et al.* 2008; Leblanc *et al.* 2005; LI-COR 1991; Mougin *et al.* 2014). They both measure the gap fraction under the canopy over the whole upper hemisphere. The gap fraction in the nadir direction should be firstly extracted to properly calculate FVC. For PCA, only the reading of the innermost ring (with view zenith ranging 0° to 7°) is appropriate for FVC estimation (LI-COR 1991). For DHP, there is only one pixel per image in the exact nadir direction. Therefore, a range of 0°–10° zenith angles around the nadir is typically used to achieve a proper trade-off between the estimation accuracy and spatial representativeness (Mougin *et al.* 2014).

Notwithstanding the popularity of PCA and DHP in *in situ* estimation, they still face several disadvantages. PCA is expensive to purchase and to maintain. DHP significantly reduces the cost but is prominently sensitive to photographic exposure setting (Macfarlane *et al.* 2014; Zhang *et al.* 2005). Automatic exposure significantly distorts gap fraction estimation, so several methods were proposed to determine the optimum exposure (Macfarlane *et al.* 2014; Zhang *et al.* 2005). However, the implementation of these methods is difficult for most common users (Pueschel *et al.* 2012). In addition, the performance of DHP is also limited by the mixed-pixel problem caused by its wide field of view (FOV) (Baret *et al.* 2010; Liu *et al.* 2013; Macfarlane 2011).

An alternative for *in situ* FVC estimation is the digital cover photography (DCP) from consumer-grade digital single lens reflex cameras (Chianucci and Cutini 2013; Chianucci *et al.* 2014). DCP cameras have a narrow FOV, generally ranging from 15° to 30°, and the FOV effects do not need dedicatedly consideration (Chen *et al.* 2016; Mu *et al.* 2015). Further, since the sky luminance is relatively homogenous

Photogrammetric Engineering & Remote Sensing
Vol. 88, No. 5, May 2022, pp. 303–310.
0099-1112/22/303–310

doi: 10.14358/PERS.21-00038R2

under these acquisition conditions (Chianucci and Cutini 2013; Chianucci *et al.* 2014), DCP is less sensitive to photographic exposure than DHP (Macfarlane *et al.* 2007b). In addition, the DCP generally has higher spatial resolution than DHP, and the small gap fractions within canopy can be readily resolved (Chianucci 2016; Ryu *et al.* 2010). DCP performs similarly or even better than DHP in the estimation of biophysical parameters (Chianucci and Cutini 2013; Chianucci *et al.* 2014; Macfarlane *et al.* 2007a; Macfarlane *et al.* 2007b; Pekin and Macfarlane 2009).

The increasing upgrade of cameras equipped on smartphones creates a new opportunity for the DCP technology. Compared with digital single lens reflex cameras, smartphones are generally cheaper and more flexible. In addition, smartphones embed several other components, e.g., global position system and gyroscope, which can be used to determine the location and orientation of captured images. These advantages explain the booming development of smartphone applications for biophysical parameter estimation, including LAISmart (Qu *et al.* 2016) and PocketLAI (Confalonieri *et al.* 2013). However, smartphone cameras often have a wider FOV than digital single lens reflex cameras, and the FOV is not explicitly provided by many phone manufacturers. Qu *et al.* (2017) found that the FOV effects of smartphone cameras cause an underestimation of gap fraction, and consequently an overestimation of FVC. This uncertainty is induced by the stretched path length in the slant view zenith angle (Yin *et al.* 2020; Yin *et al.* 2018). Moreover, most of the recent smartphones use computational method to fuse information from two or more cameras into one image and the integrated FOV is unknown even when the FOV for each camera is specified. Therefore, the characterization and correction of the FOV effects of smartphone cameras need dedicated consideration.

The main objective of this study was to develop a practical method for FVC estimation with digital cover photography from smartphones. We proposed a novel method to characterize the FOV of smartphone cameras and to extract the optimal range of observation zenith angle in image acquisitions for FVC estimation. A global binary threshold classification method was then applied to classify the sky and canopy pixels in upward images and calculated the FVC. The performance of the developed method was assessed through comparison with the widely used DHP technology. Finally, we assessed the potential of smartphone FVC estimates for the validation of satellite FVC products. The FVC product derived from *GF-1* data was used for this purpose.

Materials and Methods

Field Measurements

Fisheye and smartphone photographs were collected in 23 mountainous plots located at Southwestern China (~32°50′N, 104°3′E) on 29–30 June 2019. Details of the study site can be found in Yin *et al.* (2017a). The plots represent conifer forests, broadleaf forests, and shrub forests. Each plot covers approximately 16 m × 16 m area. Five subplots were sampled within each plot to capture its spatial variation: one located at the center of the plot and others at the four corners. The FVC estimate at plot level results from averaging the five subplot-level FVC estimates. At each subplot, fisheye and cover photographs were simultaneously collected in upward direction under overcast sky conditions.

Fisheye photographs were taken using a Nikon D810 equipped with a Sigma 8 mm f3.5 EX DG fisheye lens. The camera lens was levelled with a two-axis bubble. As recommended by Macfarlane (2011), three exposures were used at each subplot: auto-exposure, and under-exposed by one and two stops. The exposure which maximizes the contrast between sky and canopy was manually selected for further processing. All captured photographs were saved in TIF format with a size of 7360 × 4912 pixels.

Cover photographs were taken from a Huawei Mate 10 smartphone equipped with a dual-lens camera combining a 12-megapixel color sensor and a 20-megapixel monochrome sensor. It also benefits from the novel optical image stabilization (OIS) technology. The dual-lens setup and the OIS ensure the acquisition of high spatial resolution photographs with high quality even under poor illumination conditions (e.g., too dark or too bright). The smartphone was oriented in a horizontal position for taking upward photographs. At each subplot, three photographs were collected under automatic mode and the one with the most vertical view was manually selected for further processing. The photographs were stored in TIF format, with a size of 3968 × 2976 pixels.

GF-1 Satellite Product

To assess smartphone photography for satellite validation purposes, the field measurements in the in 23 mountainous plots were compared with the concurrent high spatial resolution (16 m) FVC map generated from wide field view (WFV) sensor on board the Chinese *GF-1* satellite. For comparison purposes, we used the FVC values for the nearest pixels to the field plots from the FVC *GF-1* satellite product for the concomitant date with the field campaign, i.e., 30 June 2019 (Figure 1).

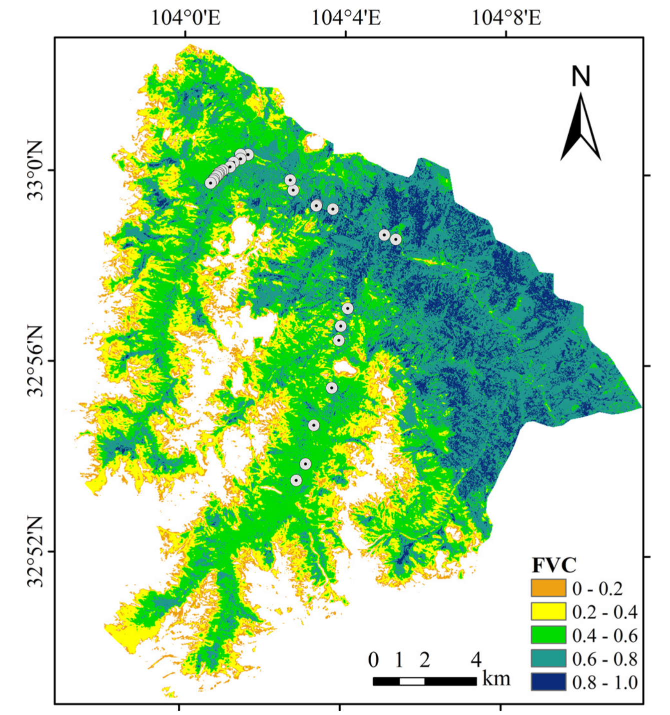

Figure 1. Fractional vegetation cover (FVC) estimated from the *GF-1* WFV image on 30 June 2019. The dots represent the plots of the in situ measurements.

The *GF-1* WFV snapshoots land surface with high spatial resolution (16 m), wide coverage (800 km) and high revisit frequency (four days). The FVC retrieval algorithm is based on a back propagation neural network trained with PROSPECT + SAIL radiative transfer model simulations (Jacquemoud *et al.* 2009). Top of the canopy *GF-1* surface reflects in green, red, and near-infrared spectral bands are the input of the neural network. Details regarding the *GF-1* data and the retrieval algorithm can be found in Jia *et al.* (2016).

Estimation of the FOV of the Smartphone Camera

Estimation Method

The FOV of a smartphone describes the angular range that its lens can image in a particular direction. For convenience, we focus here on the long dimension of a photograph, and the FOV in other directions can be easily estimated based on linear assumption for the projection function of photographs.

Suppose a smartphone takes a photograph of an object with a physical length of L (in meter), which is located at a distance D from the camera. The angle formed by two rays emanating from the camera to the endpoints of the object can be expressed as:

$$\beta = L/D \tag{1}$$

Assuming the object is far away from the camera, which is often the case for field FVC measurement, the FOV of the camera can be approximated as:

$$\text{FOV} = N/D \quad (2)$$

where N (in meter) corresponds to the physical distance the camera can image along the direction of L. Combining Equations 1 and 2:

$$\beta = \text{FOV } L/N \quad (3)$$

If L and N (both in meter) are, respectively, recorded in a photography as l and n, (both in pixel number), Equation 3 is equivalent to:

$$\beta = \text{FOV } l/n \quad (4)$$

According to Equations 1 and 4, FOV can be expressed as:

$$L/D = \text{FOV } l/n \quad (5)$$

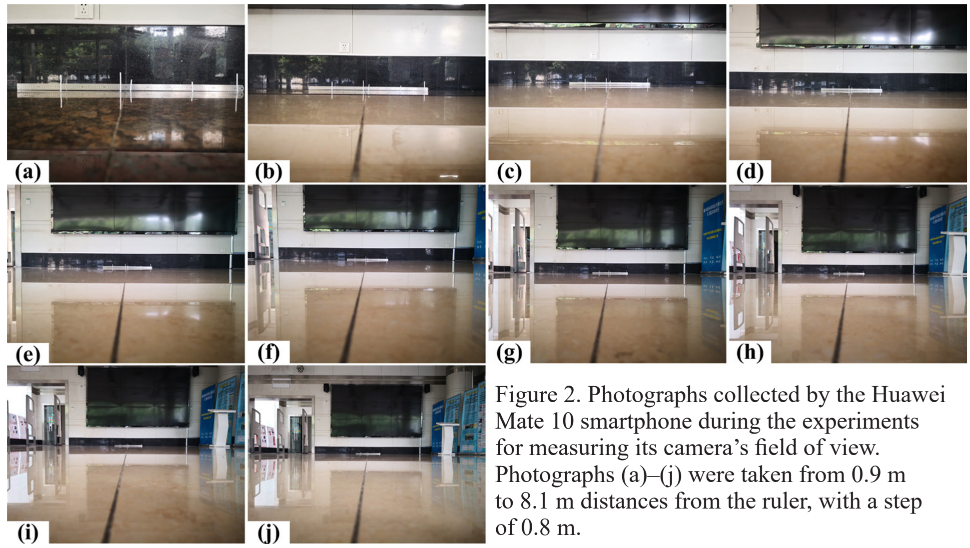

Figure 2. Photographs collected by the Huawei Mate 10 smartphone during the experiments for measuring its camera's field of view. Photographs (a)–(j) were taken from 0.9 m to 8.1 m distances from the ruler, with a step of 0.8 m.

Therefore, the FOV is the slope of the fitted line between L/D and l/n, and it can be estimated through ordinary least square method.

Experiment for FOV Estimation

We designed an indoor experiment to estimate the FOV of the Huawei Mate 10 smartphone based on the above-mentioned method. First, a ruler was stuck to the wall. Second, 10 photographs were taken at different locations ranging from 0.9 m to 8.1 m from the ruler, with a step of 0.8m. At each photograph, four virtual objects were defined as segments spanning from the ruler tick of 0 cm to 20 cm, 50 cm, 80 cm, and 100 cm, respectively. This configuration ensured the objects on the ruler were nearly parallel to the long dimension in all the 10 photographs. Finally, the length in pixels of each object on the ruler were counted from all the 10 photographs, and a scatter between L/D and l/n was plotted. The FOV was estimated from the scatter diagram as the slope of the regressed line (see Equation 5). Figure 2 illustrates the 10 photographs taken at increasing distances from the ruler.

Image Classification and FVC Estimation

After estimating the FOV of the smartphone camera, the zenith angles ranging from 0° to 10° were extracted from the cover images to ensure geometric consistence with DHP technology (Morsdorf *et al.* 2006; Mougin *et al.* 2014). The sky luminance within the limited zenith range is relatively homogenous, and the sky and canopy pixels can be easily distinguished in the upward-pointing images. The Otsu algorithm (Otsu 1979) was used for image classification. The basic principle of the Otsu algorithm is to find an optimal global threshold that, simultaneously, minimizes the intraclass variance and maximizes the inter-class variance. The band selection has a significant influence on the classification performance (Pueschel *et al.* 2012). We used the blue band because it provides the highest contrast between sky and canopy pixels (Lang *et al.* 2017; Leblanc *et al.* 2005; Yan *et al.* 2019). After classification, FVC is calculated as the number of canopy pixels divided by the total number of pixels.

Method Evaluation

Three statistical metrics, namely, the coefficient of determination (R^2), the root-mean-square error (RMSE) and the bias were used to evaluate FVC estimated from smartphone against those from fisheye photographs and *GF-1* satellite:

$$R^2 = 1 - \frac{\sum_{k=1}^{N}\left(\text{FVC}_k^{SM} - \text{FVC}_k^{B}\right)^2}{\sum_{k=1}^{N}\left(\text{FVC}_k^{SM} - \overline{\text{FVC}_k^{SM}}\right)^2} \quad (6)$$

$$\text{RMSE} = \sqrt{\sum_{k=1}^{N}\left(\text{FVC}_k^{SM} - \text{FVC}_k^{B}\right)^2 / N} \quad (7)$$

$$\text{bias} = \sqrt{\sum_{k=1}^{N}\left(\text{FVC}_k^{SM} - \text{FVC}_k^{B}\right) / N} \quad (8)$$

where FVC^{SM} and FVC^{B} are, respectively, the FVC values derived from the smartphone and the benchmark method (i.e., fisheye photographs or *GF-1* satellite).

Results

FOV Estimation

A zero-intercepted linear regression between L/D and l/n was observed with R^2 equal to 0.999 (Figure 3). The slope of the regressed line, representing the FOV for the long dimension of the smartphone images (Equation 5), is 1.214 rad = 69.55°.

Comparison of Smartphone and Fisheye Photography FVC Estimates

Figure 4 illustrates concurrent fisheye and cover images for typical conifer (the left column), broadleaf (the middle column), and shrub (the

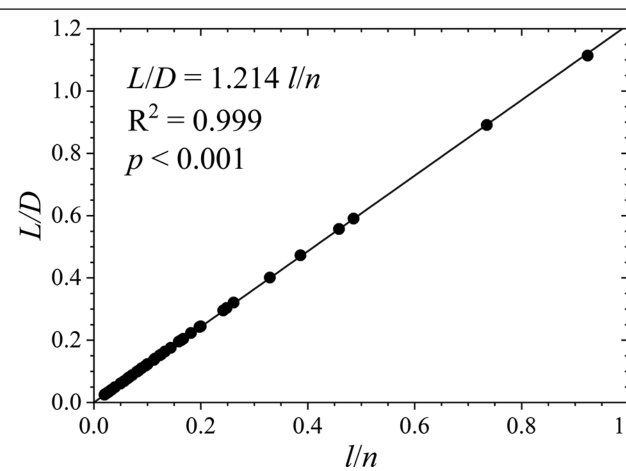

Figure 3. Regression between L/D and l/n. L and D are the physical length of the object and the distance between the camera and the object (both in meter), respectively. l and n are the length in pixels of the object and that of the long dimension of the photography, respectively.

right column) forests. The fisheye photographs capture the forest over the whole upper hemisphere (FOV of 180º) while the maximum FOV of smartphone photographs is 69.55° (see also Figure 3).

Figure 5 shows the variation of canopy closure with view zenith angle for fisheye and smartphone photographs over the selected forest samples (Figure 4). Note that canopy closure is defined as complementary of gap fraction, and FVC is the canopy closure for nadir viewing. For the conifer case (Figure 5a), the canopy closure increases with zenith angle, consistently with the gap fraction theory (Nilson 1999). Yet, the increasing tread for the broadleaf forest (Figure 5b) and shrub cases (Figure 5c) is not obvious, because of the spatial heterogeneity (Figure 4b and 4e) and topographic effects (Figure 4c and 4f). The canopy closure from smartphone photographs is higher than the one from fisheye photographs, particularly, for open forest samples (Figure 5a and 5b) while marginal differences are observed for closed shrub forest (Figure 5c).

Figure 6 shows the sub-photographs for the 0°–10° zenith angle range as extracted from fisheye and smartphone camera acquisitions (Figure 4). The proposed FOV estimation method allows to satisfactorily align sub-photographs from the smartphone camera with those from the fisheye camera. Some small vegetation elements or gaps were not captured in the fisheye photographs (Figure 6, top), which can bias actual FVC with an underestimation for open canopies (Figure 6a and 6b) and an overestimation for closed canopies (Figure 6c), while spatial details were well retained in smartphone photographs (Figure 6, bottom).

Figure 7 shows the comparison between FVC estimated from fisheye and smartphone photographs before (Figure 7a) and after (Figure 7b) the proposed correction of FOV effects. Neglecting FOV effects for smartphone cameras induced remarkable FVC overestimation, especially for conifer forests (Figure 7a), because of the high values of canopy closure for oblique observations (Figure 5). The correction of FOV effects significantly improved the agreement between smartphone and fisheye camera FVC estimates: the coefficient of determination R^2 increased from 0.353 to 0.719, the RMSE decreased from 0.242 to 0.103 and the systematic positive bias of the original smartphone estimates before FOV correction was highly reduced from 0.213 to 0.074. The residual positive differences of smartphone compared to fisheye estimates for intermediate FVC values (Figure 7b) can partially be explained due to a slight underestimation of actual FVC values for fisheye photography due to its lower pixel resolution (Figure 6).

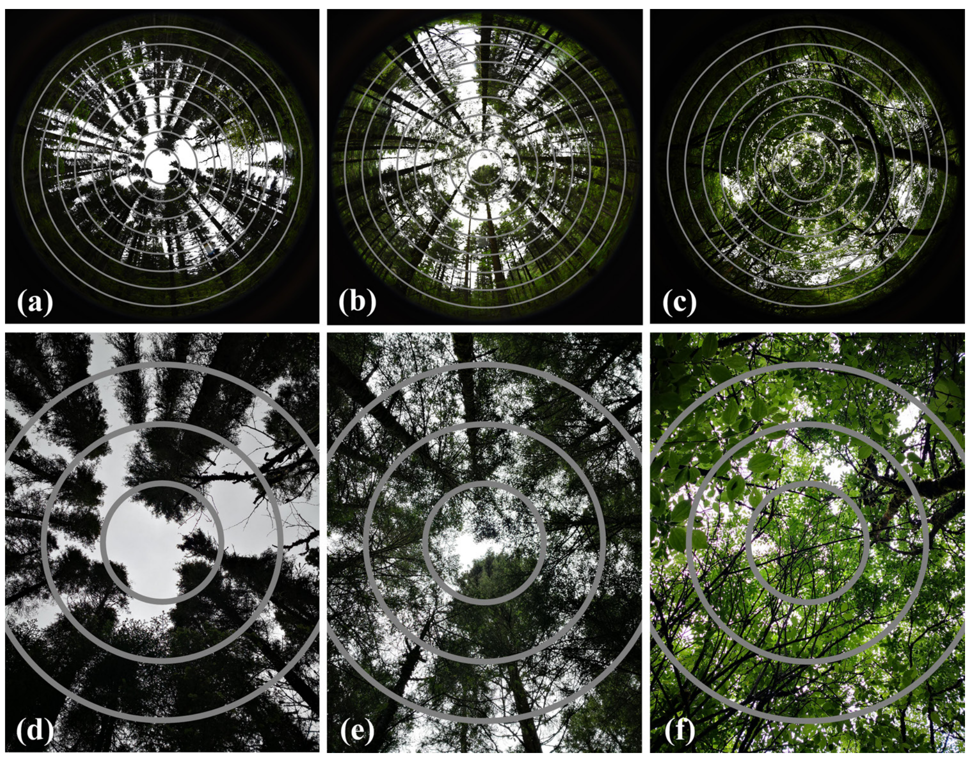

Figure 4. Comparison between fisheye (top) and smartphone photographs (bottom) for (a, d) a conifer forest, (b, e) a broadleaf forest, and (c, f) a shrub forest. The gray circles represent the zenith angle isolines with 10° step. The innermost isolines (0–10º) define the boundaries used for FVC extraction.

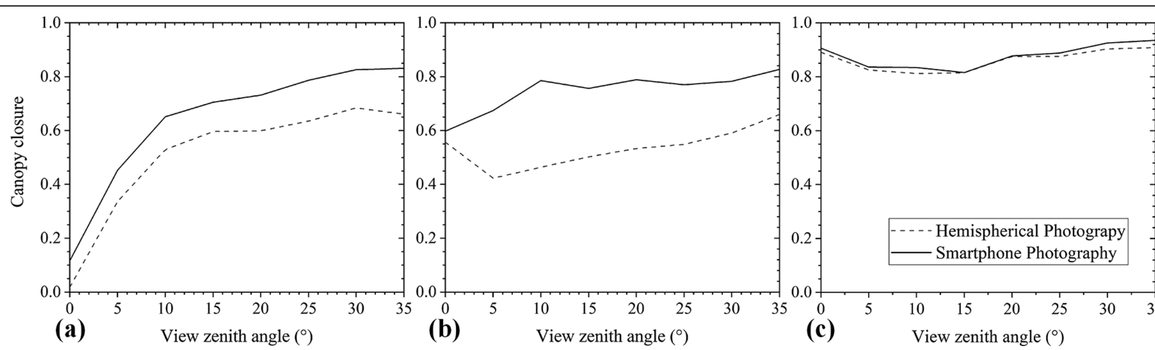

Figure 5. Canopy closure versus view zenith angle for fisheye and smartphone photography over (a) a conifer forest, (b) a broadleaf forest, and (c) a shrub forest (cf. Figure 4).

Comparison of Smartphone FVC Estimates and *GF-1* Satellite Product

The comparison of smartphone FVC estimates to *GF-1* WFV satellite-derived FVC (Figure 8) exhibits a similar pattern as that to fisheye photography comparison (Figure 7): smartphone derived FVC, before dedicatedly FOV consideration, systematically overestimated the satellite retrievals (bias = 0.135), and the consistency was relatively low (R^2

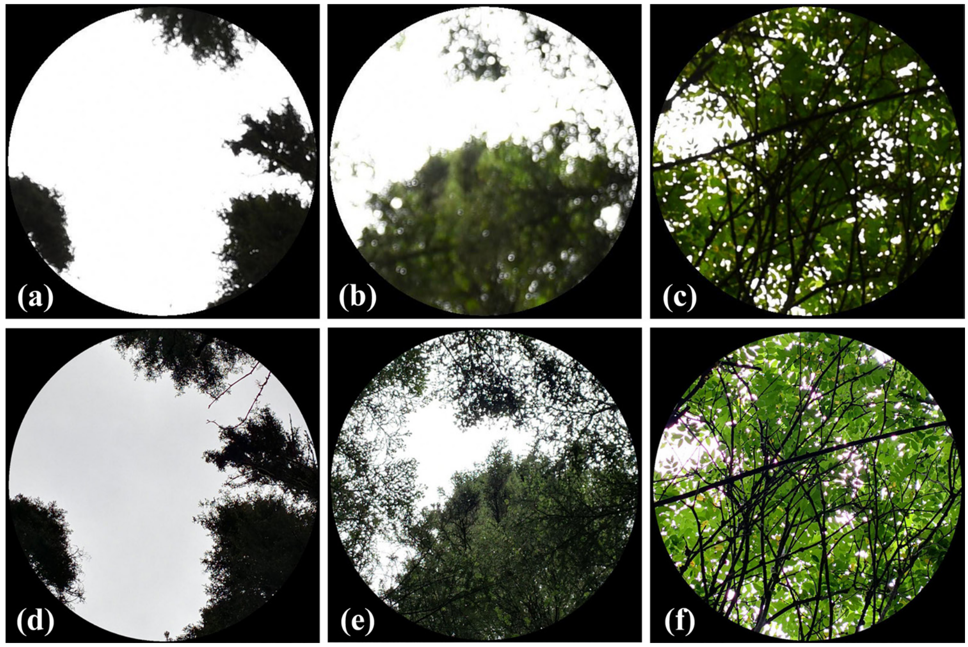

Figure 6. Extracted sub-photographs for FVC estimation from fisheye (top) and smartphone photographs (bottom) in (a,d) a conifer forest, (b,e) a broadleaf forest, and (c, f) a shrub forest.

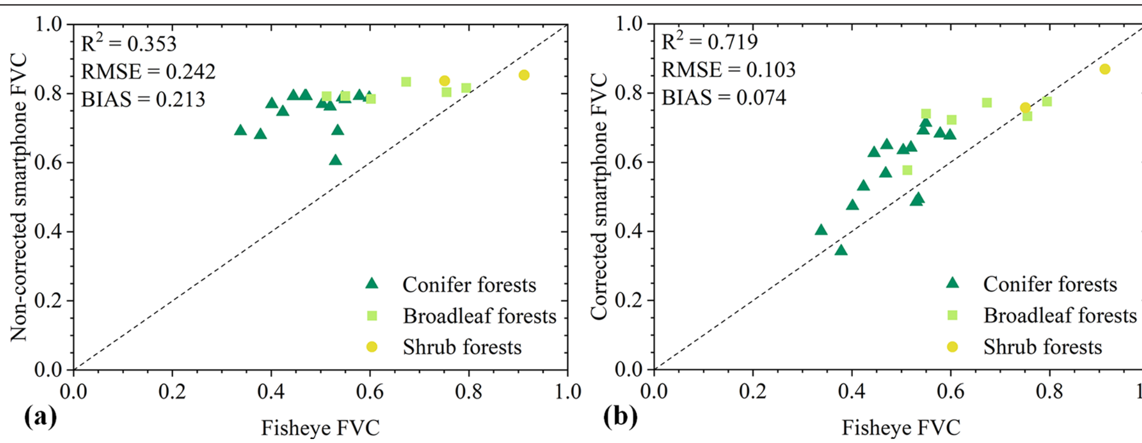

Figure 7. Comparison between FVC estimates from fisheye and smartphone photography before (a) and after (b) FOV correction.

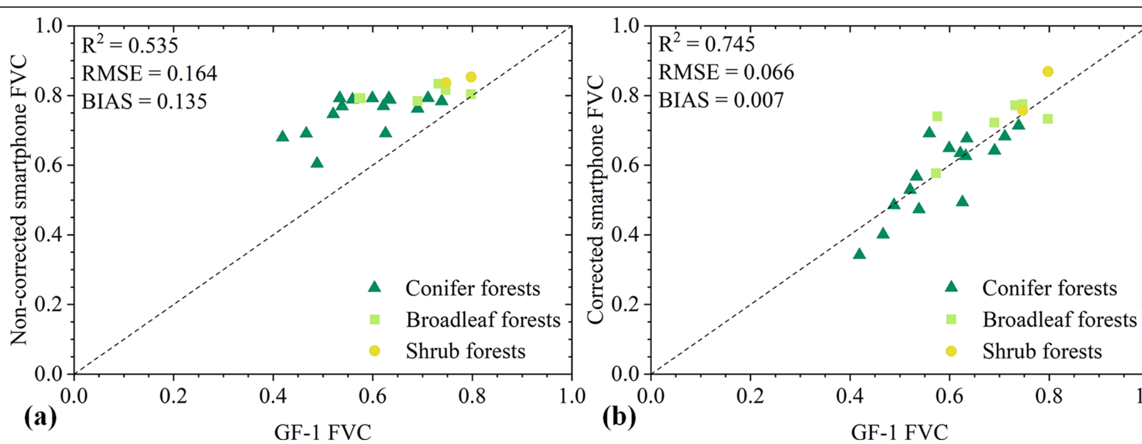

Figure 8. Comparison between FVC estimated from *GF-1* and smartphone photographs (a) before and (b) after FOV correction.

= 0.535). The observed bias was substantially reduced (bias = 0.007) and the consistency improved (R^2 = 0.745) after the FOV correction in smartphone processing. The overall RMSE between the smartphone and fisheye FVC estimates was reduced from 0.164 to 0.066 after correction. The FVC field measurements from fisheye photography showed similar performances when compared with the *GF-1* satellite retrievals (R^2 = 0.707, RMSE = 0.078) but slightly underestimated intermediate FVC values (bias = –0.070, Figure A1).

Discussion

Projection Function Characterization

The characterization of the projection function, relating the distance (in pixel number) from image center to view zenith angle, is a prerequisite for quantifying the angular variation of the gap fraction, and further estimating vegetation parameters (e.g., FVC). Several methods have been developed to characterize the projection function for fisheye photographs (Baret and Weiss 2017; Lang *et al.* 2010). These methods were delicately designed for fisheye cameras, in which a wide FOV is required to ensure a robust regression between distance and zenith. However, these methods cannot be directly applied to smartphones with a limited FOV as compared to fisheye cameras.

This study proposed a practical method for estimating FOV of smartphone cameras (Section "*GF-1* Satellite Product") in which the zenith angle for each pixel in the smartphone photographs is computed based on a linear projection function assumption. The significant ($p < 0.01$) linear regression between L/D and l/n (Figure 3) demonstrates the robustness of the proposed FOV estimation method and the validity of the linear assumption for the projection function.

Advantages of Smartphones for *in situ* Vegetation Parameter Estimation

Adjusting the photographic exposure of DHP for vegetation parameter estimation is challenging (Leblanc *et al.* 2005; Macfarlane *et al.* 2014; Zhang *et al.* 2005). The difficulty of exposure setting arises from the different definition of optimum exposure regarding camera design and vegetation parameter estimation. For satisfactory visualization, camera tends to please human eye such that the imaged objectives should be seen as 18% reflector (Unwin 1980), yet the main purpose of exposure setting in in situ measurements is to achieve the greatest contrast between sky and canopy (Macfarlane *et al.* 2014; Zhang *et al.* 2005). Several protocols have been proposed for DHP, including using two stops of more exposure than the reference exposure measured in open sky (Zhang *et al.* 2005), taking multiple photographs under different exposures and visually selecting the best one (Macfarlane 2011), and reconstructing above-canopy reference from below-canopy hemispherical photographs (Lang *et al.* 2010). However, these methods are not straightforward for common users during field campaigns, impeding a consistent compatibility with other measurement methods (Pueschel *et al.* 2012).

Photographic exposure is no longer a big issue for smartphone. Figure 6 illustrates that smartphone photographs, under automatic exposure, can provide a greater contrast between sky and canopy than the fisheye acquisitions with the best exposure. Furthermore, spatial details were well retained in smartphone photographs, while lots of them were lost in the fisheye photographs. The loss of fine granularity information in fisheye photographs is mainly due to the overexposure close to nadir directions, which was also revealed by Macfarlane (2011), Pueschel *et al.* (2012), and Zhang *et al.* (2005). The overexposure of DHP is especially obvious for tall trees with small leaves or needles (see Figure 6a and 6b). The exposure discrepancy incurs systematic bias between DHP and DCP measurements (Mougin *et al.* 2014; Pekin and Macfarlane 2009; Ryu *et al.* 2010). Considering that the overexposure phenomenon of fisheye photographs in nadir directions would cause an underestimation of FVC in these canopies (Figure A1), the smartphone estimated FVC may be closer to the true value than DHP (Figure 7b).

The higher spatial resolution of smartphone is also a factor explaining its outperformance over fisheye cameras in resolving small foliage. For DHP, with lower spatial resolution than smartphones, the mixed-pixel problem is a key source of uncertainty in estimating vegetation parameters (Macfarlane 2011) and robust unmixing algorithms are needed to separate mixed pixels into sky and canopy components (Leblanc *et al.* 2005; Ryu *et al.* 2012). On the opposite, the unmixing is not necessary for smartphones, given their improved spatial resolution.

Smartphone is a promising tool to collect *in situ* vegetation measurements also because of its low cost and portability. Smartphones are becoming a popular tool and citizen could contribute for field measurements in a crowdsourcing manner. This would bring a booming increase in field data volume, facilitating the big-data research.

Uncertainties in the Estimated FVC

This study proposed a practical method to estimate the FVC from smartphone photographs. The improved agreement of smartphone FVC estimates with DHP estimates demonstrated the utility of the proposed approach for correcting FOV effects. However, several sources of uncertainty still limit the accuracy of ground-based FVC estimates.

First, for the photograph acquisition and analysis, the automatic photographic exposure and the automatic thresholding Ostu (1979) algorithm were used, respectively. Satisfactory FVC estimation was obtained under these automatic processes (Figure 7b). However, the uncertainty caused by these automatic processes is worth of assessment to further improve our method.

Second, spatial representativeness of measurements should be carefully considered to capture the variation within a plot (Xu *et al.* 2016). Close inspection of Figure 5 revealed that, contrarily to gap fraction theory (Nilson 1999), the canopy closure variation with zenith angle was not monotonically increasing, particularly for angle values close to the nadir direction, because the spatial coverage in this direction is very limited to capture the plot scale variation (Ryu *et al.* 2012). Sampling multiple subplots within each plot is mandatory. The influence of the subplot number on FVC estimation is also worth investigation.

Finally, our study site is located in a mountainous area. It has been well recognized that topography significantly influences the gap faction of forest canopy, and further reduces vegetation parameter retrieval accuracy (Cao *et al.* 2015; María Luisa *et al.* 2008). As illustrated in Figure 4c, the upper left part (up-slopes) seems denser than bottom right part (down-slopes) caused by the distorted path length with topography (Yin *et al.* 2020; Yin *et al.* 2017b). The topographic influence on the gap fraction in the nadir direction is very limited compared to slant directions (María Luisa *et al.* 2008). For this reason, the topographic influence on FVC estimation was neglected in this study.

Prospects for Future Studies

Several issues still merit to be further investigated to improve the practicability of the proposed method.

First, the proposed method was tested using a Huawei Mate 10 smartphone, and the application of the method to other smartphones should be assessed.

Second, the comparison to satellite-derived FVC (Figure 8) confirmed the rational of the proposed method to validate remote sensing products. Therefore, more field campaigns will be implemented in future to compile a representative ground data supporting validation activities of existing FVC products.

Third, the horizontal position of the smartphone was maintained manually in the current study. Gyroscope imbedded in smartphones can be used to guarantee horizontality in future studies.

Fourth, no distinction was made between green leaves and other non-photosynthetic elements. Considering the higher spatial resolution and less sensitivity to exposure setting of smartphone images than fisheye ones, the green elements of vegetation can be potentially extracted from smartphone images, and this may benefit the study of photosynthetic process.

Finally, the zenith and azimuth angles of smartphone camera can be measured and controlled through gyroscope, so the reconstruction of hemispherical observations from smartphones is possible (Tichý 2016). This treatment will provide more detailed description of canopy architecture. The potential of smartphones to reconstruct hemispherical gap fraction and accordingly measure more vegetation parameters (e.g., leaf area index, clumping index and leaf inclination angle) will be assessed in a near future study.

Conclusions

We proposed a practical method to estimate the fractional vegetation cover (FVC) from smartphone photography. The cameras equipped in smartphones typically have a wider field of view (FOV) than the digital single lens reflex cameras used for traditional digital cover photography. This study highlighted that the FOV effect is a key source of uncertainty when estimating vegetation parameters and, particularly, the FVC from smartphone photography. The proposed FOV characterization method allows determining the projection function of the smartphones and limit the acquisitions to the appropriate zenith range close to nadir view for FVC estimation.

This method was assessed in a mountainous forest area in China by comparison with fisheye camera acquisitions and *GF-1* FVC product. The root-mean-square errors (RMSE) of smartphone FVC estimates as compared with both fisheye ground measurements and *GF-1* satellite product were reduced by 40% after the correction of FOV effects. The resulting FVC estimates showed no bias and corrected the observed overestimation in FVC values of original smartphone estimates. Since smartphone photographs are insensitive to the camera exposure setting and to the classification method selection, the proposed method has a promising prospect to support FVC product validation.

Appendix

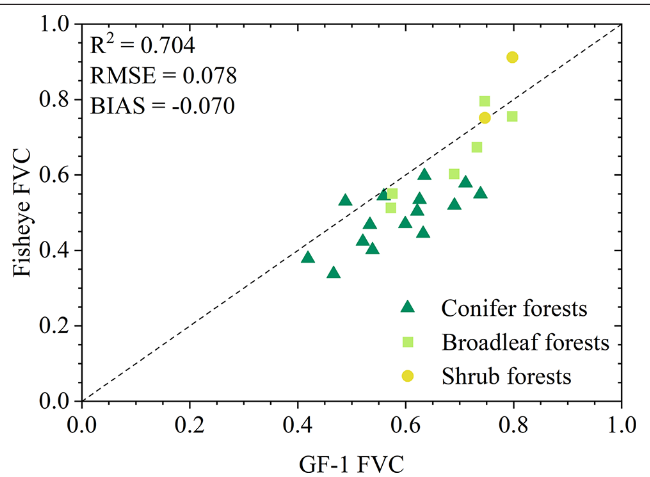

Figure A1. Comparison between FVC estimated from fisheye photographs and *GF-1* satellite.

Acknowledgments

This research was funded by the National Natural Science Foundation of China (41971282), Sichuan Science and Technology Program (2021JDJQ0007; 2020JDTD0003), and the Marie Skłodowska-Curie grant of European Union's Horizon 2020 research and innovation programme (835541). This work also represents a contribution to the CSIC Thematic Interdisciplinary Platform PTI TELEDETECT.

References

Arneth, A. 2015. Uncertain future for vegetation cover. *Nature*, 524, 44–45.

Baret, F., B. de Solan, R. Lopez-Lozano, K. Ma and M. Weiss. 2010. GAI estimates of row crops from downward looking digital photos taken perpendicular to rows at 57.5 degrees zenith angle: Theoretical considerations based on 3D architecture models and application to wheat crops. *Agricultural and Forest Meteorology*, 150, 1393–1401.

Baret, F. and M. Weiss. 2017. *Can_eye V6.4.91 User Manual*.

Baret, F., M. Weiss, R. Lacaze, F. Camacho, H. Makhmara, P. Pacholcyzk and B. Smets. 2013. GEOV1: LAI and FAPAR essential climate variables and FCOVER global time series capitalizing over existing products. Part 1: Principles of development and production. *Remote Sensing of Environment*, 137, 299–309.

Bonan, G. B. and S. C. Doney. 2018. Climate, ecosystems, and planetary futures: The challenge to predict life in Earth system models. *Science*, 359.

Cao, B., Y. Du, J. Li, H. Li, L. Li, Y. Zhang, J. Zou and Q. Liu. 2015. Comparison of five slope correction methods for leaf area index estimation from hemispherical photography. *IEEE Geoscience and Remote Sensing Letters*, 12, 1958–1962.

Confalonieri, R., M. Foi, R. Casa, S. Aquaro, E. Tona, M. Peterle, A. Boldini, G. De Carli, A. Ferrari, G. Finotto, T. Guarneri, V. Manzoni, E. Movedi, A. Nisoli, L. Paleari, I. Radici, M. Suardi, D. Veronesi, S. Bregaglio, G. Cappelli, M. E. Chiodini, P. Dominoni, C. Francone, N. Frasso, T. Stella and M. Acutis. 2013. Development of an app for estimating leaf area index using a smartphone. Trueness and precision determination and comparison with other indirect methods. *Computers and Electronics in Agriculture*, 96, 67–74.

Chen, J., S. Yi, Y. Qin and X. Wang. 2016. Improving estimates of fractional vegetation cover based on UAV in alpine grassland on the Qinghai–Tibetan Plateau. *International Journal of Remote Sensing*, 37, 1922–1936.

Chianucci, F. 2016. A note on estimating canopy cover from digital cover and hemispherical photography. *Silva Fennica*, 50.

Chianucci, F. and A. Cutini. 2013. Estimation of canopy properties in deciduous forests with digital hemispherical and cover photography. *Agricultural and Forest Meteorology*, 168, 130–139.

Chianucci, F., A. Cutini, P. Corona and N. Puletti. 2014. Estimation of leaf area index in understory deciduous trees using digital photography. *Agricultural and Forest Meteorology*, 198–199, 259–264.

Demarez, V., S. Duthoit, F. Baret, M. Weiss and G. Dedieu. 2008. Estimation of leaf area and clumping indexes of crops with hemispherical photographs. *Agricultural and Forest Meteorology*, 148, 644–655.

García-Haro, F. J., M. Campos-Taberner, J. Muñoz-Marí, V. Laparra, F. Camacho, J. Sánchez-Zapero and G. Camps-Valls. 2018. Derivation of global vegetation biophysical parameters from EUMETSAT Polar System. *ISPRS Journal of Photogrammetry and Remote Sensing*, 139, 57–74.

Garrigues, S., N. V. Shabanov, K. Swanson, J. T. Morisette, F. Baret and R. B. Myneni. 2008. Intercomparison and sensitivity analysis of Leaf Area Index retrievals from LAI-2000, AccuPAR, and digital hemispherical photography over croplands. *Agricultural and Forest Meteorology*, 148, 1193–1209.

Jacquemoud, S., W. Verhoef, F. Baret, C. Bacour, P. J. Zarco-Tejada, G. P. Asner, C. Francois and S. L. Ustin. 2009. PROSPECT plus SAIL models: A review of use for vegetation characterization. *Remote Sensing of Environment*, 113, S56–S66.

Jia, K., S. Liang, X. Gu, F. Baret, X. Wei, X. Wang, Y. Yao, L. Yang and Y. Li. 2016. Fractional vegetation cover estimation algorithm for Chinese GF-1 wide field view data. *Remote Sensing of Environment*, 177, 184–191.

Jia, K., L. Yang, S. Liang, Z. Xiao, X. Zhao, Y. Yao, X. Zhang, B. Jiang and D. Liu. 2019. Long-Term Global Land Surface Satellite (GLASS) Fractional Vegetation Cover Product Derived From MODIS and AVHRR Data. *IEEE Journal of Selected Topics in Applied Earth Observations and Remote Sensing*, 12, 508–518.

Jiapaer, G., X. Chen and A. Bao. 2011. A comparison of methods for estimating fractional vegetation cover in arid regions. *Agricultural and Forest Meteorology*, 151, 1698–1710.

Laliberte, A. S., A. Rango, J. E. Herrick, E. L. Fredrickson and L. Burkett. 2007. An object-based image analysis approach for determining fractional cover of senescent and green vegetation with digital plot photography. *Journal of Arid Environments*, 69, 1–14.

Lang, M., A. Kuusk, M. Mõttus, M. Rautiainen and T. Nilson. 2010. Canopy gap fraction estimation from digital hemispherical images using sky radiance models and a linear conversion method. *Agricultural and Forest Meteorology*, 150, 20–29.

Lang, M., T. Nilson, A. Kuusk, J. Pisek, L. Korhonen and V. Uri. 2017. Digital photography for tracking the phenology of an evergreen conifer stand. *Agricultural and Forest Meteorology*, 246, 15–21.

Leblanc, S. G., J. M. Chen, R. Fernandes, D. W. Deering and A. Conley. 2005. Methodology comparison for canopy structure parameters extraction from digital hemispherical photography in boreal forests. *Agricultural and Forest Meteorology*, 129, 187–207.

LI-COR. 1991. *LAI-2000 Plant Canopy Analyzer Operating Manual.*

Liu, J., E. Pattey and S. Admiral. 2013. Assessment of in situ crop LAI measurement using unidirectional view digital photography. *Agricultural and Forest Meteorology*, 169, 25–34.

Macfarlane, C. 2011. Classification method of mixed pixels does not affect canopy metrics from digital images of forest overstorey. *Agricultural and Forest Meteorology*, 151, 833–840.

Macfarlane, C., A. Grigg and C. Evangelista. 2007a. Estimating forest leaf area using cover and fullframe fisheye photography: Thinking inside the circle. *Agricultural and Forest Meteorology*, 146, 1.

Macfarlane, C., M. Hoffman, D. Eamus, N. Kerp, S. Higginson, R. McMurtrie and M. Adams. 2007b. Estimation of leaf area index in eucalypt forest using digital photography. *Agricultural and Forest Meteorology*, 143, 176–188.

Macfarlane, C., Y. Ryu, G. N. Ogden and O. Sonnentag. 2014. Digital canopy photography: Exposed and in the raw. *Agricultural and Forest Meteorology*, 197, 244–253.

María Luisa, E., B. Frédéric and W. Marie. 2008. Slope correction for LAI estimation from gap fraction measurements. *Agricultural and Forest Meteorology*, 148, 1553–1562.

Morsdorf, F., B. Kötz, E. Meier, K. I. Itten and B. Allgöwer. 2006. Estimation of LAI and fractional cover from small footprint airborne laser scanning data based on gap fraction. *Remote Sensing of Environment*, 104, 50–61.

Mougin, E., V. Demarez, M. Diawara, P. Hiernaux, N. Soumaguel and A. Berg. 2014. Estimation of LAI, fAPAR and fCover of Sahel rangelands (Gourma, Mali). *Agricultural and Forest Meteorology*, 198–199, 155–167.

Mu, X., S. Huang, H. Ren, G. Yan, W. Song and G. Ruan. 2015. Validating GEOV1 fractional vegetation cover derived from coarse-resolution remote sensing images over croplands. *IEEE Journal of Selected Topics in Applied Earth Observations and Remote Sensing*, 8, 439–446.

Mu, X., W. Song, Z. Gao, T. R. McVicar, R. J. Donohue and G. Yan. 2018. Fractional vegetation cover estimation by using multi-angle vegetation index. *Remote Sensing of Environment*, 216, 44–56.

Nilson, T. (1999). Inversion of gap frequency data in forest stands. *Agricultural and Forest Meteorology*, 98–9, 437–448.

Okin, G. S., K. D. Clarke and M. M. Lewis. 2013. Comparison of methods for estimation of absolute vegetation and soil fractional cover using MODIS normalized BRDF-adjusted reflectance data. *Remote Sensing of Environment*, 130, 266–279.

Otsu, N. 1979. A threshold selection method from gray-level histograms. *IEEE Transactions on Systems, Man, and Cybernetics*, 9, 62–66.

Pekin, B. and C. Macfarlane. 2009. Measurement of crown cover and leaf area index using digital cover photography and its application to remote sensing. *Remote Sensing*, 1, 1298–1320.

Pueschel, P., H. Buddenbaum and J. Hill. 2012. An efficient approach to standardizing the processing of hemispherical images for the estimation of forest structural attributes. *Agricultural and Forest Meteorology*, 160, 1–13.

Qu, Y., J. Meng, H. Wan and Y. Li. 2016. Preliminary study on integrated wireless smart terminals for leaf area index measurement. *Computers and Electronics in Agriculture*, 129, 56–65.

Qu, Y., J. Wang, J. Song and J. Wang. 2017. Potential and limits of retrieving conifer leaf area index using smartphone-based method. *Forests*, 8.

Ryu, Y., O. Sonnentag, T. Nilson, R. Vargas, H. Kobayashi, R. Wenk and D. D. Baldocchi. 2010. How to quantify tree leaf area index in an open savanna ecosystem: A multi-instrument and multi-model approach. *Agricultural and Forest Meteorology*, 150, 63–76.

Ryu, Y., J. Verfaillie, C. Macfarlane, H. Kobayashi, O. Sonnentag, R. Vargas, S. Ma and D. D. Baldocchi. 2012. Continuous observation of tree leaf area index at ecosystem scale using upward-pointing digital cameras. *Remote Sensing of Environment*, 126, 116–125.

Tichý, L. 2016. Field test of canopy cover estimation by hemispherical photographs taken with a smartphone. *Journal of Vegetation Science*, 27, 427–435.

Unwin, D. M. 1980. *Microclimate Measurement for Ecologists*. London: Academic Press.

Verger, A., F. Baret and M. Weiss. 2014. Near real-time vegetation monitoring at global scale. *IEEE Journal of Selected Topics in Applied Earth Observations and Remote Sensing*, 7, 3473–3481.

White, M. A., G. P. Asner, R. R. Nemani, J. L. Privette and S. W. Running. 2000. Measuring fractional cover and leaf area index in arid ecosystems: Digital camera, radiation transmittance, and laser altimetry methods. *Remote Sensing of Environment*, 74, 45–57.

Xu, B., J. Li, Q. Liu, A. R. Huete, Q. Yu, Y. Zeng, G. Yin, J. Zhao and L. Yang. 2016. Evaluating spatial representativeness of station observations for remotely sensed leaf area index products. *IEEE Journal of Selected Topics in Applied Earth Observations and Remote Sensing*, 9, 3267–3282.

Yan, G., R. Hu, J. Luo, M. Weiss, H. Jiang, X. Mu, D. Xie and W. Zhang. 2019. Review of indirect optical measurements of leaf area index: Recent advances, challenges, and perspectives. *Agricultural and Forest Meteorology*, 265, 390–411.

Yin, G., B. Cao, J. Li, W. Fan, Y. Zeng, B. Xu and W. Zhao. 2020. Path length correction for improving leaf area index measurements over sloping terrains: A deep analysis through computer simulation. *IEEE Transactions on Geoscience and Remote Sensing*, 58, 4573–4589.

Yin, G., A., Li and A. Verger. 2017a. Spatiotemporally representative and cost-efficient sampling design for validation activities in Wanglang experimental site. *Remote Sensing*, 9.

Yin, G. F., A. N. Li, S. B. Wu, W. L. Fan, Y. L. Zeng, K. Yan, B. D. Xu, J. Li and Q. H. Liu. 2018. PLC: A simple and semi-physical topographic correction method for vegetation canopies based on path length correction. *Remote Sensing of Environment*, 215, 184–198.

Yin, G. F., A. N. Li, W. Zhao, H. A. Jin, J. H. Bian and S.B.A. Wu. 2017b. Modeling canopy reflectance over sloping terrain based on path length correction. *IEEE Transactions on Geoscience and Remote Sensing*, 55, 4597–4609.

Zhang, Y. Q., J. M. Chen and J. R. Miller. 2005. Determining digital hemispherical photograph exposure for leaf area index estimation. *Agricultural and Forest Meteorology*, 133, 166–181.

A Low-Cost and Portable Indoor 3D Mapping Approach Using Biaxial Line Laser Scanners and a One-Dimension Laser Range Finder Integrated with Microelectromechanical Systems

Xuzhe Duan, Qingwu Hu, Pengcheng Zhao, and Shaohua Wang

Abstract

Existing indoor 3D mapping solutions suffer from high cost and poor portability. In this article, a low-cost and portable indoor 3D mapping approach using biaxial line laser scanners and a one-dimension laser range finder integrated with microelectromechanical systems is proposed. A multiple-sensor calibration approach is presented to perform the extrinsic calibration of the integrated 3D mapping system. The 2D point cloud acquired by the horizontal laser scanner and the orientation information obtained by the microelectromechanical systems are used as inputs for a simultaneous localization and mapping framework to estimate the 2D poses. The height information acquired by the laser range finder is then fused to obtain the 3D pose, which is applied to restore the actual position and orientation of the 2D point cloud generated by the tilted laser scanner to reconstruct the 3D point cloud of the indoor environment. The experimental results—three typical indoor scenes—demonstrate that the proposed approach can achieve accuracies of 3 cm and 2°. Therefore, the proposed approach is a low-cost, portable, and accurate solution for indoor 3D mapping.

Introduction

Multiple-sensor-integration mobile mapping technology is a cutting-edge technology that integrates positioning, attitude determination, and measurement (D. Li 2006). Different from traditional measurement, which requires the instrument to be fixed at several predetermined stations, mobile measurement technology realizes measurements in motion and avoids the waste of human and time resources caused by the migration of instruments among multiple stations. It also improves the degree of freedom of the platform and solves the problem of blind spots that can exist with traditional methods. A typical mobile measurement system consists of a laser scanner, an optical camera, a global navigation satellite system (GNSS), and an inertial measurement unit (IMU); the GNSS and IMU are responsible for determining the trajectory of the platform, whereas the laser scanner and the optical camera are applied to sense the surrounding environment (Puente *et al.* 2013; Zhao *et al.* 2018).

Generalized mobile measurement refers to the collection of spatial-position and attribute data of roadside features with mobile vehicles as platforms (D. Li 2006; Gong *et al.* 2015). However, with continuous improvements in the quality of life, the spatial information of the indoor environment—which accounts for more than 90% of the time spent by human beings—has begun to receive more and more attention. Accurate indoor 3D spatial information can be applied to many fields, such as indoor navigation for mobile robots, digital reconstruction and conservation of ancient ruins, and emergency escape guidance for sudden indoor disasters. The rapid establishment of accurate indoor maps has become a prerequisite for building information modeling/management, indoor location-based services, and augmented and virtual reality applications (Domínguez Martin *et al.* 2011; Zlatanova and Isikdag 2015; Chen and Clarke 2020).

Ensuring that the sensor's position can be determined while it is in motion is a precondition for the effective implementation of mobile measurement solutions. However, it is often not possible to obtain valid GNSS satellite signals to evaluate the trajectory of the platform in indoor environments (Li *et al.* 2020). Simultaneous localization and mapping (SLAM) is a popular technology for solving indoor localization problems. It aims to build a model of the surrounding environment and estimate the platform's own motion state by using a specific sensor without prior environmental information (Dissanayake *et al.* 2001). The increasing maturity of SLAM technology provides strong technical support for indoor mobile measurement, which has addressed the problem of how platforms can "localize themselves" in the absence of GNSS signals.

SLAM can be divided into visual SLAM and laser SLAM, depending on the sensor type. The positioning and mapping technology that uses a monocular, stereo, or depth camera as the only exteroceptive sensor is called visual SLAM (Davison *et al.* 2007; Comport *et al.* 2010; Fuentes-Pacheco *et al.* 2015; Forster *et al.* 2017; Mur-Artal and Tardós 2017). It has the characteristics of small size, low power consumption, and rich information acquisition, which can provide rich environment texture information (Di *et al.* 2019). With the continuous optimization of image-matching algorithms, research on visual SLAM has grown stronger (J. Li *et al.* 2017; Li *et al.* 2020; Mao *et al.* 2020; Cao *et al.* 2021). However, since cameras are susceptible to visual-field limitations, bad weather, backlight, and other unsatisfactory conditions, visual SLAM is often very dependent on the working environment, and has low accuracy (Huang *et al.* 2018).

Laser SLAM has gradually become the most popular area of research in the field of SLAM. Benefiting from the characteristics of a laser scanner, laser SLAM has the advantages of high measurement accuracy, high directionality, and low computational effort (Debeunne and Vivet 2020; Wei *et al.* 2020). According to the mathematical optimization framework adopted, laser SLAM can be further divided into filter-based and graph optimization-based. FastSLAM is a typical filter-based laser SLAM scheme (Montemerlo *et al.* 2002). In this algorithm, the platform's poses are estimated by a particle filter, and each particle is propagated by the kinematics model. For the propagated particles, the weight is calculated by the observation model and the map is constructed according to the estimated poses. On this basis, a Gmapping scheme that uses a Rao–Blackwellized particle filter to synchronize the position and orientation of the platform has been proposed (Grisetti *et al.* 2007). Gmapping solves FastSLAM's problems of high memory consumption

Xuzhe Duan, Qingwu Hu, Pengcheng Zhao, and Shaohua Wang are with the School of Remote Sensing and Information Engineering, Wuhan University, Wuhan 430079, China (shwang@whu.edu.cn).

Contributed by Rongjun Qin, June 30, 2021 (sent for review August 5, 2021; reviewed by Kaleel M Al-Durgham, Ruofei Zhong).

Photogrammetric Engineering & Remote Sensing
Vol. 88, No. 5, May 2022, pp. 311–321.
0099-1112/22/311–321

doi: 10.14358/PERS.21-00037R2

and particle dissipation, but is still heavily geared toward odometry information.

The Hector SLAM scheme is an algorithm with front-end scan matching only and no back-end optimization (Kohlbrecher *et al.* 2011). It solves the scan-matching problem using the Gauss–Newton method and achieves reliable localization and mapping capabilities by using fast approximation of map gradients and multi-resolution grids. Google's Cartographer (Hess *et al.* 2016) scheme focuses on a method of creating local submaps and a scan-matching strategy for detecting loop closure. Local errors are optimized by an extended Kalman filter (EKF), and global errors are allocated by a graph-optimized scheme. In the field of 3D laser SLAM, the LOAM scheme is based on scan matching of feature points and uses a nonlinear optimization method for laser-map matching (J. Zhang and Singh 2014). The algorithm has become a classical framework for 3D laser SLAM. In the LeGO-LOAM scheme, a segmentation process for point clouds is introduced (Shan and Englot 2018). The ground points and the points that remain after segmentation are labeled, and feature extraction and frame matching are performed on the two separately. Shan's team then proposed the LIO-SAM scheme, which uses the idea of a factor graph to perform optimization of loop closure and further improves the robustness of 3D SLAM (Shan *et al.* 2020). However, these 3D SLAM schemes all require a multi-line laser scanner that obtains 3D point clouds.

In terms of hardware, representative mobile mapping devices for laser SLAM on the market mainly include trolley-type devices, represented by the NavVis M6 (https://www.navvis.com/M6), backpack-type devices, represented by the Leica Pegasus Backpack (https://www.faro.com/en/Products/Hardware/Focus-Laser-Scanners), and handheld devices, represented by the GeoSLAM ZEB-REVO (https://geoslam.com/solutions/zeb-revo-rt). The most portable is the GeoSLAM ZEB-REVO; it weighs 3.5 kg, which is not convenient for large-scale and long-term operation. All three types of devices have relatively high costs, and therefore are not suitable for low-budget research and production.

Materials and Methods

The proposed low-cost and portable indoor 3D mapping approach integrates two line laser scanners, a one-dimension laser range finder, and microelectromechanical systems (MEMS). The general idea for 3D mapping is illustrated in Figure 1.

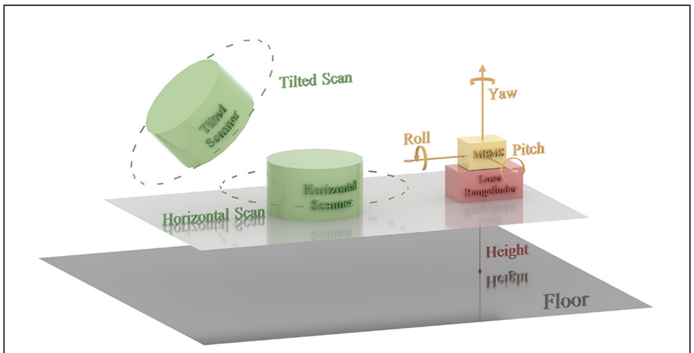

Figure 1. Mapping principle.

As the figure shows, each of the two line laser scanners (colored in green) captures a 2D point cloud in its own plane, the MEMS (colored in yellow) acquires the 3D orientation information, and the one-dimension laser range finder (colored in red) outputs the height information. The horizontal 2D plane point cloud and the MEMS orientation data are used as the inputs of SLAM to evaluate the trajectory of the platform. As the spatial height of our platform is not consistent and the platform bumps as the operator walks, a height observation is required to supplement 2D SLAM to estimate the actual position of the platform in 3D space. We assume that the ground in the scene is consistent during data acquisition, so that the range information acquired by the laser range finder can be corrected with the MEMS to evaluate the actual height of the platform. With the estimated 3D poses, the 2D point clouds obtained by the tilted scanner are then converted into the 3D point clouds in a push-broom way.

The overall workflow is shown in Figure 2. The next section introduces the system and materials. The following section proposes the multiple-sensor calibration approach, and then comes a section showing the SLAM scheme, including how to map the indoor environment, estimate the platform poses, and output the trajectory information. Then we describe the method of fusing data collected by multiple sensors and reconstructing a 3D point cloud.

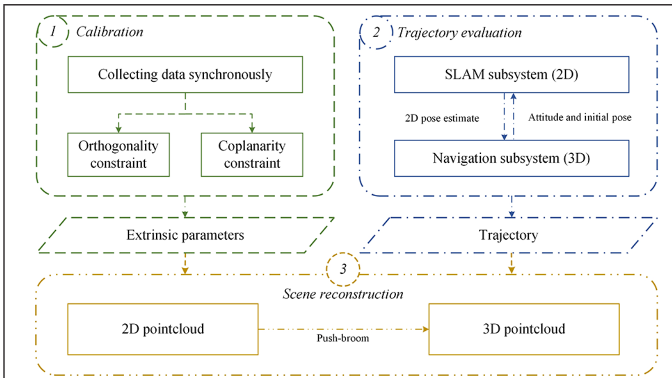

Figure 2. Study workflow chart.

System and Materials

The proposed indoor 3D mapping approach in this article assembles a MEMS-IMU (HI226), a laser range finder (LDM_L1), and two line laser scanners (ScannerS1 and ScannerA3), as shown in Figure 3a. Based on experience in mobile measurement systems and previous knowledge (Thomson *et al.* 2013; Vosselman 2014), we design the axial orientations of the two laser scanners and their scanning pattern as shown in Figure 3b. The plane of the red dashed line is the scanning plane of the horizontal ScannerA3, and that of the green dashed line is the scanning plane of the tilted ScannerS1. With a total weight of 2.6 kg and an ergonomic handle, the device can be easily held in one hand by surveying personnel.

The HI226 MEMS-IMU, produced by HiPNUC, integrates a three-axis accelerometer, a three-axis gyroscope, and a low-power microprocessor, which can output the roll, pitch, and relative yaw angle based on local geographic coordinates by a sensor fusion algorithm (https://hipnuc.com/HI226_229.html). The LDM_L1 laser range finder, manufactured by MyAntenna, measures the distance of the target object by detecting the phase difference of the laser, and can achieve millimeter-level resolution in the measurement range of 0.05 to 40 m (http://imyantenna.com/pro_view-62.html). Two line laser scanners, RPLIDAR A3 (https://www.slamtec.com/en/Lidar/A3) and RPLIDAR S1 (https://www.slamtec.com/en/Lidar/S1) from Slamtec, are integrated on the device. The RPLIDAR A3 horizontal laser scanner can sample up to 16 000 times/s at a frequency of 20 Hz, with a maximum measurement range of 25 m and an angular resolution of 0.3375°. The high-frequency characteristics make it suitable for the SLAM process, especially for building solid maps even during turns. The RPLIDAR S1 tilted laser scanner can sample 9200 times/s at 15 Hz, with a measurement radius up to 40 m and a measurement resolution of 3 cm, which guarantees the accuracy of the final 3D point cloud. An industrial personal computer (IPC) with an AAEON UP-APL01 mainboard and an Intel Pentium N4200 1.10-GHz processor is also installed inside the device to control power supply, store data, implement real-time SLAM in the robot operating system, and publish map services for the mobile terminal. The entire system costs about 11 500 yuan, which is a fairly low price for a handheld 3D laser scanning device on the market today.

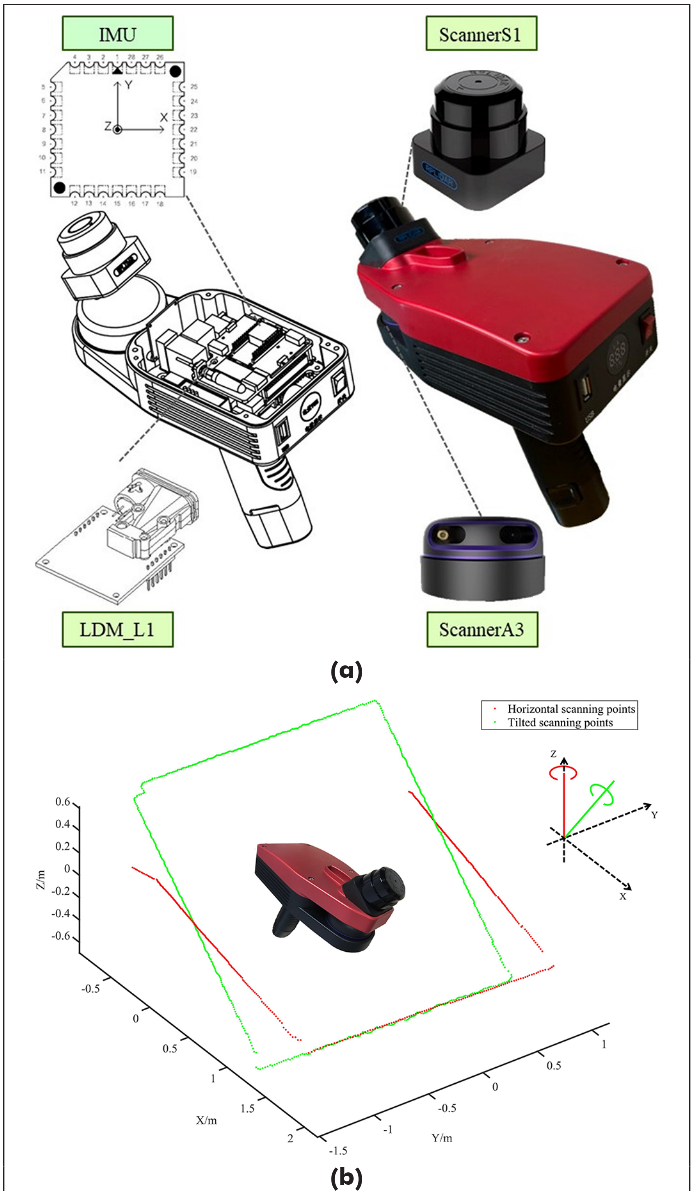

Figure 3. Device design scheme: (a) device components; (b) scanning pattern.

System Calibration

Calibration Principle

Extrinsic calibration among sensors is the premise of multi-sensor data fusion. For our approach, the extrinsic parameters between the horizontal laser scanner and the tilted laser scanner directly affect the accuracy of the 3D point cloud. A 2D line laser scanner can only obtain a point cloud on the plane where it is located (e.g., the two dashed lines in Figure 3b). Therefore, unlike extrinsic calibration of multiple 3D laser scanners, multiple depth cameras, or even one laser scanner and one camera, the extrinsic calibration process for 2D line laser scanners cannot be achieved by simply finding preplaced retroreflective targets or identifiable features in the 3D scene. Specific constraints need to be constructed to calibrate the 2D line laser scanners using a given scene (in this case a cuboid-shaped corridor) as the georeferenced target.

The essence of extrinsic calibration for two laser scanners is to find the relative rotation and translation parameters from one scanner to the other. The coordinate frames of the two laser scanners are denoted as S_1 and S_2, respectively. Ideally, when a cuboid-shaped corridor is scanned using two laser scanners, two parallelograms will be obtained, and all the sides of the parallelograms will be on the surfaces of the corridor. The coplanarity constraint and the orthogonality constraint are expressed as

$$(\mathbf{R}_1\mathbf{I}_1^a \times \mathbf{R}_2\mathbf{I}_2^a) \cdot (\mathbf{R}_1\mathbf{C}_1^a + \mathbf{T}_1 - \mathbf{R}_2\mathbf{C}_2^a - \mathbf{T}_2) = 0 \tag{1}$$

and

$$\mathbf{n}^a \cdot \mathbf{n}^b = (\mathbf{R}_1\mathbf{I}_1^a \times \mathbf{R}_2\mathbf{I}_2^a) \cdot (\mathbf{R}_1\mathbf{I}_1^b \times \mathbf{R}_2\mathbf{I}_2^b) \tag{2}$$

where a and b denote two adjacent surfaces in the corridor, C_i^k and I_i^k represent the center point and the direction vector of the line L_i^k (i = 1, 2; k = 1, 2, 3, 4) scanned by the ith laser scanner on the surface k, $[R_1\,|T_1] \in \mathbb{R}^3$ and $[R_2\,|T_2] \in \mathbb{R}^3$ denote the poses of the two laser scanners with respect to a common reference frame, and $\mathbf{n}^k$ represents the normal vector of the surface k, as shown in Figure 4. The coplanarity constraint indicates that when scan lines fall on the same surface of the corridor, they should be on the same 3D plane. In Equation 1, it is expressed as the two dashed lines (colored in blue) perpendicular to each other in Figure 4. The orthogonality constraint means that two adjacent surfaces of the corridor should be perpendicular. In Equation 2, it is expressed as the two plane normal vectors (colored in light yellow and dark yellow, respectively) perpendicular to each other in Figure 4. The Levenberg–Marquardt algorithm is adopted to solve the nonlinear optimization problem with constraints, and the relative relationship between sensors can be calculated (Fernández-Moral *et al.* 2015; Yin *et al.* 2018).

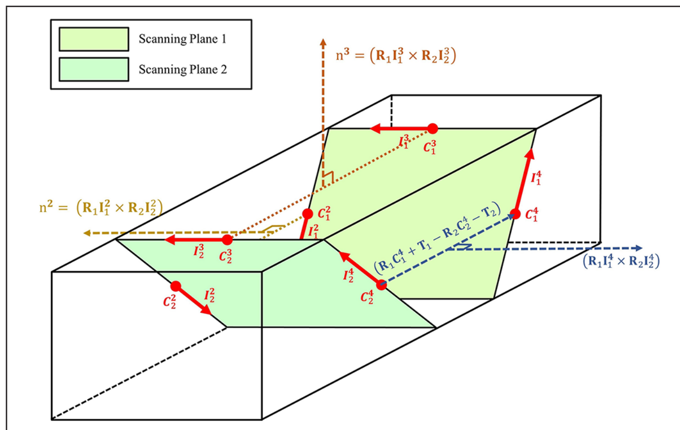

Figure 4. 3D view of two scanned parallelograms.

The whole calibration procedure has four parts (Figure 5): collecting observations, extracting lines, constructing constraints, and calculating calibration results.

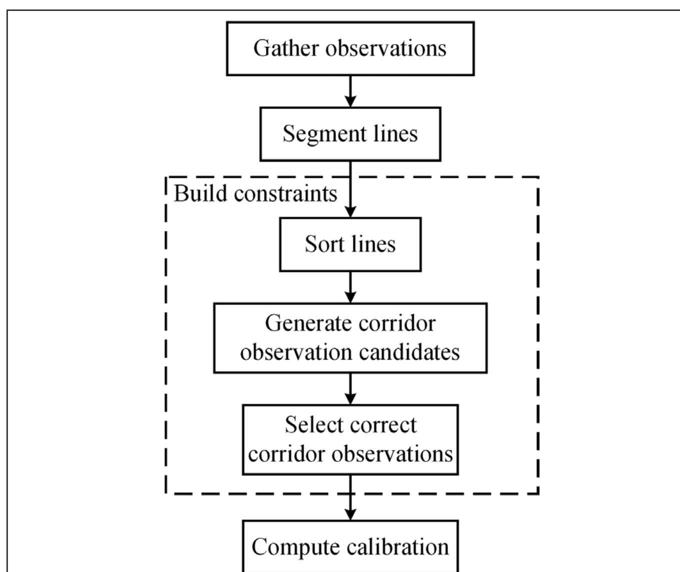

Figure 5. Extrinsic calibration workflow chart.

First, the random sample consensus (RANSAC) algorithm is used to detect lines. RANSAC can effectively cluster lines that are interrupted by the dead view zone of the scanner into a continuous line, thus increasing the number of constraints (Fischler and Bolles 1987). Constraints including the nearest sampling distance threshold, the maximum sampling distance threshold, and the minimum distance threshold between two sampling points are added to the RANSAC algorithm to extract lines. Line-fitted models are constructed by randomly sampling two points in the point set. All other points are verified on the model, being divided into inliers and outliers. The model with the highest ratio of inliers to outliers is selected as the detected-line model. This cycle is repeated four times in each group of observations to detect up to four lines with the highest confidence.

Second, by determining the subordinate relationship between the line and the corridor surface, the valid corridor observations in each set of data are found, and the coplanarity and orthogonality constraints are constructed. Assuming that n lines ($n \leq 4$) are extracted from the scan results at each moment, these lines must be sorted to determine the corresponding relationship between lines and corridor surfaces. The line-sorting method is applied as follows:

(1) Finding the center points of each line;
(2) Sorting the lines by the angle between the vector from zero point to center point and the vector of the positive x-axis direction;
(3) Setting the index of the first line as *1st* and determining whether the next line belongs to the opposite surface, the previous adjacent surface, or the next adjacent surface, based on the relationship between the direction vectors until each line is set an index.

After the line-sorting process, a sorted line set is generated in each group of data:

$$\mathrm{SL} = \{\mathrm{SSL_i}\}\ (i = 1, 2, \ldots, n_{\mathrm{LRFs}}) \tag{3}$$

where n_{LRFs} is the number of laser scanners and

$$\mathrm{SSL_i} = \{L_i^j\}\ (i = 1, 2, \ldots, n_{\mathrm{LRFs}}) \tag{4}$$

where L_i^j denotes the sorted line with an index of j in the lines from the ith laser scanner.

A corridor observation can be regarded as a set containing four lines:

$$\mathrm{CO} = \{S_1, S_2, S_3, S_4\} \tag{5}$$

where S_a (a = 1, 2, 3, 4) denotes the line set with respect to the corridor surface a:

$$S_a = \{L_i^a\}\ (a = 1, 2, 3, 4;\ i = 1, 2, \ldots, n_{\mathrm{LRFs}}) \tag{6}$$

Comparing Equations 4 and 6, we can find that the essence of obtaining CO is to convert L_i^j to L_i^a—that is, to find the correct arrangement conversion from the line index to the corridor surface index. In this way, lines with the same corridor surface index are coplanar line pairs; lines with adjacent corridor surface indexes are located on two mutually perpendicular surfaces. We adopt an evaluation method based on coplanarity to find the correct observations from the candidates. For any two lines extracted from the scan results, their four endpoints form a tetrahedron. Assuming $\vec{a}$, $\vec{b}$, and $\vec{c}$ are the three vectors from one vertex to the other three vertices in the tetrahedron, the volume of the tetrahedron can be computed as

$$V_{tetrahedron} = \left| \frac{(\vec{a} \times \vec{b}) \cdot \vec{c}}{6} \right| \tag{7}$$

The relationship between the two line segments can be determined by whether $V_{\mathrm{tetrahedron}}$ is close to zero. With all possible corridor observations generated previously, each can be assessed by the sum of all the tetrahedron volumes in all four corridor surfaces:

$$V_{\mathrm{CO}} = \sum_{w=1}^{4} \Phi\left(l_1, l_2, \ldots, l_{n_w}\right) \tag{8}$$

where n_w denotes the number of lines in the corridor surface w, the function Φ calculates the sum of the tetrahedron volumes, and V_{CO} is the assessment score of the corridor observation. The corridor observation with the smallest V_{CO} is taken as the correct observation.

Finally, the calibration problem is transformed into a nonlinear optimization problem with the coplanarity and orthogonality constrains, expressed as

$$\begin{aligned} \underset{\{\mathbf{R},\mathrm{T}\}}{\operatorname{argmin}} \sum_{i=1}^{N} \Bigg(& \sum_{a=1}^{4} \omega_i^a \left(\left(\mathbf{R}_j \mathbf{I}_j^a \times \mathbf{R}_k \mathbf{I}_k^a \right) \cdot \left(\mathbf{R}_j \mathbf{c}_j^a + \mathbf{T}_j - \mathbf{R}_k \mathbf{c}_k^a - \mathbf{T}_k \right) \right)^2 + \\ & \sum_{a=1}^{3} \omega_i^{a,a+1} \left(\left(\mathbf{R}_j \mathbf{I}_j^a \times \mathbf{R}_k \mathbf{I}_k^a \right) \cdot \left(\mathbf{R}_j \mathbf{I}_j^{a+1} \times \mathbf{R}_k \mathbf{I}_k^{a+1} \right) \right)^2 \Bigg) \end{aligned} \tag{9}$$

where N is the number of corridor observations, j is the index of the laser scanner to be calibrated, k is the index of the reference laser scanner, a is the surface index of the corridor, and w_i is the weight of the corresponding residual from CO_i. The Levenberg–Marquardt method is used to iteratively solve the nonlinear least-squares problem:

$$[\mu_2^k \Delta \mathrm{T}_2^k, \ldots, \mu_m^k \Delta \mathrm{T}_m^k]^T = -(H + \lambda \mathrm{diag}(H))^{-1} g \tag{10}$$

where m is the number of laser scanners, k is the index of the iteration, μ_j^k (j=2,…,m) represents the rotation increment represented by the exponential map ($e^{u_j} \mathbf{R}_j$), $\Delta \mathrm{T}_m^k$ indicates the increment of translation transformation, λ is the Levenberg–Marquardt damping factor, H is a $6(m-1)$-dimensional Hessian matrix, and g is the gradient of the cost function. The rotation matrix is then updated using the exponential map as

$$\mathbf{R}_j^{k+1} = e^{\mu_j^k} \mathbf{R}_j^k,\ \mathbf{T}_j^{k+1} = \Delta \mathbf{T}_j^k + \mathbf{T}_j^k\ (j \in [2, m]) \tag{11}$$

from an initial guess which can be obtained from a rough measurement of the device.

Calibration Process

Figure 6 shows the cuboid-shaped corridor selected for our calibration. The length of the corridor was about 6.5 m, and its width and height were 2.2 and 2.3 m, respectively. The corridor had a regular shape and was free of doors, windows, and other clutter to interfere with the calibration process. The scan frequency of the two line laser scanners was unified at 15 Hz and the platform was steadily rotated and translated in the corridor. Data from the two scanners were collected simultaneously for about 1 min as an independent group of observations. The acquisition process was repeated several times to yield five groups of high-quality independent observations.

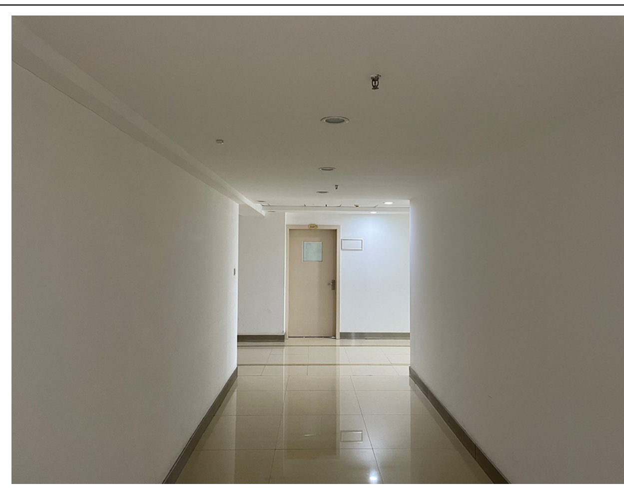

Figure 6. Extrinsic calibration site.

Referring to the design drawing of the device, the initial pose of the tilted laser scanner relative to the horizontal laser scanner was set as [0°, 30°, 0°] and [0.00 mm, 0.00 mm, −64.81 mm]. Figure 7 shows the line-detection results for some frames. Two to four lines (colored in gray) could be detected in the point clouds (colored in red and green) obtained from the laser scanners. The calibration was repeated 100 times for each observation group, and error processing was performed on the results (Pukelsheim 1994). The mean of the five calibration results was calculated as the final extrinsic parameters. The standard deviation of each set of observations was then computed to measure the accuracy of the calibration results, as shown in Table 1.

Table 1. Calibration results between two laser scanners.

Item	Rotation (°)	Translation (mm)
No. 1	−0.22, 31.37, −1.31	11.91, −8.81, −60.27
No. 2	−0.17, 31.41, −1.24	10.29, −7.81, −61.86
No. 3	−0.17, 31.25, −1.33	11.94, −3.62, −60.47
No. 4	−0.15, 31.45, −1.43	8.51, −3.23, −60.55
No. 5	−0.18, 31.30, −1.36	12.20, −2.84, −62.80
Extrinsic parameters	−0.18, 31.36, −1.33	10.97, −5.26, −61.02
Standard deviation	0.02, 0.07, 0.06	1.40, 2.52, 0.72

As can be seen from Table 1, the standard deviation of the calibration result was kept within 0.1° and 2.6 mm, which corresponded to the accuracy of the subsequent 3D reconstruction. It is also noticeable that the y-axis translation deviation and the pitch deviation were greater than those on the other two axes. This phenomenon is normal, because it was difficult to provide the platform with a large pitch angle in practice, and consequently the constraints in the y-direction and the pitch angle were weak.

Trajectory Evaluation

Framework of Trajectory Evaluation

Considering the scan frequency of the RPLIDAR A3 and the computing performance of the IPC, Hector SLAM was selected as the foundation for real-time positioning and mapping in our solution. Referring to the existing SLAM frameworks (Kohlbrecher *et al.* 2011, 2014), the trajectory-evaluation scheme in this article is shown in Figure 8. It combines a scan-matching approach using a laser scanner with a 3D estimate module based on additional measurements. The 2D SLAM consists of three steps: data preprocessing, scan matching, and plane-map

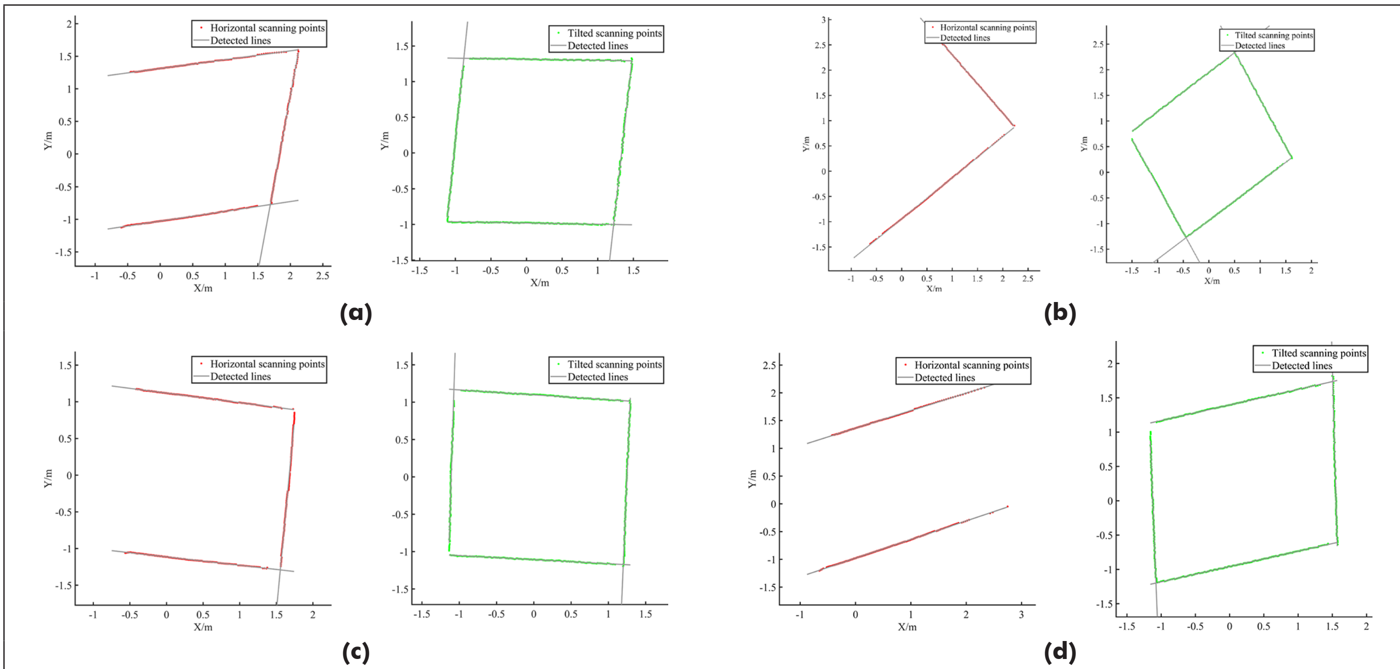

Figure 7. The line-detection results for some frames: (a) frame 32, (b) frame 404, (c) frame 860, (d) frame 1052.

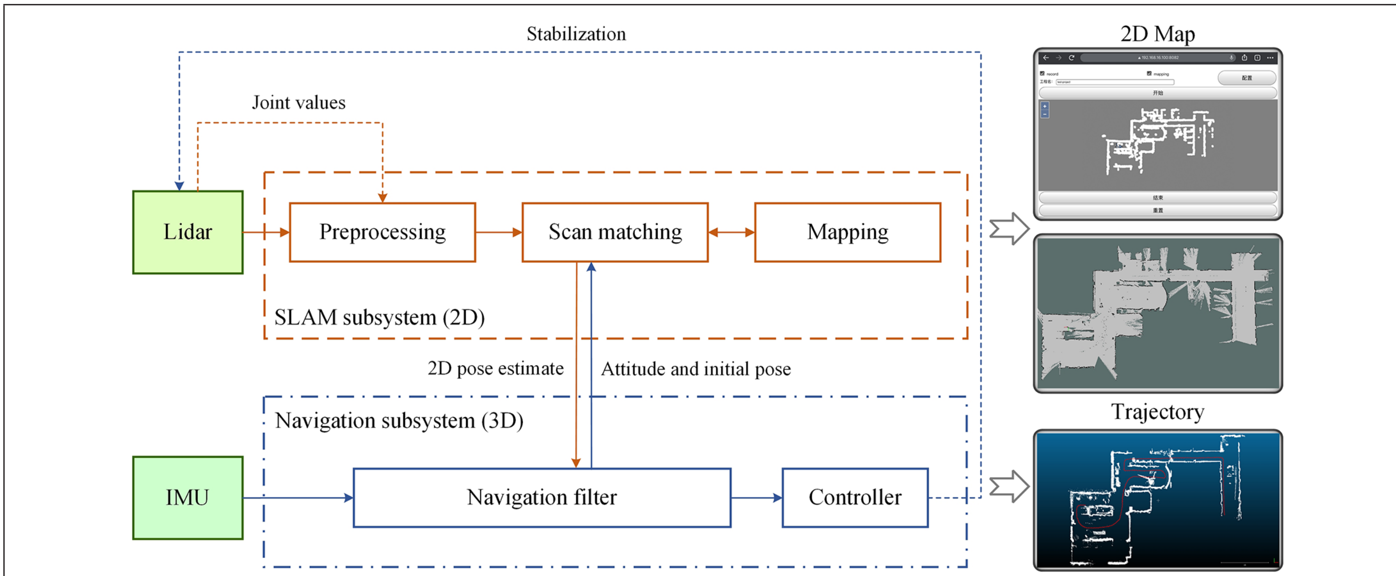

Figure 8. Trajectory-evaluation flowchart.

construction. In the 3D navigation, the filter fuses the inertial and height information to form a consistent 3D solution. Both estimates are updated individually and loosely coupled, to keep synchronized over time. The two modules interact with each other to output the pose of the platform at every moment.

The state of the platform is represented as $x = (\Omega^T, p^T, v^T)^T$, where $\Omega = (\phi, \theta, \psi)^T$ represents the roll, pitch, and yaw Euler angles, and $p = (p_x, p_y, p_z)^T$ and $v = (v_x, v_y, v_z)^T$ are the position and velocity of the platform, respectively. The angular velocity $\omega = (\omega_x, \omega_y, \omega_z)^T$ and the acceleration $a = (a_x, a_y, a_z)^T$ obtained by the IMU constitute the input vector $u = (\omega^T, a^T)^T$. The motion of the platform is described by the nonlinear differential-equation system

$$\dot{\Omega} = E_\Omega \cdot w \tag{12}$$

$$\dot{p} = v \tag{13}$$

$$\dot{v} = R_\Omega \cdot a + g \tag{14}$$

where R_Ω is the direction cosine matrix that maps a vector in the body frame to the navigation frame, E_Ω maps the angular rate to the derivative of the Euler angles, and g is the constant gravity vector (Kuipers 1999).

2D SLAM for Planar Localization

An occupancy grid map is used to represent the arbitrary environments. The process is divided into two main stages: map access and scan matching. The continuous environmental information is first discretized with the laser data. These discrete laser scans are then matched and local maps are fused to form global maps (Thrun 2002). Depending on the actual scenario and the characteristics of the laser scanner, the point cloud can be preprocessed, for example by downsampling the number of points or removing the outliers, so as to better match the scan results in the subsequent processing.

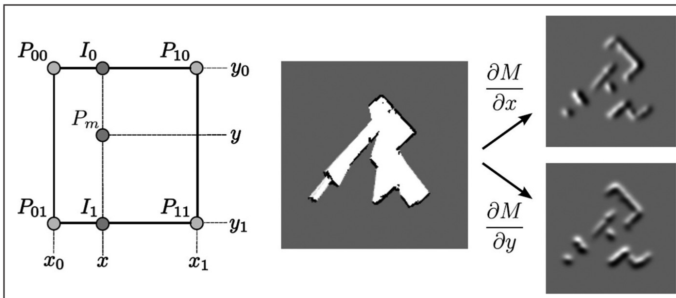

Figure 9. Bilinear interpolation and gradient descent (Kohlbrecher *et al.* 2011).

The occupancy probabilities and derivatives are estimated by bilinear interpolation. For a given continuous map coordinate P_m, the occupancy $M(P_m)$ and the gradient $\nabla M(P_m) = \left(\frac{\partial M}{\partial x}(P_m), \frac{\partial M}{\partial y}(P_m)\right)$ can be approximated by using the four closest integer coordinates P_{11}, P_{10}, P_{01}, and P_{00}, as depicted in Figure 9. Then the linear interpolation along the x- and y-axes yields

$$\begin{aligned} M(P_m) \approx\ & \frac{y - y_0}{y_1 - y_0}\left(\frac{x - x_0}{x_1 - x_0} M(P_{11}) + \frac{x_1 - x}{x_1 - x_0} M(P_{01})\right) \\ & + \frac{y_1 - y}{y_1 - y_0}\left(\frac{x - x_0}{x_1 - x_0} M(P_{10}) + \frac{x_1 - x}{x_1 - x_0} M(P_{00})\right) \end{aligned} \tag{15}$$

The derivatives can be approximated by

$$\frac{\partial M}{\partial x}(P_m) \approx \frac{y - y_0}{y_1 - y_0}\big(M(P_{11}) - M(P_{01})\big) + \frac{y_1 - y}{y_1 - y_0}\big(M(P_{10}) - M(P_{00})\big) \tag{16}$$

$$\frac{\partial M}{\partial y}(P_m) \approx \frac{x - x_0}{x_1 - x_0}\big(M(P_{11}) - M(P_{10})\big) + \frac{x_1 - x}{x_1 - x_0}\big(M(P_{01}) - M(P_{00})\big) \tag{17}$$

Scan matching is the process of aligning laser scans with each other or with an existing map. To achieve the best alignment between the laser scan and the map, we seek to find the transformation $\xi = (p_x, p_y, \psi)^T$ that minimizes

$$\xi^* = \underset{\xi}{\operatorname{argmin}} \sum_{i=1}^{n} \left[1 - M(\mathrm{S}_i(\xi))\right]^2 \tag{18}$$

where $\mathrm{S}_i(\xi)$ is the world coordinates of the obstacle measured by the ith laser beam when the scanner transforms as ξ. The function $M(\mathrm{S}_i(\xi))$ returns the map value at the coordinates generated by $\mathrm{S}_i(\xi)$. Given an initial estimate of ξ, the following equation is used to estimate $\Delta\xi$ so that the error measure is optimized:

$$\sum_{i=1}^{n} \left[1 - M(S_i(\xi + \Delta\xi))\right]^2 \to 0 \tag{19}$$

The Gauss–Newton iterative method is used to solve the nonlinear optimization problem (Lucas and Kanade 1981). In this process, the covariance matrix can be calculated as

$$R = \mathrm{Var}\{\xi\} = \sigma^2 \cdot H^{-1} \tag{20}$$

where σ is a scale factor that depends on the performance of the laser scanner and H represents the Hessian matrix

$$H = \left[\nabla M(S_i(\xi)) \frac{\partial S_i(\xi)}{\partial \xi}\right]^T \left[\nabla M(S_i(\xi)) \frac{\partial S_i(\xi)}{\partial \xi}\right] \tag{21}$$

To avoid the risk of converging into wrong local minima and keep the different map layers updated simultaneously, a multi-resolution map representation is adopted to gradually substitute the low-resolution map pose estimate into the high-resolution map.

3D Navigation for State Estimation

The 2D position and orientation in the plane are updated by the scan matcher, but for the full 3D estimation, an additional height sensor is needed. For best performance, the EKF with the general platform model defined by Equations 12–14 is used in 3D navigation (Sorenson 1985; Senne 1972). As shown in Figure 8, the information between the 2D SLAM and the 3D EKF estimate needs to be exchanged in both directions. On the one hand, the pose estimate from the EKF is used as the initial guess for optimizing the scan matcher. On the other hand, covariance intersection is used for fusing the SLAM pose with the full belief state to enhance the effect of the Kalman measurement update (Julier and Uhlmann 2007).

Denoting the Kalman estimate of the scanning process as xˆand the covariance as P, the fusion result can be given by

$$(P^+)^{-1} = (1 - \omega)\, P^{-1} + \omega \cdot C^T \mathrm{R}^{-1} C \tag{22}$$

and

$$\hat{x}^+ = P^+((1 - \omega) \cdot P^{-1} \hat{x} + \omega \cdot C^T R^{-1} \xi^*)^{-1} \tag{23}$$

where ξ^* and R are calculated as in Equations 18 and 20, respectively, and C is the observation matrix.

With the mutual optimization of 2D localization and 3D EKF estimation, the system can calculate its own 3D position and orientation in real time during the data-acquisition process. The evaluated trajectory comes with a timestamp that is aligned with the time when the sensors collect data and is saved in the IPC.

Scene Reconstruction

Although all data are unified at the robot operating system time, there is no guarantee that each frame of data collected by different sensors has exactly the same timestamp, due to differences in the power-up sequence and sampling frequency. The time synchronization of the trajectory data and the other measurement data is key to reconstructing the 3D point cloud. Denoting the system pose at time t as (R^t, T^t), it can be calculated as

$$(R^t, T^t) = \text{interpolate}\left((R^f, T^f), (R^b, T^b)\right) \tag{24}$$

where f and b are the time before and the time after t, respectively. Since the addition operation of the transformation matrix is unclosed, the function "interpolate" is uncertain for a transformation matrix. It is automatic to convert the transformation matrix into a quaternion representation first, and then linearly average the quaternions according to the properties of quaternions (F. Zhang 1997).

The 3D point cloud can be reconstructed by the trajectory and the extrinsic parameters. Supposing that after calibration, the coordinate system of the tilted laser scanner relative to the horizontal one is (R_s, T_s), the trajectory estimated by SLAM relative to the world coordinate system at time t is (R_d^t, T_d^t), and the coordinate of the point scanned by the tilted laser scanner at time t in its own coordinate system is p_0, the coordinate of the point in the world coordinate system can be described as

$$p_w = R_d^t(R_s \cdot P_o + T_s) + T_d^t \tag{25}$$

In order to obtain a better 3D point cloud, some additional processing is required before and after the reconstruction. Uniform spatial sampling of the point cloud can not only eliminate the redundant points caused by uneven scanning but also facilitate the subsequent point-cloud processing. Before the point cloud can be used for semantic understanding and other tasks, anomalous points caused by high reflectivity, sparse point-cloud bands caused by moving objects, and other obviously erroneous points also need to be manually eliminated.

Results

Experimental Data

The sites of the experiment are three scenes inside a library building: an underground garage, a study room on the first floor, and a reading room on the fourth floor, with a total area of about 2700 m^2. The underground garage, with an area of about 1400 m^2, is the largest and emptiest among the three scenes; the study room on the first floor, with an area of about 600 m^2, has a simple structure and a wide field of view; the reading room on the fourth floor, with an area of about 700 m^2, has dense bookshelves, a complex structure, and poor scene visibility. We conducted the experiment when there were as few people in the library as possible, to reduce the interference of pedestrian movement. The surveying personnel held the device in one hand, placed it directly in front, and moved at a constant speed in the scene while monitoring the mapping effect. In Figure 10, the picture on the left records the data-acquisition process, and the screenshot on the right shows the 2D mapping result updated in real time on the mobile terminal.

In addition to using our indoor 3D mapping approach for data acquisition, the station-type FARO FocusS 150 3D laser scanner (https://www.faro.com/en/Products/Hardware/Focus-Laser-Scanners) and the handheld GeoSLAM ZEB-REVO RT 3D laser scanner were used to form the control group. Figure 11 illustrates the two devices used to conduct the controlled trial. Before the FARO FocusS 150 3D laser scanner is used, the scene must be surveyed and station setup planned. Since the underground garage had a large area and a wide field of view, a total of three stations were set up; the study room on the first floor had a small area and a wide field of view, so only one station could achieve the scanning of most of the scene; the fourth floor had a complex structure and poor visibility, so a total of five stations were set up to scan the entire scene. For the collected data from multiple stations, postprocessing was needed to register the point clouds in order to obtain a complete 3D point cloud of the scene. The SLAM algorithm of the GeoSLAM ZEB-REVO RT 3D laser scanner provides a global optimization strategy, so the environment of the scene needs to be surveyed and a closed-loop route planned. Since the SLAM strategy based on our approach does not require detection of loop closure, data can be collected directly without conducting environmental surveys. The point-cloud file was generated directly by the data-processing program, and no other postprocessing operations were required. In practice, the time consumed by our solution is typically less than that with the FARO equipment and comparable to that with the GeoSLAM device.

Figure 10. Snapshot of acquisition process.

(a) (b)

Figure 11. Devices used in the controlled trial: (a) FARO FocusS 150, (b) GeoSLAM ZEB-REVO RT.

Trajectory Results and Planar Maps

Since the SLAM framework used in this article does not contain back-end optimization, the complete trajectory can be evaluated and saved directly during data acquisition. Figure 12 shows the 2D planar point clouds, evaluated trajectories, and station locations obtained with the three solutions. The point clouds colored in white are the scanned environment boundaries, the lines colored in red are the trajectories, and the points colored in yellow are the station locations of the FARO FocusS 150.

Intuitively, the scanning results of our solution are relatively satisfactory in the study room on the first floor but inadequate in the underground garage. The reasons are twofold. On the one hand, the study room has a small area and obvious features, which is conducive for the SLAM algorithm to achieve scan matching. On the other hand, the underground garage is empty and contains few features, resulting in poor mapping by the SLAM algorithm. Therefore, our solution can perform the best trajectory evaluation and 2D mapping in environments with relatively small area and rich scene features.

Scene Reconstruction and Accuracy Evaluation

Based on the trajectory estimated by the SLAM scheme, the 3D point clouds of the scenes were reconstructed. On a desktop computer with an Intel Core i7-9700 CPU running at 3.0 GHz and with 16 GB of memory, data from a 476-s, 103-MB laser scan were converted into a 3D point cloud in just 48 s. Figure 13 shows the 3D point-cloud reconstruction results with the roofs removed. The point clouds scanned by the FARO equipment are regarded as the ground truth, and the qualitative and quantitative accuracy analyses are respectively performed on the 3D point clouds generated by the GeoSLAM device and our solution.

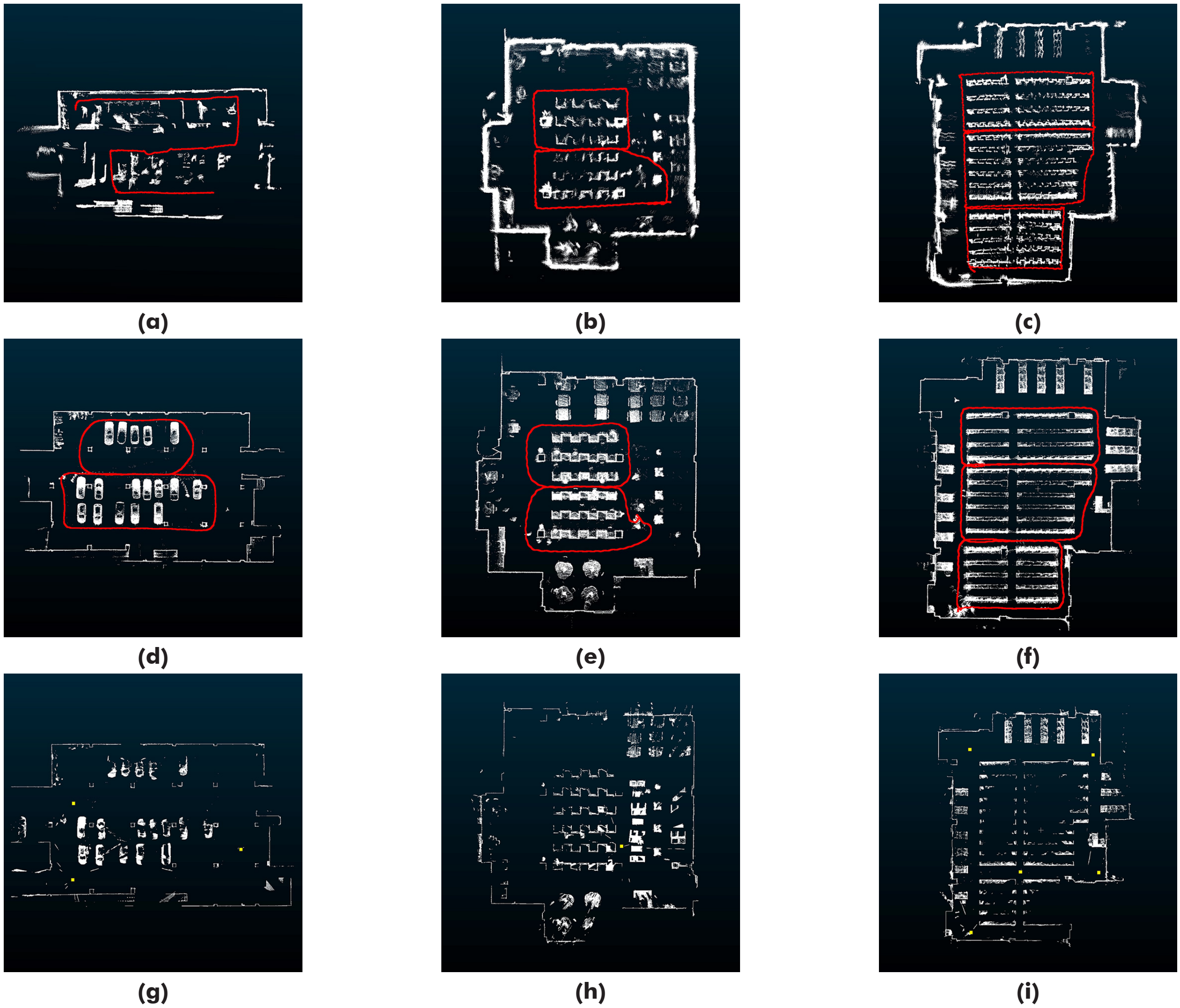

Figure 12. Trajectories and 2D maps: (a, d, g) the garage, (b, e, h) the first floor, and (c, f, i) the fourth floor, using (a to c) our solution, (d to f) GeoSLAM, and (g to i) FARO.

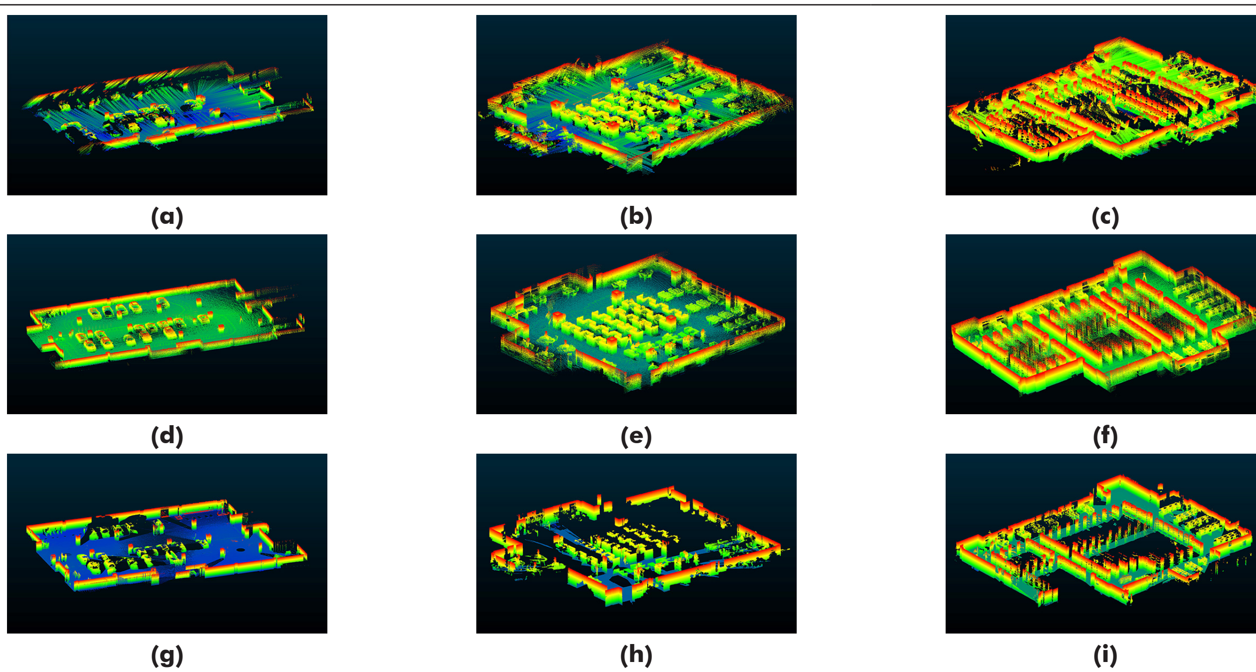

Figure 13. 3D scene reconstructions: (a, d, g) the garage, (b, e, h) the first floor, and (c, f, i) the fourth floor, using (a to c) our solution, (d to f) GeoSLAM, and (g to i) FARO.

From the qualitative point of view, although multiple stations were set up using the FARO equipment, there were still some areas that were not scanned due to obstruction, such as the walls in the underground garage obstructed by cars and the bookshelves in the reading room obstructed by each other; for the study room on the first floor, where only one station was set up, most of the ground information was obstructed and was incompletely scanned. In contrast, our 3D mapping solution and the GeoSLAM device can collect richer scanning data and reconstruct more complete 3D point clouds in a shorter time. The quality of these 3D point clouds largely depends on the results of trajectory evaluation. For example, during the trajectory-evaluation process for the reading room on the fourth floor (Figure 12c), the 2D point cloud of the left wall is anamorphic and the evaluated overall trajectory has errors, resulting in a slight distortion in the 3D point cloud in Figure 13c. Different from the three-axis laser-scanner design scheme (Zhao *et al.* 2018), our solution uses only one tilted laser scanner to restore the 3D point cloud, so the density of the generated 3D point cloud is limited.

From the quantitative point of view, the accuracy of the 3D scene reconstruction was evaluated through the following two steps:

(1) Measuring the distance and angle values of the 3D point clouds generated by the three experimental groups. Taking the scanning result of the FARO equipment as the ground truth, we randomly measured 15 line segments in each 3D point cloud to evaluate the distance accuracy of our solution and the GeoSLAM device, and then 15 angles in each 3D point cloud to evaluate their angle accuracy, as shown in Table 2. The specific distance and angle measurements are given in Table A1 in the Appendix.

(2) With the point clouds scanned by the FARO equipment as a reference, registering the point clouds generated by our solution and by the GeoSLAM device. The iterative closest-point registration algorithm was performed on the point cloud to be evaluated and the reference point cloud. The result of the point-cloud registration was evaluated by the root-mean-square (RMS) error, which decreased as the registration result became better. The RMS error between two point clouds is calculated as

$$\mathrm{RMS}=\sqrt{\sum_{i=1}^{n}\mathrm{dist}(\mathrm{point\_comp}_i,\mathrm{point\_ref\_nearest}_j)^2/n} \qquad (26)$$

where point_comp$_i$ denotes the ith point in the compared point cloud, point_ref_nearest$_j$ denotes the jth point that is closest to point_comp$_i$ in the reference point cloud, the function “dist” calculates the Euclidean distance between two points, and n is the number of points in the compared point cloud. By comparing the registration RMSs, we examined the similarity between the compared point clouds and the reference point cloud, as shown in Table 3.

Table 2 shows that for our solution, the average distance and angle errors of the study room on the first floor were the smallest, followed by the reading room on the fourth floor, and the underground garage had the largest error, which is consistent with the characteristics of the 2D map summarized under “Trajectory Results and Planar Maps.” The average errors of the point cloud obtained by our solution can be controlled within 3 cm and 2°, and the standard deviations within 2 cm and 1°, which are not too different from the accuracy of the mainstream GeoSLAM device. In Table 3, the registration RMS values are relatively large. We suspect this is due to the incompleteness of the reference point cloud scanned by the FARO equipment. Due to obstruction, the compared point clouds differ from the reference point cloud in the corresponding areas. However, these metric values between the two compared point clouds are close to each other, indicating that the accuracies of our solution and the GeoSLAM device are at the same level. Therefore, we consider that these 3D point clouds can be used to accomplish the actual indoor scene-modeling task.

Table 2. Distance and angle measurements.

Scene	Solution	Distance error (cm)		Angle error (°)	
		Mean	SD	Mean	SD
Underground garage	Our solution	2.64	1.55	1.34	0.93
	GeoSLAM	1.50	0.98	0.65	0.57
First floor	Our solution	1.62	1.61	0.87	0.49
	GeoSLAM	1.59	1.82	1.09	1.08
Fourth floor	Our solution	1.87	1.21	1.00	0.61
	GeoSLAM	1.93	1.82	0.70	0.47

Table 3. Accuracy evaluation of the devices.

Scene	Solution	Root-Mean-Square Error (cm)
Underground garage	Our solution	24.92
	GeoSLAM	22.32
First floor	Our solution	23.07
	GeoSLAM	22.87
Fourth floor	Our solution	20.05
	GeoSLAM	18.98

Discussion

This article mainly introduces a low-cost and portable indoor 3D mapping approach using biaxial line laser scanners and a laser range finder integrated with MEMS. The core technology reconstructs the 3D real scene using the extrinsic parameters and the trajectory evaluated by SLAM. To control the costs, we choose consumer-grade hardware to integrate the scanning device, and some compromises will be made consequently on the 3D point-cloud accuracy, which can be made up for by standardizing the workflow of data collection.

In terms of the hardware, the two line laser scanners assembled on our solution are the RPLIDAR A3 and the RPLIDAR S1 produced by Slamtec. The maximum scan frequency of the RPLIDAR A3 used for 2D SLAM is 20 Hz. When the system rotates horizontally at too fast a speed, the slow-update scan data will lead to a large interframe offset that will be updated to the map as the key frame, resulting in map drift error. The RPLIDAR S1 used to reconstruct 3D point clouds has a maximum scan frequency of 15 Hz, which determines that the surveying personnel should move at a relatively slow speed to ensure that the final 3D point cloud is not too sparse. Therefore, in the data-collection process, the surveying personnel must keep the translation and rotation of the system at low speeds to obtain a satisfactory 3D point cloud. In the subsequent optimization, motion detection and rotation determination can also be implemented to eliminate map drift error.

In terms of the SLAM algorithm, we draw on the idea of the Hector SLAM algorithm to fuse the horizontal laser scans, the MEMS-IMU data, and the height information for localization, mapping, and trajectory output. Excluding detection of loop closure, this algorithm can reduce the complexity of the surveying personnel’s work to a certain extent, but on the other hand, the accuracy is lower than with a SLAM scheme containing loop-closure detection, such as Cartographer. However, Cartographer is a CPU-demanding algorithm that exacts high computational costs in back-end optimization (Hess *et al.* 2016). Considering the performance of the IPC and the requirement for real-time display of the mapping process, we believe that it is reasonable and necessary to select the Hector SLAM framework as the core of the SLAM part in this article.

Future work will aim to further enrich the types of sensors integrated in the system, such as assembling a consumer-grade panoramic camera, and simultaneously collect laser scans and panoramic images. Based on the reconstruction of the 3D scene, the panoramic image will be mapped to the 3D point cloud, and the coloring of the point cloud will be realized to enhance the effect of the 3D scene. Supplementing with a GNSS antenna and fusing GNSS data are regarded as further meaningful research content to ensure that the system can more accurately evaluate its own trajectory information outdoors. Furthermore, the 3D point cloud will be converted into models, and the semantic understanding of the scene will be attached in the unit of the model object.

Conclusions

A low-cost and portable indoor 3D mapping approach using biaxial line laser scanners and a one-dimension laser range finder integrated with MEMS is proposed in this article. Compared with the traditional station-type 3D point-cloud acquisition scheme, the solution proposed in this article has a higher degree of flexibility and more efficient data acquisition and processing. Compared with the mature handheld 3D laser scanning devices on the market, our solution has advantages of being less costly and more lightweight.

Three scenes in a library building were modeled as experimental cases. The sites were scanned using a station-type FARO FocusS 150 3D laser scanner, a handheld GeoSLAM ZEB-REVO RT 3D laser scanner, and our solution. The accuracy of our solution was evaluated by comparing the distance errors, angle errors, and registration RMS errors of the 3D point clouds. The results demonstrate that in the same scene, our solution has the fastest point-cloud acquisition and processing. For each evaluation metric, the accuracy of our solution is not too different from that of the mainstream GeoSLAM product. In summary, the proposed approach is a low-cost, portable, and accurate solution for indoor 3D mapping.

Acknowledgments

The authors are grateful to Deyu Yin for his help with the information and guidance on the calibration site. This work is supported by the National Key R&D Program of China (grant 2020YFC1521900). There are no relevant financial or nonfinancial competing interests to report. Some or all data, models, or code that support the findings of this study are available from the corresponding author upon reasonable request.

References

Cao, M., H. Gao and W. Jia. 2021. Stable image matching for 3D reconstruction in outdoor. *International Journal of Circuit Theory and Applications* 49(7):2274–2289. https://doi.org/10.1002/cta.2997.

Chen, J. and K. C. Clarke. 2020. Indoor cartography. *Cartography and Geographic Information Science* 47(2):95–109. https://doi.org/10.1080/15230406.2019.1619482.

Comport, A. I., E. Malis and P. Rives. 2010. Real-time quadrifocal visual odometry. *International Journal of Robotics Research* 29(2-3):245–266. https://doi.org/10.1177/0278364909356601.

Davison, A. J., I. D. Reid, N. D. Molton and O. Stasse. 2007. MonoSLAM: Real-time single camera SLAM. *IEEE Transactions on Pattern Analysis and Machine Intelligence* 29(6):1052–1067. https://doi.org/10.1109/TPAMI.2007.1049.

Debeunne, C. and D. Vivet. 2020. A review of visual-LiDAR fusion based simultaneous localization and mapping. *Sensors* 20(7):2068. https://doi.org/10.3390/s20072068.

Di, K., W. Wan, H. Zhao, Z. Liu, R. Wang and F. Zhang. 2019. Progress and applications of visual SLAM. *Journal of Geodesy and Geoinformation Science* 2(2):38–49. https://doi.org/10.11947/j.JGGS.2019.0205.

Dissanayake, M.W.M.G., P. Newman, S. Clark, H. F. Durrant-Whyte and M. Csorba. 2001. A solution to the simultaneous localization and map building (SLAM) problem. *IEEE Transactions on Robotics and Automation* 17(3):229–241.

Domínguez Martin, B., Á. L. García Fernández and F. R. Feito Higueruela. 2011. Semantic and topological representation of building indoors: An overview. Pages PPP–PPP in *Proceedings of the ISPRS Joint Workshop on 3D City Modeling & Applications and the 6th 3D GeoInfo Conference*, held in Wuhan, China, 26–28 June 2011.

Fernández-Moral, E., J. González-Jiménez and V. Arévalo. 2015. Extrinsic calibration of 2D laser rangefinders from perpendicular plane observations. *The International Journal of Robotics Research* 34(11):1401–1417. https://doi.org/10.1177/0278364915580683.

Fischler, M. A. and R. C. Bolles. 1987. Random Sample Consensus: A paradigm for model fitting with applications to image analysis and automated cartography. In *Readings in Computer Vision: Issues, Problem, Principles, and Paradigms*, edited by M. A. Fischler and O. Firschein, 726–740. Location: Morgan Kaufmann.

Forster, C., Z. Zhang, M. Gassner, M. Werlberger and D. Scaramuzza. 2017. SVO: Semidirect visual odometry for monocular and multicamera systems. *IEEE Transactions on Robotics* 33(2):249–265. https://doi.org/10.1109/TRO.2016.2623335.

Fuentes-Pacheco, J., J. Ruiz-Ascencio and J. M. Rendón-Mancha. 2015. Visual simultaneous localization and mapping: A survey. *Artificial Intelligence Review* 43(1): 55–81. https://doi.org/10.1007/s10462-012-9365-8.

Gong, J., T. Cui, J. Shan, S. Ji and Y. Huang. 2015. A survey on facade modeling using LiDAR point clouds and image sequences collected by mobile mapping systems. *Geomatics and Information Science of Wuhan University* 40(9):1137–1143. https://doi.org/10.13203/j.whugis20150173.

Grisetti, G., C. Stachniss and W. Burgard. 2007. Improved techniques for grid mapping with Rao-Blackwellized particle filters. *IEEE Transactions on Robotics* 23(1):34–46. https://doi.org/10.1109/TRO.2006.889486.

Hess, W., D. Kohler, H. Rapp and D. Andor. 2016. Real-time loop closure in 2D LIDAR SLAM. Pages 1271–1278 in *2016 IEEE International Conference on Robotics and Automation (ICRA)*, held in Stockholm, Sweden, 16–21 May 2016. Edited by J. Editor. Location: IEEE. https://doi.org/10.1109/ICRA.2016.7487258.

Huang, H., G. Tong, L. Xia, Y. Li, X. Yue and B. Jiang. 2018. SLAM technology and its application in surveying and mapping. *Bulletin of Surveying and Mapping* 3:18–24. https://doi.org/10.13474/j.cnki.11-2246.2018.0069.

Julier, S. J. and J. K. Uhlmann. 2007. Using covariance intersection for SLAM. *Robotics and Autonomous Systems* 55(1):3–20. https://doi.org/10.1016/j.robot.2006.06.011.

Kohlbrecher, S., J. Meyer, T. Graber, K. Petersen, U. Klingauf and O. von Stryk. 2014. Hector open source modules for autonomous mapping and navigation with rescue robots. In *RoboCup 2013: Robot World Cup XVII*, edited by S. Behnke, M. Velow, A. Visser, and R. Xiong, 624–361. Berlin: Springer. https://doi.org/10.1007/978-3-662-44468-9_58.

Kohlbrecher, S., O. von Stryk, J. Meyer and U. Klingauf. 2011. A flexible and scalable SLAM system with full 3D motion estimation. Pages 155–160 in *2011 IEEE International Symposium on Safety, Security, and Rescue Robotics*, held in Kyoto, Japan, 1–5 November 2011. Edited by J. Editor. Location: IEEE. https://doi.org/10.1109/SSRR.2011.6106777.

Kuipers, J. B. 1999. *Quaternions and Rotation Sequences: A Primer with Applications to Orbits, Aerospace and Virtual Reality*. Princeton, N.J.: Princeton University Press. https://doi.org/10.1515/9780691211701.

Li, C. T., J.C.P. Cheng and K. Chen. 2020. Top 10 technologies for indoor positioning on construction sites. *Automation in Construction* 118:103309. https://doi.org/10.1016/j.autcon.2020.103309.

Li, D. Mobile mapping technology and its applications. 2006. *Geospatial Information* 4(4):1–5.

Li, J., Q. Hu and M. Ai. 2020. RIFT: Multi-modal image matching based on radiation-variation insensitive feature transform. *IEEE Transactions on Image Processing* 29:3296–3310. https://doi.org/10.1109/TIP.2019.2959244.

Li, J., Q. Hu, M. Ai and R. Zhong. 2017. Robust feature matching via support-line voting and affine-invariant ratios. *ISPRS Journal of Photogrammetry and Remote Sensing* 132:61–76. https://doi.org/10.1016/j.isprsjprs.2017.08.009.

Lucas, B. D. and T. Kanade. 1981. An iterative image registration technique with an application to stereo vision. Pages 674–679 in *Proceedings of the 7th International Joint Conference on Artificial Intelligence*, held in Vancouver, BC, Canada, 24 - 28 August 1981..

Mao, X., K. Liu and Y. Hang. 2020. Feature extraction and matching of Slam image based on improved SIFT algorithm. Pages 18–23 in *SSPS 2020: 2020 2nd Symposium on Signal Processing Systems*, held in Guangdong, China, 11–13 July 2020. Edited by J. Editor. New York: Association for Computing Machinery. https://doi.org/10.1145/3421515.3421528.

Montemerlo, M., S. Thrun, D. Koller and B. Wegbreit. 2002. FastSLAM: A factored solution to the simultaneous localization and mapping problem. Pages 593–598 in *Eighteenth National Conference on Artificial Intelligence*, held in Edmonton, Alberta, 28 July–1 August 2002. Edited by R. Dechter, M. Kearns, and R. Sutton. Menlo Park, Calif.: American Association for Artificial Intelligence.

Mur-Artal, R. and J. D. Tardós. 2017. ORB-SLAM2: An open-source SLAM system for monocular, stereo and RGB-D cameras. *IEEE Transactions on Robotics* 33(5):1255–1262. https://doi.org/10.1109/TRO.2017.2705103.

Puente, I., H. González-Jorge, J. Martínez-Sánchez and P. Arias. 2013. Review of mobile mapping and surveying technologies. *Measurement* 46(7):2127–2145. https://doi.org/10.1016/j.measurement.2013.03.006.

Pukelsheim, F. 1994. The three sigma rule. *The American Statistician* 48(2):88–91. https://doi.org/10.1080/00031305.1994.10476030.

Senne, K. 1972. Stochastic processes and filtering theory. *IEEE Transactions on Automatic Control* 17(5):752–753. https://doi.org/10.1109/TAC.1972.1100136.

Shan, T. and B. Englot. 2018. LeGO-LOAM: Lightweight and groundoptimized lidar odometry and mapping on variable terrain. Pages 4758–4765 in *2018 IEEE/RSJ International Conference on Intelligent Robots and Systems (IROS)*, held in Madrid, Spain, 1–5 October 2018. IEEE. https://doi.org/10.1109/IROS.2018.8594299.

Shan, T., B. Englot, D. Meyers, W. Wang, C. Ratti and D. Rus. 2020. LIO-SAM: Tightly-coupled lidar inertial odometry via smoothing and mapping. Pages 5135–5142 in *2020 IEEE/RSJ International Conference on Intelligent Robots and Systems (IROS)*, held in Las Vegas, Nev., 24 October 2020–24 January 2021. Edited by J. Editor. Location: IEEE. https://doi.org/10.1109/IROS45743.2020.9341176.

Sorenson, H. 1985. *Kalman Filtering: Theory and Application.* Piscataway, NJ. IEEE.

Thomson, C., G. Apostolopoulos, D. Backes and J. Boehm. 2013. Mobile laser scanning for indoor modelling. *ISPRS Annals of the Photogrammetry, Remote Sensing and Spatial Information Sciences* II(5/W2):289–293. https://doi.org/10.5194/isprsannals-II-5-W2-289-2013.

Thrun, S. 2002. Probabilistic robotics. *Communications of the ACM* 45(3):52–57. https://doi.org/10.1145/504729.504754.

Vosselman, G. 2014. Design of an indoor mapping system using three 2D laser scanners and 6 DOF SLAM. *ISPRS Annals of the Photogrammetry, Remote Sensing and Spatial Information Sciences* II(3):173–179. https://doi.org/10.5194/isprsannals-II-3-173-2014.

Wei, S., F. Pang, Z. Liu and X. Shi. 2020. Survey of LiDAR-based SLAM algorithm. *Application Research of Computers* 37(2):13–18. https://doi.org/10.19734/j.issn.1001-3695.2018.09.0674.

Yin, D., J. Liu, T. Wu, K. Liu, J. Hyyppä and R. Chen. 2018. Extrinsic calibration of 2D laser rangefinders using an existing cuboid-shaped corridor as the reference. *Sensors* 18(12):4371. https://doi.org/10.3390/s18124371.

Zhang, F. 1997. Quaternions and matrices of quaternions. *Linear Algebra and Its Applications* 251:21–57. https://doi.org/10.1016/0024-3795(95)00543-9.

Zhang, J. and S. Singh. 2014. LOAM: Lidar odometry and mapping in realtime. Pages 109–111 in *Proceedings of the Robotics: Science and Systems Conference (RSS)*, held in Berkeley, CA, USA, 14–16 July 2014. IEEE. https://doi.org/10.15607/RSS.2014.X.007.

Zhao, P., Q. Hu, S. Wang, M. Ai and Q. Mao. 2018. Panoramic image and three-axis laser scanner integrated approach for indoor 3D mapping. *Remote Sensing* 10(8):1269. https://doi.org/10.3390/rs10081269.

Zlatanova, S. and U. Isikdag. 2015. 3D indoor models and their applications. In *Encyclopedia of GIS*, edited by S. Shekhar, H. Xiong, and X. Zhou. Cham, Switzerland: Springer. https://doi.org/10.1007/978-3-319-23519-6_1551-1.

Appendix

Table A1. Accuracy evaluation measurements of the solutions.

	Distance (cm)					Angle (°)				
Scene	**FARO**	**Our Solution**	**Error 1**	**GeoSLAM**	**Error 2**	**FARO**	**Our Solution**	**Error 1**	**GeoSLAM**	**Error 2**
	88.49	89.92	1.43	86.91	1.58	89.46	89.78	0.32	89.44	0.02
	455.67	452.91	2.76	457.03	1.36	179.88	179.63	0.25	179.89	0.01
	2482.57	2478.80	3.77	2483.90	1.33	90.07	91.06	0.99	89.71	0.36
	863.94	859.58	4.36	861.01	2.93	53.31	52.83	0.48	53.39	0.08
	879.67	876.23	3.44	880.68	1.01	108.79	106.73	2.06	108.83	0.04
	796.14	798.15	2.01	798.78	2.64	14.84	15.64	0.80	16.49	1.65
	67.24	68.13	0.89	67.70	0.46	157.37	156.75	0.62	156.23	1.14
Underground garage	1125.77	1126.38	0.61	1124.14	1.63	169.13	169.72	0.59	170.82	1.69
	349.54	348.26	1.28	349.25	0.29	150.89	152.49	1.60	150.28	0.61
	876.23	872.07	4.16	875.84	0.39	89.31	86.90	2.41	90.13	0.82
	554.43	552.77	1.66	557.00	2.57	133.69	134.53	0.84	134.24	0.55
	247.23	249.74	2.51	247.63	0.40	176.66	178.14	1.48	176.08	0.58
	334.11	328.20	5.91	336.37	2.26	91.99	89.13	2.86	90.48	1.51
	508.95	509.56	0.61	509.41	0.46	67.93	69.27	1.34	68.12	0.19
	1048.62	1044.44	4.18	1051.88	3.26	98.64	95.23	3.41	99.07	0.43
	192.69	193.25	0.56	192.95	0.26	84.19	85.01	0.82	84.38	0.19
	586.62	586.13	0.49	588.19	1.57	91.80	90.76	1.04	91.73	0.07
	1984.41	1983.56	0.85	1980.86	3.55	89.09	89.28	0.19	88.45	0.64
	101.30	100.62	0.68	101.90	0.60	90.03	90.50	0.47	92.62	2.59
	869.38	870.15	0.77	869.17	0.21	89.85	90.35	0.50	89.42	0.43
	207.53	206.55	0.98	208.99	1.46	89.08	88.12	0.96	88.67	0.41
	608.41	609.13	0.72	609.05	0.64	23.75	24.88	1.13	25.35	1.60
First floor	134.26	135.69	1.43	134.28	0.02	178.97	178.40	0.57	178.49	0.48
	933.98	929.12	4.86	928.80	5.18	177.28	176.51	0.77	177.00	0.28
	246.49	247.00	0.51	247.25	0.76	146.20	147.63	1.43	147.16	0.96
	108.42	109.41	0.99	108.03	0.39	38.93	39.53	0.60	38.79	0.14
	149.19	149.62	0.43	149.51	0.32	133.99	134.10	0.11	133.99	2.59
	335.30	330.16	5.14	336.82	1.52	90.66	88.97	1.69	91.10	0.44
	70.86	66.62	4.24	69.75	1.11	90.40	89.48	0.92	94.13	3.73
	196.94	195.26	1.68	203.13	6.19	87.80	85.94	1.86	89.57	1.77
	690.41	692.35	1.94	691.96	1.55	179.02	178.65	0.37	179.50	0.48
	695.46	694.00	1.46	699.45	3.99	88.71	88.26	0.45	88.86	0.15
	1895.50	1894.03	1.47	1898.88	3.38	108.51	109.87	1.36	109.03	0.52
	499.43	500.34	0.91	498.25	1.18	90.61	91.85	1.24	90.35	0.26
	538.75	536.07	2.68	534.75	4.00	118.12	120.45	2.33	117.70	0.42
	1667.12	1663.15	3.97	1673.85	6.73	174.14	175.00	0.86	173.56	0.58
	245.87	245.40	0.47	243.41	2.46	47.26	45.86	1.40	45.82	1.44
Fourth floor	1529.79	1529.83	0.04	1527.44	2.35	155.94	156.01	0.07	155.78	0.16
	69.38	68.36	1.02	68.63	0.75	20.66	20.50	0.16	21.09	0.43
	88.19	89.93	1.74	87.40	0.79	12.27	11.92	0.35	11.80	0.47
	697.14	698.39	1.25	697.00	0.14	2.61	3.88	1.27	3.59	0.98
	1218.69	1217.34	1.35	1218.56	0.13	21.51	20.13	1.38	20.44	1.07
	330.50	325.97	4.53	330.19	0.31	89.28	87.56	1.72	91.09	1.81
	326.27	323.09	3.18	325.76	0.51	90.93	89.90	1.03	90.34	0.59
	598.26	596.27	1.99	599.05	0.79	91.26	90.27	0.99	90.09	1.17

IN-PRESS ARTICLES

Gaofei Yin. Smartphone Digital Photography for Fractional Vegetation Cover Estimation.

Xuzhe Duan, Qingwu Hu, Pengcheng Zhao, and Shaohua Wang. A low-cost and portable indoor 3D mapping approach using biaxial line laser scanners and a one-dimension laser rangefinder integrated with MEMS.

Toshihiro Sakamoto, Daisuke Ogawa, Satoko Hiura, Nobusuke Iwasaki. Alternative procedure to improve the positioning accuracy of orthomosaic images acquired with Agisoft Metashape and DJI P4 Multispectral for crop growth observation

Guangyun Li, Senzhen Sun, Yangjun Gao, Li Wang. Robust Dynamic Indoor Visible Light Positioning Method Based on CMOS Image Sensor.

Zhenfeng Shao, Hongping Zhang, Wenfu Wu, Xiao Huang, Jisong Sun, Jinqi Zhao, Yewen Fan. Comparing the sensitivity of pixel-based and sub-watershed-based AHP to weighting criteria for flood hazard estimation.

Gang Qiao, Hongwei Li. Lake Water Footprint Determination Using Linear Clustering-based Algorithm and Lake Water Changes in the Tibetan Plateau from 2002 to 2020.

Jason Parent, Chandi Witharana, Michael Bradley. Classifying and georeferencing indoor point clouds with ARCGIS.

Paul Pope, Brandon Crawford, Anita Lavadie-Bulnes, Emily Schultz-Fellenz, Damien Milazzo, Kurt Solander, Carl Talsma. Towards Automated/Semi-Automated Extraction of Faults from Lidar Data

Li Tan, Guoming Li, Xin Liu, Aike Kan. Feature-based convolutional neural network for very-high-resolution urban imagery classification

Ravi Dwivedi, Syed Azeemuddin. Conjunctive use of Landsat-8 OLI and MODIS Data for Delineation of Burned Areas

Chih-Hung Hsu, Che-Hao Chang, Chih-Tsung Hsu, Shiang-Jen Wu, Po-Hsien Chung. Hydrological Topography Dataset (HTD) - the Dataset for High Resolution 2D Urban Flood Modeling.

Xiaojun Yang, Feilin Lai. Improving land cover classification over a large coastal city through stacked generalization with filtered training samples.

Xiaoyue Wang, Hongxin Zhang, Dailiang Peng. Evaluation of urban vegetation phenology using 250 m MODIS vegetation indices.

Zhihua Xu, Xingzheng Lu, Wenliang Wang, Ershuai Xu, Rongjun Qin, Yiru Niu, Xu Qiao, Feng Yang, Rui Yan. Monocular Video Frame Optimization through Feature-based Parallax Analysis for 3D Pipe Reconstruction.

Lin Ding, Hanchao Zhang, Deren Li, Monitoring and Analysis of Urban Sprawl based on Road Network Data and High-resolution Remote Sensing Imagery: A Case Study of China's Provincial Capitals.

Xueyan Li, Heqing Zhang, Zhenxin Wang, Junfeng Song. Transformer for the Building Segmentation of Urban Remote Sensing.

Alternative Procedure to Improve the Positioning Accuracy of Orthomosaic Images Acquired with Agisoft Metashape and DJI P4 Multispectral for Crop Growth Observation

Toshihiro Sakamoto, Daisuke Ogawa, Satoko Hiura, and Nobusuke Iwasaki

Abstract

Vegetation indices (VIs), such as the green chlorophyll index and normalized difference vegetation index, are calculated from visible and near-infrared band images for plant diagnosis in crop breeding and field management. The DJI P4 Multispectral drone combined with the Agisoft Metashape Structure from Motion/Multi View Stereo software is some of the most cost-effective equipment for creating high-resolution orthomosaic VI images. However, the manufacturer's procedure results in remarkable location estimation inaccuracy (average error: 3.27–3.45 cm) and alignment errors between spectral bands (average error: 2.80–2.84 cm). We developed alternative processing procedures to overcome these issues, and we achieved a higher positioning accuracy (average error: 1.32–1.38 cm) and better alignment accuracy between spectral bands (average error: 0.26–0.32 cm). The proposed procedure enables precise VI analysis, especially when using the green chlorophyll index for corn, and may help accelerate the application of remote sensing techniques to agriculture.

Introduction

Remote sensing is a cost-effective tool for monitoring crop growth in vast fields. In the past, agricultural research commonly used multispectral images obtained by spaceborne or airborne remote sensing sensors for field monitoring (Boegh *et al.* 2002; Maas and Rajan 2008; Borgogno-Mondino *et al.* 2018). Recently, the use of drones (unmanned aerial vehicles) has become more popular, especially for field-scale agricultural observations and management (Huang *et al.* 2018; Maes and Steppe 2019; Peter *et al.* 2020). One of the reasons is that drone-based remote sensing provides multispectral images of crop lines with higher spatial and temporal resolution. Another reason is the advent of reasonably priced small drones equipped with dedicated cameras and Structure from Motion/Multi View Stereo (SfM/MVS) software, such as Agisoft Metashape Professional (Agisoft LLC, St. Petersburg, Russia) and Pix4D mapper (Pix4D, Lausanne, Switzerland), which enable beginners in remote sensing to create orthomosaic images. These technological advancements allow phenological observation of seasonal changes in crop growth with higher spatial resolution (Malambo *et al.* 2018; Che *et al.* 2020).

Toshihiro Sakamoto* is with Institute for Agro-Environmental Sciences, NARO, 3-1-3 Kannondai, Tsukuba, Ibaraki, Japan (*corresponding author: sakamt@affrc.go.jp).

Daisuke Ogawa is with Institute of Crop Science, NARO, 2-1-2 Kannondai, Tsukuba, Ibaraki, Japan.

Satoko Hiura is with Tohoku Agricultural Research Center, NARO, 4 Akahira, Shimo-kuriyagawa, Morioka, Iwate, Japan.

Nobusuke Iwasaki is with Institute for Agro-Environmental Sciences, NARO, 3-1-3 Kannondai, Tsukuba, Ibaraki, Japan.

Contributed by Rongjun Qin, September 9, 2021 (sent for review September 17, 2021; reviewed by Xiao Ling, Zhihua Xu).

In the field of breeding, drones are used as a high-throughput phenotyping tool for the monitoring of various phenotypic features, such as vegetation fraction, plant height, and disease symptoms (Reynolds *et al.* 2020). Recently, we developed image analysis methods for evaluating the vegetation fraction and plant architecture of rice using data obtained with a DJI Phantom 4 Pro drone (P4P; DJI, Shenzhen, China), which has an RGB camera equipped with a 1-in. sensor (Ogawa *et al.* 2019, 2021). Until 2019, in reports of high-throughput phenotyping with drone remote sensing technology, RGB images were more commonly used than multispectral images (Vargas *et al.* 2019; Zhang *et al.* 2020; Svensgaard *et al.* 2021; Tang *et al.* 2021). This was because small drones equipped with an RGB camera were cheaper than large drones or sophisticated small drones equipped with a multispectral camera, such as the Bluegrass Fields drone (Parrot, Paris, France) (Sun *et al.* 2019; Qi *et al.* 2021). In October 2019, DJI launched a new small drone, named P4 Multispectral (P4M), designed for agricultural monitoring. It has a six-lens multispectral camera, spectral sunlight sensor, and high-precision global navigation satellite system (GNSS) receiver for automatic navigation flight using real-time kinematic (RTK). On the other hand, the Metashape SfM/MVS software has the largest market share in business and research applications, such as 3D work progress control for civil engineering work and orthomosaic image creation for agricultural environmental monitoring. A Google Scholar search for the key words "Metashape" (or "Photoscan") and "Pix4D" yielded 11,750 and 5,390 hits, respectively (date of search: 9 August 2021). According to the results of a questionnaire survey conducted by the Forest Agency of Japan among forest owner cooperatives, forestry organizations, and local governments in 2020, 55% of the respondents had used Metashape, whereas only 6.1% had used Pix4D (Blue Innovation Co. Ltd 2020). The advantages of Metashape are that there are numerous blogs that explain how to use it and that it is highly price competitive in terms of its low initial cost and no upgrade fees (up to version 1.99) regardless of its versatility.

Although Metashape and P4M are among the most cost-effective combinations of aerial photography equipment for creating multispectral orthomosaic images, Metashape does not have a dedicated processing mode for P4M data until at least version 1.7.3, build 12473 (64 bit). Instead, the Agisoft Helpdesk web page officially introduces how to process the P4M data by using a general processing flow called a "multi-camera system" (Agisoft Helpdesk Portal 2021) (last updated on 25 May 2021). As a preliminary experiment, we created a multispectral orthomosaic image from P4M-derived aerial images by following the manufacturer's tutorial, and we visually assessed the quality of the tutorial-derived multispectral orthomosaic image by overlaying it onto an orthomosaic image created from P4P-derived aerial RGB color

Photogrammetric Engineering & Remote Sensing
Vol. 88, No. 5, May 2022, pp. 323–332.
0099-1112/22/323–332

doi: 10.14358/PERS.21-00064R2

images. In doing so, the following issues were found: (1) The positions of ground control points (GCPs) on orthomosaic images derived from P4M and P4P did not agree with each other. (2) There were obvious misalignment errors between spectral band images in the P4M-derived multispectral orthomosaic images; therefore, when the GCPs were visualized in false color composite (near-infrared [NIR]-red-green) images, the edges of the white squared parts of GCPs were colored with a gradient from blue to red. These misalignment issues would negatively influence data analysis. In the Agisoft user forum (https://www.agisoft.com/forum/index.php?topic=12894.msg57129#msg57129), a similar issue has been pointed out with regard to the processing of multispectral images using Metashape. However, no specific solution has been presented. Therefore, it is necessary to improve the methodology to create orthomosaic images from a series of P4M multispectral images using the Metashape software.

In this study, we comprehensively evaluated the absolute location accuracy and band alignment accuracy of multispectral orthomosaic images created based on the tutorial procedure. In addition, we devised alternative processing procedures that combine the other general processing steps of Metashape to improve multispectral orthomosaic image quality. Finally, we demonstrated that the alternative processing procedures provided higher accuracy in terms of geolocation and image alignment between the spectral bands than the manufacturer's tutorial procedure.

Experimental Fields

The experimental fields were located on the campus of the NARO Institute for Agro-Environmental Sciences in Tsukuba, Japan (36°01′29″ N, 140°06′37.2″ E; Figure 1A and 1B, see next page). The target crops for aerial photography were forage dent corn (*Zea mays* L. cv. New dent 100) and paddy rice (*Oryza sativa* L. cv. Koshihikari). Twelve plots (1.28×1.28 m) were set as regions of interest in nine concrete-framed fields of 8×8 m. The amount of chemical nitrogen fertilizer was varied from 0 to 25 kg N/10 a in the six corn plots and from 0 to 8 kg N/10 a in the six rice plots (Figure 1C). Corn seeds were sowed by hand on 27 May 2021, with a row width of 75 cm and an inter-hill space of 20 cm. Rice seedlings were transplanted by hand on 2 June 2021, with a row width of 30 cm and an inter-hill space of 18 cm.

Twenty ground control points (GCPs) had been painted onto the concrete ground using black and white paint for road signs. Half of the GCPs (numbers 1, 4, 7, 8, 11, 14, 15, 17, 18, and 20) were used for internal camera calibration for SfM/MVS analysis using Metashape. The other half (numbers 2, 3, 5, 6, 9, 10, 12, 13, 16, and 19) were used for location accuracy verification of the multispectral orthomosaic images acquired with the three procedures evaluated.

Materials

The P4M drone was automatically controlled by dedicated flight control software, DJI GS Pro (2.0.16 [10657] (DJI), installed on an iPad mini (Apple Inc., Elk Grove, Calif., USA). The P4M can take five spectral images (blue [450 ± 16 nm], green [560 ± 16 nm], red [650 ± 16 nm], red edge [730 ± 16 nm], NIR [840 ± 26 nm]) and one RGB color image simultaneously. Automatic flight photography using the P4M was conducted at two flight heights (20 and 30 m) around 8:30 A.M. on 6 July 2021 and around 13:00 P.M. on 13 July 2021. We investigated four aerial photo sets assembled from photographs acquired at two different observation dates and two different flight heights. We acquired 204 sets of multispectral images on 6 July and 185 on 13 July at a height of 20 m (resolution: 1.1 cm/pixel) and 114 on each of 6 July and 13 July at a height of 30 m (resolution: 1.6 cm/pixel). The parameters of automatic flight photography using DJI GS Pro were set as listed in Table 1.

The P4M was automatically operated in RTK positioning mode coupled with the use of high-precision GNSS correction information distribution service of the Virtual Reference Station (JENOBA Co., Ltd, Tokyo, Japan). The images of the MicaSense Calibration Reflectance Panel (MicaSense Inc., Seattle, Wash., USA) (Mamaghani and Salvaggio 2019), which were used for reflectance calibration, were taken before and after each flight with manual operation. The range of

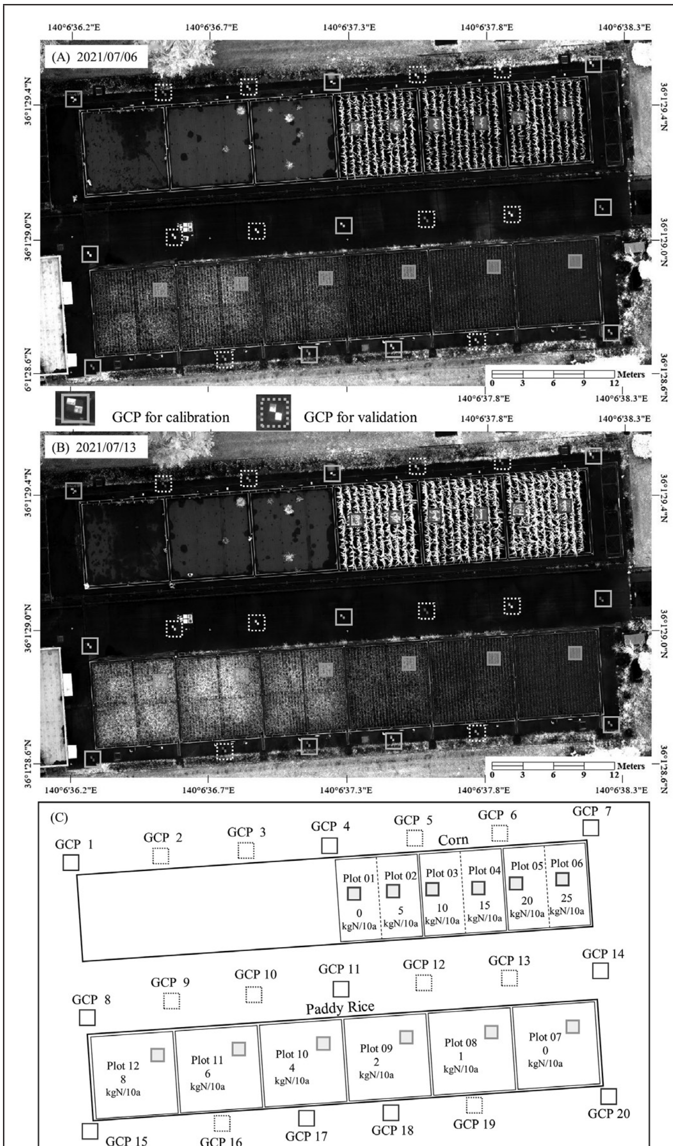

Figure 1. Near-infrared (NIR) orthomosaic images of the experimental field for 6 July 2021 (A) and 13 July 2021 (B) and layouts of the ground control points (GCPs) and plots (regions of interest) with the amounts of nitrogen fertilizer applied (C).

Table 1. Flight parameters used in the experiments.

Parameter	Description
Shooting angle	Parallel to main path
Capture mode	Capture at time interval
Flight course mode	Inside mode
Flight speed	1.3 m/s
Front overlap ratio	80%
Side overlap ratio	80%
Course angle	184°
Gimbal pitch angle	−90°

the automatic flight route at 20-m height was partially narrower than that at 30 m to prevent collision with trees. Accordingly, GCP1 and GCP2 are not shown in aerial images at 20-m height.

Agisoft Metashape Professional SfM/MVS software was used to create multispectral orthomosaic images from the aerial images. The latest software version (version 1.7.3, build 12473 [64 bit], 5 July 2021) was installed. A general-purpose remote sensing software, ENVI 5.6 (API version 3.6; Harris Geospatial, Broomfield, Colo., USA), was used for postprocessing, including format conversion and image subset and layer stacking of spectral band images.

Methods

Processing Procedures for Creating Multispectral Orthomosaic Images Using Metashape

We considered the official processing procedure communicated on the Agisoft Helpdesk Portal Web page (Agisoft Helpdesk Portal 2021) to be the most common standard procedure when analyzing P4M data with Agisoft Metashape Professional version 1.7.3, build 12473 (64 bit), and named it "tutorial procedure" (TP). We newly developed two alternative processing procedures—alternative procedure 1 (AP1) and alternative procedure 2 (AP2)—and compared them with TP. The work flows of the procedures evaluated are shown in Figure 2.

The major common aspects of data processing in the three methods are as follows. RTK positioning information of each spectral camera, stored as XMP metadata in the header file of each TIFF file, was used for internal camera calibration, along with precisely surveyed coordinate information of the GCP markers. The unit for the height of the coordinate information of GCP markers was the ellipsoid height in accordance with the RTK positioning information of the multispectral camera.

Universal Transverse Mercator (UTM) (zone: 54 N; datum: WGS84) was used for map projection of the orthomosaic images. The output spatial resolution was set to 1 cm/pixel regardless of flight height. The 16-bit unsigned integer pixel values of the orthomosaic images exported from Metashape were divided by 32,768 for conversion to 32-bit float pixel values of spectral reflectance ranging from 0.0 to 1.0. The output orthomosaic images were cropped to obtain 6000×3400-pixel square regions with a fixed location based on the geographic information (Figure 1A and 1B). Assuming the use of multispectral orthomosaic images for crop growth monitoring, we assessed the impact of the three procedures on observed values of vegetation indices (VIs), including the green chlorophyll index (CI_{green}) and normalized difference vegetation index (NDVI) (Rouse *et al.* 1974).

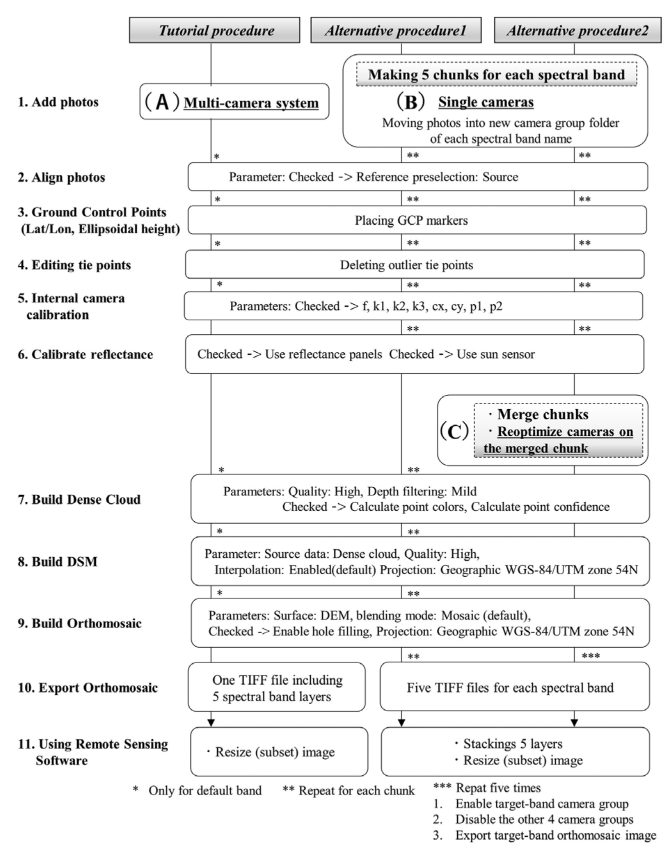

Figure 2. Work flows of the three procedures for creating multispectral orthomosaic images using Agisoft Metashape evaluated in this study.

Agisoft TP

The main feature of TP is the use of a dedicated processing mode named the "multi-camera system" in Metashape (Figure 2A), in which all spectral band images are imported at once into a working folder named "chunk." The advantage of the "multi-camera system" mode is that the time-consuming manual work of defining the GCP marker locations needs to be done only for default blue band images, not for the other four spectral bands, resulting in a shorter processing time. A digital surface model (DSM) was made from a high-quality dense cloud that was built as a common data set for all spectral bands. Multispectral orthomosaic images were built in reference to the DSM and were exported as a single TIFF file containing five spectral band images.

AP1

AP1 used a general processing flow named "single camera" in Metashape instead of the "multi-camera system" mode. First, we created five chunks of working folders named after the spectral bands (blue, green, red, red edge, and NIR) in a working project file (Figure 2B). Next, the multispectral band images were imported separately into each chunk with the corresponding spectral band. The following steps were repeated as many times as the number of chunks (spectral bands) created: manual placement of GCP marker locations on each image, internal camera calibration, dense cloud building, DSM, and creation of single-band orthomosaic images. The single-band orthomosaic images were individually exported from each chunk. Therefore, the workload of AP1 was estimated to be approximately five times that of TP. In addition, the five TIFF files were layer stacked into a single file containing multispectral band images using the general-purpose remote sensing software ENVI or IDL5.6.

AP2

AP2 was a further improvement of AP1. AP2 also preliminarily created five chunks in the working project file. Furthermore, AP2 created new subfolders called "camera group folder" within each chunk and named the subfolders according to the corresponding spectral band. The original spectral band images were separately moved into the new subfolders. This was a preliminary step to make it easier to merge the five chunks described later. Internal camera calibration was repeated for every chunk. The major process difference between AP1 and AP2 was that the separately created chunks were merged into one common chunk to integrate tie points and GCP markers for each spectral band in AP2. Then internal camera calibration was reconducted for the newly merged common chunk using the integrated tie points and GCP markers to establish one common camera parameter for all spectral bands (Figure 2C). Only one common dense cloud or DSM layer was created in the merged chunk. Single-band orthomosaic images were repeatedly created as follows. For example, when creating a blue band orthomosaic image, the other subfolders of the camera group folder (green, red, red-edge, and NIR) were preliminarily disabled before building the blue band orthomosaic. These steps were repeated as many times as the number of spectral bands in the merged chunk. The way of stacking the five TIFF files into one file was the same as in AP1.

Accuracy Assessment of Estimated GCP Locations

Coordinate data of the GCPs (latitude, longitude, and ellipsoid height) were measured by postprocessing static (PPS) surveys using GNSS data acquired simultaneously from two paired GNSS receivers. GNSS rover data of each GCP marker were logged by compact GNSS receivers using a NEO-M8P RTK GNSS receiver board (Etehs SIA, Riga, Latvia) for more than 30 minutes. Data of a GNSS continuously operating reference station named "Tsukuba 3" were used as base station data. The station is located 9 km away from the experimental field and is operated by the Geographical Survey Institute of Japan. The PPS surveys were conducted using an open-source program package for GNSS positioning, RTKLIB (version 2.4.3b34) (http://www.rtklib.com). The GNSS-derived

GCP coordinate information was converted from latitude and longitude to the UTM coordinate system for comparison with the estimated coordinate information of the corresponding GCPs for verification based on the orthomosaic images. UTM coordinate information of the GCPs was manually read for each spectral band individually using ENVI/IDL 5.6 software.

Accuracy Assessment of Misalignment Between Five Spectral Band Images

The relative alignment error between five spectral band images was evaluated according to the following criteria, without using the ground-truth coordination data measured by the GNSS receiver. For each single GCP, information of five coordinates could be read as the P4M-derived multispectral orthomosaic image comprised of five spectral band images.

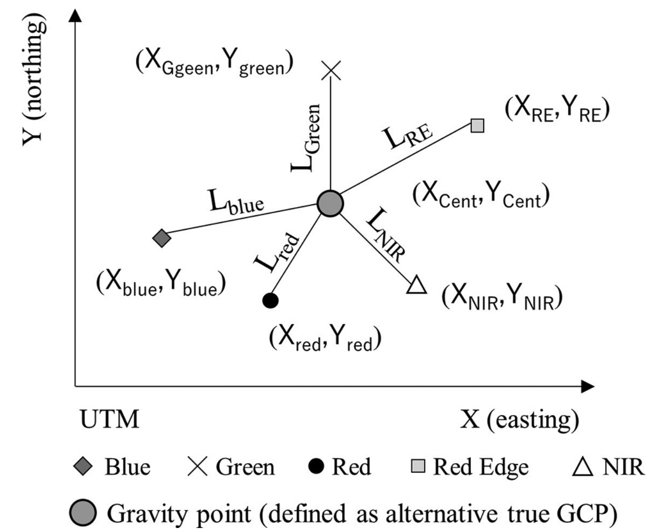

Figure 3. Diagram of the estimated ground control point (GCP) locations for validation derived from five spectral bands and the center of gravity point of those locations. The distance between the gravity point and each estimated location was defined as a scale for measuring the relative misalignment between spectral bands.

As shown in Figure 3, we assumed the center of gravity of the five coordinate points as hypothetical true GCP location rather than the GNSS receiver-derived coordinate location. The coordinate information of the gravity point (X_{grav}, Y_{grav}) was calculated with Equation 1. Next, the five distances (L_{band}) from the gravity point to these five points were calculated with Equation 2. The average value of the five distances was defined as a scale (S_{mis}) to measure the relative misalignment between spectral bands (Equation 3):

$$X_{\text{grav}} = \frac{1}{5}\sum_{i=\text{band}} X_i, \quad Y_{\text{grav}} = \frac{1}{5}\sum_{i=\text{band}} Y_i \tag{1}$$

$$L_{\text{band}} = \sqrt{\left(X_{\text{grav}} - X_{\text{band}}\right)^2 + \left(Y_{\text{grav}} - Y_{\text{band}}\right)^2} \tag{2}$$

$$S_{\text{mis}} = \frac{1}{5}\sum_{i=\text{band}} L_i \tag{3}$$

where band is blue, green, red, red edge, or NIR.

VIs

We evaluated the effect of quality differences of the multispectral orthomosaic images due to the different processing procedures on observed VI values. CI_{green} and NDVI were calculated using Equations 4 and 5:

$$\text{CI}_{\text{green}} = \frac{\rho_{\text{NIR}}}{\rho_{\text{green}}} \tag{4}$$

$$\text{NDVI} = \frac{\rho_{\text{NIR}} - \rho_{\text{red}}}{\rho_{\text{NIR}} + \rho_{\text{red}}} \tag{5}$$

where ρ_{NIR}, ρ_{green}, and ρ_{red} are spectral reflectance values (0–1.0) in the NIR (840 ± 26 nm), red (650 ± 16 nm), and green (560 ± 16 nm) bands.

CI_{green} is correlated with the canopy chlorophyll content, which is the amount of chlorophyll per unit area (Wu *et al.* 2012; Schlemmer *et al.* 2013; Inoue *et al.* 2016; Clevers *et al.* 2017) or nitrogen concentration in plant leaves (Cai *et al.* 2019). CI_{green} is widely used as a remote sensing–based indicator useful for estimating photosynthetic carbon assimilation in various fields (Peng and Gitelson 2011; Zhang *et al.* 2015). Gitelson *et al.* (2003, 2005) found that CI_{green} is related to canopy photosynthesis of irrigated maize. It can be used as an alternative indicator to the product of light use efficiency (ε) and fraction of absorbed photosynthetically active radiation (fPAR) in the light use efficiency model (Peng and Gitelson 2012) described by the following equation (Monteith 1972) to estimate gross primary production (GPP):

$$\text{GPP} = \varepsilon \times \text{fPAR} \times \text{PAR} \tag{6}$$

$$\text{GPP} \propto \text{CI}_{\text{green}} \times \text{PAR} \tag{7}$$

NDVI remains the most popular multipurpose VI used for crop monitoring of various features, including leaf nitrogen concentration, aboveground biomass, fraction of absorbed photosynthetically active radiation, and damage caused by diseases (Thenkabail *et al.* 1994; Franke and Menz 2007; Sakamoto *et al.* 2012; Shibayama *et al.* 2012). In recent years, with the advent of affordable small drones with multispectral cameras, many researchers who are starting to apply drone-based remote sensing for crop growth monitoring in Japan tend to use NDVI as a de facto standard VI under a national trend in precision agriculture research called "smart agriculture" (Morimoto and Hayashi 2017; Guan *et al.* 2019; Osaki 2019; Inoue 2020).

Comparison of Pixel-Level or Region-Averaged VIs at Fixed Locations Between Multispectral Orthomosaic Images Obtained at 20- and 30-m Flight Height

The effect of misalignment due the processing procedure on the VI was evaluated as follows. Multispectral orthomosaic images with a 1-cm pixel resolution were generated from the data sets acquired on the same day but at different flight heights. A one-by-one comparison of pixel-level VI and region-averaged VI was performed for the 12 plots for each procedure evaluated in anticipation of the creation of gridded vegetation growth maps for designing variable-rate fertilization in precision agriculture (Veroustraete 2015; McKinnon 2016; Saiz-Rubio and Rovira-Más 2020). The square (grid) size for measuring region-averaged VIs was varied at seven levels (2×2, 4×4, 8×8, 16×16, 32×32, 64×64, and 128×128 pixels) to investigate the effect of square size on the observed VI value. If there is no misalignment effect, the observed VI should consistently be approximately the same at the same location regardless of the flight height. The lower the misalignment effect, the closer the data points in a scatter plot are distributed to the one-by-one straight trend line. In other words, the procedure that showed the highest correlation or lowest root mean square error (RMSE) between VI images obtained at different flight heights could be regarded as having the best performance without a misalignment problem.

Results and Discussion

Location Estimation Accuracy of GCPs for Verification

Figure 4 shows the GCP location estimation error for verification based on the GNSS-derived true position. Some of the TP-derived results had errors of more than 6 cm at any combination of flight height and observation date (Figure 4A1–4). When using TP, the number (percentage) of GCPs with errors of less than 1.5 and 3.0 cm were 40 (21.1%) and 97 (51.1%) out of the total (190) GCPs, respectively. Although it was unclear why the TP-derived location error tended to be more spread out in the east–west direction than in the north–south direction, this error trend may be related to the fact that the GCP locations were widely spread in the east–west direction in the experimental fields. The AP1-derived results had little directional error variation, especially in the east–west direction, and the variability of error was substantially smaller than that of the TP results. AP1 did not produce errors of more than 6 cm (Figure 4B1–4). The number of GCPs with errors less than 1.5 and 3.0 cm were 103 (54.2%) and 173 (91.1%) out of the total (190) GCPs, respectively. The AP2-derived results showed similar overall trends in error variation as the AP1 results. There was no GCP with an error greater than 6 cm based on the GNSS-derived true locations. When we focused on local trends in error variation, we observed a smaller variability of the errors, especially between spectral bands, than in AP1 (Figure 4C1–4). When using AP2, the number of GCPs with errors of less than 1.5 and 3.0 cm were 125 (65.8%) and 185 (97.6%) out of the total (190) GCPs, respectively. Thus, AP2 produced the smallest error.

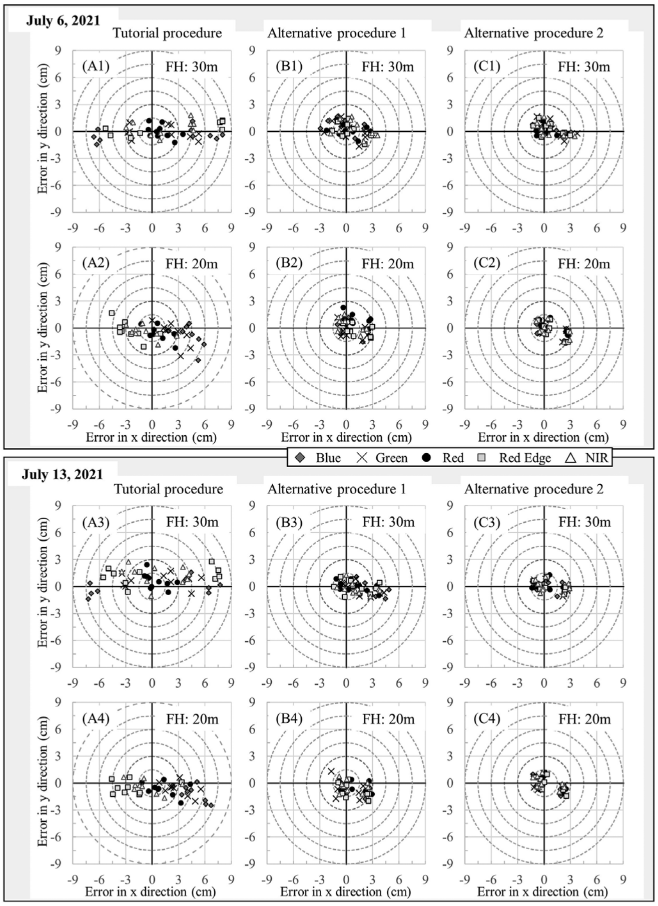

Figure 4. Comparison of GCP location estimation errors by the three procedures (A1-4: tutorial procedure [TP]; B1-4: alternative procedure 1 [AP1]; C1-4: alternative procedure [AP2]) and at different flight heights.

Table 2 shows a summary of statistics for errors in the estimated GCP locations. The average values of the GCP location estimation error of TP for all spectral bands were 2.70–3.01 cm at 20-m flight height and 3.78–3.85 cm at 30-m flight height. The GCP location estimation error of TP was about twice that of AP2 (average error: 1.35–1.40 cm at 20 m, 1.30–1.36 cm at 30 m). Only for the red band, which had the best location estimation accuracy, was the estimation error comparable between AP1 and AP2, although we used mainly the default blue-band images for placing GCP markers manually and internal camera calibration. Unlike in the case of TP, when AP1 and AP2 were used, there were no extreme differences in location estimation errors depending on specific spectral cameras. The estimation location accuracy of AP2 was comparable to that of a drone designed for surveying work, that is, the DJI Phantom 4 RTK (Taddia *et al.* 2020).

Table 3 summarizes paired t-test results of GCP location estimation error comparison between TP and AP1 and between AP1 and AP2. The location estimation error of AP1 was significantly smaller than of TP at the 1% level in two-tailed tests. The average location estimation error of AP2 was smaller than that of AP1; except for a few cases, no significant difference was found between these procedures for data obtained at 20-m flight height. However, at the 1% level, the location estimation error of AP2 was significantly smaller than that of AP1 only for data obtained at 30-m flight height. These data clearly indicated that the absolute location estimation accuracy of TP was inferior to that of AP1 and AP2. Considering that the positioning accuracy of the PPS survey using GNSS data used to measure the coordinates of the GCPs is approximately 1 cm, the estimation accuracy of AP1 and AP2 can be considered almost similar.

The most interesting finding in this study was that estimation accuracy typically depended on the spectral cameras position when using TP; the spectral cameras showing better location estimation results, in order from best to worst, were red, NIR, green, red edge, and blue. This tendency was commonly observed regardless of the observation date or flight height. The multispectral cameras of the P4M are arranged in a 3×2 horizontal and vertical pattern. The red and NIR band cameras, which had the best and second-best location estimation accuracy, respectively, are placed in the center of the arrangement, while the green, red-edge¬, and blue band cameras are placed in the four corners. RTK-measured position information of each spectral camera

Table 2. Summary of GCP location estimation errors at each spectral band and flight level among the three procedures evaluated on 6 and 13 July 2021.

		TP		AP1		AP2	
	Flight Height	**30 m**	**20 m**	**30 m**	**20 m**	**30 m**	**20 m**
Date	**Band**	**Average (SD), cm**	**Average (SD), cm**	**Average (SD), cm**	**Average (SD), cm**	**Average (SD), cm**	**Average (SD), cm**
6 July 2021	Blue	6.12 (1.19)	4.40 (1.42)	1.78 (0.66)	1.39 (0.79)	1.22 (0.83)	1.36 (1.07)
	Green	3.22 (1.29)	2.68 (1.47)	1.64 (0.73)	1.32 (0.85)	1.43 (1.14)	1.29 (0.97)
	Red	1.42 (1.04)	1.61 (1.11)	1.41 (0.86)	1.77 (0.88)	1.22 (0.67)	1.42 (1.06)
	Red edge	5.22 (2.70)	2.93 (1.16)	1.59 (1.02)	1.48 (1.15)	1.46 (0.79)	1.46 (1.16)
	NIR	2.94 (1.68)	1.87 (0.82)	1.82 (0.92)	1.43 (0.53)	1.46 (0.99)	1.46 (1.19)
	All	3.78 (2.35)	2.70 (1.53)	1.65 (0.83)	1.48 (0.84)	1.36 (0.87)	1.40 (1.04)
13 July 2021	Blue	6.06 (1.44)	4.84 (1.57)	2.09 (1.73)	1.37 (1.08)	1.27 (0.67)	1.47 (0.67)
	Green	3.36 (1.20)	3.10 (1.63)	1.96 (1.38)	1.54 (0.72)	1.26 (1.00)	1.34 (0.70)
	Red	1.41 (0.91)	1.89 (1.41)	1.66 (1.20)	1.37 (1.06)	1.40 (0.81)	1.29 (0.87)
	Red edge	5.36 (2.14)	3.22 (1.05)	1.80 (1.14)	1.50 (1.16)	1.27 (0.90)	1.32 (0.94)
	NIR	3.04 (1.31)	2.00 (0.88)	1.77 (1.26)	1.33 (0.86)	1.30 (1.03)	1.34 (0.67)
	All	3.85 (2.20)	3.01 (1.67)	1.86 (1.31)	1.42 (0.95)	1.30 (0.85)	1.35 (0.75)

GCP = ground control point; TP = tutorial procedure; AP1 = alternative procedure 1; AP2 = alternative procedure 2; SD = standard deviation; NIR = near infrared.

was individually recorded in the header of TIFF image. Latitude and longitude coordinate information was recorded with a resolution of up to eight decimal places, which corresponded to a millimeter-level of resolution. This implies that the P4M is designed to record GNSS-derived positional information with sufficient resolution to understand the relative positions between individual spectral cameras. Our results suggested that the algorithm used in "multi-camera system" mode in TP may not properly use the precise RTK position information of each spectral camera during internal camera calibration, which may have resulted in systematic alignment errors between spectral bands, at least when using Agisoft Metashape Professional, version 1.7.3, build 12473 (64 bit). Accuracy evaluation in the height direction of the orthomosaic images was not the subject of this study because the height difference between the GCP markers placed on the concrete ground was less than 2.6 cm, which is not sufficient for quantitative verification.

Alignment Error Between Five Spectral Band Images

Table 4 summarizes paired *t*-test results comparing the average distance from the gravity point to the estimated GCP locations (S_{mis}) between TP and AP1 and between AP1 and AP2. The TP-derived alignment error between spectral bands was an order of magnitude larger than those for AP1 and AP2. The average S_{mis} derived from TP was 2.82 cm (n = 190), which was 525% to 972% larger than those derived with AP1 (0.52 cm) and AP2 (0.29 cm). The alignment accuracy differed significantly between TP and AP1 and between AP1 and AP2 at the 1% level in two-tailed tests. The misalignment distance of AP2 was 46% smaller than that of AP1. Considering that the average corn and rice leaf widths are approximately 9 and 1 cm, respectively, a few centimeter-level misalignments between spectral bands of multispectral orthomosaic images derived from TP would produce an error of magnitude that cannot be ignored in VI calculations to evaluate leaf color. The results suggested that the additional step in AP2, that is, integrating tie points and GCP markers created separately for the five spectral bands into a merged chunk, effectively reduces the alignment error between spectral band images from AP1.

Figure 5 shows the false color composite of NIR-red-green images and spectral reflectance images of GCP10, Plot 03 (corn), and Plot 07 (rice). The center points of the GCP markers were manually traced with crosshairs for each spectral band and superimposed on a single partial figure. In addition, the boundaries between the background and the vegetation in the middle row were manually traced and superimposed on Plots 03 and 07. As can be seen from the superimposition of the

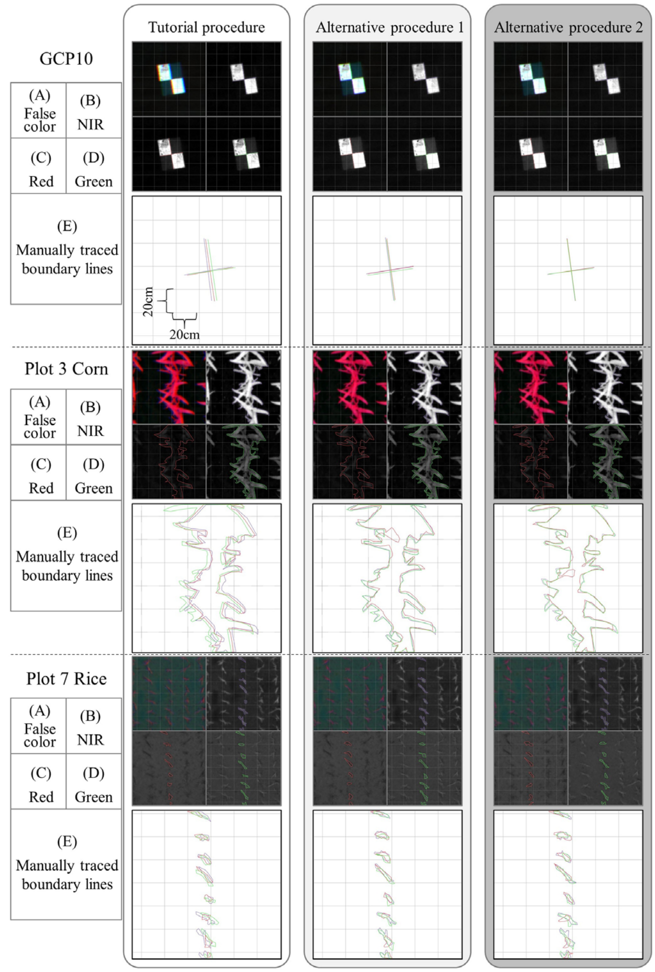

Figure 5. Enlarged false color composite of near-infrared (NIR)-red-green images of Plot 03, Plot 07, and GCP10 (A) on 6 July 2021, spectral band images with manually traced lines of vegetation and center of the ground control point (GCP) marker (B–D) and superimposed images.

Table 3. Average GCP location estimation errors of five spectral bands at each flight level among the three procedures evaluated on 6 and 13 July 2021.

	Flight Height (m)	*n*	TP Mean (V), cm	← Paired *t*-Test *p*-Value	→	AP1 Mean (V), cm	← Paired *t*-Test *p*-Value	→	AP2 Mean (V), cm
6 July 2021	30	50	3.78 (5.51)	4.79×10^{-7}	**	1.65 (0.68)	2.87×10^{-3}	*	1.36 (0.76)
	20	45	2.70 (2.33)	8.97×10^{-6}	**	1.48 (0.70)	2.89×10^{-1}		1.40 (1.09)
	All	95	3.27 (4.26)	4.97×10^{-11}	**	1.57 (0.69)	2.20×10^{-3}	*	1.38 (0.90)
13 July 2021	30	50	3.85 (4.82)	7.81×10^{-7}	**	1.86 (1.71)	5.32×10^{-5}	**	1.30 (0.73)
	20	45	3.01 (2.80)	5.05×10^{-8}	**	1.42 (0.90)	3.89×10^{-1}		1.35 (0.56)
	All	95	3.45 (4.00)	8.48×10^{-13}	**	1.65 (1.36)	9.04×10^{-5}	**	1.32 (0.64)

GCP = ground control point; TP = tutorial procedure; AP1 = alternative procedure 1; AP2 = alternative procedure 2; V = variance.
*p < 0.05, **p < 0.01.

Table 4. Summary of alignment errors between spectral bands at each flight level among the three procedures evaluated on 6 and 13 July 2021.

	Flight Height (m)	*n*	TP Average (SD), cm	← Paired *t*-Test *p*-Value	→	AP1 Average (SD), cm	← Paired *t*-Test *p*-Value	→	AP2 Average (SD), cm
6 July 2021	30	50	3.42 (5.01)	2.08×10^{-12}	**	0.55 (0.050)	2.62×10^{-3}	**	0.41 (0.048)
	20	45	2.11 (1.49)	3.71×10^{-9}	**	0.67 (0.064)	6.43×10^{-13}	**	0.22 (0.024)
	All	95	2.80 (3.74)	1.78×10^{-18}	**	0.61 (0.059)	1.62×10^{-12}	**	0.32 (0.045)
13 July 2021	30	50	3.43 (4.86)	8.99×10^{-13}	**	0.47 (0.053)	3.97×10^{-6}	**	0.28 (0.025)
	20	45	2.18 (1.86)	4.61×10^{-10}	**	0.46 (0.055)	1.21×10^{-6}	**	0.23 (0.018)
	All	95	2.84 (3.80)	3.64×10^{-20}	**	0.47 (0.054)	1.57×10^{-11}	**	0.26 (0.022)

SD = standard deviation; TP = tutorial procedure; AP1 = alternative procedure 1; AP2 = alternative procedure 2.
*p < 0.05, **p<0.01.

traced lines, the spectral reflectance images derived from TP were misaligned by a few centimeters. The trace lines of AP1 were more closely overlaid than those of TP; however, a misalignment between the red and green band images was still noticeable. The misalignment between spectral band images of AP2 was further reduced compared to that of AP1, especially for GCP10 and Plot 03. The cross lines for GCP10 nearly perfectly overlapped and were centered on the GCP marker. Similar improvement was seen in Plot 03 (corn). As for Plot 07 (rice), there was no obvious improvement in the alignment error between AP1 and AP2, while there was an improvement in AP1 or AP2 versus TP. Possibly, the difference in misalignment could not be visualized by manual tracing, as rice leaves are substantially smaller than corn leaves, making it harder to recognize the edges between the background and vegetation. We cannot conclude whether AP1 or AP2 is more suitable based on visual assessment of Plot 03 alone; however, AP2 provided more accurate coordinate information and reduced the interspectral band misalignment error.

Comparison of Pixel-Level VIs Derived Multispectral Orthomosaic Images Acquired at Different Heights at the Same Location

Figure 6 shows scatter plots of the VIs for the 12 plots ($N = 128{\times}128{\times}12 = 196{,}608$ pixels) based on multispectral orthomosaic images obtained at different flight heights (20 or 30 m) with the three processing procedures. The TP-derived results (Figure 6A1–6A4) showed the largest data variability and the lowest correlation coefficients regardless of the observation date or VI. The scatter plots obtained with AP2 showed a smaller variability and higher correlation coefficients than those obtained with AP1, especially for CI_{green} (Figure 6B1, 6B2, 6C1, 6C2). However, when using NDVI, there was no obvious difference between the two procedures in terms of degree of agreement (Figure 6B3, 6B4, 6C3, 6C4).

Table 5 summarizes the correlation coefficients between the pixel-level VIs per plot. The correlation coefficients tended to be lower on 13 July than on 6 July for both CI_{green} and NDVI. This was probably due to the limited dynamic range of VI within each plot and vegetation growth in one week. The vegetation cover fraction (i.e., the area percentage of vegetation covering the background area) rapidly increased with the leaf expansion during this phenological stage. Thus, the percentage of vegetated pixels within each plot increased in one week, and the dynamic range of VI was proportionally biased toward vegetated pixels over background pixels. Interestingly, AP2-derived CI_{green} values had the highest correlation coefficients in all plots and on both observation

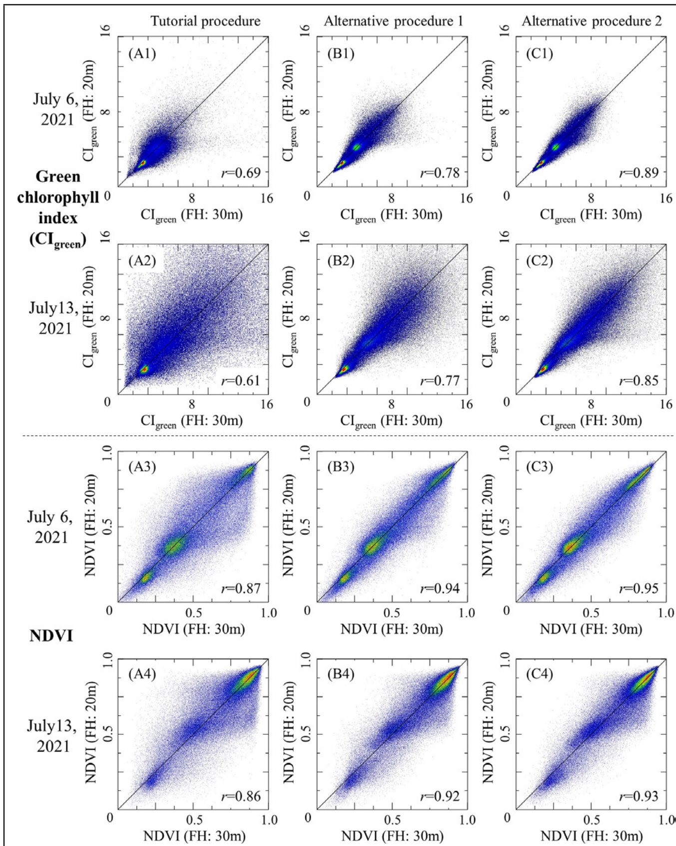

Figure 6. Density scatter plots of pixel-level green chlorophyll index (CI_{green}) (top) and normalized difference vegetation index (NDVI) (bottom) data for the 12 plots shown in Figure 1, based on the tutorial procedure (TP), alternative procedure 1 (AP1), and alternative procedure 2 (AP2). Data were derived from multispectral orthomosaic images acquired at different flight heights (20 and 30 m) on 6 and 13 July 2021.

Table 5. Correlation coefficients of pixel-level CI and NDVI data between multispectral orthomosaic images obtained at 20- and 30-m flight heights.[a]

			CI_{green} Correlation Coefficient (r)						NDVI Correlation Coefficient (r)					
		Fertilizer	6 July 2021			13 July 2021			6 July 2021			13 July 2021		
Plot	Crop	(N kg/10 acres)	TP	AP1	AP2	TP	AP1	AP2	TP	AP1	AP2	TP	AP1	AP2
1	Corn	0	0.65	0.52	**0.80**	0.54	0.16	**0.56**	0.82	0.95	**0.97**	0.66	0.77	0.76
2		5	0.51	0.56	**0.80**	0.50	0.43	**0.64**	0.71	0.88	**0.91**	0.67	0.71	0.68
3		10	0.62	0.60	**0.77**	0.56	0.51	**0.73**	0.81	0.92	**0.95**	0.70	0.71	**0.75**
4		15	0.73	0.56	**0.79**	0.55	0.63	**0.71**	0.85	0.90	**0.95**	0.75	0.71	**0.78**
5		20	0.65	0.53	**0.66**	0.54	0.49	**0.59**	0.82	0.91	**0.92**	0.66	0.61	**0.67**
6		25	0.71	0.58	**0.79**	0.71	0.67	**0.76**	0.81	0.89	**0.94**	**0.80**	0.74	0.76
7	Rice	0	0.39	0.68	**0.82**	0.35	0.62	**0.74**	0.67	0.82	**0.89**	**0.63**	0.44	0.60
8		1	0.69	0.82	**0.93**	0.57	0.80	**0.88**	0.82	0.89	**0.93**	0.73	0.69	**0.78**
9		2	0.61	0.80	**0.87**	0.39	0.73	**0.77**	0.78	0.896	**0.901**	0.61	**0.66**	0.65
10		4	0.66	0.85	**0.91**	0.42	0.74	**0.81**	0.80	0.95	0.92	0.67	**0.77**	0.69
11		6	0.58	0.85	**0.90**	0.39	0.62	**0.72**	0.78	0.94	0.92	**0.73**	0.58	0.56
12		8	0.58	0.83	**0.83**	0.24	0.54	**0.60**	0.68	0.93	0.87	**0.54**	0.48	0.40
All			0.69	0.78	**0.89**	0.61	0.77	**0.85**	0.87	0.94	**0.95**	0.86	0.92	**0.93**

CI = chlorophyll index; NDVI = normalized difference vegetation index; CIgreen = green chlorophyll index; TP = tutorial procedure; AP1 = alternative procedure 1; AP2 = alternative procedure 2.
[a]Boldface values indicate higher correlation coefficients than those obtained with the other procedures.

dates. AP2-derived NDVI values also tended to have higher correlation coefficients than those obtained with the other procedures in most cases. The highest correlation coefficients were observed for plots 1–9 on 6 July and for plots 3–5 and 8 on 13 July.

As shown in Figure 6, NDVI was less sensitive than CI_{green} to absolute and relative misalignment related to the procedure used. The robustness of NDVI to the misalignment problem of multispectral orthomosaic images was highlighted with the increase in vegetative fraction in each plot. The difference in sensitivity of NDVI and CI_{green} to misalignment can be interpreted based on the difference in reflectance between leaf and background. As shown in Figure 5, the contrast between the leaf cover and background in the green reflectance images was higher than that in the red reflectance images, especially for corn (Viña *et al.* 2004). As for NDVI, the NIR reflectance of leaves was approximately 50% and was nearly ten times higher than that of the background, whereas the red reflectance of leaves and background were similar and low (a few percents). Therefore, NDVI is intrinsically less sensitive to changes in red reflectance than to changes in NIR reflectance (Gitelson 2004) given how it is calculated (Equation 5). In contrast, CI_{green} is intrinsically more susceptible to misalignment between these spectral band images, especially at the borders between leaf and background areas, as it considers the ratio of NIR to green reflectance (Equation 4).

Comparison of Region-Averaged VIs Derived from Multispectral Orthomosaic Images Acquired at Different Flight Heights

Figure 7 compares region-averaged VIs derived from orthomosaic images acquired at different heights for the 12 plots using seven different grid sizes. Determination coefficients were calculated using all plot data, without considering the observation dates (N = 24 [12 plots×2 days]). The determination coefficients obtained with TP were consistently smaller than those obtained with AP1 and AP2 for both CI_{green} and NDVI. AP2 showed the best performance in terms of the degree of agreement of the observed value of region-averaged VIs under different aerial photography conditions, especially for CI_{green} (Figure 7A). The determination coefficients plateaued at a grid size of 32×32 pixels for all three procedures and both VIs. As for the region-averaged NDVI, there were no substantial differences between AP1 and AP2 results (Figure 7B). When focusing on the effect of grid size for region averaging, the determination coefficients for CI_{green} decreased more rapidly than those for NDVI with decreasing grid size. This was also due to the lower sensitivity of NDVI to the alignment error between spectral bands. Even when using TP, the determination coefficient of the region-averaged NDVI based on a 2×2-pixel grid was high, 0.895, which was 0.15 greater than that of CI_{green}. However, there were still noticeable negative effects of a low alignment accuracy on the observed value of the region-averaged NDVI, especially when comparing TP with the other procedures. Increasing the grid size for region averaging could mitigate the negative effects, and the optimal grid size for the spatial resolution (flight level) of aerial photography using the P4M, which ranges from 1.1 cm/pixel (20 m) to 1.6 cm/pixel (30 m), was 32×32 pixels.

Figure 8 shows scatter plots of region-averaged VIs with the grid size fixed at 32×32 pixels. The RMSEs for rice and corn were compared to investigate the effect of the processing procedure applied on the results. The scatter plot of CI_{green} obtained with TP in Figure 8A1 shows that region-averaged CI_{green} of corn was more affected by misalignment than that of paddy rice (RMSE = 0.61, which was the worst error observed). The difference in the RMSE of CI_{green} between AP1 and AP2 was low; thus, both procedures showed comparable accuracy. In contrast, the 32×32-pixel-based region-averaged NDVI showed no differences in accuracy regardless of the processing procedure applied or the crop species. This result suggested that calculating region-averaged VIs using a 32×32-pixel grid size is an effective way to minimize the negative effect of misalignment on observed values, except for the CI_{green} of corn. Moreover, the region-averaged NDVI is more robust to the misalignment problem than CI_{green} regardless of crop species.

This study focused on evaluating the geometric correction results of the proposed procedures and its improvement effect on VIs without a detailed analysis of the effects on radiometric correction. Although Fawcett *et al.* (2020) suggested that drone-derived NDVI had relatively good agreement with those derived from an airborne imaging spectrometer and an optical satellite image in a maize field, they demonstrated that drone-based hemispherical-conical reflectance factor values exhibited bias when compared to spectroradiometer measurement data, particularly over lower reflective surfaces. Meanwhile, although the commercial SfM/MVS software packages can easily perform radiometric correction, details on their calculation algorithms are not disclosed. Therefore, we believe that further verification of the accuracy of radiometric correction is necessary in future studies.

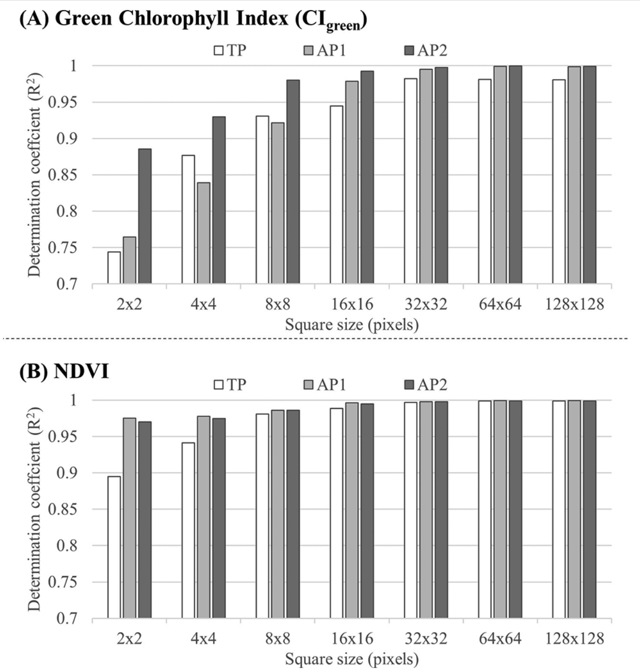

Figure 7. Determination coefficients of region-averaged green chlorophyll index (CI_{green}) (A) and normalized difference vegetation index (NDVI) (B) data based on the tutorial procedure (TP), alternative procedure 1 (AP1), and alternative procedure 2 (AP2). Data were derived from multispectral orthomosaic images acquired at different flight heights.

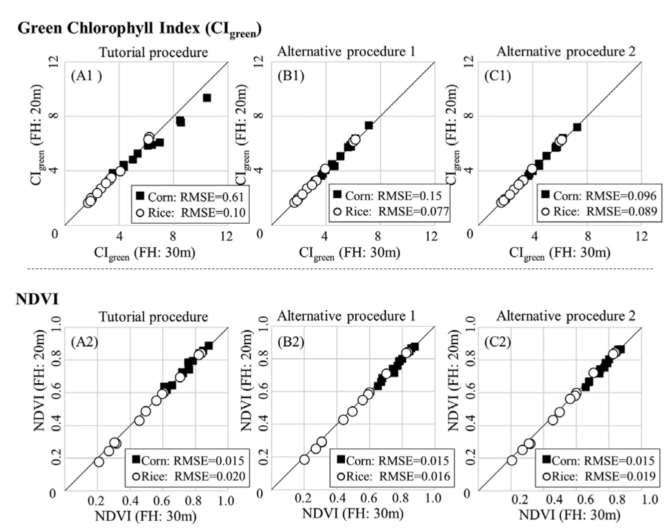

Figure 8. Scatter plots of region-averaged green chlorophyll index (CI_{green}) (A) and normalized difference vegetation index (NDVI) (B) data based on the tutorial procedure (TP), alternative procedure 1 (AP1), and alternative procedure 2 (AP2). Data were derived from multispectral orthomosaic images acquired at different flight heights. The grid size for region averaging was set to 32×32 pixels (32×32 cm).

Conclusion

We examined the location estimation accuracy of three processing procedures to propose an appropriate procedure for creating high-quality multispectral orthomosaic images acquired with the P4M in conjunction with the Agisoft Metashape SfM/MVS software. The standard processing procedure (TP) that can be found on the Agisoft Helpdesk website showed remarkable inaccuracy in terms of location estimation and alignment between spectral band images in this study. The degree of alignment error caused by TP obviously varied depending on the spectral camera. This finding suggested the presence of a program bug in the processing flow of the "multi-camera system" mode of Agisoft Metashape (as of version 1.7.3, build 12473 [64 bit]) that interferes with internal camera calibration using RTK-derived precise position information individually recorded by the multispectral camera. Here, we developed alternative processing procedures (AP1 and AP2) for P4M data analysis using Agisoft Metashape. AP1 uses the "single camera" generic processing mode to individually import P4M-derived aerial images by spectral band to separately create five single-band orthomosaic images. Then the five single-band orthomosaic images are stacked in a single file containing five spectral band images. The location estimation error of AP1 was significantly reduced to about half of that of TP. Compared to using TP, the absolute location estimation accuracy of GCPs for verification in AP1 was significantly improved by the altered procedure, which processed the multispectral images separately by spectral band. AP2 has one more processing step than AP1. It merges the five chunks of tie points and GCP markers created separately for each spectral band into a single chunk and then reconducts internal camera calibration. The alignment accuracy between spectral bands of AP2 was significantly better than that of AP1. We conclude that band-to-band misalignment can be minimized by a second internal camera calibration after integrating tie points and GCP markers preliminarily processed for each spectral band separately. While the mean absolute location estimation error of AP2 was 1.32–1.38 cm, the mean of band-to-band misalignment was 0.26–0.32 cm.

The effect of the differences in the processing procedures on observed NDVI and CI_{green} value was investigated in 12 plots cropped with corn and paddy rice. The use of region-averaged VIs based on at least 32×32-pixel square size was effective to minimize the negative impact of misalignment on observed VI values for all procedures. Overall, AP2 yielded the best location estimation and band alignment accuracy of multispectral orthomosaic images among all procedures evaluated, especially for monitoring corn growth with the P4M drone. The proposed alternative procedure for the Agisoft Metashape software (for version 1.7.3, build 12473 [64 bit]) in conjunction with the P4M contributes to more precise VI analysis in crop breeding and field management in agriculture until the software flaws are fixed.

Acknowledgments

We gratefully acknowledge the support of Takahiro Ara, Toyoshi Omizu, Tomiyama Hirokazu, Naoki Nagata, Misaki Onaka, Yuki Muto, Ryouji Imse, and Dr. Shouji Taniguchi for field experiments and thank Dr. Mizuki Morishita for providing the P4M drone. We offer special thanks to Dr. Tsutomu Kanno, Dr. Yoshihito Sunaga, Yuki Akamatsu, and Kozue Suzuki for providing materials for the corn cultivation experiment. This study was partially supported by a grant from the Ministry of Agriculture, Forestry, and Fisheries of Japan (Smart-Breeding System for Innovative Agriculture, grant BAC1003) to D.O. We also appreciate the valuable comments and suggestions of the anonymous reviewers.

References

Agisoft Helpdesk Portal. 2021. DJI Phantom 4 Multispectral Data Processing. <https://agisoft.freshdesk.com/support/solutions/articles/31000159853-dji-phantom-4-multispectral-data-processing> Accessed 19 August 2021.

Blue Innovation Co. Ltd. 2020. Implementation Report of the Project for Introduction and Demonstration of New Technologies for Forestation—Remote Sensing Training (in Japanese). <https://www.rinya.maff.go.jp/j/seibi/sinrin_seibi/attach/pdf/sinsei_kensa-13.pdf>Accessed 19 August 2021.

Boegh, E., H. Soegaard, N. Broge, C. B. Hasager, N. O. Jensen, K. Schelde, and A. Thomsen. 2002. Airborne multispectral data for quantifying leaf area index, nitrogen concentration, and photosynthetic efficiency in agriculture. *Remote Sensing of Environment* 81(2–3):179–193.

Borgogno-Mondino, E., A. Lessio, L. Tarricone, V. Novello, and L. de Palma. 2018. A comparison between multispectral aerial and satellite imagery in precision viticulture. *Precision Agriculture* 19(2):195–217.

Cai, Y. P., K. Y. Guan, F. Nafziger, G. Chowdhary, B. Peng, Z. N. Jin, S. W. Wang, and S. B. Wang. 2019. Detecting in-season crop nitrogen stress of corn for field trials using UAV- and CubeSat-based multispectral sensing. *IEEE Journal of Selected Topics in Applied Earth Observations and Remote Sensing* 12(12):5153–5166.

Che, Y. P., Q. Wang, Z. W. Xie, L. Zhou, S. W. Li, F. Hui, X. Q. Wang, B. G. Li, and Y. T. Ma. 2020. Estimation of maize plant height and leaf area index dynamics using an unmanned aerial vehicle with oblique and nadir photography. *Annals of Botany* 126(4):765–773.

Clevers, J.G.P.W., L. Kooistra, and M.M.M. van den Brande. 2017. Using Sentinel-2 data for retrieving LAI and leaf and canopy chlorophyll content of a potato crop. *Remote Sensing* 9(5):405. <https://doi.org/10.3390/rs9050405>.

Fawcett, D., C. Panigada, G. Tagliabue, M. Boschetti, M. Celesti, A. Evdokimov, K. Biriukova, R. Colombo, F. Miglietta, U. Rascher, and K. Anderson. 2020. Multi-scale evaluation of drone-based multispectral surface reflectance and vegetation indices in operational conditions. *Remote Sensing* 12(3):514.<doi:10.3390/rs12030514>.

Franke, J. and G. Menz. 2007. Multi-temporal wheat disease detection by multi-spectral remote sensing. *Precision Agriculture* 8(3):161–172.

Gitelson, A. A. 2004. Wide dynamic range vegetation index for remote quantification of biophysical characteristics of vegetation. *Journal of Plant Physiology* 161(2):165–173.

Gitelson, A. A., S. B. Verma, A. Viña, D. C. Rundquist, G. Keydan, B. Leavitt, T. J. Arkebauer, G. G. Burba, and A. E. Suyker. 2003. Novel technique for remote estimation of CO2 flux in maize. *Geophysical Research Letters* 30(9):1486. <doi:10.1029/2002gl016543>.

Gitelson, A. A., A. Viña, V. Ciganda, D. C. Rundquist, and T. J. Arkebauer. 2005. Remote estimation of canopy chlorophyll content in crops. *Geophysical Research Letters* 32(8):L08403. <https://doi.org/10.1029/2005GL022688>.

Guan, S. L., K. Fukami, H. Matsunaka, M. Okami, R. Tanaka, H. Nakano, T. Sakai, K. Nakano, H. Ohdan, and K. Takahashi. 2019. Assessing correlation of high-resolution NDVI with fertilizer application level and yield of rice and wheat crops using small UAVs. *Remote Sensing* 11(2):112. <https://doi.org/10.3390/rs11020112>.

Huang, Y. B., K. N. Reddy, R. S. Fletcher, and D. Pennington. 2018. UAV low-altitude remote sensing for precision weed management. *Weed Technology* 32(1):2–6.

Inoue, Y. 2020. Satellite-and drone-based remote sensing of crops and soils for smart farming–A review. *Soil Science and Plant Nutrition* 66(6):798–810.

Inoue, Y., M. Guerif, F. Baret, A. Skidmore, A. Gitelson, M. Schlerf, R. Darvishzadeh, and A. Olioso. 2016. Simple and robust methods for remote sensing of canopy chlorophyll content: A comparative analysis of hyperspectral data for different types of vegetation. *Plant Cell and Environment* 39(12):2609–2623.

Maas, S. J. and N. Rajan. 2008. Estimating ground cover of field crops using medium-resolution multispectral satellite imagery. *Agronomy Journal* 100(2):320–327.

Maes, W.H. and Steppe, K., 2019. Perspectives for remote sensing with unmanned aerial vehicles in precision agriculture. *Trends in Plant Science* 24(2):152–164.

Malambo, L., S. C. Popescu, S.C. Murray, E. Putman, N. A. Pugh, D. W. Horne, G. Richardson, R. Sheridan, W. L. Rooney, R. Avant, M. Vidrinec, B. McCutchen, D. Baltensperger, and M. Bishop. 2018. Multitemporal field-based plant height estimation using 3D point clouds generated from small unmanned aerial systems high-resolution imagery. *International Journal of Applied Earth Observation and Geoinformation* 64:31–42.

Mamaghani, B. and C. Salvaggio. 2019. Multispectral sensor calibration and characterization for sUAS remote sensing. *Sensors* 19(20):4453. <https://doi.org/10.3390/s19204453>.

McKinnon, T., 2016. *Agricultural Drones: What Farmers Need to Know*. Agribotix white papers. https://agribotix.com/whitepapers/farmers-need-know-agricultural-drones.

Monteith, J. L. 1972. Solar-radiation and productivity in tropical ecosystems. *Journal of Applied Ecology* 9(3):747–766.

Morimoto, E. and K. Hayashi. 2017. Design of smart agriculture Japan model. *Advances in Animal Biosciences* 8(2):713–717.

Ogawa, D., T. Sakamoto, H. Tsunematsu, N. Kanno, Y. Nonoue, and J. I. Yonemaru. 2021. Haplotype analysis from unmanned aerial vehicle imagery of rice MAGIC population for the trait dissection of biomass and plant architecture. *Journal of Experimental Botany* 72(7):2371–2382.

Ogawa, D., T. Sakamoto, H. Tsunematsu, T. Yamamoto, N. Kanno, Y. Nonoue, and J. Yonemaru. 2019. Surveillance of panicle positions by unmanned aerial vehicle to reveal morphological features of rice. *PLoS One* 14(10): e0224386. <https://doi.org/10.1371/journal.pone.0224386>.

Osaki, K., 2019. Utilization of digital cameras for proximal remote sensing. *Nihon Gazo Gakkaishi* 58(6):651–658.

Peng, Y. and A. A. Gitelson. 2011. Application of chlorophyll-related vegetation indices for remote estimation of maize productivity. *Agricultural and Forest Meteorology* 151(9):1267–1276.

Peng, Y. and A. A. Gitelson. 2012. Remote estimation of gross primary productivity in soybean and maize based on total crop chlorophyll content. *Remote Sensing of Environment* 117:440–448.

Peter, B. G., J. P. Messina, J. W. Carroll, J. J. Zhi, V. Chimonyo, S. P. Lin, and S. S. Snapp. 2020. Multi-spatial resolution satellite and sUAS imagery for precision agriculture on smallholder farms in Malawi. *Photogrammetric Engineering and Remote Sensing* 86(2):107–119.

Qi, H., Z. Wu, L. Zhang, J. Li, J. Zhou, Z. Jun, and B. Zhu. 2021. Monitoring of peanut leaves chlorophyll content based on drone-based multispectral image feature extraction. *Computers and Electronics in Agriculture* 187:106292.

Reynolds, M., S. Chapman, L. Crespo-Herrera, G. Molero, S. Mondal, D.N.L. Pequeno, F. Pinto, F. J. Pinera-Chavez, J. Poland, C. Rivera-Amado, C. Saint Pierre, and S. Sukumaran. 2020. Breeder friendly phenotyping. *Plant Science* 295:110396.

Rouse, J. W., R. H. Haas, J. A. Schell, and D. W. Deering. 1974. Monitoring vegetation systems in the Great Plains with ERTS. *NASA Special Publication* 351(1974):309.

Saiz-Rubio, V. and F. Rovira-Más. 2020. From smart farming towards agriculture 5.0: A review on crop data management. *Agronomy* 10(2):207.

Sakamoto, T., A. A. Gitelson, A. L. Nguy-Robertson, T. J. Arkebauer, B. D. Wardlow, A. E. Suyker, S. B. Verma, and M. Shibayama. 2012. An alternative method using digital cameras for continuous monitoring of crop status. *Agricultural and Forest Meteorology* 154:113–126.

Schlemmer, M., A. Gitelson, J. Schepers, R. Ferguson, Y. Peng, J. Shanahan, and D. Rundquist. 2013. Remote estimation of nitrogen and chlorophyll contents in maize at leaf and canopy levels. *International Journal of Applied Earth Observation and Geoinformation* 25:47–54.

Shibayama, M., T. Sakamoto, E. Takada, A. Inoue, K. Morita, T. Yamaguchi, W. Takahashi, and A. Kimura. 2012. Estimating rice leaf greenness (SPAD) using fixed-point continuous observations of visible red and near infrared narrow-band digital images. *Plant Production Science* 15(4):293–309.

Sun, G. X., X. C. Wang, Y. Q. Ding, W. Lu, and Y. Sun. 2019. Remote measurement of apple orchard canopy information using unmanned aerial vehicle photogrammetry. *Agronomy-Basel* 9(11):774.

Svensgaard, J., S. M. Jensen, S. Christensen, and J. Rasmussen. 2021. The importance of spectral correction of UAV-based phenotyping with RGB cameras. *Field Crops Research* 269:9840192.

Taddia, Y., F. Stecchi, and A. Pellegrinelli. 2020. Coastal mapping using DJI Phantom 4 RTK in post-processing kinematic mode. *Drones* 4(2):9.

Tang, Z., A. Parajuli, C. J. Chen, Y. Hu, S. Revolinski, C. A. Medina, S. Lin, Z. W. Zhang, and L. X. Yu. 2021. Validation of UAV-based alfalfa biomass predictability using photogrammetry with fully automatic plot segmentation. *Scientific Reports* 11(1):3336.

Thenkabail, P. S., A. D. Ward, and J. G. Lyon. 1994. Impacts of agricultural management-practices on soybean and corn crops evident in ground-truth data and thematic mapper vegetation indexes. *Transactions of the ASAE* 37(3):989–995.

Vargas, J.J.Q., C. Y. Zhang, J. A. Smitchger, R. J. McGee, and S. Sankaran. 2019. Phenotyping of plant biomass and performance traits using remote sensing techniques in pea (*Pisum sativum*, L.). *Sensors* 19(9):2031.

Veroustraete, F. 2015. The rise of the drones in agriculture. *EC Agriculture* 2(2):325–327.

Viña, A., A. A. Gitelson, D. C. Rundquist, G. Keydan, B. Leavitt, and J. Schepers. 2004. Remote sensing—Monitoring maize (*Zea mays* L.) phenology with remote sensing. *Agronomy Journal* 96(4):1139–1147.

Wu, C. Y., Z. Niu, and S. Gao. 2012. The potential of the satellite derived green chlorophyll index for estimating midday light use efficiency in maize, coniferous forest and grassland. *Ecological Indicators* 14(1):66–73.

Zhang, C. Y., W. A. Craine, R. J. McGee, G. J. Vandemark, J. B. Davis, J. Brown, S. H. Hulbert, and S. Sankaran. 2020. Image-based phenotyping of flowering intensity in cool-season crops. *Sensors* 20(5):1450.

Zhang, Q. Y., Y. B. Cheng, A. I. Lyapustin, Y. J. Wang, X. Y. Zhang, A. Suyker, S. Verma, Y. M. Shuai, and E. M. Middleton. 2015. Estimation of crop gross primary production (GPP): II. Do scaled MODIS vegetation indices improve performance? *Agricultural and Forest Meteorology* 200:1–8.

Robust Dynamic Indoor Visible Light Positioning Method Based on CMOS Image Sensor

Senzhen Sun, Guangyun Li, Yangjun Gao, and Li Wang

Abstract

A real-time imaging recognition and positioning method based on visible light communication flat light source is proposed. This method images the visible light communication flat light source through the rolling shutter effect of the complementary metal-oxide semiconductor imaging sensor and obtains the rectangular area outline of the light source. The light and dark stripe information of image with the digital image processing method realizes light source matching recognition by defining the concept, the autocorrelation sequence, which can be used to obtain the identity of the light source, and the rectangular vertex coordinate information of flat light source achieves high-precision vision positioning on the basis of inertial measurement unit attitude sensor-assisted imaging. Simultaneously, the corresponding positioning module is developed for positioning testing. The test results indicate that the plane positioning error is less than 4.5 cm, and the positioning frequency is greater than 10 Hz, which provides a high-precision visual positioning solution for indoor positioning.

Introduction

With the development of urbanization, the demand for indoor positioning technology is increasing in areas such as large building venues, automated factories, underground spaces, and so on. The global satellite navigation system can basically meet the navigation and positioning requirements in most outdoor areas, but it cannot work indoors because of the difficulty in receiving satellite signals. Therefore, base station wireless indoor positioning technologies based on Wi-Fi, Bluetooth, ultrawide band (UWB), pseudosatellite, radio frequency, and so on came into being (Li *et al.* 2020). However, indoor structure is diverse and the electromagnetic environment is complex. Taking the UWB base station-type wireless indoor positioning solution as an example, it needs to set additional positioning base stations, dedicated receiving equipment, special data processing center, and dedicated personnel maintenance. This kind of base station wireless indoor positioning technology requires a balance between positioning accuracy and operation cost, and its versatility is poor. With the development of deep learning technology, indoor positioning methods based on multi-sensor fusion technologies such as semantic simultaneous localization and mapping (SLAM) have made great progress (Huang *et al.* 2021), but the engineering application of large-scale SLAM technology is difficult to adapt to dynamic application scenarios (Shao *et al.* 2019), and absolute position calibration is required. With the wide application of the light-emitting diode (LED) lighting system, the indoor positioning technology based on visible light communication technology shows the prospect of a broad application. For example, the visible light positioning (VLP) system based on imaging has fewer changes to the environment, takes both lighting and positioning into account, and has the advantages of high positioning accuracy, low system cost, no electromagnetic interference (Luo *et al.* 2017), and is very suitable for mobile robot position calibration.

The implementation models of indoor visible light communication positioning technologies are mainly divided into imaging methods and nonimaging methods according to the types of receivers. The nonimaging positioning method of visible light communication mainly uses the photodiode (PD) at the receiving terminal to receive and analyze the signals and intensity information of multiple light sources to achieve visible light localization; its main implementation methods include the fingerprint matching method and geometric measurement method (Yan *et al.* 2019; Amsters *et al.* 2021; Li *et al.* 2018; Almadani *et al.* 2021; Zheng *et al.* 2017). The image sensor-based visible light communication positioning method mainly includes LED-identification (LED-IDs) (Xie *et al.* 2018) and imaging measurement. LEDs transmit IDs or geographical location information mainly by using the rolling shutter mechanism of complementary metal-oxide-semiconductor (CMOS) sensors (Do and Yoo 2016; Chen *et al.* 2017; Ma *et al.* 2019; Guan *et al.* 2018). On the other hand, the imaging positioning method is based on the principle of photography to achieve positioning, which is to perform imaging measurements on the light source by recognizing and detecting the geometric key points of the light source through digital image processing technology, and by determining the spatial relationship between the camera and the light source according to the photographic geometric relationship (Guan *et al.* 2019). The image sensor-based visible light communication imaging positioning method shows high positioning accuracy and strong portability, while the PD-based visible light communication imaging positioning method shows high positioning rate, but it shows complicated systematic design and poor portability. With the wide application of CMOS imaging sensors in smart terminals, the visible light communication positioning method based on mobile phone imaging has achieved more research and application results (Zhang *et al.* 2019; Wu *et al.* 2019; Ji *et al.* 2019; Kim *et al.* 2016; Sun *et al.* 2020).

Aiming at the decoding problem of visible light communication imaging, Do and Yoo (2016) systematically analyzed the imaging communication mechanism of CMOS sensor's rolling shutter, Chen *et al.* (2017), Ma *et al.* (2019), and Guan *et al.* (2018) analyzed the communication demodulation method based on the rolling shutter of the CMOS sensor, and discussed the method of reducing the bit-free rate. In terms of light source ID recognition, Xie *et al.* (2018) converted the identification of light source ID into an image classification problem and realized the recognition of light source. As for the application research, Guan *et al.* (2019) achieved the positioning accuracy of 4.38 cm by simultaneously recognizing three LED light sources based on the light source image classification and recognition method. Zhang *et al.* (2019) proposed an LED-optical fringe code (OFC) modulation and recognition algorithm using red, green, blue (RGB)-LED as a positioning light source; meanwhile, a Convolution Neural Network was used to recognize light source images, which improved the recognition accuracy and recognition distance of light source. Wu *et al.* (2019) comprehensively considered the positioning accuracy, robustness, and

Senzhen Sun, Guangyun Li, Yangjun Gao, and Li Wang are with the School of Geospatial Information, Information Engineering University, Zhengzhou, Henan 450001, China (guangyun_li_chxy@163.com).

Yangjun Gao and Li Wang are also with the State Key Laboratory of Geo-Information Engineering, Xi'an, Shaanxi 710054, China..

Contributed by Bo Wu, October 6, 2021 (sent for review November 4, 2021; reviewed by Yaxin Li, Shengjun Tang).

Photogrammetric Engineering & Remote Sensing
Vol. 88, No. 5, May 2022, pp. 333–342.
0099-1112/22/333–342

doi: 10.14358/PERS.21-00077R3

real-time performance of the VLP system, and adopted particle filters to achieve fast tracking of light source, which improved the anti-interference ability of the image sensor-based VLP system. Ji *et al.* (2019) used a mobile phone as a positioning terminal and used a single LED light source to achieve centimeter-level positioning. Ji *et al.* (2019) then used two LED light sources and a single image sensor to evaluate the positioning accuracy at different distances. Sun *et al.* (2020) proposed a VLP system based on binocular vision, and developed a positioning module for verification, which was used for indoor robot mobile positioning.

At present, VLP positioning systems based on a CMOS sensor generally requires higher imaging quality. Usually, the circular LED light source with a diameter of less than 30 cm is used as the positioning beacon, so the imaging communication capacity of a single image is limited due to the limitation of size of the source. The high-performance CMOS imaging sensor can obtain relatively clear light and dark strip images of the visible light communication light source, which can directly perform image binarization to distinguish high and low signals for decoding. Common CMOS sensors have poor sensitivity to light, and the distinction between light and dark stripes is small due to the influence of random noise. Therefore, it is difficult to perform image binarization to distinguish high and low signals by fixed threshold or adaptive threshold for decoding. In terms of light source identification and matching, Xie *et al.* (2018) modulated a circular light source, set a certain duty cycle, and classified the light source barcode with a machine learning method according to the proportion of light and dark stripes in the image of the light source, so as to realize light source recognition. In order to take into account lighting, the capacity of duty cycle method is limited. With the upgrading of LED lighting systems, flat panel LEDs have been widely used. As shown in Figure 1, the rectangular light sources in underground parking lots and indoors are usually about 2–3 m away from each other, and about 3 m from the ground, arranged neatly, are large in size, and have significant rectangular visual characteristics, which makes it easy to meet the decoding requirements of high-performance CMOS sensors. When ordinary CMOS imaging sensors cannot be decoded directly, template matching can be performed according to the light and dark fringe signals imaged by the light source. However, this method needs to establish a template database; the larger the database capacity is, the more matches are needed, which leads to efficiency problems.

Aiming at the problem of matching efficiency and robustness, a visual VLP method based on visible light communication rectangular flat-panel LEDs is proposed, which uses ordinary CMOS sensors for visual imaging, uses signal autocorrelation analysis to extract the signal cycle of the light source, and establishes a signal feature library to achieve rapid identification and matching of the light source. What's more, to verify the applicability of this method, the visual positioning module is also demonstrated in this paper.

The rest of this paper is organized as follows. The section "System Principles and Methods" elaborates the proposed positioning system, including the LED recognition method based on signal autocorrelation sequence and the visual three-dimensional localization algorithm model assisted by inertial measurement unit (IMU). The experimental results are shown and discussed in the sections "Experiment and Results" and the "Discussion". Finally, conclusions are drawn in the final section, "Conclusions".

System Principles and Methods

Principle of Using COMS Sensor in Visible Light Communication (VLC)

The signal-modulated LED positioning light source circularly broadcasts the ID information through light and shade flashing. As shown in Figure 2a, a CMOS imaging sensor is used to image two rectangular flat light sources, one of which modulates the visible light communication ID signal to form a light and dark stripe image. The principle is shown in Figure 2b. The CMOS imaging sensor is exposed from top to bottom in sequence. After each row is exposed, the data writing operation is performed, and then the next cycle is performed after a period of time. The time of image generation for each frame is from data writing for the first row to the end of writing data for the last row. This period is

(a) (b)

Figure 1. Indoor scene using a flat light source.

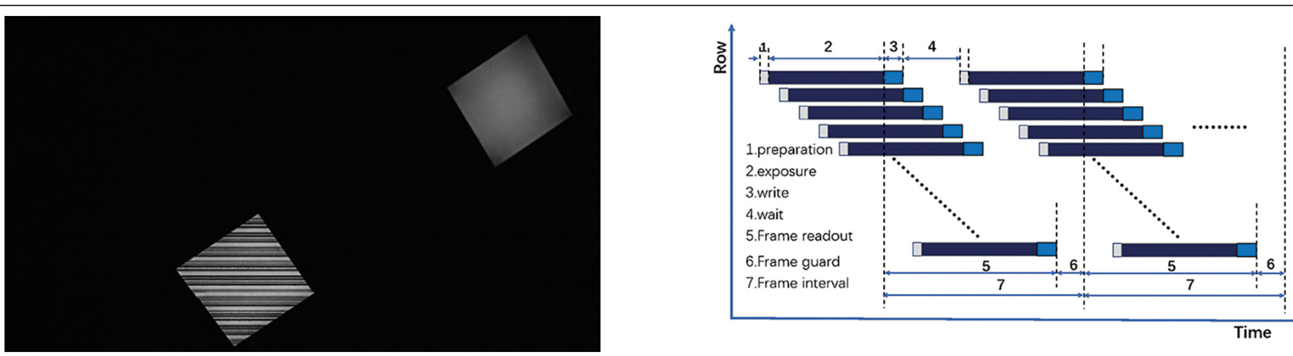

(a) (b)

Figure 2. (a) Communication light source and imaging effect. (b) Analysis of complementary metal-oxide semiconductor (CMOS) rolling shutter imaging cycle.

the frame, which is read t_f. During this period, the grayscale fringe image is obtained by perceiving the light and shade flicker of communication by the light source line by line. Most CMOS cameras have a threshold delay after reading the line-by-line image, which is called t_g, so the frame interval is the sum of the two.

When imaging the light source, the CMOS is exposed line by line, and the signal of the light source on and off is recorded to form a light and dark fringe image, as shown in Figure 3. In order to realize the imaging communication, the modulation frequency of a visible light communication (VLC) light source signal is required to adapt to the CMOS line exposure imaging time. Generally, the modulation time interval is required to be more than two times of CMOS line exposure time t_h. At the same time, considering the requirements of indoor lighting, the bytecode should be converted into Manchester code, and the starting bit mark should be added before each bytecode to facilitate decoding. A bytecode can represent a hexadecimal number, and multiple bytecodes are concatenated to form the LED light source ID.

In visible light communication, the light and dark interval of the fringe signal (VLC_IFS) is related to the sending frequency of LED_ID signal's modulation, and the frame rate and resolution of the imaging sensor. The clarity of fringe imaging is related to the camera's sensitivity value's setting and the sensitivity of the sensor (Do and Yoo 2016).

Taking the imaging of flat-panel light source as an example, the following four types of CMOS imaging sensors are used to image the same visible light communication light source, which are respectively the rear camera of the mobile phone used in Figure 4a, the front camera of the mobile phone used in Figure 4b, the ordinary universal serial bus (USB) camera used in Figure 4c, and the front camera of the laptop used in Figure 4d. As shown in Figure 4, the obtained fringe's density and definition are different to some extent, the imaging in Figure 4a and 4b is relatively clear, while the image's gray scale distinction between light and dark stripes in Figure 4c and 4d is not large. The fringe grayscale fluctuation curves of the two imaging sensors respectively used in Figure 4b and 4d are shown in Figure 5. The image of the sensor in Figure 4b is clear; the amplitude of the gray scale curve is large, which is easy to convert into high and low signals for decoding. While the image of the sensor in Figure 4d is blurred, the amplitude of the gray scale curve is small, which is difficult to decode.

Meanwhile, due to the threshold delay effect of the CMOS sensor, VLC_IFS is constantly moving and changing on the image, so it is difficult to extract the LED_ID image signal in a standard period.

Recognition Principle of Light Source Recognition

Visible light communication flat-panel light source cyclically broadcasts the ID information, which causes the light and dark stripe signals obtained by CMOS imaging to form significant periodic characteristics. The period of VLC_IFS can be obtained by calculating the period of the autocorrelation sequence of the VLC_IFS (VLC_IFS_AS).

According to the correlation of the discrete time signals, the imaging fringe sequence signal is defined as $y(n)$:

$$y(n) = x(n) + w(n) \tag{1}$$

where $x(n)$ is the theoretical value of fringe gray-value sequence of CMOS sensor imaging for communication light source, and the period value is T unknown. $w(n)$ represents the random noise of the fringe gray-value sequence due to factors such as sensor sensitivity. Assuming that the observation sequence has M samples, $M >> T$. When $n<0$ or $n \geq M$, if $0 \leq n \leq M - 1$, the autocorrelation sequence of $y(n)$ is as follows, where $1/M$ is the normalization factor.

$$r_{yy}(l) = \frac{1}{M}\sum_{n=0}^{M-1} y(n)y(n-l) \tag{2}$$

$$r_{yy}(l) = r_{xx}(l) + r_{xw}(l) + r_{wx}(l) + r_{ww}(l) \tag{3}$$

Since $x(n)$ is periodic, $r_{xx}(l)$ has the same period T as $x(n)$. When the value of l is an integer multiple of the period T such as 0, T, $2T$, the autocorrelation sequence curve will have a large peak value. In order

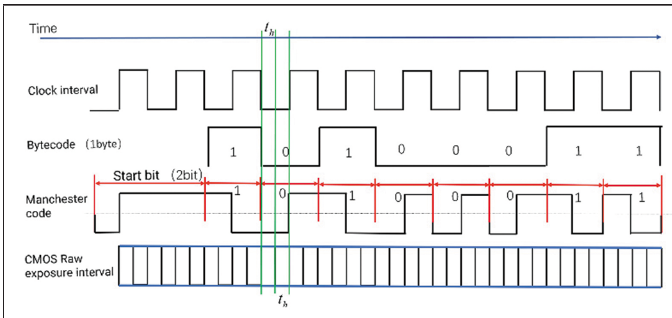

Figure 3. The modulation method of the light-emitting diode (LED) light source identification (ID).

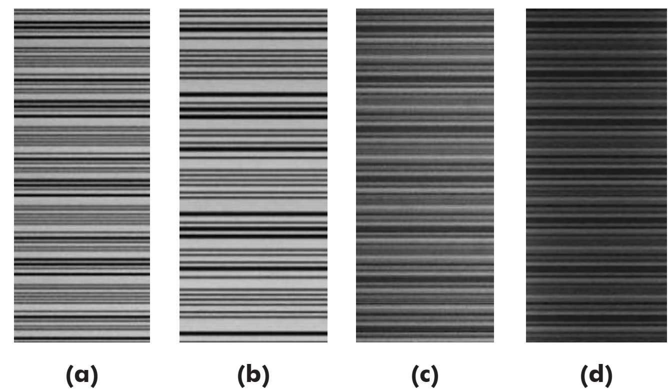

Figure 4. The imaging effect of the same light source with different complementary metal-oxide semiconductor (CMOS) imaging sensors.

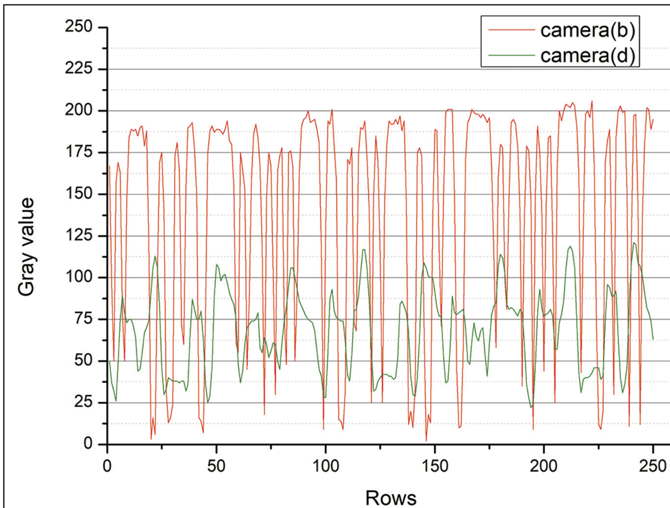

Figure 5. Grayscale fluctuation curve of image stripes.

to avoid the peak value decreasing in amplitude when l is approaching M, needs to be no greater than $M/2$. The peak value of the autocorrelation function of $w(n)$ is at $l = 0$. Due to its random characteristics, it will rapidly decay to zero. The signal $x(n)$ is completely independent of random noise $w(n)$, and its cross-correlation $r_{xw}(l)$ and $r_{wx}(l)$ can be considered relatively small. Therefore, the number of cycles T can be determined by calculating the VLC_IFS_AS. As shown in Figure 6, the autocorrelation of fringe gray signals of the four CMOS imaging sensors used in Figure 4 is calculated. The results show that the fringe signal period of the sensor used in Figure 4a is 179, the sensor used in Figure 4b is 119, the sensor used in Figure 4c is 76, and the sensor used in Figure 4d is 95, respectively. Different types of CMOS sensors image the same light source with different fringe signal periods.

Use the same model of CMOS sensor to analyze the autocorrelation sequence of the fringe signals imaged by four different communication light sources under the condition of image resolution of 1280 × 720, as shown in Figure 7, the autocorrelation period of the fringe signal of one light source is 76, and that of the rest three light sources is 90. The method of finding the period through autocorrelation can be used as a preliminary classification method to distinguish different light sources.

A light source identification and matching method based on signal autocorrelation sequence is established according to the periodic characteristics of the VLC_IFS_AS. The process is shown in Figure 8. Firstly, the stripe image is averaged row by row to generate VLC_IFS, which is called $\mathbf{V} = \{v_1, v_2, v_3, \ldots, v_i\}$, $v \in [0, 255]$. According to the sequence $\mathbf{V}$ of light and dark fringes, the signal autocorrelation calculation is carried out to obtain the signal autocorrelation sequence and its period number, which can be respectively called $\mathbf{N}$, $\mathbf{N} = \{n_1, n_2, n_3, \ldots, n_T, \ldots\}$, and T. The standardized sequence, which is called $\mathbf{X}$, $\mathbf{X} = \{x_1, x_2, x_3, \ldots, x_T\}$, $x \in [0, 1]$, is obtained by extracting the sequence value in the first period of the signal autocorrelation sequence $\mathbf{N}$ and performing normalization processing. The LED_ID matched-degree problem of two light sources is transformed into the matched-degree problem of the VLC_IFS_AS of two light sources. Define $\mathbf{D}_T$ as the matched-degree sequence of two light sources, which can be defined as follows:

$$\mathbf{D}_T = \mathbf{X1}_T - \mathbf{X2}_T \tag{4}$$

$$\mathbf{D}_T = \{d_1, d_2, d_3, \ldots, d_i\}, d \in [-1, 1] \tag{5}$$

where $\mathbf{X1}_T$ and $\mathbf{X2}_T$ respectively represent the normalized signal autocorrelation sequences of two light sources in one cycle.

Using the support vector machine (SVM) classification method, the standardized sequence $\mathbf{X}$ of light source images can obviously be used as the classification elements of light sources with the same period but different LED_IDs, and the light source LED_ID identification can be converted into a classification problem. Similarly, the light source matching degree sequence $\mathbf{D}_T$ can be used as the SVM classification element to convert the matching problem into a binary classification problem. Furthermore, the matching problem can be directly converted into a linear discriminant, and the definition of the matching degree K of two light sources is shown in Equation 6:

$$K = a \times H + b \times M + c \times S + d \times W \tag{6}$$

where a, b, c, and d are the coefficients, which are usually not less than 1. H is the different value between the maximum and minimum values of the sequence $\mathbf{D}_T$, M is the mean value of the sum of the absolute values of the sequence $\mathbf{D}_T$, S is the standard deviation of the sequence $\mathbf{D}_T$, and W is the average value of the sum of sequence values whose absolute value is greater than 0.15 in the sequence. The smaller the K value, the higher the matching degree. If the matching degree of the images of the light source with the same LED_ID is made less than that of the images of the different light sources, the determination of the parameters can be converted into a linear programming problem to solve the quaternary first order inequality equations, and the K value calculated between the matching light sources can be minimized through linear programming calculation to determine the parameter values. Obviously, the calculation elements of K can also be converted into the calculation elements of SVM regression classification to carry out light source classification and recognition.

IMU-Assisted Visual Positioning Method with Flat Panel Light Source

The corner points of the rectangular flat-panel light source are on an approximate plane. The visual imaging positioning using rectangular flat plate light source can be regarded as the Perspective-n-Point (PNP) (Lepetit *et al.* 2009) pose calculation based on four points in the plane

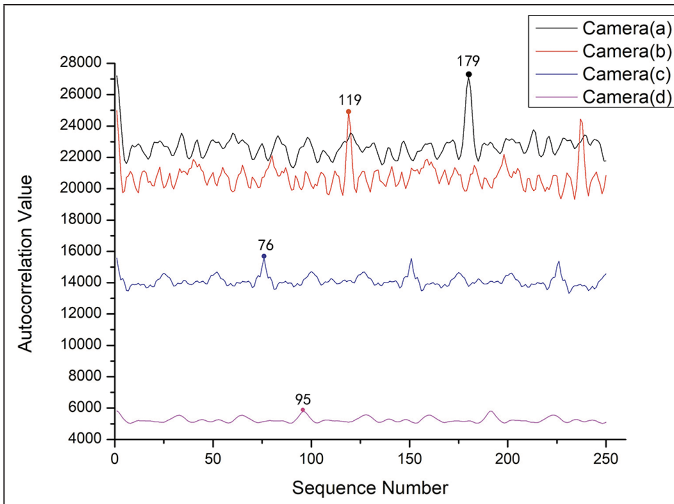

Figure 6. Autocorrelation sequence curves of the same light source with different complementary metal-oxide semiconductor (CMOS) sensors.

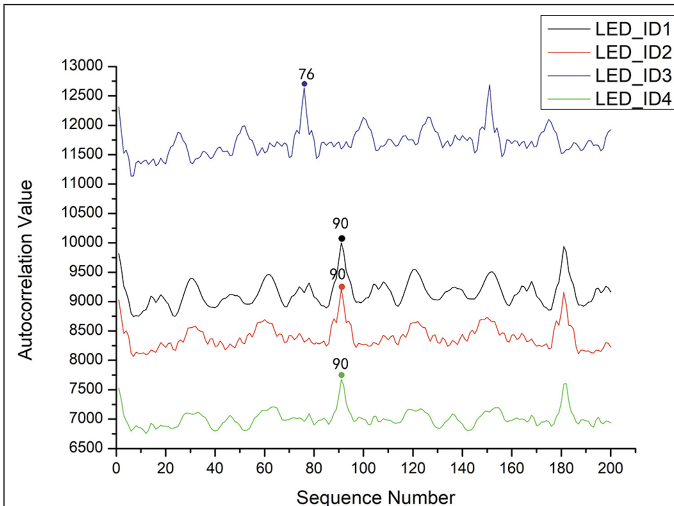

Figure 7. Autocorrelation sequence curves of different light sources with the same complementary metal-oxide semiconductor (CMOS) sensor.

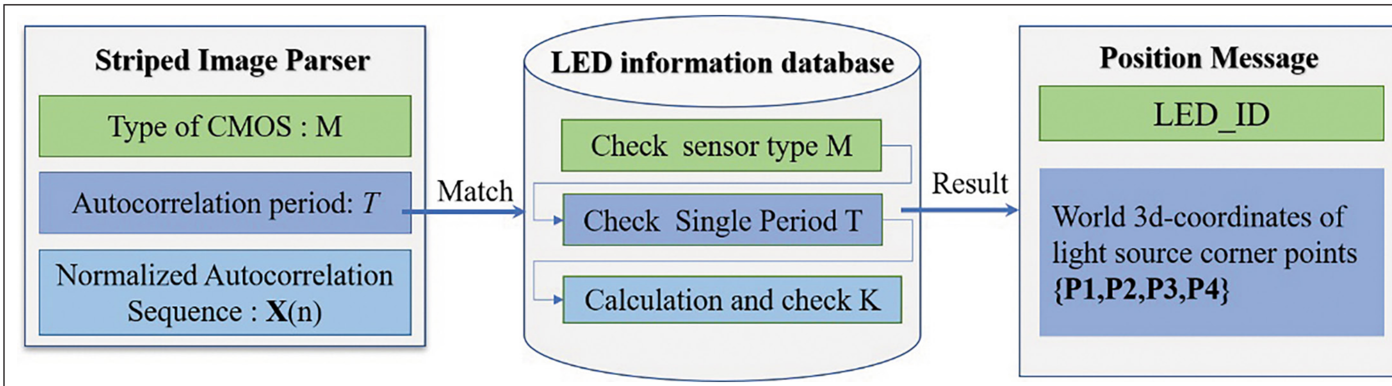

Figure 8. Light source matching process.

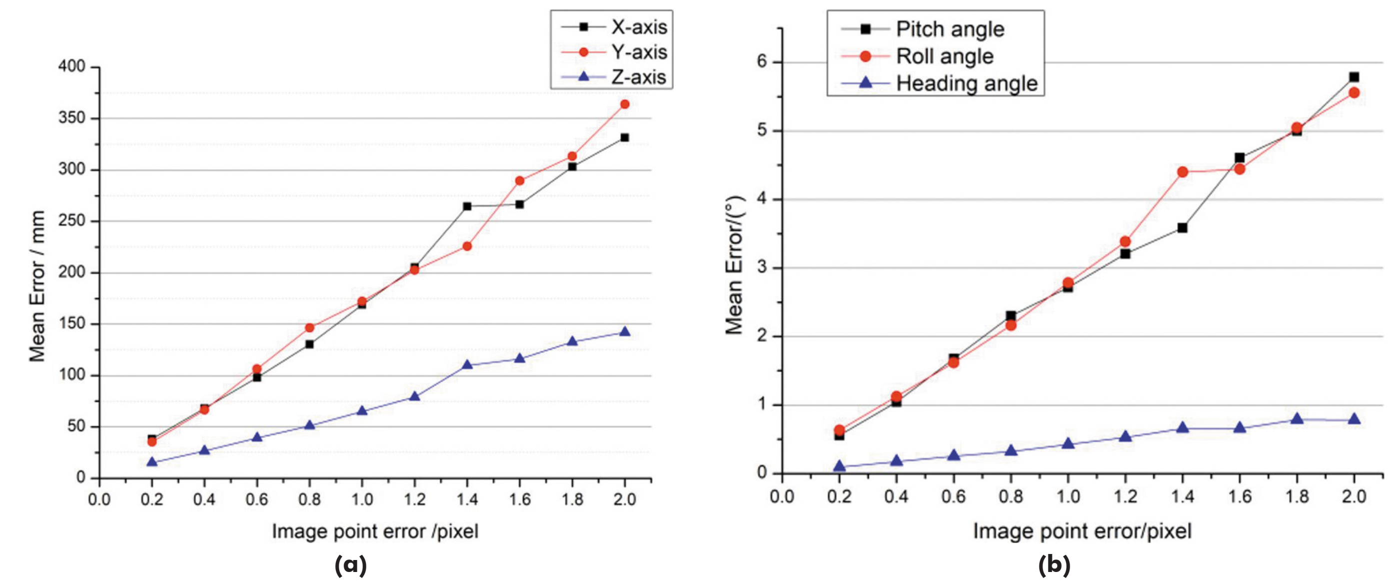

Figure 9. (a) The variation of imaging positioning error with the image point error. (b) The variation of the imaging attitude error with the image point error.

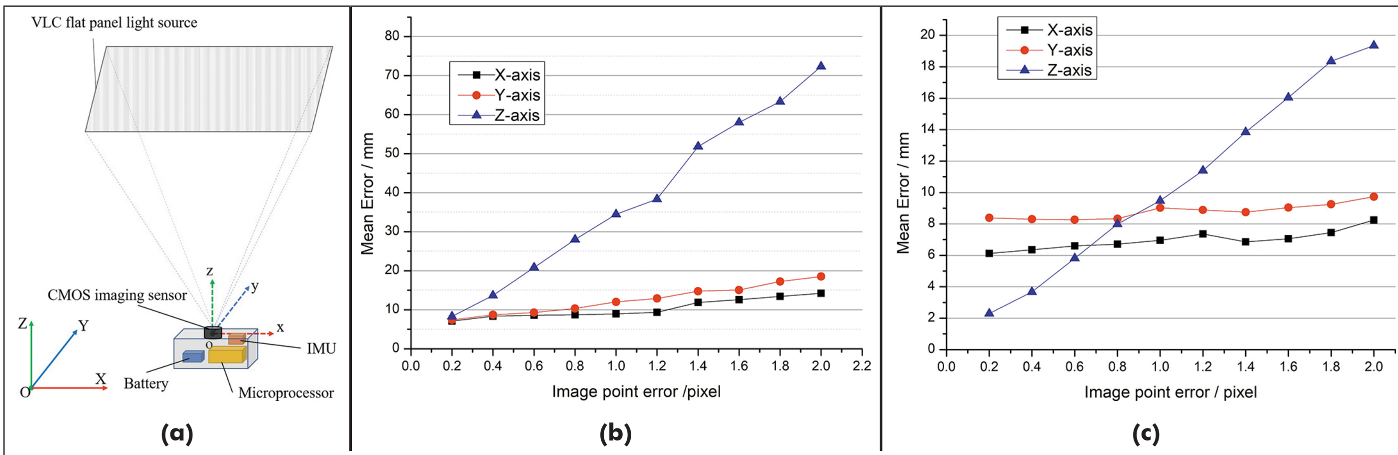

Figure 10. (a) Inertial measurement unit (IMU)-assisted visual positioning system based on visible light communication (VLC), (b) the variation of IMU-assisted positioning error with image point error, and (c) the variation of IMU-assisted iterative method positioning error with image point error.

or the issue of single image space resection. The calculation can be divided into direct method and iterative method (Sun *et al.* 2021). The direct method has high calculation efficiency, while the accuracy is poor compared with the iterative method. The calculation efficiency of the iterative method has a certain dependence on the initial value; a good initial value can reduce the number of iterations and improve the calculation efficiency. The combination of the two methods can improve the calculation accuracy and algorithm efficiency. The image point extraction error is the main source of the visual positioning error. According to the homography direct method (Sun *et al.* 2021), the Monte Carlo method is used for simulation, the focal length of the camera is set to 4.3 mm, the imaging resolution is set to 1280 × 720, the camera is located in a 2 m × 2 m plane, 3.5 m directly below the light source, and the center of the VLC light source with a size of 60 cm × 60 cm is imaged. Four theoretical image points of a rectangular VLC light source are calculated, and then random errors are attached to the four image points for simulation. Place the camera in a 2 m × 2 m plane, 3.5 m directly below the light source, and image the center of the VLC light source with a size of 60 cm × 60 cm. The simulation times are more than 1000 times, and the variation of the evaluation positioning error with the image point noise is shown in Figure 9a. With the increase of the image point error, the imaging positioning error increases linearly, and the plane error increases faster relative to the height error. The variation of the attitude angle error with the image point error is shown in Figure 9b. The growth rate of the tilt angle error is much faster than the heading angle, and the heading angle error does not exceed 1° at two pixels error levels.

In Zhang's (1999) calibration method, the homography matrix is $\mathbf{H}$, which can be expressed as follows: $\mathbf{H} = [\mathbf{h}_1\ \ \mathbf{h}_2\ \ \mathbf{h}_3]$, the $\mathbf{R}$ matrix of imaging attitude is obtained from $\mathbf{h}_1$, $\mathbf{h}_2$ in the homography matrix $\mathbf{H}$, the translation relationship between the imaging measurement coordinate system and the world coordinate system is obtained from $\mathbf{h}_3$ in the homography matrix $\mathbf{H}$, and the error of the imaging calculation attitude is transmitted to the camera position through the $\mathbf{R}$ matrix. The common IMU attitude sensors can provide a tilt angle accuracy of 0.1°, which is far better than the tilt angle accuracy of the visual calculation, but the heading angle accuracy is usually greater than 2° and is susceptible to interference. Therefore, when the IMU is used to assist the imaging positioning, the heading angle calculated by the vision and the tilt attitude angle with higher accuracy provided by the IMU are used to correct the $\mathbf{R}$ matrix, which can improve the imaging positioning accuracy (Sun *et al.* 2021).

Integrate the CMOS imaging sensor and IMU module into an imaging positioning module for an imaging positioning simulation system with VLC flat-panel light source, as shown in Figure 10a. Under the same imaging conditions, the simulation results after using a higher-precision tilt angle reorganization rotation matrix to participate in the positioning calculation are shown in Figure 10b, with the increase of the image point error, and the plane accuracy of the imaging positioning is greatly improved. The error in the height direction is also reduced, indicating that the IMU-assisted imaging tilt attitude angle can improve the positioning accuracy. Similarly, in the calculation of the iterative method, the tilt angle can be fixed, and only the positioning value and heading angle can be iterated to further improve the positioning accuracy. Under the same conditions, the iterative method positioning simulation result is shown in Figure 10c. Under the condition of two pixels errors, the mean-square-error based on the IMU-assisted imaging positioning results in the three axis directions is less than 2 cm.

The digital image processing method is used to extract the boundary of the light source's stripe region to obtain the contour points of the light source and perform identification matching to obtain the four corner points' coordinates of the rectangular flat light source corresponding to its ID information as shown in Figure 11.

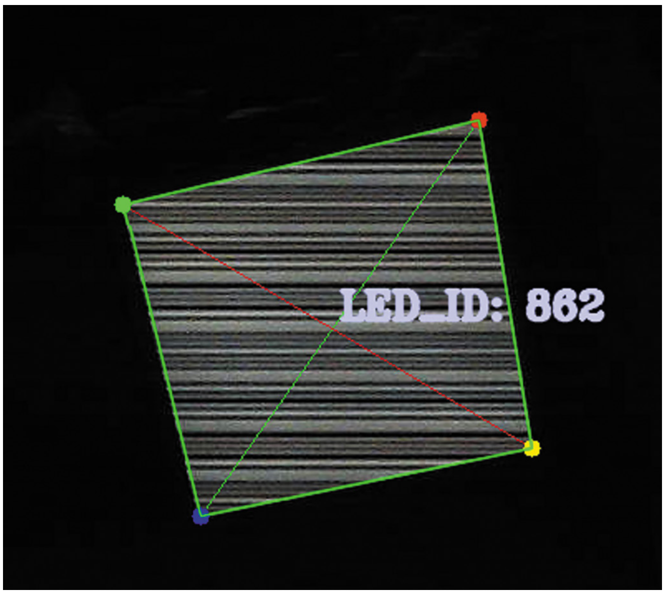

Figure 11. Visual recognition and extraction effect of rectangular communication light source.

When determining the correspondence relation between the world coordinates of the corner points and the coordinates of the image points of the rectangular light source, firstly, a corresponding relation is assumed to calculate the imaging positioning and obtain the heading angle of the module at the same time. Then, the difference between the heading angle and the geomagnetic deflection angle of the IMU sensor is calculated. If the difference is less than a certain threshold, it is the correct relation; otherwise, the assumed calculation continues. The process is as follows:

Step 1. Input the world coordinates of the corner points of the light source in a counterclockwise sequence {p1, p2, p3, p4},and the light source corner point counterclockwise sequence image coordinates {c1, c2, c3, c4};

Step 2. Assume a correspondence between the world coordinate of the four corner points of the light source and the image coordinate sequence;

Step 3. Perform visual calculation according to the assumed relationship to obtain the heading angle *H* of the positioning module. At the same time obtain the geomagnetic azimuth angle *M* of the IMU sensor;

Step 4. Calculate the deviation angle *C* between the heading angle *H* and the geomagnetic azimuth angle *M*. Determine whether *C* is more than 45 degrees. If it is, return to the second **Step 2**; otherwise, output the correspondence between the world coordinates of the light source corner points and the image coordinates; The deviation angle *C* is an empirical setting value. Usually, when the spatial coordinates of the reference point are consistent with the corresponding image point coordinates, the heading angle *H* calculated by the imaging positioning is not much different from the geomagnetic azimuth angle *M* provided by the IMU, generally not more than 10°, namely $C = |H - M| < 10$. When the local magnetic azimuth is disturbed, the value of *C* may be larger. We assume that its threshold value is 45 degrees, mainly considering that in the positioning environment, the geomagnetic azimuth based on IMU sensor is prone to interference from magnetic field. When the threshold value exceeds 45 degrees, strong magnetic field interference will be received, resulting in inaccurate geomagnetic azimuth and errors in system judgment. Therefore, the threshold of the deviation angle *C* cannot exceed 45 degrees.

There are four kinds of sequence correspondences for the four corner points, so the corresponding relationship can be determined after four calculations at most. Finally, according to the correct correspondence, the IMU-assisted iterative method is used for imaging positioning calculation.

Experiment and Results

Introduction of Imaging Positioning Module

According to the visual method of IMU-assisted imaging measurement, a positioning module is made for algorithm verification. As shown in Figure 12, it has a binocular vision measurement function. The specific parameters are shown in Table 1. The module is used to achieve visual localization based on a single VLC circular light source (Sun *et al.* 2020). In this experiment, one of the cameras is used for the monocular positioning test. The camera coordinate system and IMU coordinate system are calibrated before the test.

Figure 12. Visual imaging test positioning module.

Table 1. Positioning module parameters.

Parameters	Value
Camera focal length/mm	4.3
Maximum resolution	1920 × 1080
Binocular baseline/mm	170
IMU tilt angle accuracy/degree	0.05–0.1
IMU heading angle accuracy/degree	1–4
CPU	ARM A53@ 1.4 GHz 64
Overall dimensions/mm	210 × 72 × 38

IMU = inertial measurement unit; CPU = central processing unit

Recognition Rate and Imaging Distance Relationship

The light source recognition rate of the light source visual matching method based on signal autocorrelation is related to many factors, such as the signal modulation period of the light source, the type of CMOS imaging sensor, the imaging distance, the angular resolution, and so on. After determining the signal modulation frequency and the period of the light source, as well as the CMOS sensor's type, the recognition rate of the light source based on signal autocorrelation is mainly related to the imaging resolution, the imaging distance, the imaging angle, and the image noise. A rectangular flat-panel LED lamp with a size of 548 mm × 548 mm is used as the VLC light source, and the signal is modulated based on LED_ID technology. The modulation frequency is 16 kHz, and Manchester code is used to form three hexadecimal numbers, with a total ID capacity of 4096. The positioning module adopts an imaging resolution of 1280 × 720. The recognition rate of the light source at different imaging distances is shown in Figure 13. When the imaging distance is less than 3.9 m, the recognition rate is above 95%. When the imaging distance exceeds 4.2 m, the recognition rate drops rapidly.

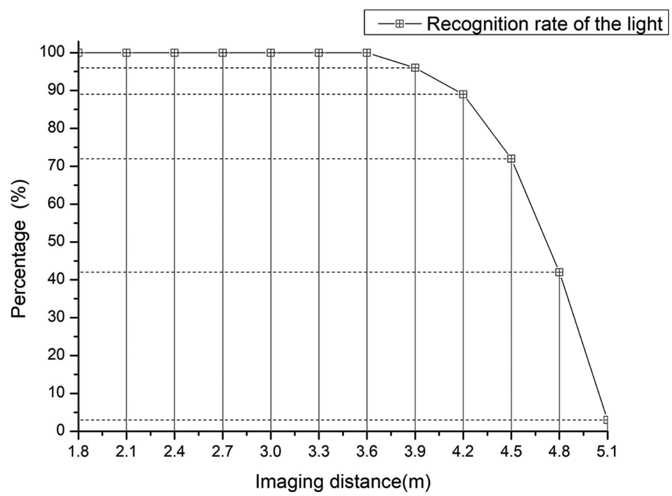

Figure 13. The relationship between the recognition rate of the light source and the imaging distance.

When the parameters of the CMOS imaging sensor are fixed, the number of imaging fringes for the communication light source is mainly related to the distance between the imaging sensor and the light source and the imaging angle. The imaging distance affects the number of imaging fringes and the fringe gray levels' degree of discrimination, but does not affect the calculation of the fringe signal's period. When the imaging angle changes, the image of the light source is shaped like an affine quadrilateral, and the number of lines in the imaging area of the light source will also change accordingly; it will decrease or increase, which affects the recognition rate. When the number of image lines extracted from the light source area is less than the number of imaging cycles (T) of the light source signal, it cannot be recognized. Therefore, the use of a large-sized flat-panel light source can meet the requirements of longer-distance visible light communication imaging and positioning.

Multi-Light Source Recognition and Positioning Test

The visual imaging positioning module is used to collect the imaging data of five rectangular flat LED light sources with the same communication frequency but different LED_IDs. The acquisition method is as follows: within the range of 3.5 m from each light source, 14 images of light sources are collected at different imaging angles and distances, and a total of 70 samples are collected. After extracting the fringe grayscale sequence images of each sample image, noise expanded image samples are added randomly to the grayscale sequence image values, the number of samples is less than 10, and then 4610 training sets and 5160 test sets are generated according to the number of autocorrelation cycles of the fringe image sequences. Three schemes are used to perform SVM classification test by selecting the optimal parameters (Wu and Wang 2009). As shown in Table 2, Scheme 1 directly intercepts the light source fringe's gray value sequence **V** within one period as the classification element. Scheme 2 uses the autocorrelation sequence and the standardized sequence **N** and the standardized sequence **X** of the fringe image in one period as the classification elements. According to Equation 4, the sequence **D** obtained by the difference between the autocorrelation sequences of two images in one period is used as the classification element, and the matching problem is transformed into a dichotomy problem.

Table 2. Support vector machine (SVM) classification accuracy rate of the three schemes under different conditions.

Scheme	Autocorrelation	Normalized	Kernel	Accuracy (%)
1	No	No	RBF	20.16
		Yes		85.32
2	Yes	No	Linear	98.64
		Yes		100
3	Yes	No	RBF	88.26
		Yes		99.18

RBF kernel = radial basis function kernel.

From the analysis of the SVM classification accuracy of the three schemes under different conditions in Table 2, extracting the autocorrelation sequence of the light source fringe image and normalizing it can ensure the accuracy of the classification. Scheme 1 directly uses the grayscale sequence of fringe image, which is not accurate. The SVM classification in Scheme 2 uses a linear kernel function, and the accuracy after normalization reaches 100%, indicating that the light source image is linearly separable after signal autocorrelation. In Scheme 3, the autocorrelation sequence of the image signals of two light sources is differentiated, and the multi-classification problem is transformed into a binary classification problem. The trained discriminant model can be extended to the matching discrimination of other light sources, and the accuracy is still above 98% in the discrimination of other light sources.

Further, according to the matching degree of the two light source images defined in Equation 6, the matching test is carried out. Ten images of each light source were selected from the collected image sets of the five light sources, and the standardized autocorrelation sequence X_i of each image was calculated respectively. Then, the average value sequence X is taken as the matching template of the light source, and five matching template libraries are established. If the coefficients of Equation 6 are all 1, the matching degree is calculated in the data set, and the values of each the component are shown in Figure 14. The first 50 data points are the matching values between 10 images of each light source and its own template, while the last 200 data points are the matching values between images of each light source and non–self-template. As can be seen from the fluctuation of K value, the maximum value of the first 50 data points is 0.53, and the minimum value of the last 200 data points is 0.59, indicating that K value can be used as the threshold value of light source matching. The coefficient of the K value's calculation formula can be adjusted by linear programming method to improve the discrimination of matching threshold. Taking the minimum K value as the matching basis, the recognition effect of multiple light sources within the imaging range is shown in Figure 15, which realizes the identification of multiple light source IDs and the extraction of rectangular contour points in the same image.

The positioning test is carried out in a laboratory environment of 11 × 8 × 3.5 m. As shown in Figure 16, there are nine flat-panel LED light sources in total in the room, and five of them are modified as VLC positioning light sources by using visible light communication technology, and the spatial coordinates of each positioning light source's four corner points is measured to establish a world coordinate system.

Using the IMU-assisted rectangular light source imaging positioning method mentioned in the section "IMU-Assisted Visual Positioning Method with Flat Panel Light Source" for the positioning test, which is divided into a static test and a mobile positioning test.When the imaging resolution of the imaging positioning module is set to 1280 × 720 and the vertical height from the light source is 3.4 m, static positioning was carried out at 21 positions in the area covered by the light source, and the positioning error of each point was shown in Figure 17. The plane positioning error of the module is less than 17 mm, and the height error is less than 30 mm.

Place the positioning module horizontally on the trolley and perform the IMU-assisted iterative mobile positioning test by controlling the trolley to move along the direction of the light source layout. When the height of the module is 3.12 m from the light source and the imaging resolution is 1280 × 720, the plane positioning trajectory is shown in Figure 18, during the positioning process, the light source is identified accurately and the transition between different light sources is smooth.

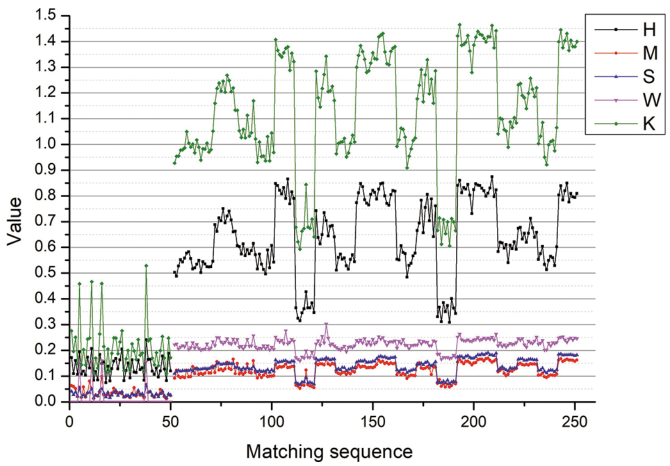

Figure 14. Matching degree and distribution of each component.

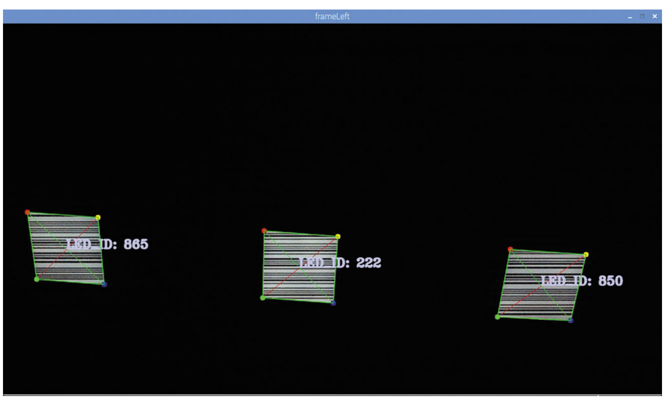

Figure 15. The recognition and matching effect of multiple light sources.

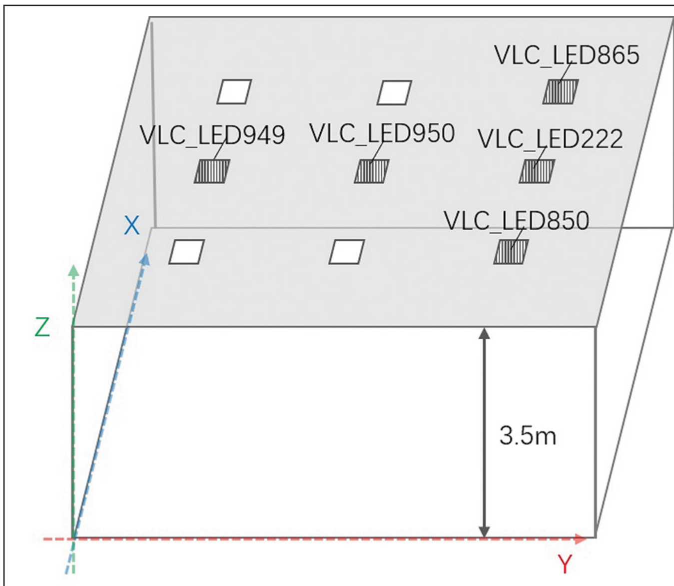

Figure 16. The layout of the communication light source in the test scenario.

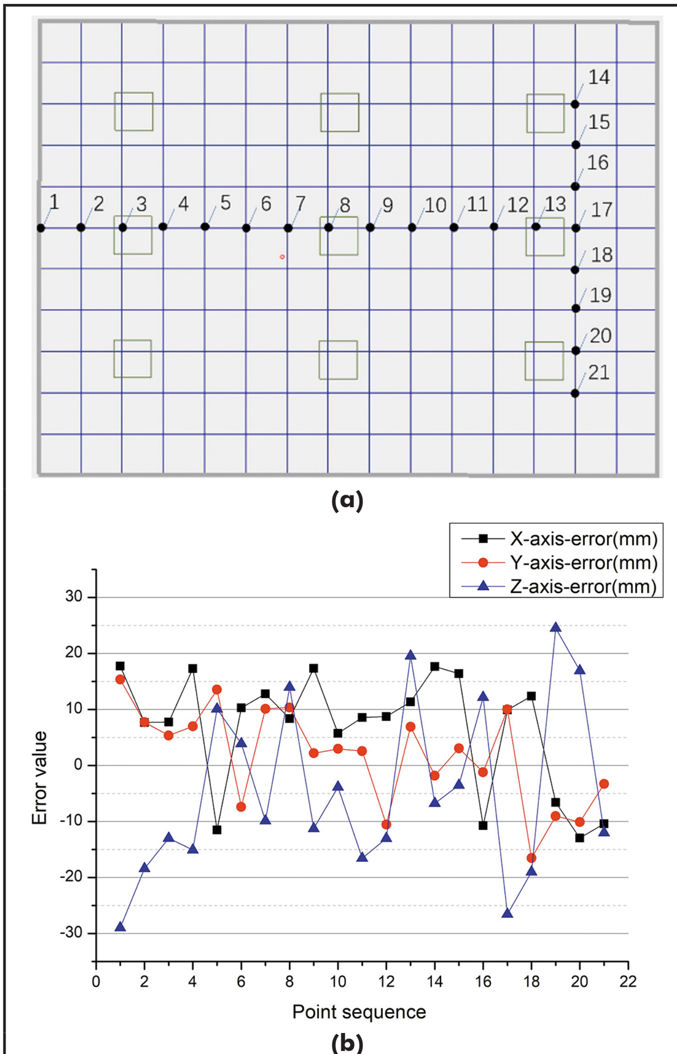

Figure 17. (a) Static positioning test's points distribution, and (b) analysis of positioning accuracy of static positioning test's points.

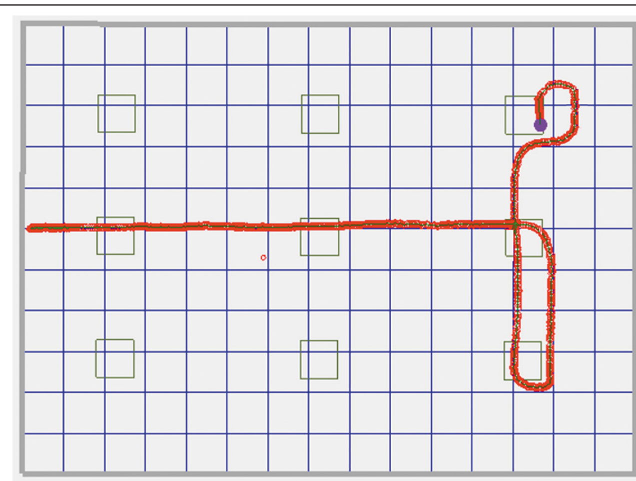
Figure 18. Moving and positioning plane trajectory among multiple light sources.

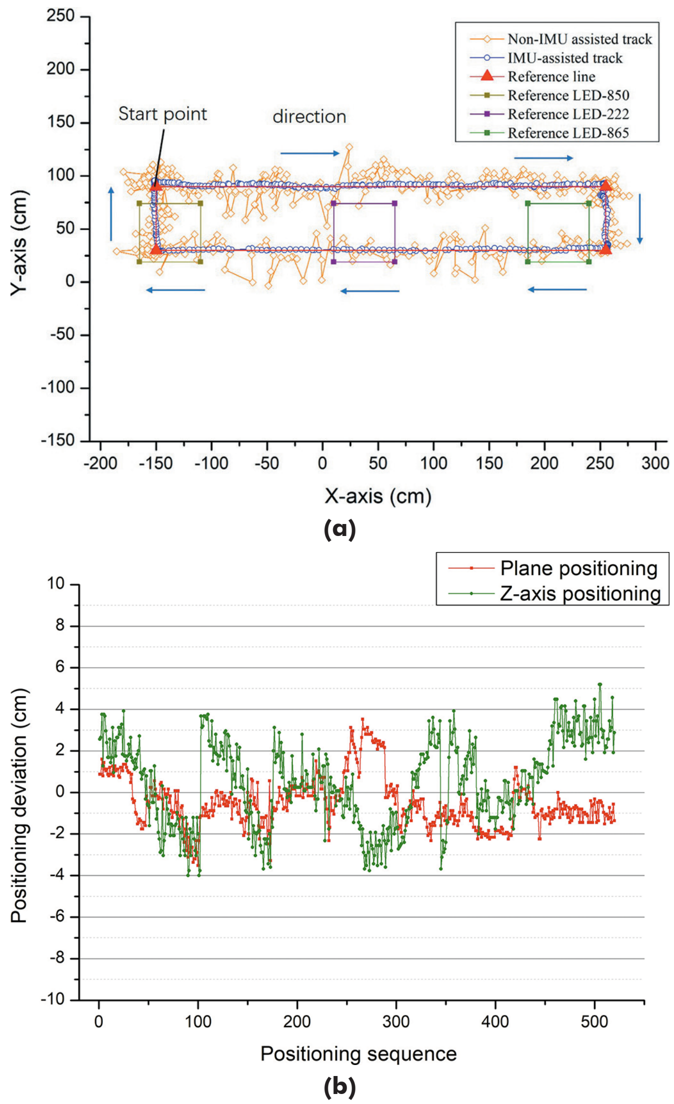

Figure 19. (a) Rectangular mobile positioning test, and (b) analysis of inertial measurement unit (IMU)-assisted mobile positioning deviation.

Operate the trolley to make it move along the fixed rectangular line. The rectangular reference point and the positioning trajectory are shown in Figure 19a, and the lines of the trajectory and the reference point are basically coincidental. Take the vertical distance between the plane positioning track point and the reference line as the plane positioning deviation, and take the difference between the positioning result along the Z-axis direction and the imaging distance as the height positioning deviation to analyze the mobile positioning accuracy. The result is shown in Figure 19b; the plane positioning deviation is less than 4.5 cm, and the height deviation is less than 6 cm. As for the fluctuation of positioning error in the Figure 19b, the initial analysis believes that it is caused by the larger mobile positioning error relative to the static positioning error, which may be caused by the fact that the corner extraction error of the light source in the moving state is relatively higher than that of the static positioning. When multiple light sources appear in the scene, the positioning accuracy is high, and the Z-axis positioning error changes dramatically due to light source switching in the visual image. These details are worth further analysis.

Discussion

The test results show that when the image resolution of 1280 × 720 and the distance of 3.5 m from the flat plate light source are adopted, the fast recognition and matching of multiple flat plate light sources with the size of 0.548 m × 0.548 m can be realized simultaneously. With the assistance of the IMU attitude sensor, the planar mobile positioning accuracy is better than 4.5 cm, and it can provide a directional reference of better than 1°, and the positioning frequency of the positioning module is greater than 10 Hz. With the upgrading of indoor lighting system, the method based on the fusion of visible light communication and visual imaging positioning provides a high-precision mobile positioning solution for indoor positioning, which can meet the application requirements of centimeter-level mobile positioning and navigation for indoor robot.

The positioning method proposed in this paper can only be effective in the area covered by a VLC rectangular light source, and the reasonable layout of light source needs to be considered to achieve indoor continuous positioning. When there is not a complete light source image in the field of vision, positioning cannot be performed, which is a limiting factor for the promotion and application of all VLC imaging positioning. In order to overcome the influence of blind areas, the use of a fisheye lens for imaging and positioning is one of the research directions to explore to overcome this problem.

Conclusion

A visual matching recognition and positioning method for visible light communication based on rectangular flat-panel LED light source is proposed. According to the CMOS shutter effect, the light and dark stripe images in the flat light source area are extracted by a digital image processing method and the signal period was obtained by calculating the signal autocorrelation sequence of the stripe images. Then, the normalized processing of the autocorrelation sequence signal in one period is carried out to transform the light source identification and matching problem into a SVM classification problem, and to establish the matching degree K's calculation method of light source image, realizing the fast recognition and matching of light source ID information. Based on the realization of light source visual recognition, an IMU sensor-assisted imaging positioning method is proposed, and a positioning module is made for testing. The positioning test results show that the visible light communication visual positioning system based on the rectangular flat panel light source meets the need for centimeter-level positioning accuracy and provides a robust solution for indoor robot navigation.

Acknowledgments

We thank the reviewers for the suggested comments. S.S. and G.L. carried out the theoretical analysis. S.S., G.L., and Y.G. designed experiments and developed the testing tools. S.S., Y.G., L.W. made the experimental tests and analyzed the data. S.S., G.L., and Y.G. wrote the manuscript. This research was funded by State Key Laboratory of Geo-Information Engineering, NO. SKLGIE2020-Z-2-1, the National Nature Science Foundation of China (No.41501491), and the National Key R&D Program of China (No.2017YFF0206001).

References

Almadani, Y., M. Ijaz, B. Adebisi, S. Rajbhandari, S. Bastiaens, W. Joseph and D. Plets. 2021. An experimental evaluation of a 3D visible light positioning system in an industrial environment with receiver tilt and multipath reflections. *Optics Communications* 483:126654.

Amsters, R., E. Demeester, N. Stevens and P. Slaets. 2021. Calibration of visible light positioning systems with a mobile robot. *Sensors* 21(7).

Chen, C. W., C. Chi-Wai, L. Yang and Y. Chien-Hung. 2017. Efficient demodulation scheme for rolling-shutter-patterning of CMOS image sensor based visible light communications. *Optics Express* 25(20), 24362.

Do, T. H. and M. Yoo. 2016. Performance analysis of visible light communication using CMOS sensors. *The Journal of Korean Institute of Communications and Information Sciences* 40(3):309.

Gong, H., T. Jiang, G. Jiang and M. Chen. 2011. A globally convergent algorithm of space resection based on quaternion. *Acta Geodaetica et Cartographica Sinica* 40(5):639–645.

Guan, W., S. Wen, L. Liu and H. Zhang. 2019. High-precision indoor positioning algorithm based on visible light communication using complementary metal–oxide–semiconductor image sensor. *Optical Engineering* 58(2):1.

Guan, W., Y. Wu, C. Xie, L. Fang, X. Liu and Y. Chen. 2018. Performance analysis and enhancement for visible light communication using CMOS sensors. *Optics Communications* 410:531–545.

Huang, Z., H. Zhou, Y. Li, B. Yang, Y. Xu, X. Zhou, H. Bao, G. Zhang and H. Li. 2021. VS-Net: Voting with segmentation for visual localization. In *Proceedings IEEE Conference on Computer Vision and Pattern Recognition (CVPR)*, held online, 19–25 June 2021.

Ji, Y. Q., C. X. Xiao, J. Gao, J. M. Ni, H. Cheng, P. C. Zhang and G. Sun. 2019. A single LED lamp positioning system based on CMOS camera and visible light communication. *Optics Communications*. https://doi.org/10.1016/j.optcom.2019.03.002.

Kim, J. Y., S. H. Yang, Y. H. Son and S. K. Han. 2016. High-resolution indoor positioning using light emitting diode visible light and camera image sensor. *IET Optoelectronics* 10(5):184–192.

Lepetit, V., F. Moreno-Noguer and P. Fua. 2009. EPNP: An accurate o(n) solution to the pnp problem. *International Journal of Computer Vision* 81(2):155–166.

Li, N., Y. Qiao, T. Zhang and Y. Lu. 2018. Dead-zone-free three-dimensional indoor positioning method based on visible light communication with dimensionality reduction algorithm. *Optical Engineering* 57(3):036114.1–036114.8.

Li, S., L. Fan, W. Chengrui and H. Yanzhao. 2020. UWB positioning enhancement using Markov chain in indoor NLOS environment. *The Journal of China Universities of Posts and Telecommunications* 27(4):54–58.

Luo, J., L. Fan and H. Li. 2017. Indoor positioning systems based on visible light communication: State of the art. *IEEE Communications Surveys & Tutorials* 19(4):2871–2893.

Ma, Y. W., J. L. Chen and Z. Z. Chen. 2019. A high accuracy and efficiency indoor positioning system with visible light communication. *Transactions on Emerging Telecommunications Technologies* e3452.

Shao, W., S. Vijayarangan, L. Cong and G. Kantor. 2019. Stereo Visual Inertial LiDAR Simultaneous Localization and Mapping. https://doi.org/10.1109/IROS40897.2019.8968012.

Sun, S. Z., G. Y. Li, L. Wang and Q. Feng. 2021. High-precision visual indoor positioning method with the rectangular light source based on visible light communication. *Journal of Geomatics Science and Technology* 38(3):8.

Sun, S .Z., G. Y. Li, Q. Q. Feng, L. Wang. 2020. Indoor positioning based on visible light communication and binocular vision. *Optics and Precision Engineering* 28(04):834–843.

Wu, K. P. and S. D. Wang. 2009. Choosing the kernel parameters for support vector machines by the inter-cluster distance in the feature space. *Pattern Recognition* 42(5):710–717.

Wu, Y., W. Guan, X. Zhang, M. Huang and J. Cao. 2019. Visible light positioning system based on CMOS image sensor using particle filter tracking and detecting algorithm. *Optics Communications* 444:9–20.

Xie, C., W. Guan, Y. Wu, L. Fang and Y. Cai. 2018. The LED-ID detection and recognition method based on visible light positioning using proximity method. *IEEE Photonics Journal* 10(2):1–16.

Yan, J., B. Zhu, L. Chen, J. Wang and J. Liu. 2019. Error analysis on indoor localization with visible light communication. *Remote Sensing* 11(4):427.

Zhang, H., Y. Li, W. Guan, J. Li, J. H. Zheng and X. Zhang. 2019. The optical fringe code modulation and recognition algorithm based on visible light communication using convolutional neural network. *Signal Processing Image Communication* 75, 128–140.

Zhang, Z. 1999. Flexible camera calibration by viewing a plane from unknown orientations. In *Proceedings Seventh IEEE International Conference on Computer Vision*, held in Kerkyra, Greece. https://doi.org/10.1109/ICCV.1999.791289.

Zheng, Z., L. Liu and W. Hu. 2017. Accuracy of ranging based on DMT visible light communication for indoor positioning. *IEEE Photonics Technology Letters* 29(8):679–682.

Comparing the Sensitivity of Pixel-Based and Sub-Watershed-Based Analytic Hierarchy Process to Weighting Criteria for Flood Hazard Estimation

Hongping Zhang, Zhenfeng Shao, Wenfu Wu, Xiao Huang, Jisong Sun, Jinqi Zhao, and Yewen Fan

Abstract

In flood hazard estimation via the analytic hierarchy process (AHP), using the pixel as the basic unit might lead to accuracy relying on the optimal weighting criteria. To this end, considering the sub-watershed as the basic unit is new. In this study, taking the Chaohu Basin in Anhui Province, China, as a study case, the accuracy of the sensitivity of the pixel-based and sub-watershed-based AHP models influenced by weighting criteria was compared. There were 48 judgment matrixes defined, following the same order of importance of the involved indicators. Validation ground truthing is constructed by the extracted flooded regions from GF-3 images. As weighting criteria changed, the results indicated that the pixel-based AHP fluctuated significantly, while the correct ratio and fit ratio derived by the sub-watershed-based AHP could improve by >35% and >5%, respectively, over the pixel-based-AHP. It indicated that the sub-watershed-based AHP has an advantage in relying less on in situ weighting criteria than the pixel-based AHP.

Introduction

Floods are worldwide natural events that commonly occur in river networks in interwoven areas, driven by extreme or continuous rainfall. These low-lying areas have a high risk of flood and waterlogging. Meanwhile, the abundant water resources bring convenience to agricultural irrigation and commercial transportation. Most of the interwoven river areas have long histories of human inhabitants. Therefore, to improve the accuracy of flood hazard estimation in river networks, interwoven areas can support better flood risk management practices.

The analytic hierarchy process (AHP) is a popular multi-criteria decision method used in flood hazard estimation. The AHP method relies on expert knowledge to determine involving indices and corresponding criteria (Liu *et al.* 2021). In AHP, the judgment matrix definition determines the final weighting (Saaty 2014), and the weighting might lead to impact flood hazard estimation results (Ohnishi and Imai 1998; Ohnishi *et al.* 2011). As in landslide detecting, Adnan *et al.* (2020) addressed that the uncertainties in the results derived by various models would create challenges in landslide management.

Efforts are still needed to reduce the impact of criteria weight sensitivity on flood hazard estimation results. For example, Koc *et al.* (2021) used a fuzzy AHP method to identify the weight of used criteria. Rahman *et al.* (2021) used the hydrodynamic model coupled with a machine learning algorithm to create a flood hazard map. Costache *et al.* (2020) focused on a combination of AHP, certainty factor, and weights of evidence on the one hand and gradient boosting trees and multi-layer perceptron on the other to evaluate flood potential areas. Ali *et al.* (2020) developed a framework for identifying flood-prone areas using geographic information systems (GIS), a multi-criteria decision making approach, bivariate statistics, and machine learning.

With spatial information techniques, flood hazard estimation can produce involved indicators by GIS and remote sensing images and using the pixel as the basic unit to prepare flood hazard estimation–related indices. The sub-watershed is a boundary reflecting pixels flowing out from the same outlets, and the sub-watershed is always considered as a basic unit to simulate rainfall-runoff processes (Abdulkareem *et al.* 2018; Shao *et al.* 2019; Wang *et al.* 2020; Zhang *et al.* 2020). Therefore, using the sub-watershed as the basic unit in AHP-based flood hazard estimation may capture the terrain features or hydrological characteristics introduced by neighborhood cells at the sub-watershed scale (Zhang *et al.* 2020; Betancourt *et al.* 2021). The sub-watershed has been widely used as the basic unit in hydrology process simulation by hydrology or numerical models, but it is new use it as a basic unit in flood hazard estimation (sub-watershed-based AHP). As a sub-watershed is a group of pixels, taking the sub-watershed as the basic unit to estimate flood hazard may reduce the uncertainty caused by weighting changes compared to using individual pixels as the basic unit. Therefore, this study aims to compare the sensitivity caused by weighting criteria definition between pixel-based AHP and sub-watershed-based AHP.

However, flood hazard map derived by AHP may choose different kinds of indices and thus might lead to individual weighting in different research. In some works (Bathrellos *et al.* 2017; Ghosh and Kar 2018; Kanani-Sadat *et al.* 2019; Shariat *et al.* 2019; Mishra and Sinha 2020; Nachappa *et al.* 2020; Nguyen *et al.* 2020; Ekmekcioglu *et al.* 2021; Pham *et al.* 2021), flood hazard estimation indices consisted of direct flood-caused factors (i.e., rainfall), runoff converging factors (i.e., slope, elevation, and water systems), and surface runoff production characters (i.e., land use type and impervious surfaces). Meanwhile, similar indices,

Hongping Zhang is with the State Key Laboratory of Information Engineering in Surveying, Mapping and Remote Sensing, Wuhan University, Wuhan 430079, China; and State Key Laboratory of Severe Weather, Chinese Academy of Meteorological Sciences, Beijing 100081, China.

Zhenfeng Shao is with the State Key Laboratory of Information Engineering in Surveying, Mapping and Remote Sensing, Wuhan University, Wuhan 430079, China.

Wenfu Wu is with the State Key Laboratory of Information Engineering in Surveying, Mapping and Remote Sensing, Wuhan University, Wuhan 430079, China.

Xiao Huang is with the Department of Geosciences, University of Arkansas, Fayetteville, AR 72701.

Jisong Sun is with the State Key Laboratory of Severe Weather, Chinese Academy of Meteorological Sciences, Beijing 100081, China.

Jinqi Zhao is with the School of Environment Science and Spatial Informatics, China University of Mining and Technology, Xuzhou 221116, China.

Yewen Fan is with the State Key Laboratory of Information Engineering in Surveying, Mapping and Remote Sensing, Wuhan University, Wuhan 430079, China.

Contributed by Desheng Liu, October 20, 2021 (sent for review November 29, 2021; reviewed by Ashraf Dewan, Neema Nicodemus Lyimo).

Photogrammetric Engineering & Remote Sensing
Vol. 88, No. 5, May 2022, pp. 343–352.
0099-1112/22/343–352

doi: 10.14358/PERS.21-00087R2

such as distance from streams, flow accumulation, and density of rivers, can represent runoff converging factors. Even using the same indices, researchers usually construct weighting criteria according to in situ expert knowledge. Exploring a cluster of candidate weighting criteria may be the conversion implement to reduce the dependency on pursuing optimized criteria in AHP-based flood hazard estimation. The sub-watershed division methods can be grouped as single flow direction and multiple flow direction algorithms, and different sub-watershed division results represent different group patterns of pixels. Therefore, the flood hazard estimation sensitivity analysis caused by weighting criteria also needs to further detail the differences caused by different watershed division methods.

This study compared the sensitivity of flood risk estimation to disparity weighting criteria between the pixel-based AHP and the sub-watershed-based AHP models, including MFD-RC, MFD-All, D8-RC, and D8-All, detailed in Section 3. The flood event that occurred in July 2020 in the Chaohu Basin, Anhui Province, China, was taken as a study case. Ground-truthing validation compares the sensitivity among the five used models constructed by flood areas extracted from remote sensing images. The structure of this article is as follows. The next section introduces the study area and the primary data sources. The methodology is described next. The results and discussions are presented, and then conclusions and limitations are presented.

Study Area and Materials

This section describes the study area and the main materials used in this research.

Study Area

Chao Lake in Anhui Province is the fifth-largest freshwater lake in China. More than 30 rivers converge into Chao Lake. Following the hydrology network of level 3 in the 2008 version, the surrounding rivers, including the Hangfu, the Fengle, the Zhao, the Xi, the Nanfei, and the Pai, make up the central water system of the Chaohu Basin. The geographical location, the hydrology network, and the digital elevation model (DEM) distribution of the study area are shown in Figure 1a.

As shown in Figure 1a, the terrain of the Chaohu Basin surrounding Chaohu is higher in the west-south and north-east than other areas. Lying downstream of the Yangtze River, the Chaohu Basin suffers a high probability of floods during the rain-rich seasons from June to August every year. According to a Hefei Municipal Hydrology and Water Resources Bureau report, the water level of Chao Lake reached 13.43 m at 10:48 on July 22, 2020, breaking the record of 12.80 m in 1991 (Anhui Net 2020). This situation brought significant threats to the cities of Chaohu and Hefei. Improving the flood risk estimation accuracy of the Chaohu Basin is important in mitigating flood-related losses. In this study, the district surrounding Chaohu in the range of the Chaohu Basin was taken as the study area, as shown in Figure 1b.

Materials

Table 1 presents the primary data sources and their descriptions. The GIS vectors were used to obtain hydrological information. The DEM was used to divide watersheds and calculate slopes. The impervious surface products contain impervious surface, water, and porous surface, which can extract land cover and hydrological infiltration information. All the pre-processing steps, including transforming, projecting, mosaicking, and clipping, were implemented in ArcGIS 10.3. Synthetic aperture radar images serve as the primary material to construct the ground truthing of high flood hazard areas.

The level 2 image of the 10-m resolution GF-3 Fine Stripmap II (FSII) model was used to extract floodwater. The threshold method for the backscatter coefficient image of GF-3 was adopted to derive water

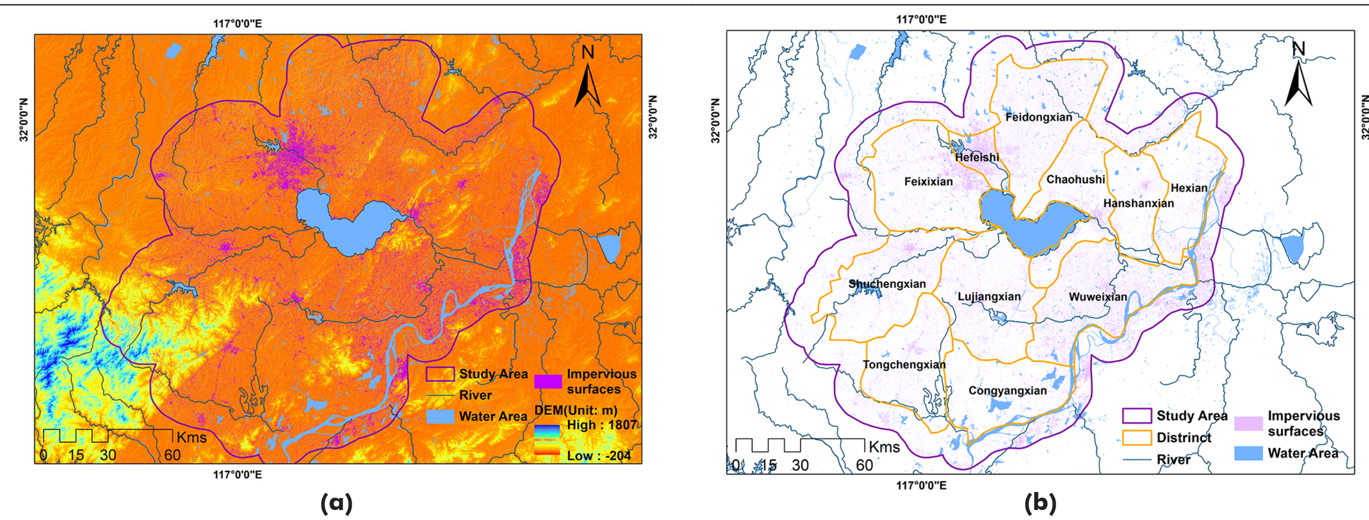

Figure 1. Geographical location of the study area (according to the China basic geographic information, 2008 version). (a) Study area and distinct distribution. (b) Study area and elevation distribution.

Table 1. Main data materials used in this study.

Data Sources	Used Data	Detailed Information
Geographic information (1:1 million)	District, hydrological layers	The vectorized distinct boundaries and hydrological layers were released in 2008. The hydrological layers, including rivers, streams, and lakes, constrain terrain as natural water bodies when delimitating sub-watersheds.
ASTER GDEM ver. 2 (30 m)	DEM	DEM downloaded from http://www.gscloud.cn. The DEM is the main material used to divide watersheds and extract digital streams. DEM is also used to derive flood risk estimation indicators, such as the slope and the elevation.
China's impervious surface product (2 m)	Water, vegetation, soil, buildings, and roads	China's impervious surface grid product (2 m) (Shao et al. 2019), which contains classification types of water, vegetation, soil, building, and roads, was adopted. And Buildings and roads consist of impervious surfaces. Vegetation and soil represent porous surfaces. Land use types, including water, impervious, and porous surfaces, were used to prepare hydrological indicators.
Images for extracting flooded areas	Water bodies	The GaoFen center of Hubei province supports the GF-3 data. GF-3 extracted the flooding areas on 24 July 2020. Landsat 8 OLI download from https://www.usgs.gov. The Landsat 8 OLI on 20 July 2020 was used to identify water areas before the flooding event.

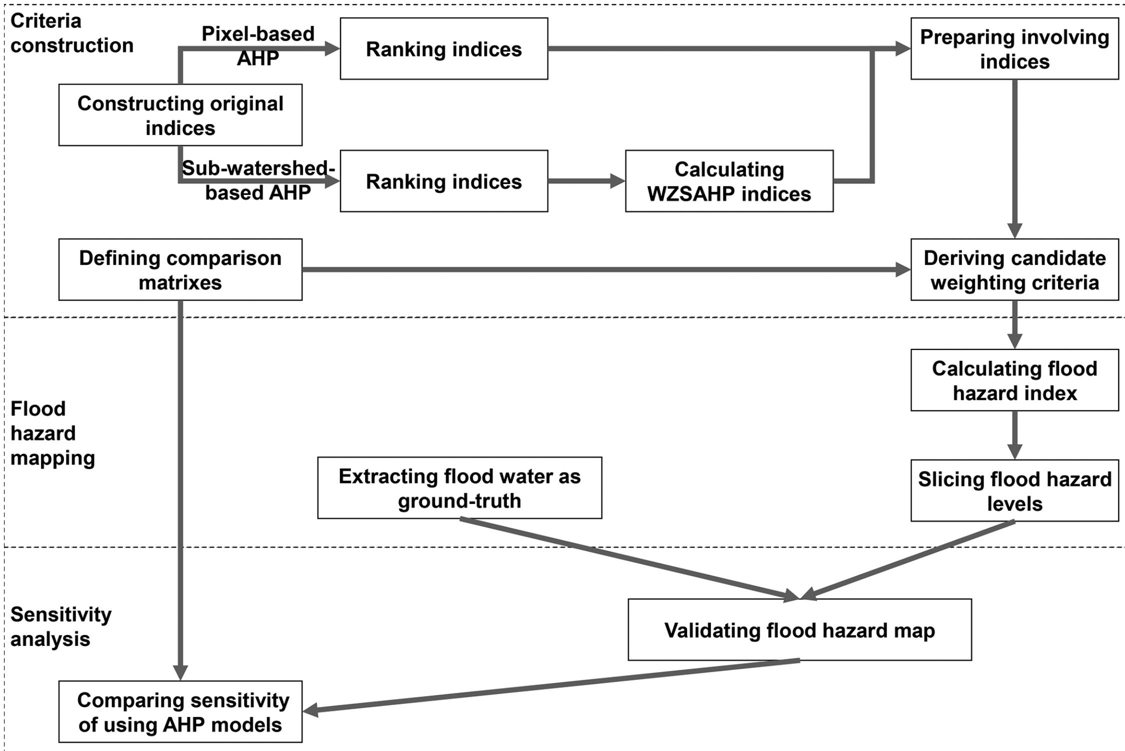

Figure 2. Overall work flow of deriving flood hazard maps and validation data sets in the study.

or no-water areas. After geometrical correction and registration, the Landsat OLI image was adopted to extract water areas by the maximum likelihood method. The water areas extracted by GF-3 and Landsat OLI were considered as the whole water range during the flood event. This water range excludes the normal water area in the 2 m of impervious surface products making up the range of the flood hazard areas.

Methodology

The technical work flow of this study is illustrated as in Figure 2. As shown in Figure 2, based on the definition of the original indices, the initial indicator distribution was ranked according to the distribution representing flood hazard levels. The pixel-based AHP model and the MFD-RC, MFD-All, D8-RC, and D8-All models adopted customized comparison matrixes to derive candidate weighting criteria. The ranking indices and weighting criteria calculated the flood hazard index.

The flood hazard maps of "very high," "high," "normal," "low," and "very low" were sliced by flood hazard index via the natural break method. The union distribution of "high" and "very high" were compared with ground truthing. The flood areas extracted from Landsat 8 OLI and GF-3 in a flood event on July 2021 made up the ground truthing. The sensitivity was analyzed by the fluctuant features of correct(%) and fit(%) (Bathrellos *et al.* 2017) among the models used.

At the criteria construction step, the WZSAHP calculated the maximum statistical value of ranked indices constraining sub-watersheds. At the flood hazard estimation step, the candidate weighting criteria were chosen by a consistency ratio higher than 0.1 (Saaty 2014). At the sensitivity analysis step, the fluctuate feature of correct (%) and fit (%) when judgment matrixes change was considered a performance of weighting criteria deriving sensitivity.

The Basic Theory of Pixel-Based AHP and WZSAHP Models

The pixel-based AHP model adopts pixels as the basic unit and constructs flood hazard estimation assisted by pixel-scale weight vectors from a group of raster layers. The WZSAHP models combine the theory of pixel-based AHP, additionally considered sub-watersheds as a basic unit to constraint-relevant indicators.

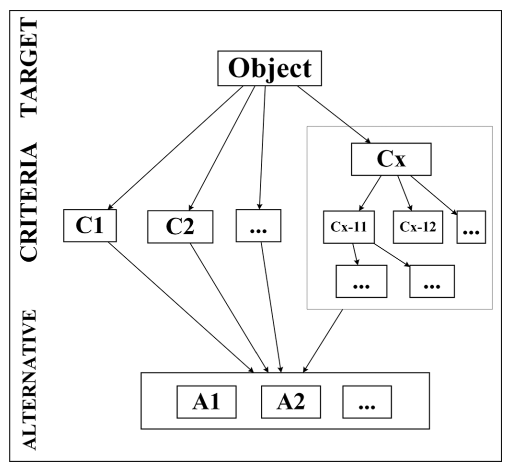

Figure 3. Structure of the AHP method.

The Pixel-Based AHP Model

AHP is composed of three levels—target, criteria, and alternatives—as shown in Figure 3. The target layer refers to the evaluation unit, the criteria (with single or multiple layers) consist of several clusters that reflect different aspects of the target, and the alternative is composed of the estimated results. The flood hazard estimation target, the criteria, and the corresponding watershed are defined as follows:

$$P = \begin{bmatrix} p_{11} & p_{12} & \dots & p_{1n} \\ p_{21} & p_{22} & \dots & p_{2n} \\ \dots & \dots & \dots & \dots \\ p_{m1} & p_{m2} & \dots & p_{mn} \end{bmatrix}, C = \begin{bmatrix} c_1 \\ c_2 \\ \dots \\ c_x \end{bmatrix}, C_x = \begin{bmatrix} c_{11} & c_{12} & \dots & c_{1n} \\ c_{21} & c_{22} & \dots & c_{2n} \\ \dots & \dots & \dots & \dots \\ c_{m1} & c_{m2} & \dots & c_{mn} \end{bmatrix} \quad (1)$$

where matrix P represents the pixel matrix in the study area with a size of $m \times n$ and C is the flood hazard estimation indicator. Each of the indicators C_x suggests a raster layer with a size of $m \times n$.

Then the flood risk index can calculate via Equation 2,

$$\mathrm{FRI} = \omega \cdot C = \sum_{i=1}^{i=n} \omega_i \cdot C_i \tag{2}$$

where FRI is the flood hazard index calculated by the cumulative sum of criteria C (using either original indices c_i and its corresponding weight ω, and n is the number of flood hazard estimation indices.

The WZSAHP Model

The WZSAHP flood hazard estimation method adopts sub-watersheds as the constraint unit to calculate maximum zonal statistical value of relevant indicators. The indices related to runoff converging, such as slope and distance from streams, are constrained by sub-watersheds via Equations 3–4. The flood hazard index calculated via Equation 5,

$$S = \begin{bmatrix} \cdots & & & \\ & S_k & S_k & \\ & & S_k & \\ & & & \cdots \end{bmatrix}_{m \times n} \tag{3}$$

$$F(S, c_x) = \text{zonal statistic } (S, c_x, \text{maximum}) \tag{4}$$

where S is the sub-watershed division raster and $F(S, c_x)$ is the constraint sub-watershed as a statistical zonal unit with updated corresponding indicator c_x. Note that the size of $F(S, c_x)$ is also $m \times n$. The index zonal statistic is calculated using the descriptive statistics of indicator cx for each sub-watershed S, and maximum suggests the maximum statistical method,

$$\mathrm{FRI} = \omega \cdot C = \sum_{i=1}^{i=m} \omega_i \cdot F(S, C_i) + \sum_{j=m+1}^{j=x} \omega_j \cdot C_j, (0 \le m \le x) \tag{5}$$

where FRI is the flood hazard index calculated by the cumulative sum of criteria C using either original index c_j or sub-watershed constraint indices $F(S, c_i)$ and its corresponding weight ω.

Constructing Weighting Criteria and Deriving Flood Risk Maps

Both AHP and WZSAHP for flood hazard estimation are hierarchic evaluation structure methods. They have the following processes: preparing involving indices → deriving candidate weighting criteria → calculating flood hazard index → slicing flood hazard levels.

The positive pairwise judgment matrix uses values from 1 to 9 to indicate the relative importance of two indices (as shown in Table 2). Eigenvector could establish weighting criteria for the hierarchic evaluation structure. The weighting criteria are calculated by the largest eigenvalue of the judgment matrix (Saaty 2014). The hierarchic evaluation structure and the deriving criteria are shown as follows:

$$J = \begin{bmatrix} 1 & j_{12} & \cdots & j_{1x} \\ \frac{1}{j_{12}} & 1 & \cdots & j_{2x} \\ \cdots & \cdots & \cdots & \cdots \\ \frac{1}{j_{1x}} & \frac{1}{j_{2x}} & \cdots & 1 \end{bmatrix}, J \cdot X = \lambda_{\max} \cdot X \rightarrow \omega_i = \frac{x_i}{\sum_{j=1}^{x} x_j}, \omega_p = \begin{bmatrix} \omega_1 \\ \omega_2 \\ \cdots \\ \omega_x \end{bmatrix}_p \tag{6}$$

where the comparison matrix J, with a size of $x \times x$, is used to determine the importance order among criteria (in Equation 1; X is the eigenvector corresponding to the largest eigenvalue $\lambda_{\max}$ of J; and ω is the weight vector corresponding to the normalized value of eigenvector X.

The consistency ratio (CR) indicates the consistency of criteria, which can be calculated following Equation 7 (Saaty 2014). The consistency ratio of a pairwise judgment matrix is the ratio of its consistency index to the corresponding random index value in Table 3. The pairwise comparison matrix can be accepted if its consistency ratio is less than 0.1 (a consistency ratio of 0 indicates that the judgment matrix is entirely consistent),

Table 2. Scales for pairwise comparison (Referring to (Saaty 2014).

Important Levels	Description	Explanation
1	Equal importance	Two activities contribute equally to the objective.
3	Moderate	Experience and judgment slightly favor one activity over another.
5	Strong importance	Experience and judgment strongly favor one activity over another.
7	Very strong importance	An activity is favored very strongly over another, its dominance demonstrated in practice.
9	Extreme importance	The evidence favoring one activity over another is of the highest possible order of affirmation.
2, 4, 6, 8	Intermediate values	The intermediate values of the above values.
Reciprocals	Inverse comparison	A reasonable assumption.

Table 3. Random index (Saaty 2014).

n	1	2	3	4	5	6	7	8	9	10
Random index	0	0	.52	.89	1.11	1.25	1.35	1.40	1.45	1.49

$$\mathrm{CI} = \frac{\lambda_{\max} - n}{n-1}, \mathrm{CR} = \frac{\mathrm{CI}}{\mathrm{RI}} \tag{7}$$

where CR is the consistency ratio, CI is the consistency index, RI is a statistic random index, RI is the average CI of a randomly generated pairwise comparison matrix of similar size (as shown in Table 3), $\lambda_{\max}$ is the largest eigenvalue of the comparison matrix, and n is the number of indicators used in criteria.

Criteria Construction

The indices and the weight criteria constructed the criteria of the AHP models. Both the pixel-based AHP and the WZSAHP models build weighting criteria via a defined judgment matrix.

Preparing Involving Indices

In flood hazard estimation, studies have shown that information regarding topography, hydrology, and geological location is considerably dominant (Kazakis *et al.* 2015; Shariat *et al.* 2019; Nachappa *et al.* 2020; Pham *et al.* 2021). The underlying surface penetration features (e.g., land use type and porous and impervious distribution) drive the rainfall-runoff production. The terrain features, such as elevation, slope, and hydrological systems (e.g., lakes, rivers, and the low-lying wetland areas), may determine the rainwater converging path. They represent the rainwater assembling pressure on the drainage system and thus influence the in situ likelihood of floods occurring.

Constructing original indices: With reference to Bathrellos *et al.* (2017), flood hazard estimation indices were constructed as $C = C_1, C_2, C_3, C_4, C_5$, where C_1 = slope, C_2= elevation, C_3= distance from streams, C_4 = hydro-lithological formations, and C_5 = land use type. The indicators could be considered rain-runoff production indicators, such as hydro-lithological formations, and rainfall-runoff converging indicators, such as slope, elevation and distance from streams.

Ranking indices: The natural distribution of indices needs to be ranked according to flood hazard level to calculate the flood risk index on the same scale. As shown in Tables 4 and 5, the original indices were ranked as a new class of (0–5) to match flood hazard levels of "none," "very low," "low," "normal," "high," and "very high." The slope and elevation factors were ranked by the natural breaking method according to their normal distribution. The factors distance from streams, land-use type, and hydro-lithological formations were ranked via expert experience.

Calculating WZSAHP indices: The WZSAHP models need to also calculate the maximum statistical value of related ranked indicators.

Table 4. Ranking classes of slope, elevation, hydro-lithological formations, and land use. types.

Factors	Classes	Rating	Factors	Classes	Rating
Slope	0	5	Hydro-lithological formations	Water	4
	0–2	4		Impervious surface	3
	2–6	3		Pervious surface	1
	6–12	2			
	12–20	1			
	>20	0			
Elevation (m)	–204–12	5	Land use type	Water	5
	12–23	4		Road	4
	23–46	3		Building	3
	46–152	2		Soil	2
	>152	1		Vegetation	1

Table 5. Ranking classes of *Distance from streams*, including the ranking class of water areas.

Stream Levels	Distance (m)	Rating	Stream Levels	Distance (m)	Rating
1	>500	0	2	>1000	0
	0–500	1		500–1000	1
				0–500	2
3	>1500	0	4	>3,000	0
	1000–1500	1		2000–3000	1
	500–1000	2		1000–2000	2
	0–500	3		0–1000	3
5	>6000	0	Rivers, lakes, and reservoirs	—	5
	4000–6000	1			
	2000–4000	2			
	1000–2000	3			
	0–1,000	4			

Table 6. Original definitions of judgment matrixes (Bathrellos *et al.* 2017). C_1 = slope, C_2 = elevation, C_3 = distance from streams, C_4 = hydro-lithological formation*s*, C_5 = land use type.

Indicators	C_1	C_2	C_3	C_4	C_5
C_1	1	4	1/2	3	1/2
C_2		1	1/3	1/2	1/4
C_3			1	3	1
C_4				1	1/3
C_5					1

Table 7. Definitions of judgment matrixes for involved criteria, C_1 = slope, C_2 = elevation, C_3 = distance from streams, C_4 = hydro-lithological formation*s*, C_5 = land use type.

Indicators	C_1	C_2	C_3	C_4	C_5
C_1	1	{4, 5, 6, 7, 8, 9}	{1/2, 1/3}	3	1/2
C_2		1	{1/3, 1/4, 1/5, 1/6}	1/2	1/4
C_3			1	3	1
C_4				1	1/3
C_5					1

MFD-All constrained MFD-derived sub-watersheds to all indicators. MFD-RC restrained MFD-derived sub-watersheds to slope, elevation, and distance from streams. D8-All used D8-derived sub-watersheds as a basic unit to calculate the maximum statistical values of each ranked indicator. In contrast, D8-RC constrained D8-derived sub-watersheds to slope, elevation, and distance to streams.

Defining Comparison Matrixes

The initial comparison matrix definition was referenced to work Bathrellos *et al.* (2017), as shown in Table 2. For the WZSAHP models, the flood hazard estimation results would be more obviously influenced by the rainfall-runoff converge indicators than the rainfall-runoff production indicators.

This study focuses on investigating the sensitivity of the pairwise judgment matrix definition of rainfall-runoff convergence targeting in flood hazard estimation results. The comparison element might be defined following the order of distance from streams > slope > elevation. The comparison element related to rainfall-runoff production was the same as the original definition in Bathrellos *et al.* (2017). Only the judgment matrix that can maintain consistency will be used to build candidate weighting criteria.

Following the candidate judgment matrix definition, the final available selection of comparison elements is shown in Table 7. The choice of the pairwise element of (slope, elevation) was in a set of {*4, 5, 6, 7, 8, 9*}, and the option of element (slope, elevation) was in a set of {*1/2, 1/3*}. The candidate value of (slope, elevation) was in a set of {*1/3, 1/4, 1/5, 1/6*}. Therefore, there were a total of 48 different judgment matrix definitions: $48 = C_6^1 \cdot C_2^1 \cdot C_4^1$.

Deriving Flood Risk Maps

For the pixel-based AHP, MFD-RC, MFD-All, D8-RC, and D8-All models, the flood risk indexes could be calculated by Equations 8–12,

$$\mathrm{FRI}(p)_{\mathrm{AHP}} = \sum_{j=1}^{j=5} \omega_{pj} \cdot C_{\mathrm{j}} \tag{8}$$

$$\mathrm{FRI}(p)_{\mathrm{MFD-All}} = \sum_{j=1}^{j=5} \omega_{pj} \cdot F(S_{\mathrm{MFD}}, C_j) \tag{9}$$

$$\mathrm{FRI}(p)_{\mathrm{MFD-RC}} = \sum_{0}^{j} \omega'_{pj} \cdot F(S_{\mathrm{MFD}}, C') + \sum_{i}^{5} \omega'_{pi} \cdot C' \tag{10}$$

$$\mathrm{FRI}(p)_{\mathrm{D8-All}} = \sum_{j=1}^{j=5} \omega_{pj} \cdot F(S_{D8}, C_j) \tag{11}$$

$$\mathrm{FRI}(p)_{\mathrm{D8-RC}} = \sum_{0}^{j} \omega'_{pj} \cdot F(S_{\mathrm{D8}}, C') + \sum_{i}^{5} \omega'_{pi} \cdot C'' \tag{12}$$

where, given the project number p, the estimation indicators are recorded as $C = C_1, C_2, C_3, C_4, C_5$, ωpj is the weight of indicator C_j of the weighting criteria of number p (information on $F(S, C)$ can be found in Equation 4), S_{D8} represents the D8 algorithm divided sub-watersheds, S_{MFD} represents the MFD algorithm delimitated sub-watersheds, C' means the indicators of slope and distance from streams, C'' describes the rest factors, and ω'_{pj} and the ω''_{pi} are responding weight elements of C' and C'', respectively.

This study produced flood risk maps via flood hazard indexes slicing by the natural break method. Each flood map consisted of five classes labeled, respectively, as "very low" (class 1), "low" (class 2), "normal" (class 3), "high" (class 4), and "very high" (class 5).

Validating Flood Risk Estimation Results

The correct and fit ratios were used to assess flood hazard estimation accuracy following Alfier *et al.* (2014) and Bates and De Roo (2000). They indicated the differences in weighting criteria influence among used models:

$$\text{Correct (\%)} = \frac{FA_{\mathrm{FRI}} \cap FA_{\mathrm{Water}}}{FA_{\mathrm{Water}}} \times 100 \tag{13}$$

$$\text{Fit (\%)} = \frac{FA_{\mathrm{FRI}} \cap FA_{\mathrm{Water}}}{FA_{\mathrm{FRI}} \cup FA_{\mathrm{Water}}} \times 100 \tag{14}$$

where Correct (%) is the correct ratio, Fit (%) is the fit ratio, FAFRI suggests areas with a high likelihood of being flooded, and FAWater represents the flood cells extracted from the GF-3 and Landsat 8 OLI images excluded the permanent water areas following (Shao *et al.* 2018).

In this study, the flood hazard levels of "high" and "very high" were considered as true to calculated correct (%) via validation water area. The flood risk levels of "very low," "low," and "normal" were considered as false to calculate Fit (%) by validation none water areas.

Results

Performance Differences Among Models

The histograms compared the increasing value of the correct and fit ratios of the WZSAHP models with the pixel-based AHP model (Figure 4). The bar diagram of Figure 4a and 4b, respectively, shows the relative correct and fit ratios as weighting criteria changed, while Figure 4c and 4d, respectively, shows the relative correct and fit ratio referring to the weighting criteria of Pr. 1.

Figure 4a indicates that the correct ratios of WZSAHP models are higher than the pixel-based AHP model, and the order of correct ratios was D8-All > MFD-RC > D8-RC > MFD-All.

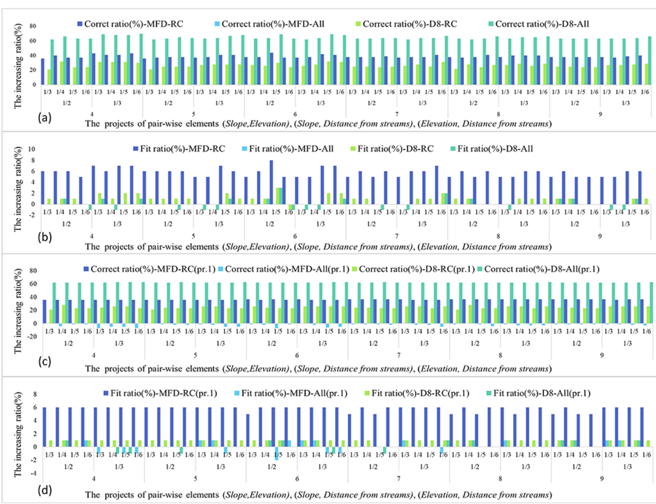

Figure 4. Performance comparison of changing criteria definitions between the pixel-based AHP with the four WZSAHP-related models. (a) Increase of the correct ratio. (b) Increase of the fit ratio of WZSAHP models reference pixel-based AHP using the changed candidate weighting criteria. Increase of correct ratio (c) and increase of fit ratio (d) of WZSAHP models compared with the pixel-based AHP using fixed weighting criteria of Pr. 1.

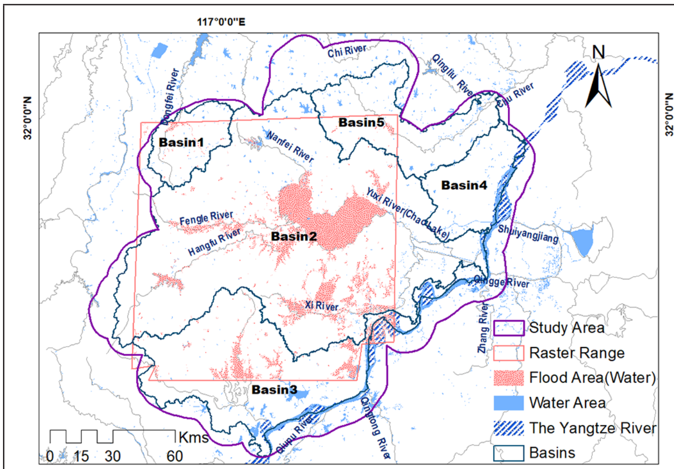

Figure 5. Distribution of the five basins in the study area.

As shown in Figure 4b, as the candidate weighting criteria changed, the increasing values of the fit ratio estimated by MFD-RC remained higher than that of the pixel-based AHP, while the fit ratio calculated by MFD-All, D8-RC, and D8-All was higher than that of the pixel-based AHP.

As shown in Figure 4c, considering the setting of the pixel-based AHP weighting criteria of Pr. 1 as a reference, the increasing correct ratio of MFD-RC, D8-RC, and D8-All was higher than that of the pixel-based AHP, and the MFD-All model always had an equal or lower correct ratio than that of the pixel-based AHP.

As shown in Figure 4d, considering the setting of the pixel-based AHP weighting criteria of Pr. 1 as a reference, the increasing fit ratio of MFD-RC always remained higher than that of the pixel-based AHP.

Influence of Weighting Criteria Definitions in MFD-RC

In this subsection, flood hazard distribution influenced by judgment matrixes among different types of basins is discussed. The outlets of the Chaohu Basin in the study area are Chao Lake and the Yangtze River, as shown in Figure 5. Three sub-basins, denoted as Basin 1, Basin 2, and Basin 3, were used for further analysis.

Figure 5 shows that Basin 1 contained no outlet, meaning that the collected rainwater flows away from the study area. Basin 2 contains Chao Lake and the Yangtze River. For the low-lying areas surrounding the Yangtze River and Chao Lake, the high water level resulted in flooding. Basin 3 was located on the north side of the Yangtze River.

Taking Basins 1–3 as mask layers, distributions of flood hazard levels are shown in Figures 6–8, respectively. The flood hazard maps were designed to follow a five-color schema: {green, light Green, yellow, orange, red} to map flood hazard levels of {"very low," "low," "normal," "high," "very high"}, respectively. As shown in Figures 6–8, the distribution of flood hazard levels was similar when using candidate weighting criteria.

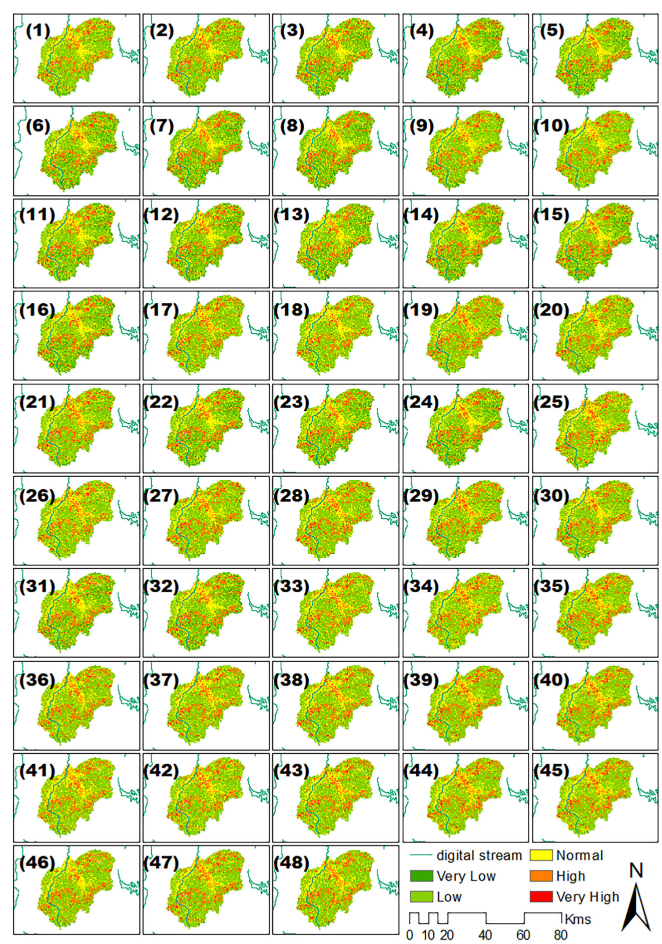

Figure 6. Distribution of flood hazard levels of Basin 1 derived by the MFD-RC via WZSAHP.

The pie charts and curve diagrams (Figure 9) show the statistical flood hazard distribution derived by 48 weighting criteria. The pie charts (Figure 9(1)–(3)) were the average flood hazard ratios of the whole weighting criteria, while the curves diagrams (Figure 9(a)1–(e)3) were the contrastive flood hazard pixels classified by pairwise element (slope, elevation) in a set of 4, 5, 6, 7, 8, 9.

Figures 9(a)1–(e)1, 9(a)2–(e)2, and 9(a)3–(e)3 show the flood hazard distribution of Basins 1–3, respectively. For Basins 2 and 3, the cure diagrams had similar fluctuated features influenced by comparison matrixes. The two basins contained similar terrain features near the Yangtze River. The results indicated that the MFD-RC reflected similar high likelihood distributions not influenced by candidate comparison matrixes.

Estimated Flood Hazard Levels Among Investigated Methods

In this study, the 48 definitions of weighting criteria (i.e., the comparison element definition for *S/E*, *S/R*, and *E/R* calculating weight criteria) were coded by projects, and the derived flood hazard maps were compared, as shown in Figure 10.

For the pixel-based AHP and WZSAHP models, the distribution pixel amount of five flood hazard levels estimated by candidate weighting criteria at the basin level were drawn in perspective view as 3D histograms (Figure 10(a)–(e)). The X-axis denotes comparison elements of weighting criteria for Basins 1–5. The Y-axis shows the accumulated flood hazard value of the basins. Meanwhile, for the pixel-based AHP, MFD-RC, MFD-All, D8-RC, and D8-All, Figure 10(a)′–(e)′, respectively, shows the curve diagrams of the flood hazard ratio to the accumulated flood hazard level value for each of the 48 weighting criteria. The X-axis denotes the comparison matrix of the weighting criteria. In contrast, the Y-axis denotes the flood hazard levels ratio to the accumulated values of all projects.

Discussion

This section discusses the performance of flood hazard influenced by drived by judgement definitions among pixel-based AHP, MFD-RC, and other WZSAHP models.

Flood Hazard Distribution via Pixel-Based AHP Influenced by Weighting Criteria

As shown in Figure 4, it indicated that the MFD-RC always had higher correct and fit ratios than the pixel-based AHP. As shown in Figure 10a and 10a′, the statistical distribution flood hazard levels derived by the pixel-based AHP were changed as the weighting criteria were reassigned. For "high" and "very high" pixels, among the candidate weighting criteria, the change regulation of MFD-RC (Figure 10b and 10b′) and D8-RC (Figure 10d and 10d′) could be observed to remain steady. For "very low," "low," and "normal" distributions, the flood risk level distribution of MFD-All (Figure 10c and 10c′) and D8-All (Figure 10e and Figure 10e′) indicated as similar as weighting criteria changing. The flood hazard distribution demonstrated that all the WZSAHP models got a higher or equal correct ratio than the pixel-based AHP and that the MFD-RC could improve both correct and fit ratios compared with the pixel-based AHP.

Flood Hazard Distribution via MFD-RC Influenced by Weighting Criteria

As shown in Figure 6, it can be noticed that the flood hazard level of the start of the Dongfei River was recognized as "normal." There were "high" and "very high" areas distributed west to east at the bottom part of Basin 1. There were "high" and "very high" areas distributed at the top edge of the north part of Basin 1. This phenomenon showed that the MFD-RC estimated "high" or "very high" areas that do not directly rely on the factor of distance from streams.

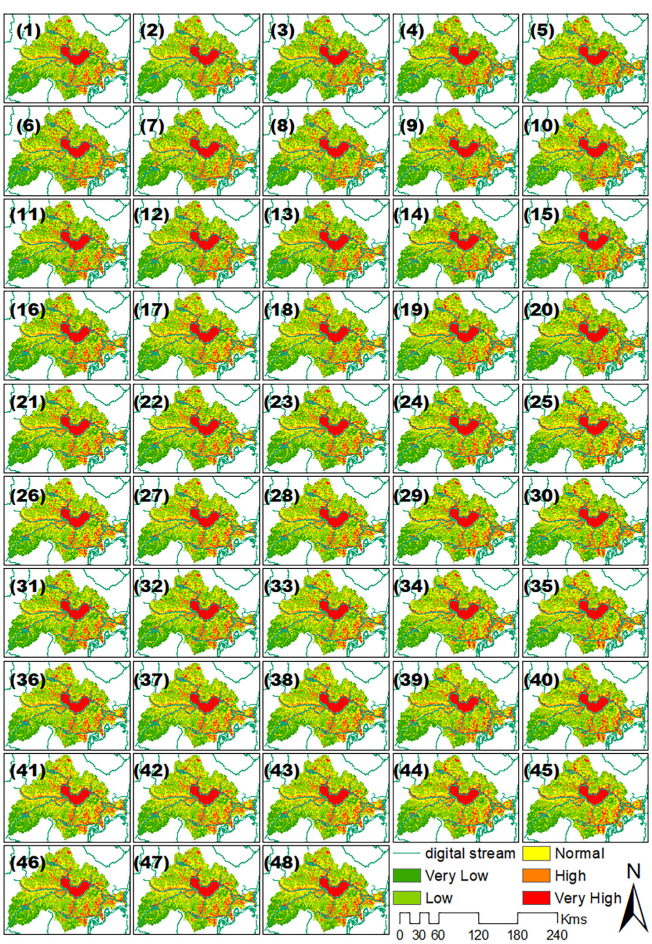

Figure 7. Distribution of flood hazard levels of Basin 2 derived by the MFD-RC via WZSAHP.

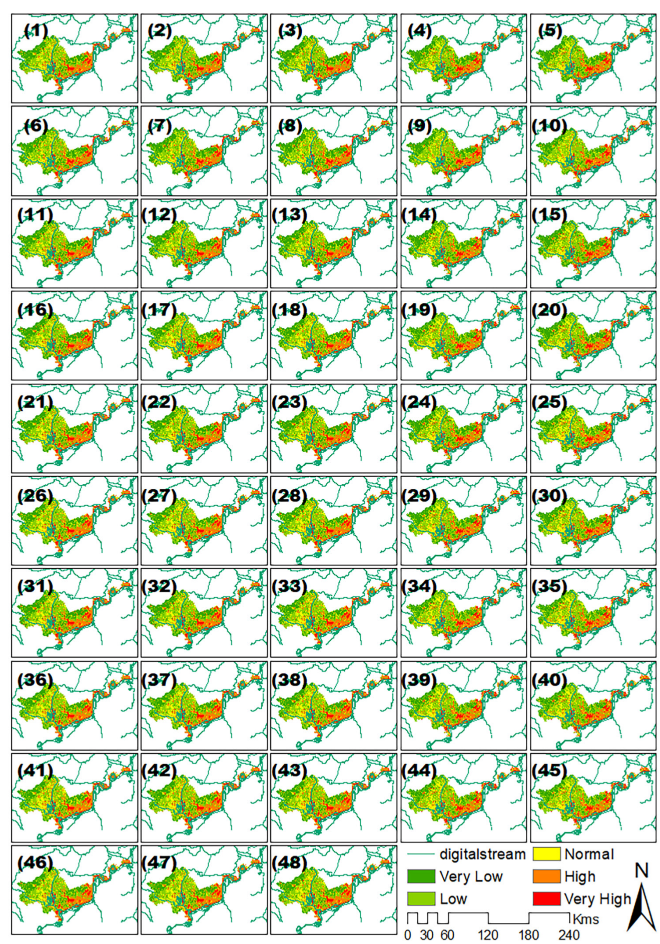

Figure 8. Distribution of flood risk levels in Basin 3, derived by the MFD-RC via WZSAHP.

As shown in Figure 7, the flood hazard distribution of Basin 2 indicated the "high" and "very high" areas distributed nearby rivers in Basin 2. Especially at the bottom of Basin 2, there were larger areas at the north beach of the Yangtze River classified as "high" and "very high" than other rivers shown in the hydrology network. This result indicated that the MFD-RC might consider the influence of local terrain distribution on flood hazard maps for river-intertwined areas.

As shown in Figure 8, the flood hazard distribution of Basin 3 was recognized as "high" and "very high" near the Yangtze River compared to the south part nearby the Yangtze River. It demonstrated that the MFD-RC could distinguish between the flood hazard differences for local terrain distribution and a certain distance to the hazard risk source.

MFD-RC Is an Optimal Model Compared with Other WZSAHP Models

Using the sub-watershed as a unit to constrain flood hazard estimation indicators might consider the similar flood hazard level brought by adjacent pixels in the same sub-watershed. Referring to the correct ratio consistently increased, while the fit ratio fluctuates, as using WZSAHP and the WZSAHP-RC (i.e., MFD-RC, D8-RC) might improve correct and fit ratios well, as in the low level of flood hazard distribution. It showed that all the WZSAHP models would derive sensitivity of high-hazard level areas, while using WZSAHP-RC would further increase the accuracy of low-hazard level areas. Reasons for MFD-RC being more optimal than other WZSAHP models are the following:

1. The sub-watershed reflects the rainwater converting feature but did not influence the rainfall-runoff production process. Therefore,

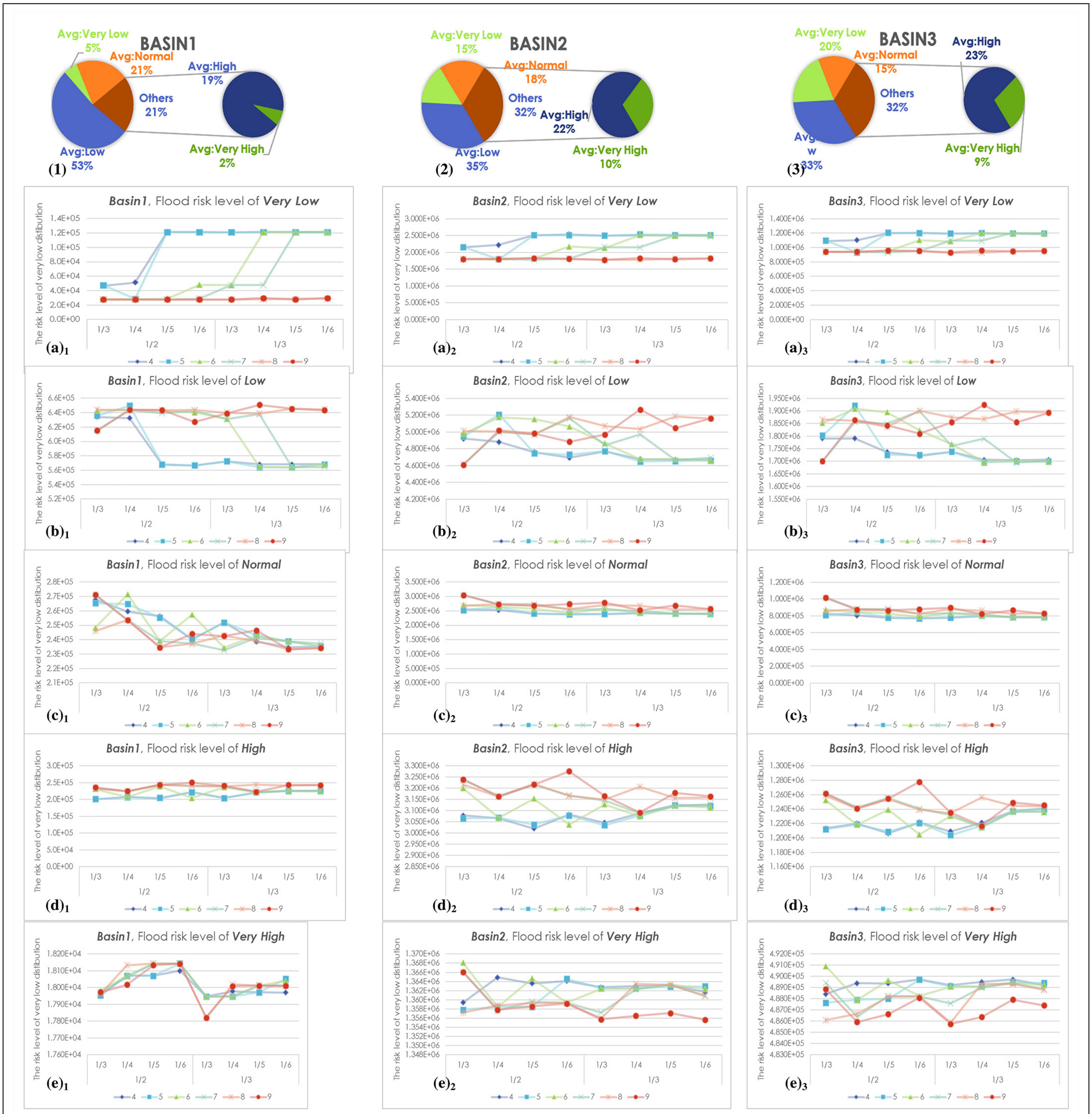

Figure 9. Quality of pixels grouped by flood risk levels in Basins 1–3.

using the sub-watershed to constrain the converging rainwater indicators (i.e., slope, elevation, and distance from streams in this study) might be more reasonable than a constraint to all indicators.

2. The MFD algorithm focuses on sink areas converging from all the higher pixels of neighborhood pixels (Zhang *et al.* 2019), while the D8 algorithm adopts the most gradient drop pixels to determine to converge path. In this perspective, the sub-watershed delimitated by MFD might focus on sink areas and perhaps be closer to the nature overflow process than D8, leading to the MFD-RC overmatching the D8-RC.

Conclusion

This study compared the sensitivity to weighting criteria between pixel-based AHP and sub-watershed-based AHP models (including MFD-RC, MFD-All, D8-RC, and D8-All). Taking the Chaohu Basin in Anhui Province, China, as the study area, the accuracy of sensitivity for three typical sub-basins was discussed. Following the same weighting criteria order, this article discussed 48 judgment matrix–derived correct and fit ratios.

The results indicate that the pixel-based AHP model is more sensitive to weighting criteria than sub-watershed-based AHP models. As the weighting criteria change, the MFD-RC model always gets better and steady correct and fit ratios. However, as the weighting criteria change, the correct and fit ratios derived by the pixel-based AHP, MFD-All, D8-RC, and D8-All may fluctuate.

Compared with the pixel-based AHP, the results demonstrate that the sub-watershed-based AHP may have an advantage in flood risk estimation, relying less on expert criteria. There is still room for further investigation and discussion on the mathematical principles and internal mechanisms of the hydrologic process of this finding.

Acknowledgments

This work was supported in part by the National Key R&D Program of China (grant number 2018YFB2100501) the Fundamental Research Funds for the Central Universities (grant number 2042021kf0007), the Open Grants of the State Key Laboratory of Severe Weather (grant number 2021LASW-A17) the National Natural Science Foundation of China under Grants 42090012, 03 special research and 5G project of Jiangxi Province in China (20212ABC03A09), Zhuhai industry university research cooperation project of China (ZH22017001210098PWC), Sichuan Science and Technology Program 2022YFN0031) and the LIESMARS Special Research Funding. The authors would like to thank the anonymous reviewers and editors for their comments, which helped us improve this article significantly..

References

Abdulkareem, J. H., B. Pradhan, W.N.A. Sulaiman, and N. R. Jamil. 2018. Quantification of runoff as influenced by morphometric characteristics in a rural complex catchment. *Earth Systems and Environment* 2(1):145–162.

Ali, S. A., F. Parvin, Q. B. Pham, M. Vojtek, J. Vojteková, R. Costache, N.T.T. Linh, H. Q. Nguyen, A. Ahmad, and M. A. Ghorbani. 2020. GIS-based comparative assessment of flood susceptibility mapping using hybrid multi-criteria decision-making approach, naïve Bayes tree, bivariate statistics and logistic regression: A case of Topvla basin, Slovakia. *Ecological Indicators* 117:106620. doi:10.1016/j.ecolind.2020.106620.

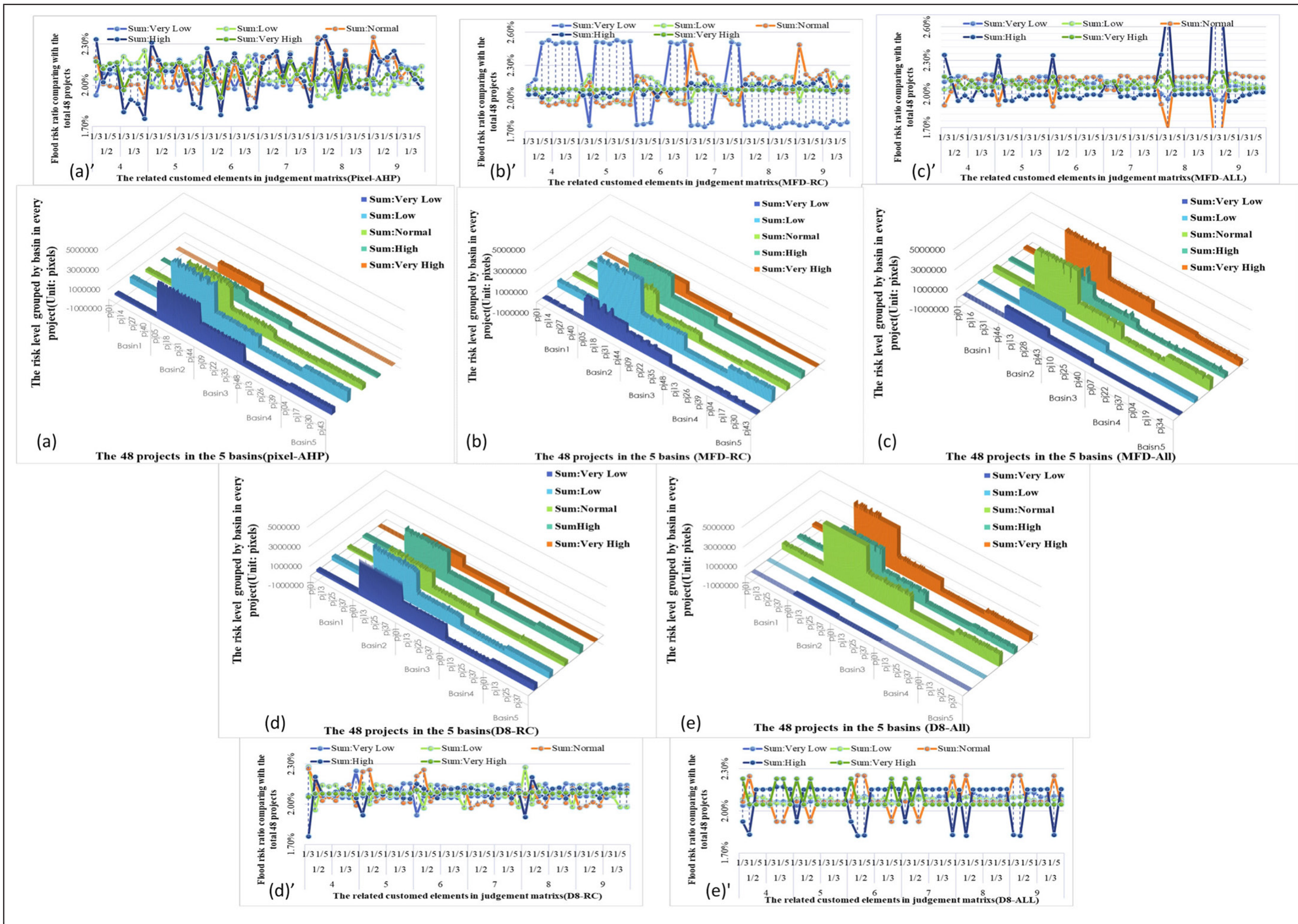

Figure 10. Flood hazard distribution of each project. (a)–(e) Count of each hazard level. (a)′–(e)′ Ratios of total projects for each flood hazard level in the five basins.

Anhui Net. 2020. What's New! the Water Level of Chaohu Lake Is Expected to Drop to 13.00m on the 31st. <http://hch.ahwang.cn/chnews/20200731/2134559.html>.

Bates, P. D. and A. De Roo. 2000. A simple raster-based model for flood inundation simulation. *Journal of Hydrology* 236(1–2):54–77.

Bathrellos, G. D., H. D. Skilodimou, K. Chousianitis, A. M. Youssef, and B. Pradhan. 2017. Suitability estimation for urban development using multi-hazard assessment map. *Science of the Total Environment* 575:119–134.

Betancourt-Suárez, V., E. Garćıa-Botella, and A. Ramon-Morte. 2021. Flood mapping proposal in small watersheds: A case study of the Rebollos and Miranda Ephemeral Streams (Cartagena, Spain). *Water* 13(1):102.

Costache, R., Q. B. Pham, M. Avand, N. T. Thuy Linh, M. Vojtek, J. Vojteková, S. Lee, D. N. Khoi, P. T. Thao Nhi, and T. D. Dung. 2020. Novel hybrid models between bivariate statistics, artificial neural networks and boosting algorithms for flood susceptibility assessment. *Journal of Environmental Management* 265:110485. doi:10.1016/j.jenvman.2020.110485.

Ekmekcioglu, O., K. Koc, and M. Ozger. 2021. District based flood risk assessment in Istanbul using fuzzy analytical hierarchy process. *Stochastic Environmental Research and Risk Assessment* 35(3):617–637.

Ghosh, A. and S. K. Kar. 2018. Application of analytical hierarchy process (AHP) for flood risk assessment: A case study in Malda district of West Bengal, India. *Natural Hazards* 94(1):349–368.

Kanani-Sadat, Y., R. Arabsheibani, F. Karimipour, and M. Nasseri. 2019. A new approach to flood susceptibility assessment in data-scarce and ungauged regions based on GIS-based hybrid multi criteria decision-making method. *Journal of Hydrology* 572:17–31.

Kazakis, N., I. Kougias, and T. Patsialis. 2015. Assessment of flood hazard areas at a regional scale using an index-based approach and analytical hierarchy process: Application in Rhodope–Evros region, Greece. *Science of the Total Environment* 538:555–563.

Koc, K., Ö. Ekmekcioglu, and M. Özger. 2021. An integrated framework for the comprehensive evaluation of low impact development strategies. *Journal of Environmental Management* 294:113023. doi:10.1016/j.jenvman.2021.113023.

Liu, P., B. Zhu, and P. Wang. 2021. A weighting model based on best–worst method and its application for environmental performance evaluation. *Applied Soft Computing* 103:107168.

Mishra, K. and R. Sinha. 2020. Flood risk assessment in the Kosi megafan using multi-criteria decision analysis: A hydro geomorphic approach. *Geomorphology* 350:106861.

Nachappa, T. G., S. T. Piralilou, K. Gholamnia, O. Ghorbanzadeh, O. Rahmati, and T. Blaschke. 2020. Flood susceptibility mapping with machine learning, multi-criteria decision analysis and ensemble using Dempster Shafer theory. *Journal of Hydrology* 590:125275.

Nguyen, H. X., A. T. Nguyen, A. T. Ngo, V. T. Phan, T. D. Nguyen, V. T. Do, D. C. Dao, D. T. Dang, A. T. Nguyen, T. K. Nguyen, and L. Hens. 2020. A hybrid approach using GIS-based fuzzy AHP-TOPSIS assessing flood hazards along the South-Central Coast of Vietnam. *Applied Sciences* 10(20):7142.

Ohnishi, S.-I., and H. Imai. 1998. Evaluation for a stability of fuzzy decision making using a sensitivity analysis. Pages 86–90 in *1998 Conference of the North American Fuzzy Information Processing Society-NAFIPS (Cat. No. 98TH8353)*.

Ohnishi, S.-I., T. Yamanoi, and H. Imai. 2011. A fuzzy representation for non-additive weights of AHP. Pages 672–675 in *2011 IEEE International Conference on Fuzzy Systems (FUZZ-IEEE 2011)*, held in Taipei, Taiwan.

Rahman, M., N. Chen, M. M. Islam, G. I. Mahmud, H. R. Pourghasemi, M. Alam, M. A. Rahim, M. A. Baig, A. Bhattacharjee, and A. Dewan. 2021. Development of flood hazard map and emergency relief operation system using hydrodynamic modeling and machine learning algorithm. *Journal of Cleaner Production* 311:127594. doi:10.1016/j.jclepro.2021.127594.

Pham, B. T., C. Luu, D. Van Dao, T. Van Phong, H. D. Nguyen, H. Van Le, J. von Meding, and I. Prakash. 2021. Flood risk assessment using deep learning integrated with multi-criteria decision analysis. *Knowledge-Based Systems* 219:106899.

Saaty, T. L. 2014. Decision making—The analytic hierarchy and network processes (AHP/ANP). *Journal of Systems Science and Systems Engineering* 13(1):1–35.

Shao, Z., H. Fu, D. Li, O. Altan, and T. Cheng. 2019. Remote sensing monitoring of multi-scale watersheds impermeability for urban hydrological evaluation. *Remote Sensing of Environment* 232:111338.

Shariat, R., A. Roozbahani, and A. Ebrahimian. 2019. Risk analysis of urban stormwater infrastructure systems using fuzzy spatial multi-criteria decision making. *Science of the Total Environment* 647:1468–1477.

Skilodimou, H. D., G. D. Bathrellos, K. Chousianitis, A. M. Youssef, and B. Pradhan. 2019. Multi-hazard assessment modeling via multi-criteria analysis and GIS: A case study, *Environmental Earth Sciences* 78(2):47.

Wang, Y., X. Xie, S. Liang, B. Zhu, Y. Yao, S. Meng, and C. Lu. 2020. Quantifying the response of potential flooding risk to urban growth in Beijing. *Science of the Total Environment* 705:135868.

Zarei, A. R., M. M. Moghimi, and E. Koohi. 2021. Sensitivity assessment to the occurrence of different types of droughts using GIS and AHP techniques. *Water Resources Management* 35(11):3593–3615.

Zhang, H., X. Cheng, L. Jin, D. Zhao, T. Feng, and K. Zheng. 2019. A method for estimating urban flood-carrying capacity using the VIS-W underlying surface model: A case study from Wuhan, China. *Water* 11(11):2345. doi:10.3390/w11112345.

Zhang, H., X. Cheng, L. Jin, D. Zhao, T. Feng, and K. Zheng. 2020. A method for dynamical sub-watershed delimitating by no-fill digital elevation model and defined precipitation: A case study of Wuhan, China. *Water* 12(2):486. doi:10.3390/w12020486.